An ultraviolet fibre-cavity for strong ion-photon interaction

Timothy George Ballance

Magdalene College
University of Cambridge

October 2016

This dissertation is submitted for the degree of
Doctor of Philosophy

Declaration

I hereby declare that dissertation is the result of my own work and includes nothing which is the outcome of work done in collaboration except as declared in the preface and specified in the text. This dissertation is not substantially the same as any that I have submitted, or, is being concurrently submitted for a degree or diploma or other qualification at the University of Cambridge or any other University or similar institution. I further state that no substantial part of my dissertation has already been submitted, or, is being concurrently submitted for any such degree, diploma or other qualification at the University of Cambridge or any other University of similar institution. This dissertation contains fewer than 60,000 words including summary, abstract, tables, footnotes and appendices.

Timothy George Ballance
October 2016

Acknowledgements

I would like to thank my supervisor Professor Michael Köhl for providing me with this great opportunity to work in a skilled and well equipped laboratory on such an exciting and cutting-edge experiment. In this environment I have been able to learn an awful lot, and I am very grateful for this.

I would also like to thank my colleague and friend Hendrik-Marten Meyer for his enthusiasm, patience and dedication. Over the years, we have worked closely together, and I will never forget the day (and night) that we managed to successfully install the fibre-cavity into the experiment.

During my PhD I have had the pleasure of working along side many people in Ion-Cavity lab to whom I am thankful, Matthias Steiner, Robert Maiwald, Jonathan Silver, Leonardo Carcagnì, Andreas Kell and Ashwin Boddeti. I would especially like to thank Jonathan and Ashwin for the many long evenings and weekends we have spent together in the lab discussing all manor of problems. I am also thankful for the company of the next-generation Ion-Cavity experimentalists, Kilian Kluge and Pascal Kobel, who I am sure will lead the group into a new era of success.

I would like to thank my colleagues who work with cold Fermi gases for their friendship, Alexandra Behrle, Tim Harrison, Eugenio Cocchi, Luke Miller, Daniel Pertot and Carl Cheung. Similarly Jan Drewes, Gao Kuiyi, Jeffrey Chan, Marcell Gall and Martin Link. I would also like to thank our group administrator in Bonn, Tina Naggert, and in Cambridge, Pam Smith, who have both provided an immense amount of help during my time in the group.

Finally, I am truly grateful to my parents, my two brothers, my Aunt Shirley and my girlfriend Sonia for their encouragement and support throughout my PhD. I can't imagine life without them.

Abstract

An ultraviolet fibre-cavity for strong ion-photon interaction
Timothy George Ballance, Magdalene College, University of Cambridge, 2016.

We investigate the coupling of a single trapped ion to a miniature optical cavity operating in the ultraviolet. Our cavity provides a source of single photons at a high rate into a single spatial mode. Using our apparatus, we have demonstrated the highest atom-cavity coupling rate achieved with a single ion by an order of magnitude. When the ion is continuously excited, we observe phase-sensitive correlations between emission into free-space and into the cavity mode, which can be explained by a cavity induced back-action effect on a driven dipole. We demonstrate coherent manipulation of a hyperfine qubit and ultra-short optical π rotations, which are essential tools for creation and detection of spin-photon entanglement.

To this end, we have developed optical fibre-based Fabry-Pérot cavities in the ultraviolet spectral range. These cavities operate near the primary dipole transition of Yb^+ at 370 nm, and allow us to couple a pure atomic two-level system offered by a single trapped ion to the cavity mode. A new Paul trap apparatus in an ultra-high vacuum chamber has been built which allows for the integration of these cavities at very small ion-mirror separations. In order for independent operation of the trap, a compact system of diode lasers has been built which are stabilised to low-drift optical reference cavities. Coherent control of the hyperfine qubit in $^{171}Yb^+$ is achieved through application of microwave radiation, and ultra-short optical π rotations are performed with resonant light pulses derived from a frequency-doubled mode-locked titanium-sapphire laser. The experiment is controlled through a system of hardware and software which has been developed in a modular fashion and will allow for efficient control on the nanosecond time-scale when several such systems are interconnected.

The success of our system opens the door to future experiments with trapped ions which will reach the strong coupling regime with a single ion. Furthermore, when operated in the fast-cavity regime, systems based on our approach will enable high-efficiency collection of photons from the ion into the single mode of an optical fibre. These systems will allow for the generation of distributed entanglement and will prove ideal as nodes in a larger quantum network of trapped ions.

Contents

Chapter 1

Introduction

At the turn of the 20th century the first discoveries were made which pointed towards the universe's quantised nature. Since that time, quantum mechanics has become one of the fundamental pillars of modern physics and has dramatically changed the way we view our world.

Despite the apparent maturity of the theory of quantum mechanics, it still has more to offer: the second quantum revolution is upon us [1]. Over the past two decades there has been increasing interest in the engineering of quantum systems to produce new technologies whose operation is governed by the laws of quantum mechanics. Known as *quantum technology*, these devices promise numerous benefits including computers able to solve certain problems in shorter times than currently possible (quantum computers [2]), improved precision metrology (quantum metrology [3]) and provably secure communication channels (quantum cryptography [4]).

While each of these applications provide improvements over classical implementations, their performance can be enhanced by coherently combining several spatially separate nodes to form a *quantum network* [5]. To realise such a network, one requires technology which can convert quantum states between physical systems in a reversible manner, so called *quantum interconnects*. The natural medium for building these interconnects in large networks is the photon, as single photons allow the faithful transfer of quantum information due to their relatively weak interaction with the environment. However, as a result of their low interaction strength in general, interfacing single photons with the stationary systems which form the nodes in the network presents a major technical challenge, and one which depends heavily on the chosen stationary system. In recent years a great many systems have been studied as possible candidates for the processing and storage of quantum information. Promising candidates include

superconducting Josephson junctions [6], quantum dots [7], nitrogen-vacancy (NV) centres in diamond [8], trapped atoms [9], and trapped ions [10].

One way to transfer quantum information across a network is to map the quantum state of one node, the **stationary qubit**, onto a single photon, a **flying qubit**, and then perform a further mapping from the photon onto the second node. In this way, the state is directly transferred between the two nodes via the photon. Although conceptually simple to understand, the fidelity of the resulting quantum state transfer process is determined by the quality of the transport: any loss in the photon channel will directly impact the fidelity. In practice, the task of producing a high enough fidelity process with direct transfer presents an almost insurmountable challenge with current technology.

A second, more practical, approach uses the properties of entangled quantum systems. With a maximally entangled state, known as a Bell state, it is possible to transfer quantum information via a process called *quantum teleportation* [11]. This technique has been experimentally verified in several systems including with photons [12], nuclear magnetic resonances [13], and trapped ions [14, 15]. The real benefit of this approach over a direct transfer scheme is that the entangled state, also known as an Einstein-Podolsky-Rosen (EPR) pair, can be created independently of the quantum state to be transferred. If the quantum state is only transferred after successful creation of the entangled state, then the quality of the state transfer process can be very high even in the presence of significant losses in the transfer channel.

Development of a network based on quantum teleportation therefore requires generation of entangled states, and these states should be viewed as a fundamental resource for the distribution of quantum information. The physics of entangled states has been extensively investigated in an experimental setting using pairs of polarisation-entangled photons, first generated by atomic decay [16], and then more recently via spontaneous parametric down-conversion (SPDC) [17]. Recently, SPDC sources have opened up the possibility of experimental implementations of quantum teleportation over kilometre long distances [18, 19]. Although schemes have been proposed which can extend SPDC-based quantum teleportation networks to encompass several nodes [20], these approaches generally suffer from the problem that the EPR pairs are produced randomly and cannot be stored. In order to scale up quantum networks to operate over larger distances, it appears that storage of the states as stationary qubits will be a requirement.

Generation of an entangled state with stationary qubits in separate devices was first demonstrated using trapped ions [21], but have since also been generated with neutral atoms [22], NV centres [23], and quantum dots [24]. The approach used to generate the entanglement in most of these cases is to produce a photon from each device, each of which has a degree of freedom

which is entangled with the resulting state of the stationary system. For example, in the case of trapped ions in [21] this was achieved with photons whose energy state was entangled with the hyperfine spin state of the ion. If each system produces otherwise indistinguishable photons, and they are both incident on a non-polarising beam splitter, then detection of exactly one photon on each arm of the splitter will project the atomic states into a Bell state. In addition to the projection, the detection also provides a herald for the successful generation of the entangled state.

In the field of quantum information processing, the basic physical requirements for a quantum computer are often stated as the five *DiVincenzo criteria* [25]. An additional two criteria stipulate the requirements for quantum communication, known as *the extended DiVincenzo criteria*. Loosely speaking, in order to build networks of three or more nodes there are three important characteristics which will be required of the candidate quantum systems:

- The fidelity of local operations on the stationary systems should be high.
- The coherence time of the stationary qubits needs to be long enough to perform the necessary operations.
- The rate of successful entanglement generation determines the maximum rate of information transfer across the network, and therefore should be as large as possible.

Presently, trapped ions have significant advantages over other systems due to the high degree of coherent control available, and the long coherence times of their qubits. They currently hold the record for the highest fidelity operations ever achieved with quantum systems [26], which is an important prerequisite for fault-tolerant computing [27] in realistically noisy devices. However, the rate of entanglement achieved in ion trap systems needs to be significantly boosted to enable their use in larger networks.

The success rate of entanglement generation in ion trap experiments is mainly set by two properties of the system, the joint probability of two photons being captured by the collection optics at the same time, and the rate at which this process is repeated. Since the photons used to generate the entangled state are emitted by the ions in random directions, the probability of a photon being captured by the collection optic is dependent on its collection angle. To increase the collected fraction of light from the ion, the simplest approach is to increase the numerical aperture of the optic so that photons are collected over a larger solid angle. However, this approach is fundamentally limited to collecting less than half of the emitted photons for simple geometric reasons. One way to circumvent this limit is use a parabolic mirror to reflect

light from the second side, as has been demonstrated in [28]. As the light collection angle is increased, however, an additional source of error becomes important. The contrast between the polarisation states of the emitted photons is reduced at large emission angles, which leads to a reduction in the entanglement fidelity at large numerical apertures [29].

Another approach to increasing the collection probability involves surrounding the emitter with a low loss optical cavity which is resonant with the atomic transition. Using the physics described by cavity quantum electrodynamics (cavity-QED), it is theoretically possible to generate photons with near-unit efficiency in the cavity mode [30], which represents a most ideal solution. Furthermore, the polarisation state of the photons which are emitted remains pure for high emission probability, unlike with free-space optics. Cavity-QED has proven itself to be the method of choice for enhanced light collection in many systems, with near-unit emission probability being achieved in quantum dots [31], neutral atoms [32], and NV centres [33].

Although experiments with trapped ions have also demonstrated near-unit emission of photons into the cavity mode [34, 35], so far successful approaches to achieve high emission probability have used relatively large optical cavities with low cavity decay rates. Since the rate of entanglement is also dependent on the repetition rate of the generation process, these low cavity decay rates place unnecessary constraints on the success rate. In order to achieve a similarly large emission probability with faster decay rates, the coherent coupling between the atom and the cavity field needs to be increased. The coherent coupling strength, g, is a measure of how strongly the vacuum electric field inside the cavity interacts with the optical dipole of the atom. The value of g is therefore dependent on the atomic dipole moment, and the strength of the vacuum electric field.

In recent years, the advent of the micro-machined optical fibre Fabry-Pérot cavity [36] (or simply, the fibre-cavity) has allowed for the miniaturisation of optical cavity experiments. Owing to the smaller radius of curvature of mirrors produced through this method, it has been possible to build high quality fibre-cavities with dimensions on the $\sim 10\,\mu\text{m}$ scale [37], thereby significantly reducing the modal volume and increasing the coherent coupling. This technology has been applied with great success in several fields including with atoms [38], quantum dots [39], and NV centres [40]. The adoption of fibre-cavities in trapped ion experiments has however so far been slow, as the charge sensitivity of the ion makes trapping close to the dielectric surfaces of the mirrors challenging.

Despite the difficulty in combining trapped ions with fibre-cavities, there have been several recent successes along these lines [41, 42, 43]. However, so far fibre-cavity technology has only been used to couple to the optical dipole transitions with wavelengths in the infrared.

Since these transitions generally have unfavourable branching ratios out of their excited atomic state, the collection efficiency into the cavity is reduced.

Motivated by the strength of the lowest lying dipole transitions in trapped ions, which are primarily in the ultraviolet and blue spectral region, in this thesis we develop the first fibre-cavities which operate at these wavelengths. We show that this technology is compatible with trapped ions and demonstrate coupling to a single Yb^+ ion in a Paul trap. Using the strong atomic dipole moment in combination with the reduction in the mode volume due the shorter wavelength, we have reached a coherent coupling strength an order of magnitude higher than has previously been attained with single trapped ions. We investigate the properties of our system as a source of single photons in a well defined spatial mode. This great achievement lays the foundations for future cavities coupling to the primary dipole transitions which are optimised for high-rate photon production.

Additionally, the high coupling strength which we have achieved has allowed us to probe the driven Jaynes-Cummings model in a previously untested parameter space which is, however, important for the generation of light from these systems. We investigate correlation between the photoemission rate into free-space and the cavity in our apparatus, and determine that the back-action of the cavity-field cannot be neglected even when the cavity decay rate strongly dominates the system dynamics, termed the 'fast-cavity' regime. We observe enhancement and suppression of the total photoemission rate of the system which occur as a result of interference between the driving and back-action field at the position of the ion. This interference can be tuned by adjusting the length of the cavity, which determines the relative phase of the cavity back-action field. Measurement of the enhancement and suppression caused by the interference proves useful as a technique to accurately determine the cooperativity of cavity-QED systems in the fast-cavity regime.

1.1 Preface

The broad goal of my thesis has been to develop an experimental platform upon which we can study the physics of quantum networks. I started by designing a new ion trap chamber based on the work of the two then-PhD students, Matthias Steiner and Hendrik-Marten Meyer. During their projects they had demonstrated for the first time coupling between a trapped ion and a fibre-cavity. The new design for the second experimental chamber sought to improve upon some of the shortcomings of the original chamber, such as being able to drive microwave transitions within the hyperfine ground state qubit of $^{171}Yb^+$ and reducing the number of parts

that need to be removed when replacing a cavity. Additionally, a new laser system was required which could be operated independently of the original system.

In October 2013 the research group relocated to University of Bonn. Design and construction of the new ion trap and laser system were nearly completed before the final move date was decided. In the few remaining months before the move, I began the testing of the new ultraviolet coated fibre-cavity substrates which had been machined by Matthias Steiner and Hendrik-Marten Meyer at the beginning of that year. Initial results with the ultraviolet fibre-cavities were very promising. Owing to the success of the ultraviolet fibre-cavity substrates, we decided that for the new ion trap system we should make an attempt to use a fibre-cavity which operates on the $^2S_{1/2} \rightarrow {}^2P_{1/2}$ transition of Yb^+ at 370 nm, instead of the previously used repump transition at 935 nm.

After setting up the labs in Bonn, I completed building the new ion trap system. Initially I worked with $^{174}Yb^+$, which is the simplest isotope of Yb as it has no nuclear spin, in order to establish operation of the trap hardware. At this point I developed the hardware and software known as the Fast Experimental Control System (FECS) which will allow us to efficiently control a number of ion trap-cavity systems which are linked with probabilistic entanglement techniques. While I was working on commissioning the ion trap, there were plans for an ultraviolet fibre-cavity to be simultaneously built for this experiment, however these fell through and no progress was made in this area.

During Summer 2014 I began to work with $^{171}Yb^+$ which has nuclear spin $1/2$ and provides the basis of our plans for entanglement generation using the $^2S_{1/2} \rightarrow {}^2P_{1/2}$ transition. At this point I set up the experiment to perform state preparation, state readout, and coherent manipulation of the hyperfine ground state qubit using microwaves. Parallel to this development, as part of a Bachelors project Andreas Kell installed and set up a frequency doubled mode-locked Titanium Sapphire laser, to be used for pulsed excitation of the ion. In the Autumn of 2014, I continued to work with the mode-locked laser and set up a spectral filter cavity to narrow the frequency content of the pulses. With this functional, I was able to observe the ultra-fast Rabi oscillations driven by the pulsed laser with $^{171}Yb^+$.

After this result the ion trap and laser system were ready to work with a cavity. Over the period between December 2014 and August 2015 I worked closely with H.-M. Meyer to develop an ultraviolet fibre-cavity for use in the experiment. During this time, we made several unsuccessful attempts, each time learning of new problems that needed to be solved in order to achieve our goal. In August 2015, we produced a fibre-cavity and mounting structure which survived the ultra-high vacuum bakeout procedure for the first time. I found that it was possible

to trap the ion inside the fibre-cavity and observed the first signs of coupling with the ion. However, the performance of the ion trap was very poor, and I determined that some of the electrical connections associated with the fibre-cavity were broken. We repaired the connections and performed a second bakeout, however after initially trapping I quickly determined that a new connection has become damaged. After the third bakeout, the ion trap performance was good and I began to establish the cavity properties from December 2015 onwards. During the time spent baking out the system, I determined that mechanical resonances in the fibre-cavity mounting structure presented a problem for applying standard active length stabilisation techniques, even though we had put a lot of thought into the design of the structure in this regard.

Measurements with the ion-cavity system began in earnest in January 2015. I first set up the Hanbury Brown and Twiss measurement to determine the second-order coherence of produced photons. After this, I developed a technique whereby I could generate an error signal and effectively lock the cavity length whilst scanning even though the length was changing by more than a cavity linewidth due to environmental noise coupling to the mechanical resonances. This technique allowed me to measure the properties of the ion-cavity system for specific cavity-atom detunings, even though I could not stabilise the cavity length against the mechanical noise. Using this technique, I took a series of data measuring the photoemission from the ion into free-space and the cavity mode while the system is being driven with a laser from the side. The theoretical models which explain this data were analytically solved by H.-M. Meyer, and we worked together closely to analyse the experimental results. Determination of the cavity linewidth proved not possible using the same techniques we had used during construction, however the cavity lock technique which was employed provided a means to measure this. From this measurement, I was able to determine that the cavity linewidth had increased significantly since it was built. After fully understanding our system, we have summarised these results in a manuscript which has been published in Physical Review A [44].

1.2 Thesis outline

The remaining chapters of this thesis are structured as follows:

Chapter 2 provides the framework for describing the interaction between atoms and electromagnetic radiation. The semi-classical theory of a two-level system in a classical field is introduced, necessary for working with trapped ions in the laboratory setting. Interaction with a quantised field is also introduced in order to describe the physics relevant for an ion inside an

optical cavity.

Chapter 3 introduces concepts used for trapping and cooling ions in quadrupole ion traps. Particular focus is placed on the technical challenges involved in designing ion traps which allow close integration of optical fibre-cavities. We give the design and operational parameters of the ion trap used for the experiments in this thesis.

Chapter 4 provides a detailed introduction to Fabry-Pérot optical cavities, particularly the properties which are important for the construction of fibre-cavities. We describe the design considerations and techniques used for building our ultraviolet fibre-cavity mounting structure. During operation, an increase in optical losses within the cavity has been observed, and this is described and put into context with other published experimental results.

Chapter 5 describes the apparatus which is used in the following experimental chapters. The setup has been designed and built in order to provide a compact platform for future photonic entanglement experiments, allowing for several of these systems to be operated at independent locations.

Chapter 6 details the experimental measurements showing the strong interaction afforded by combining an ultraviolet fibre-cavity with a trapped ion. We determine the atom-cavity coupling rate with two independent measurements, show that our apparatus provides an excellent source of single photons, and investigate the system under continuous excitation from an external classical field.

Chapter 7 describes the experimental measurements made to establish coherent control of the qubit which will be used for atom-photon entanglement. The qubit is introduced and the techniques described for state preparation, readout, magnetic field calibration, and ultrafast excitation. Based on measured cavity parameters, the atom-photon entanglement scheme is described along with the expected success rate.

Chapter 8 concludes the thesis, providing an overview of what has been achieved. This work is put into context with several possible short-term improvements, and future lines of investigation are described building upon our results.

Chapter 2

Atom-light interaction

In the thesis that follows, the interaction between a single ion and various light fields is investigated. This interaction is primarily governed by the laws of quantum mechanics. In this chapter, the theoretical concepts which will be used later are introduced. We start with a brief review of interaction with a classical light field, which is necessary to understand the processes of Rabi oscillations and saturation of a two level system. Following this, the interaction with a quantised field is introduced, first phenomenologically with a perturbation theory approach, then more rigorously with Jaynes-Cummings model. Finally, the Jaynes-Cummings model is extended by adding driving terms which are important when working with a 'real' system in the laboratory.

2.1 Interaction with a classical field

The Hamiltonian for a two level system with states $|g\rangle$ and $|e\rangle$ is given by

$$\hat{H}_0 = \hbar\omega_0 |e\rangle\langle e| \tag{2.1}$$

where $\hbar\omega_0$ is the energy difference between the two states. This can equivalently be written in terms of the Pauli-z spin matrix

$$\hat{H}_0 = -\frac{\hbar\omega_0}{2}\hat{\sigma}_z. \tag{2.2}$$

Interaction with radiation is introduced by adding the associated energy term into the Hamiltonian. In this case we assume the interaction is predominantly dipolar, so the energy is given by that of a dipole in an electric field,

$$\hat{H}_\mathrm{I} = -\vec{\hat{d}} \cdot \vec{E}(t) \tag{2.3}$$

where $\vec{E}(t)$ is the electric field at the position of the atom, and $\vec{\hat{d}}$ is the electric dipole operator, which can be expressed in terms of Pauli spin matrices, and is given by

$$\vec{\hat{d}} = (\hat{\sigma}^+ \vec{d}_{12} + \hat{\sigma}^- \vec{d}^*_{12}) \tag{2.4}$$

where

$$\vec{d_{12}} = e_0 \langle g | \vec{\hat{x}} | e \rangle , \tag{2.5}$$

which is known as the dipole matrix element.

A classical linearly polarised monochromatic electric field at angular frequency ω_{L} is given by

$$\vec{E}(t) = \vec{\varepsilon} E_0 \cos(\omega_{\mathrm{L}} t) = \frac{1}{2} \vec{\varepsilon} E_0 \left(e^{i\omega_{\mathrm{L}} t} + e^{-i\omega_{\mathrm{L}} t} \right) \tag{2.6}$$

where $\vec{\varepsilon}$ is the normalised polarisation vector, and E_0 is the electric field amplitude at the position of the atom which is real for linear polarisation. The Hamiltonian associated with this dipolar interaction is then given by

$$\hat{H}_{\mathrm{I}} = -\hbar \left(\Omega \hat{\sigma}^+ + \Omega^* \hat{\sigma}^- \right) \left[e^{i\omega_{\mathrm{L}} t} + e^{-i\omega_{\mathrm{L}} t} \right] , \tag{2.7}$$

where we have introduced the Rabi frequency Ω, defined by

$$\Omega = \frac{1}{2\hbar} (\vec{\varepsilon} \cdot \vec{d}_{12}) E_0 . \tag{2.8}$$

resulting in the following equation for the total Hamiltonian

$$\hat{H} = -\frac{\hbar \omega_0}{2} \hat{\sigma}_z - \frac{\hbar}{2} \left(\Omega \hat{\sigma}^+ + \Omega^* \hat{\sigma}^- \right) \left[e^{i\omega_{\mathrm{L}} t} + e^{-i\omega_{\mathrm{L}} t} \right] \tag{2.9}$$

Simplification of this Hamiltonian can made be performing a transformation into the rotating frame. When the state vectors are transformed by a unitary transformation $\hat{U}$, then the Hamiltonian also needs to be transformed with

$$\left| \psi' \right\rangle = \hat{U} \left| \psi \right\rangle \tag{2.10}$$

$$\hat{H}' = \hat{U} \hat{H} \hat{U}^\dagger - i\hbar \frac{\partial \hat{U}^\dagger}{\partial t} . \tag{2.11}$$

By applying the transformation $\hat{U} = \exp(i\omega_{\mathrm{L}} t \hat{\sigma}_z / 2)$[1], the Hamiltonian now reads

$$\hat{H}' = \frac{\hbar \Delta_{\mathrm{L}}}{2} \hat{\sigma}_z - \frac{\hbar}{2} \left(\Omega \hat{\sigma}^+ \left[1 + e^{2i\omega_{\mathrm{L}} t} \right] + H.c. \right) . \tag{2.12}$$

[1] Here we make use of the relation $e^{i\omega_{\mathrm{L}} t \hat{\sigma}_z / 2} \hat{\sigma}^\pm e^{-i\omega_{\mathrm{L}} t \hat{\sigma}_z / 2} = \hat{\sigma}^\pm e^{\pm i\omega_{\mathrm{L}} t}$.

In the rotating frame introduced by the unitary transformation, the dynamics that the system describes are the same. However, when the time evolution of the system is investigated, one finds that the interaction terms which are proportional to $e^{\pm 2i\omega_L t}$ have negligible effect on the state vector. In the rotating wave approximation [45], these terms are ignored, and this approximation is generally very good since Δ_L/ω_L is typically very small in all cases we are concerned with here. After application of this approximation, the Hamiltonian is given by

$$\hat{H}' = \frac{\hbar\Delta_L}{2}\hat{\sigma}_z - \frac{\hbar}{2}\Omega\hat{\sigma}^+ - \frac{\hbar}{2}\Omega^*\hat{\sigma}^-. \tag{2.13}$$

2.1.1 Rabi oscillations

The solution to this set of coupled first order differential equations can be found by diagonalising the Hamiltonian. In the case where the system is initially in the ground state, i.e. $|\psi\rangle = |g\rangle$, the probability of finding the ion in the excited state after a time t is given by

$$|\langle e|\psi(t)\rangle|^2 = \frac{|\Omega|^2}{\Omega_R^2}\sin^2\left(\frac{\Omega_R t}{2}\right) \tag{2.14}$$

where $\Omega_R^2 = |\Omega|^2 + \Delta_L^2$ is known as the generalised Rabi frequency. This solution describes sinusoidal oscillations of the probability density between the ground and excited state at the generalised Rabi frequency. When the field is detuned from resonance, the amplitude of the oscillations decreases. If the atomic system is initially in the ground state, these oscillations can be used to deterministically control the atomic state of the system. For instance, complete transfer of population from the ground to excited state can be performed by driving oscillations with a resonant field for a time which satisfies $\Omega_R t = \pi$, known as a π pulse.

2.1.2 Dissipation

So far we have discussed the interaction of an atom with a classical field for the case where there is no spontaneous emission from the excited state. However, since all physical quantum systems experience spontaneous decay, it is important to be able to model this process.

Population decays from the excited state to the ground state by emitting a photons at a rate Γ. If the photon goes on to interact with an environment, as is often the case in the laboratory, then the state of the atom becomes entangled with the environment. However, unless we include the quantum state of the environment in our model, this information is lost. This interaction with the environment is then said to cause decoherence of the atomic state, as the continuous

'measurements' cause the atomic state to repeatedly collapse into the ground state. In order to model this probabilistic process, it is necessary to move away from the pure state description we have used previously into a density matrix approach which can handle statistical mixtures of states.

The density operator [46, p. 298] for a pure state is defined by

$$\hat{\rho}_k = |\psi_k\rangle \langle\psi_k| . \tag{2.15}$$

Generalisation to a statistical mixture of states, known as a mixed state, is achieved by a weighted sum over the constituent pure states

$$\hat{\rho} = \sum_k a_k \hat{\rho}_k, \tag{2.16}$$

where a_k are the weights. Time evolution of the density operator is given by

$$\frac{d}{dt}\hat{\rho} = -i\big[\hat{H}, \hat{\rho}\big]. \tag{2.17}$$

Several approaches exist for tackling this case of an atom coupled to the environment. Here we use a formalism for handling the dynamics of quantum systems which are coupled to the open systems [47], which will also be relevant when later working with a cavity. Direct calculations rely on the so-called Markov approximation which states that the decay of the quantum system does not affect the state of the environment. Under this approximation, the dynamics can be solved via the quantum mechanical master equation

$$\frac{d}{dt}\rho(t) = -\frac{i}{\hbar}\left[\hat{H}, \rho(t)\right] + \mathcal{L}(\rho(t)), \tag{2.18}$$

where $\mathcal{L}$ is known as the Liouvillian superoperator and describes the non-hermitian evolution of the system as a result of its coupling to the environment. The Liouvillian, in the so-called Lindblad form [47, p. 369], is given by

$$\mathcal{L}(\rho) = \sum_i \left(\hat{C}_i \rho \hat{C}_i^\dagger - \frac{1}{2}\hat{C}_i^\dagger \hat{C}_i \rho - \frac{1}{2}\rho \hat{C}_i^\dagger \hat{C}_i \right), \tag{2.19}$$

where $\hat{C}_i$ are the system collapse operators, also known as jump operators, describing each decay path. In this simple case, there is only one collapse operator which transfers population from the excited state to the ground state. It is given by

$$\hat{C}_{\text{atom}} = \sqrt{\Gamma/2}\,\hat{\sigma}^- \tag{2.20}$$

where Γ is the excited state decay rate.

The new set of coupled differential equations fully encompass the dynamics of the system coupled to the Markovian environment. The equation can be solved analytically, however this is not shown here. The result we are primarily interested in for this thesis is how the system observables behave in the laboratory setting, where we almost exclusively observe the rate of fluorescence produced by the atomic system under a continuous classical drive field. The average rate at which photons are emitted from a two-level system is given by

$$R_{4\pi} = \langle \rho_{ee} \rangle \Gamma, \tag{2.21}$$

where $\rho_{ee} = \langle e|\rho|e\rangle$ is the population of the excited state, and $R_{4\pi}$ the rate at which photons are emitted in all directions. This non-standard notation for the emission rate is used throughout this thesis to make a clear distinction between emission rates into different solid angles, which is relevant in the analysis of the effects of the cavity on the system. When the atomic system reaches a steady state, the excited state population is given by

$$\rho_{ee} = \frac{s/2}{1+s+(2\Delta_{\mathrm{L}}/\Gamma)^2}, \tag{2.22}$$

where s is defined through the relation $\Omega = \Gamma\sqrt{s/2}$, and is known as the saturation parameter.

2.2 An atom in a cavity

We now consider the case where the atom is placed inside a resonant optical cavity. A detailed description of Fabry-Pérot optical cavities is given later in chapter 4, but here it suffices to summarise the properties important for atom-cavity interaction.

A cavity, or optical resonator, is formed by two reflective surfaces arranged as shown in figure 2.1. The presence of the mirrors puts restrictions on the modes which are able to exist in the space inside the cavity: these modes must obey the boundary conditions imposed by mirrors, namely that the tangential field components on the surface must vanish. This means that only light with a wavelength which is a half-integer factor of the cavity length can exist within the cavity, leading to a discrete set of modes.

To see the effect that a cavity has on the photon emission properties of an atom, we take a perturbative approach. According to Fermi's golden rule the transition rate for spontaneous emission is given by

$$W = \frac{2\pi}{\hbar^2}|M_{12}|^2\rho(\omega) \tag{2.23}$$

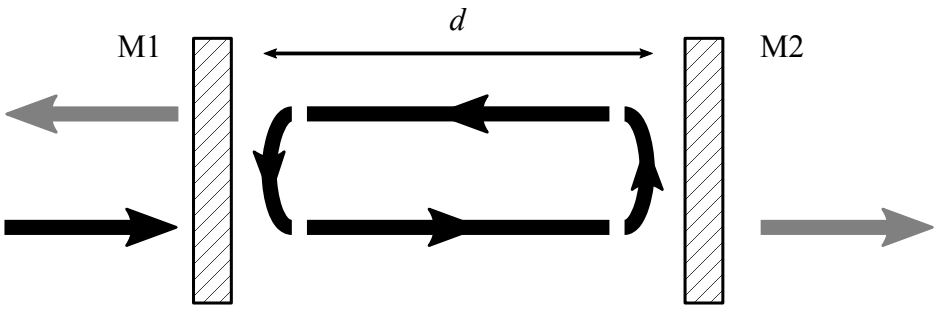

Figure 2.1: An optical cavity of length d formed by two partially reflecting mirrors M1 and M2. Light incident on mirror M1 causes the field inside the cavity to build up and destructively interfere with the reflected power for certain values of d.

where M_{12} is the transition matrix element and $\rho(\omega)$ is the density of final states. The density of states of photons in free space is given by

$$\rho_{\text{free}}(\omega) = \frac{\omega^2}{\pi^2 c^3}. \tag{2.24}$$

Within the cavity, the density of states is modified by the presence of the mirrors. If the mirrors have finite reflectivity, then the discrete set of modes becomes broadened by a Lorentzian function with full-width at half maximum $\Delta\omega_{\text{c}}$ known as the cavity linewidth. The linewidth is related to the quality factor of the cavity via the relation $Q = \omega_{\text{c}}/\Delta\omega_{\text{c}}$, with ω_{c} being the frequency of the cavity resonance.

When the cavity is on resonance with the atom, i.e. $\omega_{\text{c}} = \omega_0$, the density of states is given by

$$\rho_{\text{cav}}(\omega_0) \approx \frac{2}{\pi\Delta\omega_{\text{c}} V_{\text{m}}} = \frac{2Q}{\pi\omega_0 V_{\text{m}}} \tag{2.25}$$

where V_{m} is volume of the cavity mode, and in the approximation we have neglected the contribution of additional modes where $|\omega_{\text{c}} - \omega_0| \gg \Delta\omega_{\text{c}}$.

The ratio of spontaneous emission into the cavity versus free space is known as the Purcell factor. It can be calculated from the ratio of the density of states and is therefore given by

$$F_{\text{P}} = \frac{W_{\text{cav}}}{W_{\text{free}}} = \frac{3Q}{4\pi^2}\frac{\lambda^3}{V_{\text{m}}}, \tag{2.26}$$

where we have assumed that the atomic dipole is oriented along the cavity field direction. The numerical factor of 3 comes from the averaging of M_{12} over all spatial directions when calculating W_{free} [48]. From this model, we see that in order to have a high probability of emission into

the cavity, we should target systems with low mode volume and high quality factors. However, the approach used here is only valid when the perturbation is small.

2.2.1 The Jaynes-Cummings model

In order to have a fully quantum mechanical picture of the interaction of atoms and cavities, we need to employ quantisation of the cavity mode.

Taken on its own, the properties of a single mode of the cavity are equivalent to the properties of the quantum harmonic oscillator, with the Hamiltonian of the cavity given by

$$\hat{H}_{\mathrm{c}} = \hbar\omega_{\mathrm{c}}\left(\hat{a}^{\dagger}\hat{a} + \frac{1}{2}\right) \tag{2.27}$$

where $\hat{a}^{\dagger}$ and $\hat{a}$ are the field creation and annihilation operators for excitations of the cavity mode, and ω_{c} is the cavity resonance frequency. The eigenstates of the cavity are given by

$$|n\rangle = \frac{(\hat{a}^{\dagger})^{n}}{\sqrt{n!}}|0\rangle, \tag{2.28}$$

where n is a positive integer, and $|0\rangle$ is the vacuum state. These states correspond to distinct photon number states.

The electric field inside the cavity is given by the electric field operator

$$\hat{E} = \varepsilon_{\mathrm{c}}\left(\hat{a} + \hat{a}^{\dagger}\right), \tag{2.29}$$

where ε_{c} is the single photon electric field given by $(\hbar\omega_{\mathrm{c}}/2\varepsilon_0 V_{\mathrm{m}})^{1/2}$ [49]. We have assumed here that the cavity field polarisation is linear.

Now we introduce the atomic system to the cavity. The full Hamiltonian is the sum of the energy in the system, i.e.

$$\hat{H} = \hat{H}_a + \hat{H}_{\mathrm{c}} + \hat{H}_{\mathrm{int}}, \tag{2.30}$$

where $\hat{H}_{\mathrm{int}}$ is the Hamiltonian for the interaction between the atom and the cavity field. As in the semi-classical case before, we have

$$\hat{H}_{\mathrm{int}} = \hat{d}\hat{E} \tag{2.31}$$

where we have replaced the classical electric field with the electric field operator of the cavity mode. Using the expression for $\hat{d}$ from earlier, we see that

$$\hat{H}_{\mathrm{int}} = \varepsilon_{\mathrm{c}}\left(\hat{\sigma}^{+}d_{12} + \hat{\sigma}^{-}d_{12}^{*}\right)\left(\hat{a} + \hat{a}^{\dagger}\right). \tag{2.32}$$

By shifting into the interaction picture with $\hat{H}_0 = \hat{H}_a + \hat{H}_c$, we find terms rotating at $\pm(\omega_a - \omega_c)$ and $\pm(\omega_a + \omega_c)$. Taking the rotating wave approximation, we can ignore the latter terms. On returning to the Schrödinger picture, we find

$$\hat{H}_{\text{int}} = \varepsilon_c d_{12}\left(\hat{\sigma}^+\hat{a} + \hat{\sigma}^-\hat{a}^\dagger\right), \tag{2.33}$$

where we have also assumed d_{12} is real.

The full Hamiltonian of the atom-cavity system now reads

$$\hat{H}_{\text{JC}} = \hbar\frac{\omega_0}{2}\hat{\sigma}_z + \hbar\omega_c\hat{a}^\dagger\hat{a} + \hbar g\left(\hat{a}\hat{\sigma}^+ + \hat{a}^\dagger\hat{\sigma}^-\right), \tag{2.34}$$

where

$$g = \varepsilon_c d_{12}/\hbar = \sqrt{\frac{3\lambda^2 c\Gamma}{2\pi V_m}} \tag{2.35}$$

This is known as the **Jaynes-Cummings Hamiltonian**, and g is the single photon Rabi frequency. To calculate g we have used the relationship linking dipole transition matrix element, d_{12}, to the transition decay rate, namely $d_{12}^2 = 3\pi e_0\hbar c^3\Gamma/\omega_0^3$.

So far this Hamiltonian only describes a closed system, which is not the case as both the atomic excited state and the cavity field decay into the environment. To determine the dynamics of this system we need to use the quantum mechanical master equation we introduced earlier to tackle open systems. Now there are two decay channels, described by the collapse operators

$$\hat{C}_{\text{atom}} = \sqrt{\Gamma/2}\hat{\sigma}^- \tag{2.36}$$

$$\hat{C}_{\text{cavity}} = \sqrt{\kappa}\hat{a}, \tag{2.37}$$

where κ is the electric field decay rate of the cavity.

Now there are three parameters which govern the dynamics of the system, the atom-cavity coupling rate g, the excited state decay rate Γ, and the cavity field decay rate κ. Based on the relative values of these terms, we can split atom-cavity systems into three broad categories with distinct characteristics:

- The weak-coupling regime where $g \ll \kappa, \Gamma$. Here the system is dominated by its decohering processes, so no coherent evolution is observed and the system is well described by the perturbative approach used earlier.
- The strong-coupling regime where $g \gg \kappa, \Gamma$. The coherent atom-cavity coupling rate dominates the dynamics of the system, leading to interesting phenomena generally associated with cavity-QED such as vacuum Rabi splitting [50] and photon blockade [51].

- The bad-cavity, or fast-cavity, regime where $\kappa > g > \Gamma$. In this regime the cavity decay is the dominant process, and therefore no coherent population transfer back and forth between the atom and cavity is observed. However, since the atom couples more strongly to the cavity than to the free-space vacuum field, the probability of photon emission out of the cavity can still be large. The two terms used to refer to this regime are distinguished by the form the cavity losses take: whether they are intrinsic (*bad*) or transmissive (*fast*) losses [52]. In this thesis, the latter term is used as this represents the intended loss regime.

As motivated in chapter 1, we are primarily interested in using the atom-cavity system as a means of collecting a large fraction of the emitted light. Figure 2.2 shows the probability of a photon being emitted from the cavity after the system is instantaneously excited into the upper atomic state. In this graph, we consider the dependence of this probability on the cavity field decay rate κ for a set value of g and Γ which are similar in proportion to those achievable in our experiment. The probability is calculated from a numerical solution to the Jaynes-Cummings Hamiltonian, and the optimal probability for a given g and Γ is found when $\kappa = g$, which represents the intermediate regime between strong-coupling and fast-cavity.

The temporal probability density function, or 'shape', of the emitted photons are shown in the insets to figure 2.2. In the strong-coupling regime, the emitted photon probability density exhibits sinusoidal oscillations due to the coherent transfer of population between the atomic excited state and the cavity mode: vacuum Rabi oscillations. Here, the temporal width of the exponential envelope of the photon is determined by the cavity decay rate. On the other end of the scale, in the fast-cavity regime, the emitted photon shape is well approximated by an exponential decay determined by the atomic Γ.

For the case where the cavity decay defines the fastest time constant of the system, i.e. $\kappa \gg g, \Gamma$, the master equation for the Jaynes-Cummings Hamiltonian can be solved to find an effective lifetime of the excited state [47]. The enhanced decay rate is given by

$$\Gamma' = \Gamma_{4\pi\text{-c}} + \Gamma_{\text{c}} \tag{2.38}$$

$$\Gamma_{\text{c}} = \frac{2g^2}{\kappa} \frac{1}{1 + (\Delta_{\text{C}}/\kappa)^2}, \tag{2.39}$$

where Γ_{c} is the decay rate of the excited state into the cavity mode, and $\Gamma_{4\pi\text{-c}}$ is the decay rate into free space outside of the cavity. When the cavity takes up a small fraction of the solid angle, this is approximately equal to the decay rate without the cavity, i.e. $\Gamma_{4\pi\text{-c}} \approx \Gamma$. Under

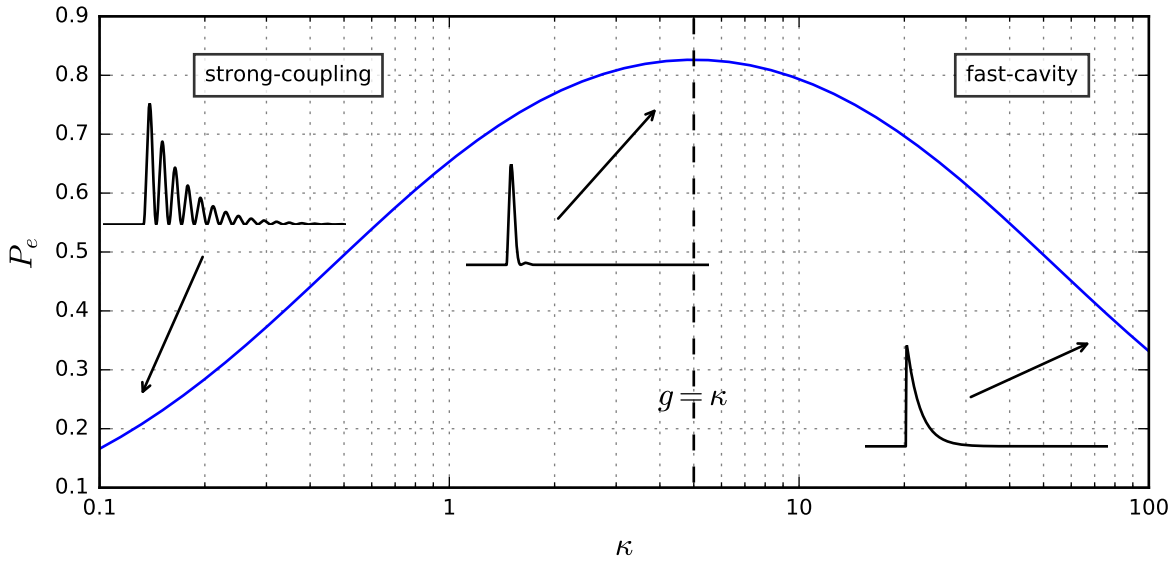

Figure 2.2: Probability of photoemission from the cavity P_e for $g, \Gamma = 5, 1$ as a function of κ using the numerically solved Jaynes-Cummings model. The parameters put the system into the strong-coupling regime on the left, and the fast-cavity regime on the right. The inset curves are the temporal probability density functions for the emitted photons in the different regimes.

this assumption the expression can be rewritten as

$$\Gamma' = \Gamma \left(1 + 2C_0 \frac{1}{1 + (\Delta_\mathrm{C}/\kappa)^2} \right), \tag{2.40}$$

where $C_0 = g^2/\kappa\Gamma$ is known as the cooperativity. The Purcell factor, which is the ratio of spontaneous emission into the cavity versus into free-space, is given by the ratio of the relevant decay rates

$$F_\mathrm{P} = \frac{\Gamma_\mathrm{c}}{\Gamma_{4\pi}} \overset{\Delta_\mathrm{C}=0}{=} 2C_0, \tag{2.41}$$

and the probability of emission into the cavity versus free-space is given by

$$P_\mathrm{e} = \frac{\Gamma_\mathrm{c}}{\Gamma'} \overset{\Delta_\mathrm{C}=0}{=} \frac{2C_0}{1 + 2C_0}. \tag{2.42}$$

This relation is useful for understanding the behaviour of the system for different combinations of parameters, but is only valid for $\kappa \gg g, \Gamma$. In figure 2.2 this represents the region on the right hand side of the graph.

In the experimental implementation of this physical model employed in this thesis, single atomic excitations will be created near instananeously, and the system will be left to decay. This process will be repeated at a rate R_{rep}, and the rate of photon emission from the cavity is given by

$$R_{\text{e}} = P_{\text{e}} R_{\text{rep}}. \tag{2.43}$$

2.2.2 The driven Jaynes-Cummings model

Although the dissipative Jaynes-Cummings model describes interesting physics in its own right, for the work performed in this thesis we need to introduce further terms to the Hamiltonian which correspond to external influences which we use to probe the system. One way of driving the atom-cavity system is to apply an additional electrical dipole field, for instance with a laser. In this case, we need to add the term associated with this interaction to the Hamiltonian, as we did earlier in section 2.1. The system is then described by

$$\begin{aligned} H &= H_0 + H_1 \\ H_0 &= \frac{1}{2}\hbar\omega_0\hat{\sigma}_z + \hbar\omega_{\text{C}}\hat{a}^\dagger\hat{a} \\ H_1 &= \hbar g[\hat{\sigma}^+\hat{a} + \hat{a}^\dagger\hat{\sigma}^-] + \frac{1}{2}\hbar\Omega[\hat{\sigma}^+ e^{-i\omega_{\text{L}}t} + \hat{\sigma}^- e^{i\omega_{\text{L}}t}], \end{aligned} \tag{2.44}$$

where Ω is the Rabi frequency associated with the dipole field with frequency ω_{L}.

We shift into the frame rotating at the laser frequency with the transformation

$$\hat{U} = \exp\Big(i\omega_{\text{L}}t[\hat{\sigma}_z/2 + \hat{a}^\dagger\hat{a}]\Big), \tag{2.45}$$

which results in the transformed Hamiltonian

$$\begin{aligned} H' =& \frac{1}{2}\hbar(\omega_0 - \omega_{\text{L}})\hat{\sigma}_z + \hbar(\omega_{\text{C}} - \omega_{\text{L}})\hat{a}^\dagger\hat{a} \\ &+ \hbar g[\hat{\sigma}^+\hat{a} + \hat{a}^\dagger\hat{\sigma}^-] + \frac{1}{2}\hbar\Omega[\hat{\sigma}^+ + \hat{\sigma}^-]. \end{aligned} \tag{2.46}$$

At this point it becomes natural to define the detunings

$$\Delta_{\text{A}}^{(\text{L})} = \omega_{\text{L}} - \omega_0 = \Delta_{\text{L}} \tag{2.47}$$

$$\Delta_{\text{C}}^{(\text{L})} = \omega_{\text{L}} - \omega_{\text{C}} = \Delta_{\text{L}} - \Delta_{\text{C}} \tag{2.48}$$

where Δ_{L} and Δ_{C} are the detunings of laser and cavity relative to the atom which have been defined earlier. These new detunings relative to the laser simplify the form to the Hamiltonian,

and are often used in literature but are not very intuitive in the laboratory. The final Hamiltonian in terms of the laser-relative detunings is given by

$$\begin{aligned}\hat{H}' = &-\frac{1}{2}\hbar\Delta_{\mathrm{A}}^{(\mathrm{L})}\hat{\sigma}_z - \hbar\Delta_{\mathrm{C}}^{(\mathrm{L})}\hat{a}^\dagger\hat{a} \\ &+\hbar g[\hat{\sigma}^+\hat{a} + \hat{a}^\dagger\hat{\sigma}^-] + \frac{1}{2}\hbar\Omega[\hat{\sigma}^+ + \hat{\sigma}^-].\end{aligned} \tag{2.49}$$

The behaviour of this system is explored further in chapter 6.

Chapter 3

Ion traps

In this chapter we introduce the concepts used for trapping and cooling ions in quadrupole ion traps. In order to trap an ion close to the dielectric surfaces that form fibre-cavities, special considerations need to be made in the design of the trap. These features are discussed, and the design chosen for this experiment is given along with its performance parameters. Since charges on these dielectric surfaces can remain for long times, it is important to be able to detect and reduce excess micromotion which is caused by their presence, and two techniques used for this are introduced and compared.

3.1 The Paul trap

The Paul trap, or quadrupole ion trap, was invented by Wolfgang Paul in the 1960s and makes use of static and time-varying electric fields to confine charged particles in three dimensions. Unfortunately, a static electric potential $\Phi(x,y,z)$ cannot have an extremum in three dimensions. This can be seen as a consequence of Laplace's law, as Laplace's equation

$$\frac{\partial^2\Phi}{\partial x^2}+\frac{\partial^2\Phi}{\partial y^2}+\frac{\partial^2\Phi}{\partial z^2}=0 \tag{3.1}$$

would be violated if the partial derivatives would all have the same sign. Confinement in three dimensions can be however achieved with an electric field which changes its polarity over time, effectively using the inertia of the confined particle to overcome phases where the particle experiences an anti-confining potential.

Operation of the Paul trap however still depends on potentials which have vanishing second

derivatives. The simplest potential which has this feature is that of the ideal quadrupole

$$\Phi(x,y,z) = \frac{1}{2}\left(\alpha x^2 + \beta y^2 + \gamma z^2\right) \tag{3.2}$$

where α, β, and γ are known as the quadrupole moments of the field. The moments are constrained by the Laplace equation to obey the condition

$$\alpha + \beta + \gamma = 0. \tag{3.3}$$

In practice a real electric potential generated in the lab will differ from the ideal quadrupole. To handle this it is useful to take a multipole expansion about the trap centre. The potential under this expansion is given by

$$\Phi(\vec{r}) = \sum_i \mathcal{D}_i r_i + \sum_{i,j} \frac{1}{2}\mathcal{T}_{ij} r_i r_j + \mathcal{O}(r^3), \tag{3.4}$$

where $\mathcal{D}$ and $\mathcal{T}$ are the dipole and quadrupole moment tensors respectively, which may be position dependent. For now, we will consider potentials which have no dipole moment, meaning that they do not have a linear component to the electric field. Satisfying Laplace's law is equivalent to the condition $\mathrm{Tr}(\mathcal{T}) = 0$, and as a second rank tensor there exist a set of orthonormal vectors which will diagonalise the matrix of elements. This set of vectors are known as the principal axes of the quadrupole moment and will be important later.

Early Paul traps were mainly built upon two special cases of the ideal quadrupole potential. The first case is where one of the coefficients is zero with the remaining two coefficients being equal and opposite. This configuration has a vanishing second derivative along one axis, and is the basis of linear Paul traps. The second special case is when $\alpha = \beta$ and therefore $\gamma = -2\alpha$, and is the configuration used in the ideal 3D Paul trap.

Figure 3.1 shows the standard electrode geometry for a 3D Paul trap. The trap has cylindrical symmetry about the z axis, and the electrodes have hyperbolic profiles which produce an ideal quadrupole electric field within the trap. The separations between the trap centre and the electrodes are r_0 and z_0 for the ring and endcap electrodes respectively. In this ideal geometry, the radius of curvature of the endcap and ring electrodes at the points nearest the centre need to be $2z_0$ and z_0 respectively, and the ratio of the electrode separations needs to follow $r_0/z_0 = \sqrt{2}$.

Without loss of generality, we can choose our coordinate system to be the one that diagonalises the quadrupole moment tensor elements. In the following analysis, we assume that we have a system of electrodes which produces an ideal quadrupole potential. When one volt is applied to the electrodes, a quadrupole moment is of α, β, and γ is generated along the x, y, and

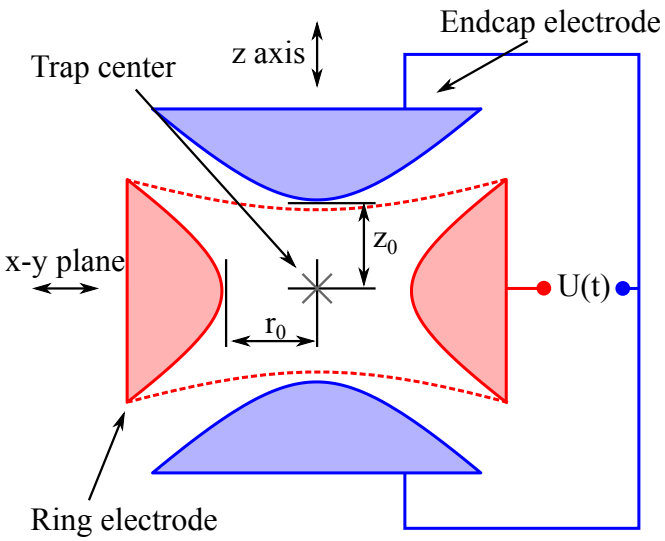

Figure 3.1: Cross-section of an ideal 3D Paul trap. The hyperbolic profile of the ring and endcap electrodes are optimal for producing the largest harmonic term in the potential.

z axes respectively. When time-varying voltage, $U(t)$, is applied to the electrodes, the resulting electric potential is given by

$$\Phi(x,y,z) = \frac{U(t)}{2}(\alpha x^2 + \beta y^2 + \gamma z^2) \tag{3.5}$$

A ion with charge Q within the trap will experience a force

$$\mathbf{F}(t) = \begin{pmatrix} F_x(t) \\ F_y(t) \\ F_z(t) \end{pmatrix} = \frac{QU(t)}{2} \begin{pmatrix} 2\alpha x \\ 2\beta y \\ 2\gamma z \end{pmatrix} \tag{3.6}$$

In the case where the voltage applied to the electrode oscillates at a fixed frequency, we can write

$$U(t) = U_{\text{dc}} + U_{\text{rf}} \cos(\Omega_{\text{rf}} t). \tag{3.7}$$

The equations of motion of the particle in this potential are now

$$\begin{pmatrix} \ddot{x} \\ \ddot{y} \\ \ddot{z} \end{pmatrix} - \frac{Q}{m}(U_{\text{dc}} + U_{\text{rf}} \cos(\Omega_{\text{rf}} t)) \begin{pmatrix} \alpha x \\ \beta y \\ \gamma z \end{pmatrix} = 0. \tag{3.8}$$

These equations can be parametrised so that they have the form of the Mathieu equation [53]

$$\frac{d^2 f}{d\zeta^2} + (a - 2q\cos(2\zeta))f = 0, \tag{3.9}$$

where a and q are known as the Mathieu parameters and $\zeta = \Omega_{\text{rf}} t/2$. For motion in the x direction, the parameters are given by

$$q_x = \frac{2QU_{\text{rf}}}{m\Omega_{\text{rf}}^2}\alpha \tag{3.10}$$

$$a_x = \frac{4QU_{\text{dc}}}{m\Omega_{\text{rf}}^2}\alpha \tag{3.11}$$

where α is the quadrupole moment per volt in the x direction. In the remaining two directions the parameters are similarly defined.

The general solution of the Mathieu equation is given by [53]

$$f(\zeta) = A \cdot e^{i\mu\zeta} \sum_{n=-\infty}^{+\infty} c_n e^{in\zeta} + B \cdot e^{-i\mu\zeta} \sum_{n=-\infty}^{+\infty} c_n e^{-in\zeta} \tag{3.12}$$

where A and B are arbitrary constants, $\mu \in \mathbb{C}$ is the stability parameter which is a function of a and q. The constants $c_n \in \mathbb{R}$, $\forall n \in \mathbb{Z}$, are independent of the initial parameters. This solution is valid for all $\mu \in \mathbb{C}$, however only solutions with μ purely real are bounded at infinity. These solutions are known as **stable** solutions. For a particle to remain confined in the trap, we require that its motion is bounded in all three directions, which leads to the **stability condition** of a particle in the trap. Figure 3.2 shows the values of a and q for which the solution to the Mathieu equation is stable.

For small a and q, the stability parameter is given by

$$\mu \approx \sqrt{a + q^2/2}, \tag{3.13}$$

and by taking the approximation presented in [55], the solution of the equation of motion can be written as

$$u(t) = u_1 \cos(\mu\Omega_{\text{rf}} t/2)\left(1 - \frac{q}{2}\cos(\Omega_{\text{rf}} t)\right), \tag{3.14}$$

where u_1 is an arbitrary constant.

This solution is the product of two terms oscillating at different angular frequencies. The slower term is known as the **secular motion**, and the faster as **micromotion**. If the micromotion

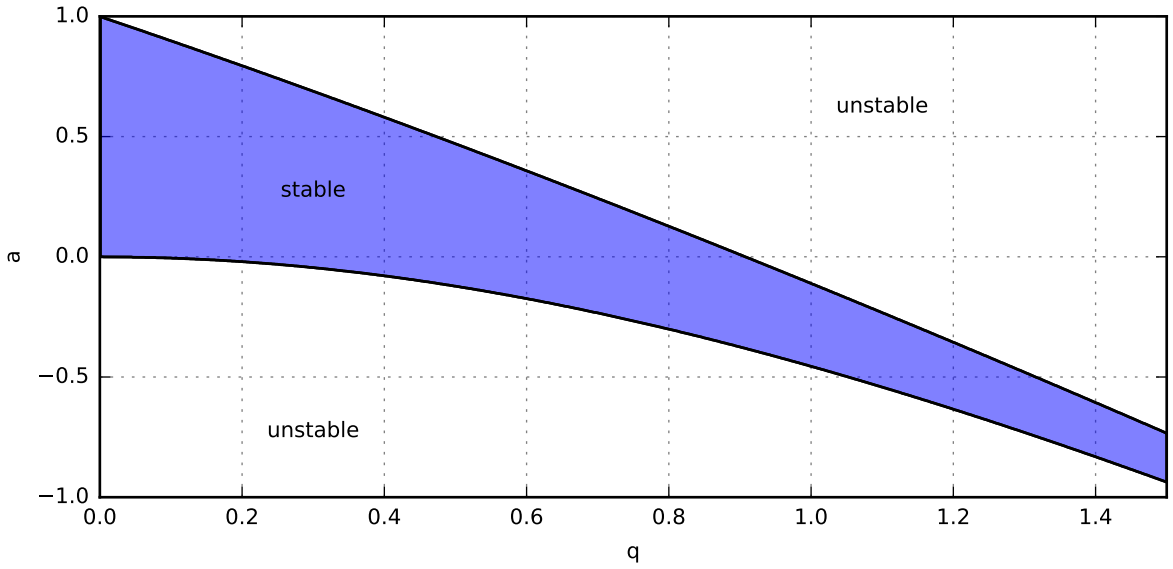

Figure 3.2: Stable solutions to the Mathieu equation are found for pairs of (a,q) which lie within the blue shaded region. This curve was calculated using the recursion formula present in Ref. [54].

term is neglected, the secular motion can be approximated by that of an harmonic oscillator with frequency

$$\omega = \frac{\mu\Omega_{\mathrm{rf}}}{2}, \tag{3.15}$$

with ω known as the **secular frequency**.

If the solution in all three directions is stable and micromotion is neglected, then the charged particle behaves as if it were confined within an effective time-independent 3D potential, known as the pseudopotential. A more formal introduction to the electric pseudopotential is presented in Ref. [56] which leads to the result

$$U_{\mathrm{eff}}(\vec{r}) = \frac{Q^2}{4m\Omega_{\mathrm{rf}}^2}|\vec{\nabla}\Phi_{\mathrm{rf}}(\vec{r})|^2 + Q\Phi_{\mathrm{dc}} \tag{3.16}$$

where $\Phi_{\mathrm{rf}}(\vec{r})$ and $\Phi_{\mathrm{dc}}(\vec{r})$ are the components of the electric potential which are oscillating at Ω_{rf} and static respectively. Since the form of the electric potential can be simulated with high accuracy using numerical methods, the pseudopotential offers a convenient approach for calculating the properties of real trap geometries which can vary significantly from ideal cases.

An important parameter for any trap is its potential depth. This is the maximum kinetic energy that a particle can have without escaping the trap. The trap depth can be calculated from the

pseudopotential, and is given by difference in potential between the lowest lying turning point and trap bottom. Near the turning point or the potential, the quadrupole moments necessarily change. The associated change in the trap stability parameters leads to trajectories with energies approaching the trap depth having marginal stability. Hence, as a rule of thumb, ion traps are typically expected to confine ions up to a temperature that corresponds to about one-tenth of their well depth [55].

Most ion traps are loaded from a thermal atomic beams with average temperatures of 500 K to 1000 K. In order to have a high loading success probability, the potential depth of the trap should be greater than ten times the thermal kinetic energy of the atoms in the beam, i.e.

$$\Delta_{\mathrm{U}} \gg 10 \times \frac{1}{2} k_{\mathrm{B}} T \approx 0.3\,\mathrm{eV}, \tag{3.17}$$

for $T = 600\,\mathrm{K}$, where the approximate factor of ten originates from the requirement described in the previous paragraph. If the trapping depth is lower than this value, then loading from a thermal atomic beam becomes inefficient, since only a fraction of the beam will have low enough energy to remain in the trap.

In addition to determining the loading efficiency of the trap, the depth is can affect the lifetime of trapped ions. Ions can escape the trap through collisions with residual gas in the vacuum chamber. The trap depth sets the energy threshold after collision below which ions will remain in the trap. An alternative loss mechanism for trapped ion is reactions with residual gases, which are not considered here.

In some situations, the ion is probed by interactions which are sensitive to the full motion of the ion. For instance, if the ion is interacting with a light field then motion will lead to a time-dependent Doppler shift of the optical frequency. In this case, the micromotion cannot be neglected and must be included in any analysis. The effect of the micromotion of the ion can be mathematically analysed by looking at the kinetic energy associated with this motion. The mean kinetic energy of the 1D solution presented in equation 3.14 is given by

$$E_{\mathrm{K}} = \frac{1}{2} m \left\langle u'(t)^2 \right\rangle \approx \frac{1}{4} m u_1^2 \omega \left(1 + \frac{q^2}{q^2 + 2a}\right), \tag{3.18}$$

where ω is the secular frequency, u_1 is the amplitude of the secular motion, and we have made the approximation for small a and q as before. The second term in the equation is the kinetic energy contribution from the micromotion.

If a static linear electric field (strength E_0) is applied to the trap, then solution to the resulting equation of motion is given by (see Ref. [57])

$$u(t) = [u_0 + u_1 \cos(\mu \Omega_{\mathrm{rf}} t/2)] \left(1 - \frac{q}{2} \cos(\Omega_{\mathrm{rf}} t)\right), \tag{3.19}$$

for small a and q where

$$u_0 \approx \frac{QE_0}{m\omega^2}. \tag{3.20}$$

From this solution, we can see that the field leads to a displacement in the average position of the ion, with value u_0. Additionally, we see the appearance of a second term oscillating at the drive frequency (Ω_{rf}) with amplitude $u_0 q/2$. This term is known as **excess micromotion**, as it is independent of the amplitude of secular motion and will be discussed further in section 3.6.

3.2 Ion traps with fibre-cavities

In this section, we discuss the specific challenges which need to be addressed when building an ion trap with an integrated fibre-cavity. The main difficulty of reaching strong coupling between ions in cavities lies in the strong charge sensitivity of the ions. This feature which has allowed for the great success of ion trapping, is the very opposite of what is desirable for strong ion-cavity interaction which is optimal when the cavity mirror surfaces are very close to the ion. High-quality cavity mirror coatings are made from dielectric materials which can charge up through the a variety of processes and store charges on their surface for long times. The uncontrolled electrical environment that these surfaces then present is very undesirable for reliable performance of the ion trap.

Initial experiments with a trapped ions in an optical cavity have been very promising. In [58] a single ion was moved into a 6 mm long optical cavity. The long trapping time and strong confinement of the ion allowed for precise measurement of the cavity mode. In the years that followed several further experiments were carried out using similarly large macroscopic cavities, coupling to single ions [59, 60, 61], and large numbers of ions [62].

In order to improve the atom-cavity coupling, it is necessary to reduce the size of the cavities employed. In Ref. [63], an ion trap was developed which used significantly shorter cavities than previous experiments. Although successfully trapping ions within a 2 mm long cavity, it proved not possible to trap within shorter length cavities using this approach [64].

With the invention of optical fibre-cavities [36] there has been renewed excitement in achieving strong coupling with ion-cavity systems. The small radii of curvature which can be achieved with this technique allow for very narrow cavity modes, which in turn means that the surface area of the dielectric mirror that needs to be exposed to the ion can be reduced. With less surface area to carry charges, the impact of charging should be reduced.

Although it is clear that fibre-cavities have strong potential in this regard, the technology

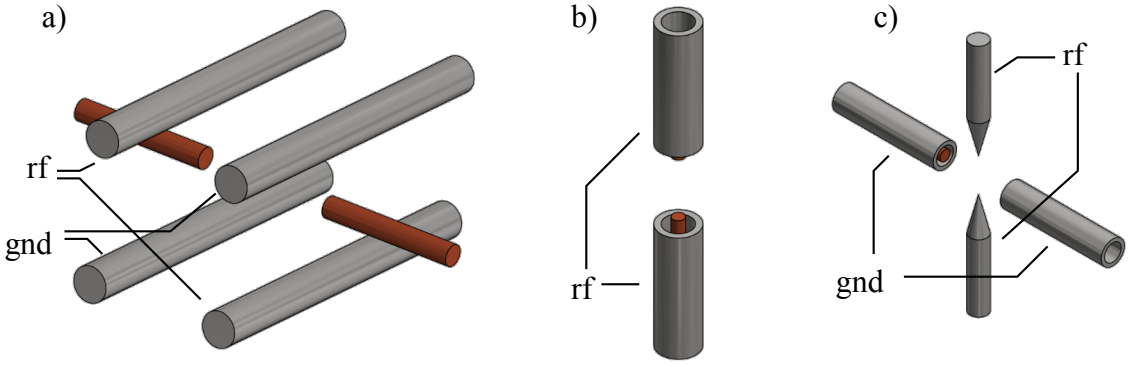

Figure 3.3: Comparison of three approaches to integration of a fibre cavity with an ion trap. a) Linear trap approach. b) An endcap trap with a concentric cavity. c) An endcap trap with a transverse cavity.

requires the development of specialised ion traps in order to incorporate them. Typical dimensions of the mode waist of a fibre-cavity are on the order of a few μm. In order to achieve the maximum atom-cavity coupling rate, the ion needs to be placed at the centre of the cavity mode structure. Alignment of the cavity mode with the trapped ions on this scale is challenging to achieve through mechanical pre-alignment, so most trap designs include a method for adjusting the relative alignment of the trap and the cavity. Currently there are three broadly different approaches to integrating a fibre cavity into an ion trap. Figure 3.3 shows the geometric arrangement for these three approaches.

Some recent experiments [43, 65] have employed modified forms of linear trap, with the cavity introduced either through the endcap electrodes or through gaps between the radial electrodes (as seen in figure 3.3 a). The advantage of this approach is that the techniques for quantum and classical control of the motion of the ions in the axial direction in linear traps are very well developed and understood. This choice allows for the direct application of these proven techniques to perform quantum logic operations using the axial mode. However if, as shown, the cavity fibres are not placed inside conductive sleeves, their outer surfaces can accumulate charges which could cause problems with trapping when introduced near to the ion. On the other hand, if the fibres are surrounded by conductive sleeves, the trapping potential would be perturbed by their presence. This would lead to deviation from the linear trap behaviour which is undesirable.

A second approach, described in [66, 67], is shown in figure 3.3 b). The trap is formed from two hollow rf electrodes which form a type of 3D Paul trap known as an endcap trap [68]. The endcap trap can be seen as a modification of the ideal geometry shown in 3.1 where the ring electrode is stretched out to infinity and the rf field is applied to the endcap electrodes. With this design the cavity fibres can be fully recessed within the rf electrodes, where they are well shielded from lasers intersecting the trap. Additionally, there is a large solid angle available for optical access. This is however a very challenging design to realise for two main reasons. Firstly, the position of the cavity mode waist needs to be aligned to the position of the trap centre with μm precision, but both of these positions are difficult to locate well until the ion trap is operational. As a result, some mechanism for adjusting their relative positions *in situ* is necessary, either by moving the fibres within the electrodes or by moving the trap centre by application of additional rf fields. In addition to difficulty in alignment, construction of this design is complicated by the fact that both the cavity and the trap must be built at the same time. This means that the system has to be very well thought through before a working design can be produced. However, once this has been achieved, the design allows for a very compact and stable system with a large degree of optical access.

The third approach discussed here was first used in [41] and is shown in figure 3.3 c). An endcap trap design is used for the rf electrodes with the cavity introduced along a perpendicular axis. The cavity fibres are recessed within hollow electrodes which are connected to the rf ground, shielding the fibres from the lasers. Though the rf electrode positions are similar to those in 3.3 b), the presence of the grounded electrodes changes the trapping potential considerably such that it resembles a truncated linear trap. With this design it is possible to move the cavity macroscopically relative the ion trap, which in combination with translation stages, allows the cavity to be positioned *in situ* such that the cavity mode maximum coincides with the trap centre. One caveat with this approach is that position of the hollow electrodes has an impact on the position of the trap centre, but this influence can be calculated and does not pose a serious problem with trap operation.

For the work performed in this thesis, we have used the third approach. A photograph of the ion trap is shown in figure 3.4. Surrounding the central rf electrodes are eight dc electrodes which can be used to apply an electric field to compensate fields caused by stray charges. This design choice was motivated by the ease of development of the system with the currently experimental cavity technology, since the cavity can be interchanged without modifying the trap. However, there are significant advantages to using design b) due to its superior compactness and inherent stability, which make it a good candidate for future experiments when fibre-cavities

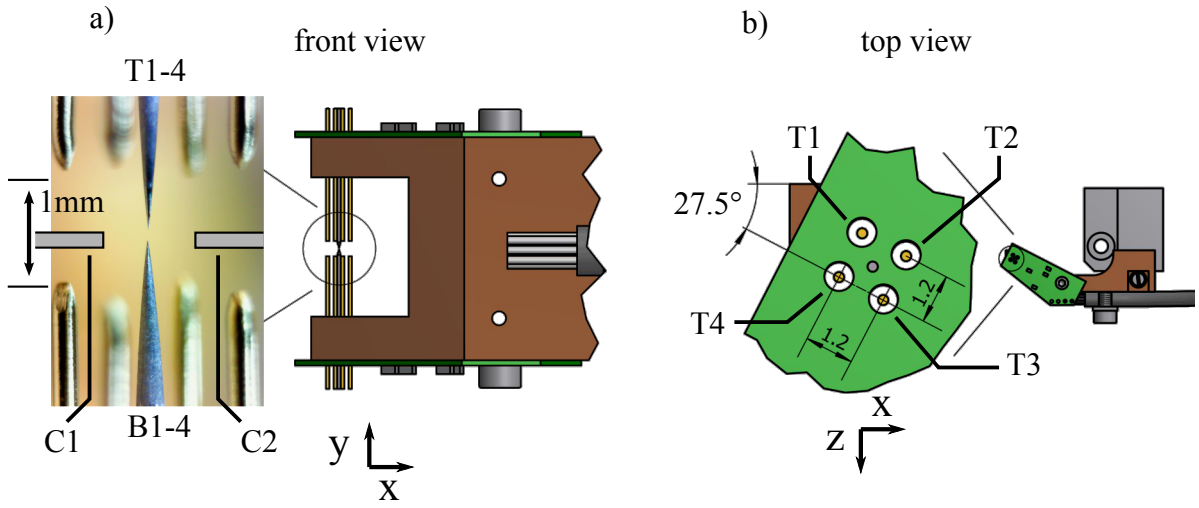

Figure 3.4: a) front view and b) top view of the trap build during this thesis, including a close-up photograph of the electrodes. The coordinate system used throughout this thesis is also defined here, with x representing the cavity axis, y representing the trap symmetry axis, and z the third axis which will later be used for imaging of the trapped ions. The trap is formed from two central rf electrodes which are separated by a distance of 84 µm. Surrounding the central electrodes are 8 independent electrodes formed from gold wire recessed by approximately 500 µm from the centre, labelled T1-4 and B1-4, which can be used to compensate for stray electric fields. Electrodes C1 and C2 are stainless steel tubes within which the Fabry-Pérot cavity fibres are housed.

with ion traps are more mature. This trap is driven with an rf voltage of approximately 75 V amplitude at 30 MHz, and typical secular frequencies of the trap with an Ytterbium ion are in the range 2 to 8 MHz.

3.3 Electrostatic simulations

In the previous section we have motivated the necessity of *tube* electrodes shielding the cavity fibres from lasers. In the trap design we have chosen (figure 3.3 c), the presence of the tube electrodes has a strong effect on the trapping potential, which can lead to changes to the direction of the principal trap axes and their relative strengths. Additionally, the fields produced by the dc electrodes used to compensate stray electric fields at the ion will be partially shielded by the

tube electrodes, so their directions and magnitudes will differ between the two configurations. Finally, changes in the relative position between the cavity and the trap electrodes will lead to slight changes in the position of the trap centre.

In order to understand these effects quantitatively, we have simulated the static electric fields produced by the electrode geometry. Simulations were performed using an open source package[1] which employs a boundary element method to solve the charge distribution on the surface of the electrodes.

3.3.1 Trap quadrupole moments

Table 3.1 provides a summary of the simulated quadrupole moments of the rf electrodes for both configurations of the trap. Without the cavity electrodes present, the trap electrodes produce a field which has the same quadrupole moments to that of an ideal 3D Paul trap, up to a scaling factor. The two weaker trap axes have approximately the same quadrupole moment in the x-z plane, and in the real case are likely defined by asymmetry in manufacture of the trap electrodes. When the cavity tubes are introduced, the principal axes are well determined by the electrode geometry. The quadrupole moments along all three axes increase in magnitude due to the now closer ground electrodes. Although the moment along the third axis (z) is stronger than in the previous case, its strength relative to the strongest moment is lower.

Configuration	Without cavity	With cavity
Principal axes	$\hat{y}$	$\hat{y}$
	x-z plane	$\hat{x}$
	x-z plane	$\hat{z}$
Quadrupole moments	65	127
$1/\mathrm{mm}^2$	-33	-82
	-33	-45

Table 3.1: Summary of trap properties obtained through simulation. Principal axes are given in terms of the coordinate system shown in 3.4. The quadrupole moments are determined along the principal axes at the position of the rf null.

[1] Simulations were carried out with BEMSolver [69] which has been packaged to work as a Python library by R. Maiwald.

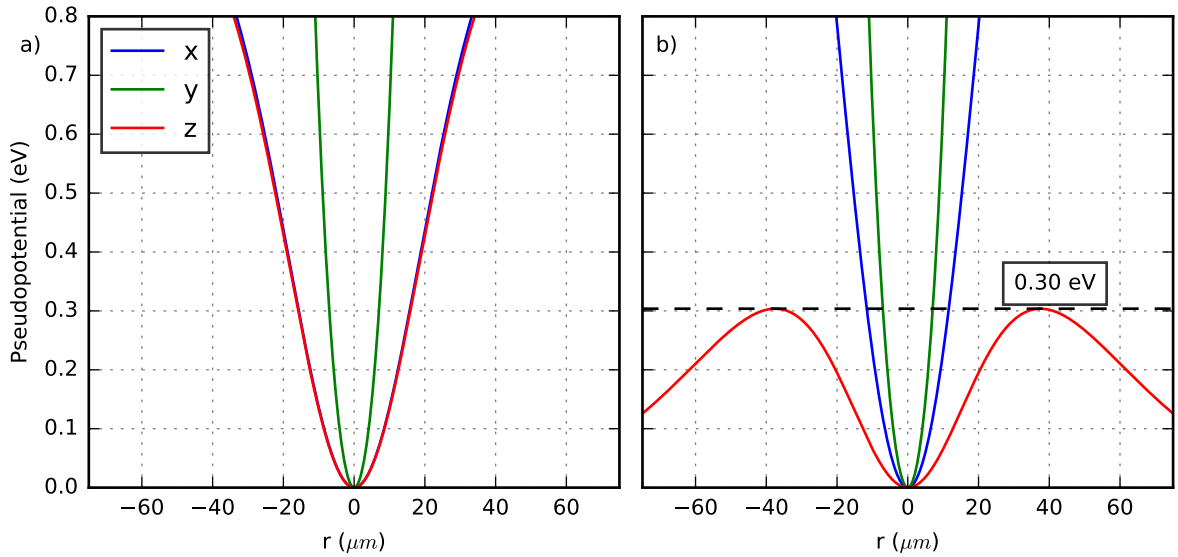

Figure 3.5: Simulation of the trap pseudopotential along x, y and z axes for $^{174}Yb^{+}$ ions with $\Omega_{rf} = 2\pi \times 30\,\text{MHz}$ for a) the trap without the cavity electrodes, and b) with the cavity electrodes. The rf voltage in each case was chosen such that all $q_i \leq 0.3$, which corresponded to a) 148 V and b) 75 V.

Figure 3.5 shows the spatial variation of the pseudopotential calculated from the electrostatic simulations using the charge and mass of $^{174}Yb^{+}$ ions. The rf voltage was chosen in each case to be as large as posible while keeping the motion along each principal axis stable within a certain margin[2]. The resulting rf voltages were 295 V and 151 V for the case without and with the cavity electrodes respectively. One can see clearly that by introducing the cavity electrodes to the trap, the pseudopotential has changed significantly, leading to a much stiffer trap in the cavity (x) direction, but much weaker in the third direction (z).

The potential depths of the two trap configurations are also shown in figure 3.5, calculated by finding the lowest turning point in pseudopotential in all directions. The lowest turning point was found along the z axis in the case with the cavity, and in the x-z plane without the cavity. By inspection we see that the depths are of the same order as the minimum depth required for loading from the thermal oven (see equation 3.17) of 0.3 eV, which may prevent efficient loading, especially in the case with the cavity electrodes present. Application of a dc field can

[2]We have chosen to use $q \leq 0.6$ as the upper limit for our stability parameter along each axis in this analysis, since this corresponds to the upper boundary of stability we find experimentally in the trap

be used to improve the trap depth and is discussed in the next subsection.

3.3.2 Static fields

Until now we have considered the form of the electric field generated by the rf electrodes, however it is also important that we understand the behaviour of the dc fields which can be applied to the trap in order to compensate stray electric fields or provide additional quadrupole moments at the ion.

The naming convention of the available dc electrodes is shown in figure 3.4. In order to cancel the contribution of an electric field at the position of the ion caused by stray charges, a total of three electrodes are required. In our trap, we have ten electrodes which allows for application of certain dc quadrupole fields in addition to stray field compensation. In order to reduce the complexity of controlling the individual electrodes, they have been grouped into subsets which provide a particular effect. These groups are given in table 3.2. Each electrode group is assigned a control voltage, and the voltage on an electrode is the sum of all the contributions from each group.

Name	T1	T2	T3	T4	B1	B2	B3	B4	C1	C2
Y	-	-	-	-	+	+	+	+		
X		-		+		-		+		
Z	+		-		+		-			
CX									-	+
Offset	+	+	+	+	+	+	+	+		
Quad	+	-	+	-	+	-	+	-		
CBias									+	+

Table 3.2: Summary of dc electrode groups. The electrode naming scheme is shown in figure 3.4. A + (-) indicates that the electrode voltage is a positively (negatively) influenced by the group voltage. For example, if the Y group is set to 1 V, then T1-4 will be set to -1 V, B1-4 will be set to 1 V, and C1-2 will be unaffected. The first set of groups is intended to produce linear fields at the ion, and the second set should produce quadrupole moments.

Configuration	Without cavity	With cavity
Dipole moment/V $(1/\mathrm{mm})$		
Y	$0.21 \times (-\hat{y})$	$0.042 \times (-\hat{y})$
X	$0.47 \times (-0.95\hat{x} + 0.30\hat{z})$	$0.036 \times (-0.20\hat{x} - 0.98\hat{z})$
Z	$0.47 \times (-0.30\hat{x} - 0.95\hat{z})$	$0.12 \times (-\hat{z})$
CX	-	$14 \times (-\hat{x})$
Quadrupole moment/V $(1/\mathrm{mm}^2)$		
Offset	(24, -47, 24)	(-4.5, -0.83, 5.3)
Quad	(-0.60, 0.00, 0.60)	(0.53, -0.038, 0.85)
CBias	-	(89, -127, 38)

Table 3.3: Summary of compensation electrode group field moments at the trap centre per volt applied to the group. The axes for the dipole moments are given in brackets. The quadrupole moments are evaluated along the trap principal axes (x, y, z), with the exception of *Quad* in the case with no cavity. In this case application of the field breaks the degeneracy of the trap potential in the x-z plane, so the moments are specified along the principal axes of the quadrupole field.

The electric field produced by each electrode group was calculated using the electrostatic simulations described earlier. The corresponding dipole and quadrupole moments are given in table 3.3. First, we consider the properties of the first four groups in the table which produce dipole moments. In the first column, without the cavity, we see that *Y*, *X*, and *Z* produce dipole moments in approximately the expected direction with the slight deviation for *X* and *Z* caused by the rotated positioning of the electrodes with respect to the coordinate system. When the cavity electrodes are introduced, shown in the second column of table 3.3, the strength of the *Y*, *X*, and *Z* moments are reduced considerably due to shielding from the cavity electrodes. Additionally, the direction of the *X* group dipole has been rotated such that the majority of the field points along the z direction. Because of this, we can only use *CX* group to provide a field along the x direction.

The second set of electrode groups are intended to apply quadrupole fields at the position of the ion, and the corresponding moments are shown in the lower section of table 3.3. Without the cavity electrodes, the *Offset* group can be used to apply a significant quadrupole field in order to strengthen the trap in the x and z directions, and *Quad* can be used to apply a slight

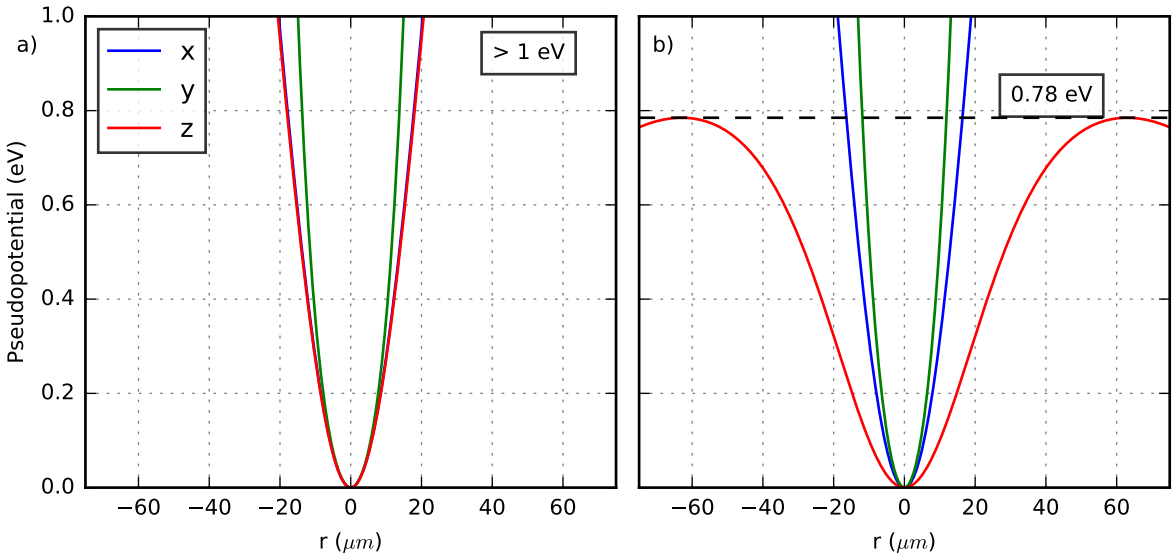

Figure 3.6: Simulation of the trap pseudopotential with dc potentials applied. The parameters are similar to figure 3.5, with an additional dc field due to a) the electrode subgroup *Offset* when no cavity is present, and b) the electrode subgroup *CBias* with the cavity electrodes present. In each case, the dc voltage was chosen to be as large as possible whilst maintaining stable solutions in all three directions. The dc voltages under this condition are a) 59 V and b) 12 V.

field which will break the symmetry in the x-z plane. When the cavity electrodes are added to the simulation, the strength of the Offset field drops due to shielding, but the *CBias* field can be used instead.

By applying voltages to the electrode groups which have significant quadrupole moments, it is possible to change the strength, and potential depth, of the trap. From the result shown earlier in figure 3.5 we understand that the trap depth without dc fields is low enough that the success rate of loading, and also the trap lifetime, may be low. One might suggest that we can arbitrarily increase the dc field to increase the depth of the trap. This however does not work as the sum of the quadrupole moments of the applied field has to vanish (see equation 3.2), so in order to increase the trap strength in one direction, we must also weaken the trap along at least one other direction. A further limitation to the dc quadrupole field that we can apply is given by the need for the solution to the Mathieu to be stable for motion along each principal axis.

Figure 3.6 shows the pseudopotential for $^{174}Yb^{+}$ ions of the trap including contributions from an applied dc field. With a strong dc quadrupole moment applied via the *Offset* group, the

depth of the trap without the cavity can be increased to well above 1 eV. In the case with the cavity electrodes in place, the maximum achievable trap depth is 0.78 eV. Finally, one could consider applying a dc bias to the rf needles to increase in the trap depth further. However, this has not been used here as it would have required a modification to the delivery of the rf voltage.

3.3.3 Trap centre displacement

In section 3.2 we have discussed the need to translate the cavity relative to the trap in order allow to being able to maximise the interaction between the ion and the cavity mode field. With the trap design presented here, the cavity is free to be mounted on a translation stage that can provide the necessary degrees of freedom. However, motion of the cavity electrodes will lead to changes in the electric fields producing the trapping potential, likely changing the position of the trap centre. As the atom-cavity coupling rate is dependent on the relative position between the cavity mode and the trapped ion, in order to make statements about the spatial extent of the cavity mode it is important to understand this behaviour quantitatively.

Using the electrostatic simulations described earlier, the position of the trap centre was located for several different positions of the cavity. Figure 3.7 shows the results of the simulations. We observe that when the cavity is translated along its symmetry axis (x), the trap centre is displaced in the same direction by approximately 54 % of the electrode displacement, reducing the relative motion between the cavity mode and ion to 46 % of the cavity displacement. In the other two directions, trap centre displacement occurs on the 2 % and 8 % level for y and z respectively. The results of this analysis are important for chapter 6.1 where the waist of the cavity mode is determined by translating the cavity.

3.4 Doppler cooling

We wish to study the interactions of a trapped ion with light either from a laser or in the cavity mode. In both cases, it is important to consider motion of the ion relative to the light field as this can lead to a Doppler shift in the frequency of the light. It is possible to use this effect to reduce the kinetic energy of the ion, using a technique known as Doppler cooling which was first examined for trapped particles in [70, 71].

A full description of Doppler cooling in an ion trap is presented in Ref. [72], however a simple qualitative explanation can be found by neglecting micromotion and treating the motion

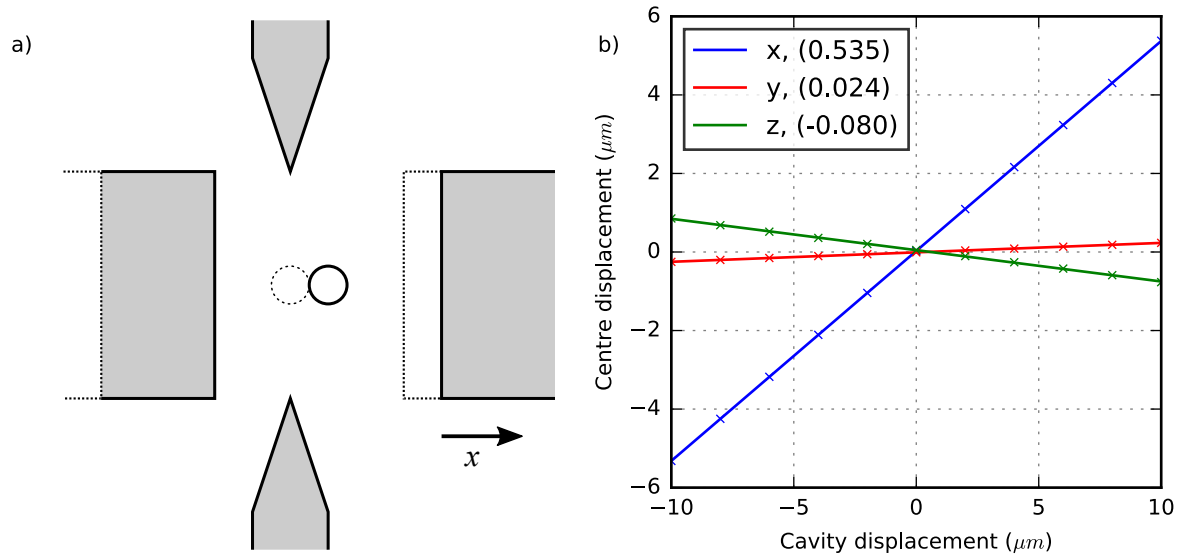

Figure 3.7: Simulated displacement of the trap centre when the cavity electrodes are offset from the geometric centre. a) Diagram showing displacement of trap centre as a result of displacement of the cavity electrodes in the x direction. b) Simulation results. The cavity electrodes are translated along the three coordinate axes (x, y, and z) and the displacement of the trap centre is measured along the corresponding axis. The number in brackets is the gradient of the linear fit (drawn with solid lines).

of the ion classically in one dimension. In this case, the velocity of the ion is given by

$$v(t) = v_0 \cos(\omega t), \tag{3.21}$$

where ω is the secular frequency of the trap. A laser field is present at the ion, with its direction of travel aligned along the motional axis we are considering. For every photon absorbed by the ion, it will experience a momentum kick of $\Delta p = \hbar k$ along the direction of the laser, while the near instantaneous (if $\omega \ll \Gamma$) emission of the photon will occur symmetrically about the axis of motion. On average, this momentum transfer due to emission will cancel out. The time-averaged effect of the laser is therefore to transfer momentum to the ion at a rate of photon absorption/emission of the ion. The force, averaged over several emission cycles, is therefore given by

$$\bar{F} = \frac{dp}{dt} = \hbar k \Gamma \rho_{ee}, \tag{3.22}$$

where ρ_{ee} is the excited state population of the two-level system excited by a classical laser

field.

From the solution presented in section 2.1.2, we have

$$\rho_{ee} = \frac{s/2}{1+s+(2\Delta_{\mathrm{L}}/\Gamma)^2}, \tag{3.23}$$

where Δ_{L} is the detuning between the laser field and the atomic transition, and s is the saturation parameter of the system. As the ion is moving with respect to the laser field, it experiences a Doppler shifted detuning given by $\Delta'_{\mathrm{L}} = \Delta_{\mathrm{L}} - kv(t)$. The average force can therefore be written as

$$\bar{F} \approx F_0(1+\mu v) \tag{3.24}$$

where we have taken the approximation for $\mu v \ll 1$, with

$$F_0 = \hbar k\Gamma \frac{s/2}{1+s+(2\Delta_{\mathrm{L}}/\Gamma)^2} \tag{3.25}$$

and

$$\mu = \frac{8k\Delta_{\mathrm{L}}/\Gamma^2}{1+s+(2\Delta_{\mathrm{L}}/\Gamma)^2}. \tag{3.26}$$

From the form of equation 3.24, we can see that the ion experiences a constant force of magnitude F_0 in addition to term proportional to velocity. The average rate of change of kinetic energy of the ion is given by

$$\frac{dE_{\mathrm{c}}}{dt} = \langle \bar{F} v \rangle = F_0(\langle v \rangle + \mu \langle v^2 \rangle) = F_0 \mu \langle v^2 \rangle, \tag{3.27}$$

where we have used $\langle v \rangle = 0$ as the ion is trapped. We can therefore change the average kinetic energy of the ion, and choice of the sign of the atomic detuning Δ_{L} determines whether the ion is heated (for positive detunings) or cooled (for negative detunings).

Equation 3.27 implies that the kinetic energy of the ion can be cooled indefinitely, which is however not the case. Although the photon emission from the ion results in no average change of momentum of the ion ($\langle \Delta p \rangle = 0$), because of the finite momentum of the photons the average magnitude of the momentum is non-zero i.e. $\langle p^2 \rangle \neq 0$. Similarly, the photon absorption also contributes to the non-zero average magnitude. This stochastic motion that results from the photon absorption and emission can be seen as an effective heating term, given by [55]

$$\frac{dE_{\mathrm{h}}}{dt} = \frac{1}{2m}(\hbar k)^2 \Gamma \rho_{ee}(v=0)(1+\zeta), \tag{3.28}$$

where ζ is a geometry factor which is determined by absorption and emission properties of the transition, taking a value of $2/5$ for dipole transitions. The system will tend toward the equilibrium where $\frac{dE_h}{dt} = \frac{dE_c}{dt}$, which gives

$$\langle v^2 \rangle = \frac{\hbar\Gamma}{8m}(1+\zeta)\Big[(1+s)\frac{\Gamma}{2\Delta_L} + \frac{2\Delta_L}{\Gamma}\Big]. \tag{3.29}$$

The temperature of the ion is given by $T = m\langle v^2 \rangle / k_B$ where k_B is the Boltzmann constant. Equation 3.29 is minimised when $\Delta_L = \Gamma\sqrt{1+s}/2$, resulting in a minimum temperature of

$$T_{\min} = \frac{\hbar\Gamma\sqrt{1+s}}{4k_B}(1+\zeta). \tag{3.30}$$

In our experiment, we wish to Doppler cool in three dimensions with a single laser. For a weak laser with detuning $\Delta_L = \Gamma/2$, the kinetic energy along each trap axis is given by [73]

$$E_{Ki} = \hbar\Gamma(1 + f_{si}/f_i)/8, \tag{3.31}$$

where f_{si} is the normalised spontaneous scattering rate along the i'th trap axis, and f_i is the normalised laser intensity along the i'th trap axis. For the ion trap used in this thesis, with the Doppler cooling laser beam angles given in table 5.1, the normalised laser intensities have values 0.58, 0.71 and 0.41 along the x, y and z axes respectively. Assuming isotropic emission, $f_{si} = 1/3$, the effective minimum temperatures are 0.37, 0.35 and 0.43 mK along the x, y and z axes respectively.

3.5 Ytterbium ions

There are several ions which are suitable for modern ion trapping experiments. Their suitability is generally determined by the availability of a dipole transition for Doppler cooling which is accessible with current laser technology, and can be 'closed' so that a large fraction of the population remains in the cooling manifold. A second suitability criterion is whether the ionic level scheme has a configuration which is amenable to quantum state preparation and readout techniques. In all the experiments carried out in this thesis we have used two isotopes of singly-ionised ytterbium ions, $^{174}Yb^+$ and $^{171}Yb^+$, with nuclear spin 0 and 1/2 respectively. In this section the physics of ytterbium atoms which is relevant in the context of ion trapping is introduced.

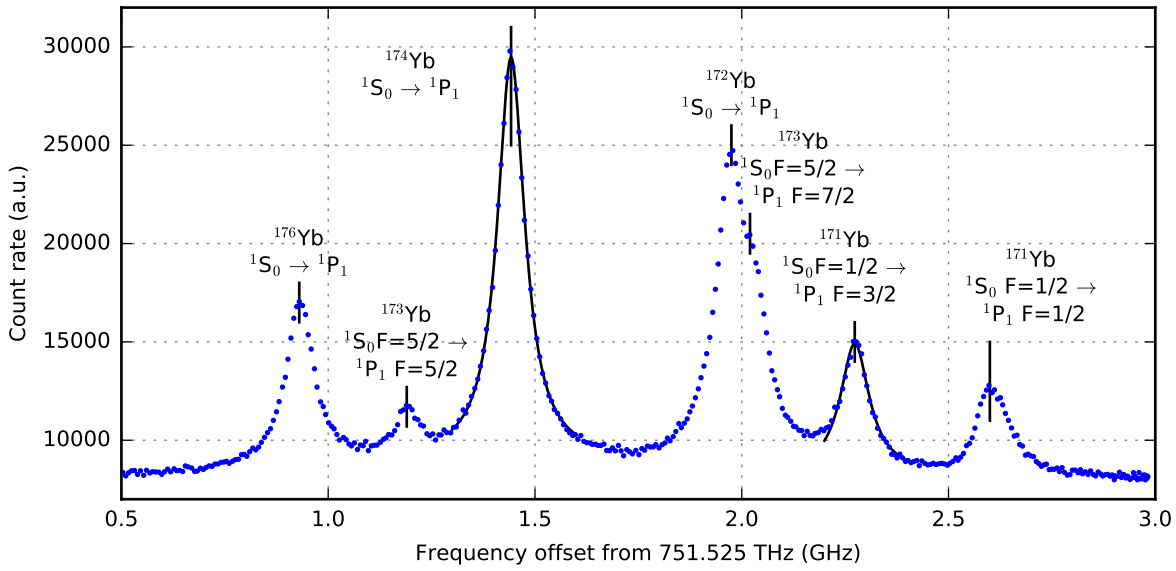

Figure 3.8: Resonance fluorescence from Yb in the atomic beam of the oven excited by the loading laser near 399 nm oriented near perpendicular to the atomic beam axis. This frequency axis was calibrated with a wavemeter (HighFinesse WS7). The transitions for the various isotopes visible in this measurement are indicated, identified using data from Ref. [76].

3.5.1 Photoionisation

In order to load the trap, we must ionise an atom which is located inside the trapping region. In our case, we photoionise ytterbium ions from a neutral atomic beam intersecting the trapping region. The process we use for this is resonance-enhanced two-photon ionisation which was first used in the context of ion trapping in Ref. [74]. Here, neutral ytterbium atoms from the beam are excited into the $^1P_0$ state with a resonant laser beam near 399 nm. From the atomic $^1P_0$ state, the photoionisation threshold corresponds to approximately 394 nm [75]. As the second photoionisation process is non-resonant, we can drive this with light near 370 nm which is also used for Doppler cooling of the ion.

In addition to providing an all optical ionisation process producing considerably less stray charge than electron impact ionisation, the isotope shift on the 399 nm transition allows for isotope selective loading. A measurement of the fluorescence observed under excitation from the loading laser is shown in figure 3.8. Doppler broadening of the transition is minimised by choosing the direction of the laser to be perpendicular to the direction of the atomic beam. The widths of the Lorentzian features in figure 3.8 are approximately 80 MHz which is consistent

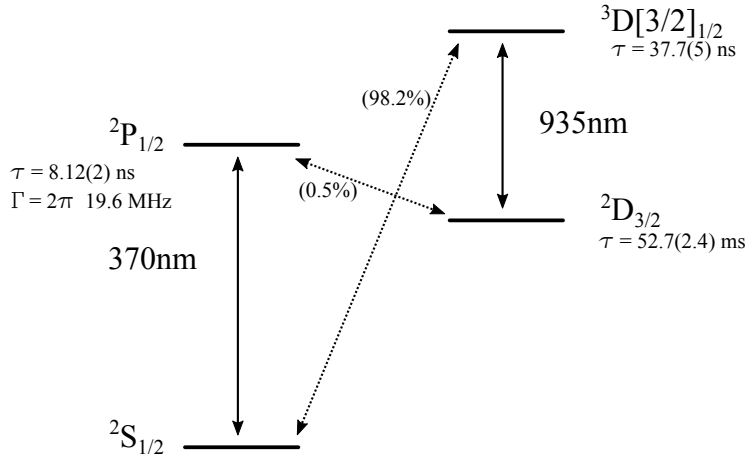

Figure 3.9: Energy levels of Yb^+ which are relevant for this work. The lifetime of the excited states $^2P_{1/2}$, $^2D_{3/2}$ and $^3D[3/2]_{3/2}$ are taken from Refs. [77], [78] and [79] respectively. The branching ratios (shown in brackets) are from [77].

with power broadening. By tuning the laser to the centre of one of these features, photoionisation will only occur with the associated species.

Due to the non-zero nuclear spin of ^{171}Yb, the $^1S_0 \rightarrow {}^1P_1$ transition is split by approximately 300 MHz. The two features are shown in figure 3.8. In this experiment we have used the $^1S_0\,|F = 1/2\rangle \rightarrow {}^1P_1\,|F = 3/2\rangle$ transition for loading $^{171}Yb^+$, as the other transition is very near to the resonance associated with ^{170}Yb.

3.5.2 Cooling

After an ion has been successfully captured in the trap, the ion's kinetic energy needs to reduced by Doppler cooling before it can be used to perform measurements. The fine level structure of Yb^+ ions is shown in figure 3.9.

Doppler cooling is performed using the $^2S_{1/2}$ to $^2P_{1/2}$ transition near 370 nm, which has a natural linewidth of $2\pi\times19.6$ MHz. From equation 3.30, which ignores the effects of micromotion, we expect the final temperature of the ion to be $\approx$0.33 mK when cooled with light below saturation at a detuning of $\Delta_L = -\Gamma/2$.

During the cooling cycle, the $^2P_{1/2}$ excited state decays into the $^2D_{3/2}$ state with a branching ratio of approximately 1/200. Population from this state is cleared out with laser resonant with the $^2D_{3/2} \rightarrow {}^3D[3/2]_{3/2}$ transition near 935 nm.

3.6 Stray field compensation

In section 3.1 we have discussed the effect of additional linear electric fields on the motion of the ion. Namely, these fields cause the ion to undergo driven motion at the trap drive frequency which is independent of the secular motion, known as excess micromotion. In general, when working with single ions in a Paul trap, it is desirable to minimise this excess micromotion, as it can lead to broadening of spectral lines of the ion due to the Doppler shift associated with the motion [57]. Additionally, in the trap used for the results of this thesis, we observe that excess micromotion leads to a reduction in the lifetime of the ion in the trap, however this effect was not investigated. Furthermore, we expect that the presence of the dielectric surfaces of the fibre-cavity so close to the ion may lead to the build up of stray charges. The influence of these charges, although reduced through the use of the cavity electrode shielding effect, may contribute significant linear electric fields (referred to as **stray fields**) at the ion which will lead to excess micromotion.

In order to minimise this excess micromotion, we can apply an arbitrary linear field which will nullify the stray field by using linear combinations of the electrode groups described in section 3.3.2. However, we must first find a method to quantify the magnitude and direction of the stray field vector at position of the ion. Several techniques for detecting excess micromotion are described in Ref. [57], however in the following only the two methods used here are discussed.

3.6.1 Fluorescence modulation

The first method we discuss here was first demonstrated in Ref. [57], and is based on the Doppler shift caused by the excess micromotion.

In section 3.1 excess micromotion has been introduced as motion occurring at the trap drive frequency with an amplitude which is independent of the secular motional amplitude. By considering the case where the excess micromotion amplitude is greater than the intrinsic micromotion, from equation 3.19 we have

$$u(t) \approx -\frac{u_0 q}{2}\cos(\Omega_{\mathrm{rf}} t), \tag{3.32}$$

where $u_0 = QE_0/m\omega^2$. When the ion is excited with a laser field along its motional axis, the ion experiences the laser frequency Doppler-shifted by $-kv(t) = -k\dot{u}$. In the case where $\Omega_{\mathrm{rf}} \ll \Gamma$, the system will reach its steady state faster than the micromotion time-scale[3]. The fluorescence

[3]This condition is not strictly met with the $^2\mathrm{S}_{1/2} \rightarrow {}^2\mathrm{P}_{1/2}$ transition in our trap, however the results of this analysis are still qualitatively relevant.

rate can be calculated from the steady state solution of ρ_{ee} from equation 2.22

$$R = \Gamma\rho_{ee} = \Gamma\frac{s/2}{1+s+\left[2\Delta_{\mathrm{L}} - 2\mu\Omega_{\mathrm{rf}}\sin(\Omega_{\mathrm{rf}}t)\right]^2/\Gamma^2}, \tag{3.33}$$

where $\mu = u_0 q/2 = QE_0 q/2m$. The resonance fluorescence rate of the ion is therefore modulated at the trap drive frequency. For a given value of μ, modulation is maximised when the detuning is chosen to be one half of the power-broadened FWHM. In this case and for small Doppler shifts, i.e. $\mu\Omega_{\mathrm{rf}} \ll \Gamma$, the modulation is linear in μ, and therefore is proportional to the stray electric field.

The fluorescence rate modulation can be detected experimentally by comparing the arrival times of photons generated by the ion with the trap drive phase. In this way, by measuring the correlation of arrival times with the trap drive frequency, the amplitude of linear electric field component can be inferred. When the problem is considered in three dimensions, the modulation is linear in the electric field component along the propagation direction of the laser beam. In order to detect and nullify an arbitrary electric field in three dimensions, it is therefore necessary to have three separate laser beams whose k vectors do not lie in a common plane.

3.6.2 Parametric excitation

An alternative method for detection of the excess micromotion is presented in Ref. [80]. Unlike the fluorescence modulation technique, this method does not place any extra requirements on laser beams apart from those necessary for Doppler cooling.

If the trap drive voltage has a weak amplitude modulation (with depth h) at frequency $\omega_{\mathrm{m}} \ll \Omega_{\mathrm{rf}}$, then the ion motion in the pseudopotential approximation is given by [80]

$$\ddot{\bar{u}} + \omega^2\left[1 + 2h\cos(\omega_{\mathrm{m}}t)\right]\bar{u} = 0, \tag{3.34}$$

where $\bar{u}(t)$ is the secular component of the ion motion, and ω is the secular motion frequency. This equation is that of a parametric oscillator, which has the property that the motion is resonantly excited when $\omega_{\mathrm{m}} = 2\omega/n$ where n is a natural number. However, if the ion is initially stationary and at the trap centre, i.e. $\bar{u} = \dot{\bar{u}} = 0$, then motion will not be excited. Therefore, the occurrence of parametric excitation can be used to detect how the ion is positioned with respect to the rf null.

When the parametric excitation resonance condition is met the ion experiences motional heating. The excitation can be observed by means of an increase in the resonance fluorescence

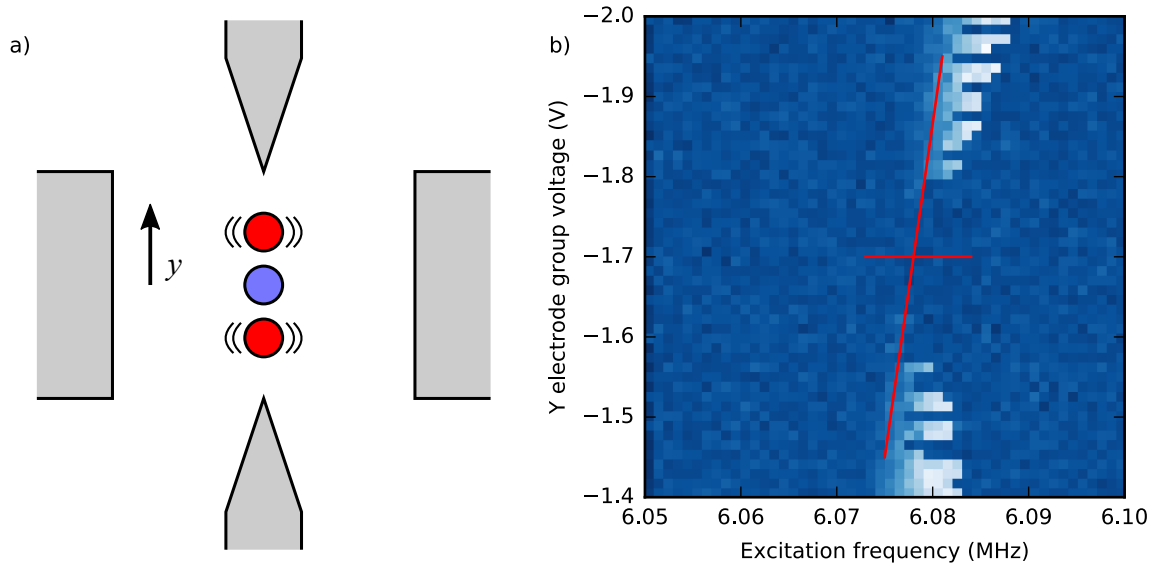

Figure 3.10: Parametric micromotion detection scheme. a) An electric field in the y direction is applied with the Y electrode group. When the ion is displaced from the centre of the trap it is heated by the parametric resonance (shown in red), whereas when it is well centred there is no heating (shown in blue). b) Measurement of resonance fluorescence from Doppler cooling of the ion whilst undergoing parametric excitation over a range of excitation frequencies. The colour scale ranges from blue, representing a low count rate, to white representing a high count rate. From this data we find that excess micromotion is minimised in the y direction when a voltage of $-1.7\,\mathrm{V}$ is applied. Equivalent measurements are made in the same way using the X/CX and Z electrode groups for compensation along the x and z trap axes.

of the ion from the Doppler cooling beam if the detuning and saturation parameter are set appropriately. For constant laser parameters, the increase in fluorescence can be minimised by applying an appropriate dipole field, thereby cancelling the stray field.

Figure 3.10 shows a typical measurement used to minimise the excess micromotion using the parametric excitation scheme. In this measurement, a weak rf signal near 6 MHz was added to the trap drive field to excite the ion at the secular motional frequency in the vertical direction ($\approx$6.08 MHz). The ion was continuously Doppler cooled during this measurement with $\Delta_\mathrm{L} = -50\,\mathrm{MHz}$ and $s = 5$, and the total measurement time was approximately one minute. In order to minimise the micromotion in three dimensions, a similar measurement is required for each principal axis of the trap. In contrast to the fluorescence modulation technique described

earlier, this method requires only one Doppler cooling laser, as the electric field components are resolved along the principal axes of the trap rather than the laser k vectors.

3.6.3 Discussion of techniques

The two methods described here for detection of excess micromotion have both been employed in this experiment. During the coarse of this experiment, we have however come to the conclusion that for future operation of this trap, the fluorescence modulation technique is preferred.

Initially, when the trap was operated without the optical fibre cavity, the parametric excitation method was used. In order to fully compensate the stray electric field at the ion in three dimensions, an iterative procedure was required because the direction of applied compensation fields were not completely orthogonal to each other. In total, the compensation procedure required approximately half an hour to complete. The main limitation of this method is that, because the applied electric fields cause the secular frequencies to change, the excitation frequency must be scanned which increases the required acquisition time.

After installation of ultraviolet fibre cavity into the ion trap, the performance of the trap changed significantly due to the shallower trap depth and presence of the additional surfaces near to the ion including the dielectric mirror coatings. We observe that the dipole moment of electric field at the position of the ion changes on the $\approx 1\,\mathrm{V/mm}$ scale daily. Additionally, we observe changes in the trap secular frequencies at the 10 % level at our standard trap operating parameters, indicating changes in the quadrupole moment of the electric field at the ion.

The combination of the reduction in trapped ion lifetime with the dynamic nature of the stray field at the ion make the parametric excitation method unsuitable for reliable field compensation. Instead, we have used the fluorescence modulation technique using only the two beams which are currently available for this method. Compensation of the stray field using these two laser beams is fast but is not able to fully determine the stray field in three dimensions, so in the future we plan to add a third beam suitable for this method. It is important to note that even though it is not possible to place a beam directly along the cavity axis, this does not limit the application of this method since the main cooling laser has a $\approx 60\%$ coefficient for micromotion in this direction due to the steep angle.

Chapter 4

Fibre-cavities

Since they were first developed in 2006 [36], optical fibre-based Fabry-Pérot cavities (or fibre-cavities for short) have provided an entry into a regime of atom-cavity interaction which had previously been unreachable.

Fibre-cavities are formed from two concave dielectric mirrors which are each machined onto the surface of cleaved optical fibres. There are three key advantages in doing this:

- It is possible to machine very small radii of curvature mirrors, which are infeasible with standard 'macroscopic' glass machining methods.
- Fibre-cavities are inherently miniaturised due to the small form factor of the fibres, especially relevant when working with trapped ions in order to reduce surface charging effects.
- If the single-mode optical fibre is used, light leaving or entering the cavity must have a defined mode. The mode-matching between cavity and fibre mode is then set by the geometry of the fibre-cavity and is independent of outside influences.

In this chapter the properties of Fabry-Pérot cavities are introduced, including parameters which are important to consider when constructing fibre-cavity systems. The specific requirements for building a fibre-cavity to be integrated into our chosen trap design are described, and the two approaches we have taken towards this goal are explained. Mechanical resonances in cavity mounting structures have been identified as problematic for the fine control of the cavity length required, and techniques are described which have been used to probe these resonances. Finally, the optical losses observed after exposure to ultra-high vacuum conditions are presented and discussed.

4.1 Theory

4.1.1 Fabry-Pérot cavities

A Fabry-Pérot cavity is an optical interferometer formed by two partially reflective mirrors facing one another. The reflectivity of the mirrors causes interference when light waves are incident on the cavity. The transmission of an ideal Fabry-Pérot cavity formed by two identical lossless mirrors with power reflectivity R and separated by length d is given by [81]

$$\mathcal{T}_{\mathrm{FP}}(\nu) = \frac{1}{1+\frac{4\mathcal{F}^2}{\pi^2}\sin^2(\pi\nu/\Delta\nu_{\mathrm{F}})} \tag{4.1}$$

where ν is the optical frequency, $\Delta\nu_{\mathrm{F}}$ is the free spectral range (FSR) defined $\Delta\nu_{\mathrm{F}} = c/2d$, and

$$\mathcal{F} = \frac{\pi\sqrt{R}}{1-R} \tag{4.2}$$

is known as the finesse of the resonator. In this lossless cavity, the reflected power from the cavity is simply given by

$$\mathcal{R}_{\mathrm{FP}}(\nu) = 1 - \mathcal{T}_{\mathrm{FP}}(\nu) \tag{4.3}$$

from conservation of energy. When the distance between the two mirrors is an integer or half-integer number of wavelengths, the interference is constructive and the corresponding transmission is unity.

In the case where the mirrors are highly reflective, i.e. $1-R \ll 1$, or equivalently $\mathcal{F} \gg 1$, the transmission near resonance has Lorentzian form with full width at half maximum given by

$$\Delta\nu_{\mathrm{c}} = \Delta\nu_{\mathrm{F}}/\mathcal{F} \tag{4.4}$$

which is known as the linewidth of the cavity.

In a real cavity, mirrors have finite losses due to the occurrence of absorption and scattering, and one may choose to form cavities with pairs of mirrors with different reflectivity. From conservation of energy, the properties of each mirror follow the condition

$$T + R + L = 1 \tag{4.5}$$

where T and L are the power transmission and non-transmissive losses for the mirror. With the properties of each mirror labelled with a subscript, the finesse is then given by

$$\mathcal{F} = \frac{\pi\sqrt[4]{R_1R_2}}{1-\sqrt{R_1R_2}} \approx \frac{2\pi}{\sum T_i + L_i} \tag{4.6}$$

where the approximation is valid for $T_i + L_i \ll 1$ and we have neglected any losses which are incurred within the cavity (i.e. from the absorption of a medium) because we are only considering cavities in a vacuum.

Now that we have introduced losses and different reflectivities for each mirror, the transmission and reflection of the cavity must be modified. The reflected power from the cavity on resonance is reduced, and given by [82]

$$\frac{I_{\text{refl}}}{I_{\text{inc}}} = Z_1^R = \left(\frac{L_1 + L_2 + T_1 - T_2}{\sum T_i + L_i}\right)^2, \tag{4.7}$$

where I_{inc} and I_{refl} are incident and reflected intensity, and Z_1^R is known as the impedance matching coefficient for the first mirror. This factor represents the disparity between the light incident on the cavity mirror, the light directly reflected from the mirror and the light leaking out of the cavity backwards through this mirror. These fields interfere at the surface of the mirror and the total reflected power is reduced, resulting in a perfect cancellation of the field when $T_2 = T_1 + L_1 + L_2$. Similarly, the transmission of the cavity on resonance is given by

$$\frac{I_{\text{trans}}}{I_{\text{inc}}} = \frac{4T_1T_2}{(\sum T_i + L_i)^2}. \tag{4.8}$$

Up to now we have discussed only classical properties of optical cavities, however since we are interested in using the cavity for generation of single photons, there are some important properties which need to be introduced. A single photon inside the cavity will remain only for a finite time. This photon lifetime within the cavity is given by

$$\tau_{\text{c}} = \frac{1}{2\pi \times \Delta\nu_{\text{c}}} = \frac{1}{2\kappa} \tag{4.9}$$

where κ is the electric field decay rate, an important parameter for cavity-QED. The rate of photons leaving the cavity is given by 2κ.

In cavities where light is generated from within, it is important to know the relative rate of leakage through the individual mirrors, and in lossy cavities, the rate of leakage through the various loss paths. Under the condition that $\sum T_i + L_i \ll 1$, κ can be expressed in the form

$$\kappa = \frac{\pi \times \Delta\nu_{\text{F}}}{\mathcal{F}} \approx \frac{\Delta\nu_{\text{F}}}{2} \sum T_i + L_i. \tag{4.10}$$

From this, it follows that κ can be written as

$$\kappa = \sum \kappa_{\text{M}i} + \kappa_{\text{L}i}, \tag{4.11}$$

where

$$\kappa_{\mathrm{M}i} = \frac{\Delta\nu_{\mathrm{F}}}{2} T_i, \quad \kappa_{\mathrm{L}i} = \frac{\Delta\nu_{\mathrm{F}}}{2} L_i. \tag{4.12}$$

The elements $2\kappa_{\mathrm{M}i}$ are the rates of photon transmission through each mirror, and $2\kappa_{\mathrm{L}i}$ are the rates of other loss processes in each mirror.

The probability that a photon in the cavity mode will exit through mirror one is then given by

$$\eta_{\mathrm{M1}} = \frac{\kappa_{\mathrm{M1}}}{\kappa} \approx \frac{T_1}{\sum T_i + L_i}. \tag{4.13}$$

This quantity is known as the cavity out-coupling efficiency and is a very important for cavities used to extract single photons. Normally a high out-coupling efficiency is desirable so it is common to build 'one-sided' cavities where the transmission of one mirror dominates the round trip losses so that the majority of the photons leave through a single pathway. In typical experimental schemes, single photon excitations are generated with a certain rate R_{gen} which is determined by the experimental repetition rate and the cavity-QED parameters of the system. The resulting average rate of single photons exiting the cavity through mirror M1 is given by

$$R_{\mathrm{M1}} = \eta_{\mathrm{M1}} R_{\mathrm{gen}}. \tag{4.14}$$

If a single photon is instantaneously[1] generated within the cavity, then temporal shape of the photon probability amplitude will be given by an exponential function with a decay rate of κ, i.e.[2]

$$\psi(t) \propto \exp(-t\kappa), \tag{4.15}$$

where $t = 0$ is the time at which the photon was instantaneously generated. Since in this thesis we are concerned with generating photons at a high rate, it is interesting to note the trade-off which occurs as a result of employing a cavity with a small κ. In order that 99.9 % of the photon probability density has left the cavity, a time of $\approx 2.3/\kappa$ is required. This naturally leads to an upper bound on the experiment repetition rate of $R_{\mathrm{rep}} \leq \kappa/2.3$. [3]

[1] Instantaneous here signifies that the process generating the photon occurs on a timescale which is much faster than the cavity field decay rate, κ.

[2] N.B. this is the total κ for the cavity, rather than that of the mirror through which the photon exits

[3] For the cavities investigated in this thesis a minimum value for κ of $2\pi \times 160 \cdot 10^6/\mathrm{s}$ is employed. The rate at which photon generation would be limited by the cavity decay rate would therefore occur at repetition rates of ≈440 MHz, which is significantly higher than the repetition rates used in chapter 7.

4.1.2 Fundamental mode

In the preceding section we have discussed the properties of Fabry-Pérot cavities without considering the shape of the mirrors; in practice the shape is very important. First and foremost, for light to be stably guided within the cavity, the geometry must obey the cavity stability condition

$$0 < \left(1 - \frac{d}{R_1}\right)\left(1 - \frac{d}{R_2}\right) < 1, \tag{4.16}$$

where R_1, R_2 are the radii of curvature of each mirror, and d is the cavity length. A simple qualitative explanation of this stability requirement is that the geometry of the cavity mirrors needs to be such that the light rays are confined within the cavity. For a more detailed analysis of this see [83].

The lowest order transverse mode that the cavity supports is the TEM_{00} mode which has a Gaussian radial profile. This radial width (the distance from the centre to where the intensity falls to $1/e$) is given by

$$w(z) = w_0\sqrt{1 + \left(\frac{z}{z_\mathrm{R}}\right)^2} \tag{4.17}$$

where w_0 is the radial width at the waist of the mode, and z_R is the Rayleigh range. These two parameters are linked through the relation

$$z_\mathrm{R} = \frac{\pi {w_0}^2}{\lambda}, \tag{4.18}$$

and the radius of curvature of the wavefronts is given by

$$R(z) = z + \frac{z_\mathrm{R}^2}{z}. \tag{4.19}$$

The condition for the mode to be supported in the cavity is that the radius of curvature of the wavefronts matches the radius of curvature of the mirrors. In the case where both mirrors have the same radius of curvature (R), this condition requires that waist of the mode is located at the midpoint between the two mirrors and has a radius of

$$w_0 = \sqrt{\frac{\lambda}{2\pi}}\left(2Rd - d^2\right)^{1/4}. \tag{4.20}$$

This configuration is known as a symmetric cavity, and is the arrangement of choice for our experiments.

In order to later estimate the mode-matching between the fibre and cavity mode, we will need to calculate the overlap integral between these two modes at the surface of the fibre mirror. For this the width of the cavity mode at the mirror is important, and is given by

$$w_{\mathrm{m}} = w(d/2) = w_0\sqrt{1+\left(\frac{d/2}{z_{\mathrm{R}}}\right)^2} \tag{4.21}$$

using the waist radius and Rayleigh range of the cavity mode.

One especially important parameter to consider when working with cavity-QED is the cavity mode volume, V_{m}. This is the integral of the electric field, normalised to unit amplitude, of the mode over all space within the cavity, and can be calculated by integrating the Gaussian mode function between the mirrors, being careful to take into account the longitudinal structure caused by the interference between the two counter-propagating modes. For the Gaussian mode the volume is given by [37]

$$V_{\mathrm{m}} = \frac{\pi}{4}w_0^2 d. \tag{4.22}$$

4.1.3 Mode matching losses

One of the key considerations when constructing a fibre-cavity is the mode-matching between the cavity mode and the fibre mode so that the experimental signal from the cavity is not strongly attenuated. Fibre-cavity mirrors can be machined onto single-mode fibre [37, 84, 85], multi-mode fibre [38, 84] and photonic crystal fibre [86].

Multi-mode fibre mirrors have very large acceptance angles, and so, almost all of the light leaving the cavity through a multi-mode fibre mirror will be guided by the fibre. This is very useful for experiments where the optical transmission of the cavity is important [38]. Multi-mode fibre mirrors are however not suitable for reliably coupling light into the cavity as the modes propagating within the fibre interfere causing unstable mode-matching into the cavity. For similar reasons, in experiments where the mode of the light is important, like collection of identical photons for quantum communication protocols, multi-mode fibre mirrors are not applicable for cavity out-coupling.

Single-mode and photonic crystal fibres both support only one the fundamental mode within their operating wavelengths. Fibre mirrors made from these fibres are more suitable for cavity in-coupling and out-coupling of light in defined modes. However, since photons leaving the optical cavity must be coupled into the fibre mode in order that they are guided, careful attention must be paid to the mode-matching between the fibre and cavity modes. Photonic crystal fibres

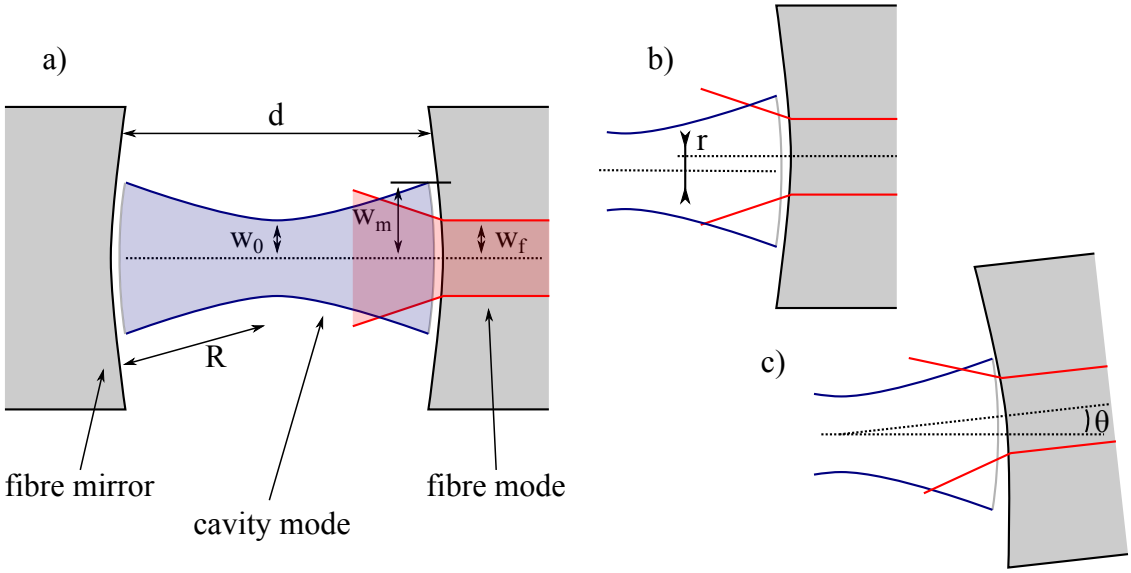

Figure 4.1: Mode matching between the cavity mode and fibre mode. a) An optimally aligned cavity with mode size mismatch between the cavity mode at the mirror (w_m) and the fibre mode (w_f). b) Cavity with a radial displacement (r) between cavity and fibre modes. c) Cavity with an angular displacement (θ) between the modes.

typically support larger mode diameters than standard single-mode fibre at a given wavelength, and so can be advantageous to use if the cavity mode diameter (at the mirror) is larger than supported by standard single-mode fibre[4].

The purpose of the cavity in this work is to provide a quantum interface for trapped ions. We are therefore most interested in single-mode fibre mirrors and consider only cavities constructed from pairs of single-mode fibre mirrors.

Here we briefly discuss the three main forms of misalignment which can cause the mode-matching to be non-ideal with single-mode fibre-cavities. These are radial displacement, angular displacement, and mode size mismatch. These forms of misalignment are depicted in figure 4.1.

The mode size mismatch error originates from a difference in the radius of the cavity mode and the fibre mode. In the case where the radius of curvature of the fibre mirror is large com-

[4]This is generally the case for the fibre-cavity dimensions investigated in this thesis since a typical single-mode fibre has a mode field diameter of 3.3 µm whereas the cavity mode has a diameter of 4.3 µm at the mirror (see figure 4.2).

pared to the mode widths at the fibre, the power coupling between the modes is well approximated by

$$\varepsilon \approx \left(\frac{2w_{\mathrm{f}}w_{\mathrm{m}}}{w_{\mathrm{f}}^2+w_{\mathrm{m}}^2}\right)^2, \tag{4.23}$$

where w_{f} is the width of the fibre mode, and w_{m} is the width of the cavity mode at the surface of the mirror. In this approximation, the radius of curvature of the wavefronts and the lensing effect of the fibre mirror are neglected. For a detailed analysis see [37].

This mismatch error is depicted in figure 4.1 a), where the width of the fibre mode is smaller than the width of the cavity mode at the mirror. Minimisation of this error is performed through careful choice of mirror radius of curvature and cavity length (which both affect the cavity mode), and fibre mode radius. In practice it is possible to achieve near 100 % coupling with infrared fibres at practical cavity lengths for trapping.

For radial misalignments, the power coupling drops off like a Gaussian and is given by [87]

$$\varepsilon = \varepsilon_0 e^{-(r/r_{\mathrm{e}})^2}, \tag{4.24}$$

where ε_0 is the maximum power coupling with perfect alignment, r is the radial distance from the optimum position and r_{e} is the radial tolerance for the mode-matching given by

$$r_{\mathrm{e}}^2 = \frac{2}{\varepsilon_0\left[1/w_0^2+1/w_{\mathrm{f}}^2\right]}. \tag{4.25}$$

Here we have assumed that the cavity and fibre modes are circular, which is generally a good approximation when working with fibre-cavities.

The angular misalignment can be treated very similarly [87], giving

$$\varepsilon = \varepsilon_0 e^{-(\theta/\theta_{\mathrm{e}})^2}, \tag{4.26}$$

where

$$\theta_{\mathrm{e}}^2 = \frac{2}{\pi\varepsilon_0\left[(w_0/\lambda)^2+(w_{\mathrm{f}}/\lambda)^2\right]}. \tag{4.27}$$

In experiments where photons are generated within the cavity, imperfect mode matching between the cavity mode and the optical fibre will lead to a reduction in the rate of successful photon generation events. Given a power mode matching coefficient $\varepsilon_{\mathrm{mm}}$, the rate of successfully out-coupled photons is given by

$$R_{\mathrm{out}} = \varepsilon_{\mathrm{mm}}\eta_{\mathrm{M1}}R_{\mathrm{e}}, \tag{4.28}$$

where η_{M1} is the cavity mirror outcoupling probability identified in equation 4.13, and R_{e} is the rate at which photons are produced inside the cavity.

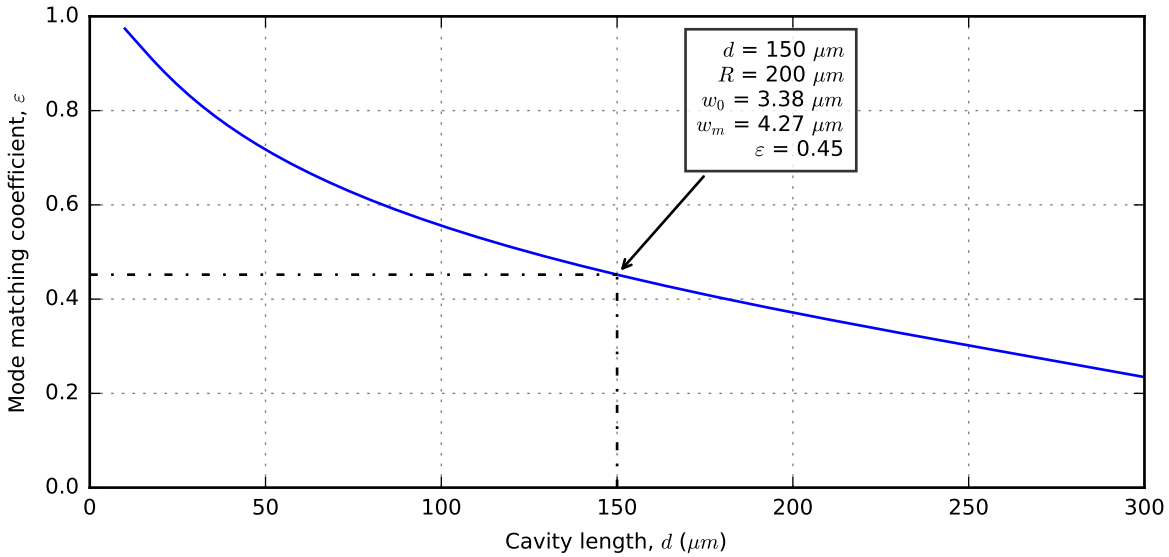

Figure 4.2: Theoretical mode-matching coefficient for a well aligned single-mode fibre-cavity at 370 nm with radius of curvature 200 mm and fibre mode width, w_f, of 1.65 µm.

4.1.4 Ultraviolet fibre-cavity parameters

Motivated by the many benefits of a cavity interacting with an ion on its primary dipole transition, we have developed to our knowledge the first fibre-cavities designed for use in the ultraviolet band. To this end, a set of fibres were machined by H. M. Meyer and M. Steiner using the fibre fabrication setup from the group of J. Reichel at the ENR in Paris. The fabrication procedure is described in more detail in [88]. The fibres were machined with radius of curvature in the range 150 µm to 250 µm, then coated with dielectric mirror coating specified to have power transmission of 1000 ppm at 370 nm. This coating transmission leads to an expected finesse of ≈ 3100. For reasons highlighted in chapter 3, the cavity length needs to be larger than the distance between the two rf electrodes which form the ion trap. As this distance is approximately 100 µm, we choose cavity lengths of 150 µm.

Figure 4.2 shows the expected mode-matching coefficient as a function of cavity length for our parameters. The mode-matching coefficient at the design length of 150 µm is 45 %, where we have assumed a fibre mode width of 1.65 µm[5]. This degree of mode-matching loss

[5]The mode field diameter of S405-XP fibre is specified to be (3.3 ± 0.5) µm at 405 nm, we assume that it is similar at 370 nm

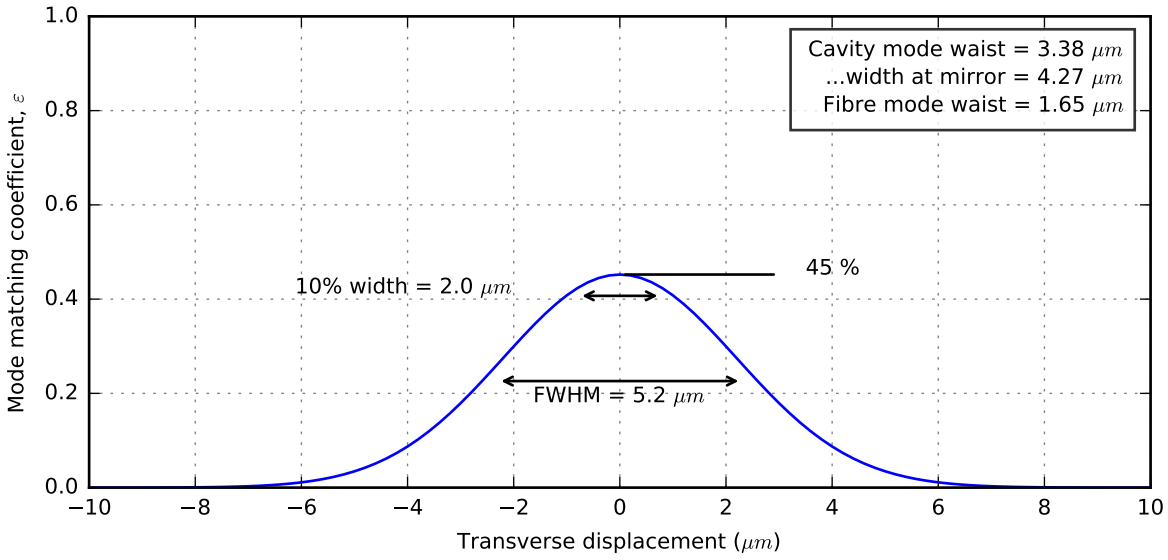

Figure 4.3: Effect of radial misalignment for the cavity design parameters $(d, R, w_f) = (150, 200, 1.65)$µm. In order to maintain 90 % of the optimal mode matching coefficient, the radial displacement must remain within 1 µm of the optimal position.

is higher than fibre-cavities working in the infrared spectral region, where near-zero mode-matching losses can be achieved [37]. The reason for the size mismatch here is simply that the fibre mode size is significantly smaller than the cavity mode at the mirror given the cavity lengths that we need to work with. This can be improved by choosing a fibre with a larger mode field diameter, such as photonic crystal fibre.

Given the mode-matching coefficient $\varepsilon = 0.45$, we can calculate the expected radial and angular tolerances for our cavities via equations 4.25 and 4.27.

Figure 4.3 shows the radial alignment tolerance for our cavity design parameters. The $1/e^2$ radial alignment tolerance is r_e =3.1 µm. As we want to minimise mode-matching losses wherever possible, it is desirable to keep within 90 % of optimum mode-matching. This translates to a single direction radial misalignment tolerance of 1 µm.

The angular tolerance for these cavity parameters is $\theta_e = 0.12$ rad. For the cavity length of 150 µm, an angular displacement of θ_e would need a radial displacement of $r(\theta_e) \approx d\theta_e/2 \approx$ 9 µm. Since $r(\theta_e) > r_e$, we can say that for small displacements of the fibre mirrors, the radial misalignment dominates the mode mismatch losses.

In addition to the narrow alignment tolerances required for ultraviolet fibre-cavities, there is

further challenge which comes about due to the fibre. Currently is it not possible to purchase single-mode fibre for use in the ultraviolet which has a ultra-high vacuum compatible coating. The fibre which we use is coated with an acrylate coating which is known to be unsuitable for UHV environments [89] so we remove the coating. Bare silica fibre however is very fragile and can fracture easily when handled. To this end we have developed a process for depositing a layer of copper onto the bare fibre which provides mechanical support and reduces the tendency of the fibre to fracture. The process is described in appendix A.

4.2 Development of mounting structure

We have shown in the previous section that in order to construct a fibre-cavity with our desired design parameters we will need to be able to position the fibre mirrors with an accuracy of <1 μm around the position of optimal cavity-fibre mode-matching. Additional requirements for the mechanical construction are as follows:

- The fibres must not move by more than 1 μm after ultra-high vacuum bake-out.
- The cavity length must be tunable over a length scale of λ so that the cavity resonance frequency can be tuned to the atomic resonance.
- The structure must present a controlled electric field to the ion.
- The system must be mechanically robust enough to lock the cavity length to the atomic resonance.

To control the length of the cavity we employ the standard approach which is to glue one of the fibre mirrors onto a shear piezo actuator with its direction of travel along the cavity axis. Recently it has been shown that thermal self-locking is possible with fibre-cavities [85], which would remove the need for a piezo actuator, however this technique requires a very mechanically stable mounting structure which does not seem compatible with an ion trap.

In order to present a controlled electric field to the ion, all surfaces directly facing the ion should be made of a conductor which has a defined potential. If this is not the case, then stray charges can build up, leading to displacing forces on the ion which can cause problems with trapping. For this reason, the cavity fibres are placed inside stainless steel tubes which are connected to an electrical feedthrough on the vacuum chamber. The details of this process can be found in [88].

From our analysis, it seems necessary to employ glue in the construction of the fibre-cavity for two reasons. The first is that a purely passively aligned system, such as two well-machined 'v'-grooves on a common substrate, requires very high concentricity in the machining of the fibre mirrors to achieve good mode-matching at the long cavity lengths we require. With the fibre mirrors used in this thesis, the concentricity was not high enough to allow this. When the cavity is assembled, the fibres need to be aligned to optimise the cavity-fibre mode-matching, and once this is performed we found that the fibres cannot be mechanically clamped without losing the alignment. The second reason is that in order to allow for one of the mirrors to move freely, part of the mounting structure must also move. We have investigated solid state spring based solutions for this, however this approach is limited in the response time of the actuator due to the mass of the spring. So far we have not found a superior alternative to gluing the fibre on top of a piezo, although micro-machined structures may provide an interesting avenue for future research.

The final requirement comes about because, in order for the cavity to remain within one cavity linewidth of the resonance of the ion, the cavity length must be stable to $\delta_L = \lambda/2\mathcal{F}$. For an ultraviolet cavity with finesse 3100, this gives $\delta_L \approx 60\,\text{pm}$. Such high length stability requirements are not uncommon for optical cavities, where this is usually achieved through a combination of solid mechanical construction and active stabilisation through a feedback controller driving a piezo actuator. However, if there are any mechanical resonances of the cavity structure which couple to the motion of the piezo within the bandwidth of the controller, then the closed loop system may become unstable. In order to build a cavity that can meet this mechanical stability requirement, there should be no strong mechanical resonances within the desired bandwidth of the feedback controller. This is discussed further in section 4.3.

Our initial plans for building a mounting structure for ultraviolet cavities were based on the experience in our group working with fibre-cavities at 935 nm. This experience taught us that it was possible to build fibre-cavities at lengths of $\approx 170\,\mu\text{m}$ using epoxy resin[6] to hold the fibres in place on the mount. The mechanical stability of previous fibre-cavities built in this way was not ideal, but these problems were addressed with a slightly altered mechanical design as described in section 4.2.1.

After construction of the cavity on this mount, described in more detail in section 4.2.1, the system was put through a vacuum bake-out procedure to determine whether it would survive, as mechanical deformation has been observed in earlier cavities. During the procedure the cavity

[6]The epoxy resin we have had most success with is Stycast 2850FT which has a good combination of low out-gassing and low shrinkage during cure

was monitored by scanning its length using the piezo and measuring the reflectance using a laser at 370 nm. The ratio of reflected power when the cavity is on resonance and far from resonance with the laser was determined from a Lorentzian fit, which allowed for continuous monitoring of the cavity reflectance on resonance despite the cavity length changing due to thermal expansion. As the cavity was heated, we observed that the reflectance on resonance increased gradually until it was no longer discernible from noise in our measurement. After the cavity had returned to room temperature, no further cavity resonance signal was observed. This result was ambiguous as it was not possible to distinguish whether the signal was lost due physical misalignment of the cavity fibres or due to an increase in intracavity losses.

In order to further analyse this problem a test cavity was built using 935 nm fibre mirrors. This incorporated a solid state translation stage which allowed one of the cavity fibres to be translated microscopically in two directions transverse to the second fibre. With this measurement, the position of maximum mode-matching could be measured before and after a bake-out procedure. We measured that the cavity fibres misaligned relative to each other in the vertical direction (aligned with gravity) by approximately 8 µm, whereas along the second axis there was no discernible shift above the measurement uncertainty (≈ 1 µm).

After positively identifying this bake-out induced misalignment, we decided to design a mounting structure which could overcome this misalignment *in situ*, described in section 4.2.2. With this adjustable cavity mount, we were able to fully recover the mode-matching of the cavity after the bake-out procedure, in spite of misalignments. Although ultimately successful at allowing us to couple the first fibre-cavities in the ultraviolet to trapped ions, the adjustable mount does not represent an ultimate solution. In the following subsections, the two different approaches for the mounting structures of the cavity are described in detail, along with their positive and negative aspects, as these will likely inform future designs.

4.2.1 Monolithic cavity mount

Figure 4.4 shows the mounting structure which was designed based on the earlier successful experiments with 935 nm fibre-cavities which are documented in [88]. The structure consists of a rigid titanium base substrate upon which the individual elements are glued in layers. Adjustment of the cavity length is achieved through two shear piezos[7] which are placed symmetrically to reduce the impact of errors in fabrication. On top of the piezos are two aluminium tube carriers which serve to support the cavity fibres and facilitate making electrical contact with the

[7]The shear piezos used were CSAP03 from Noliac

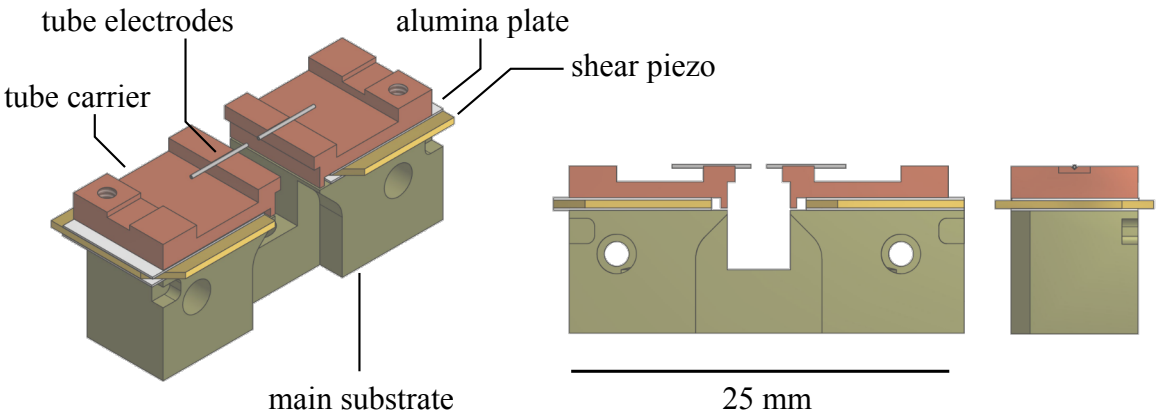

Figure 4.4: CAD drawing of the monolithic cavity mounting structure.

cavity tube electrodes. Thin alumina sheets are placed between the surfaces on both sides of the piezos in order to insulate them from the grounded substrate and the tube carriers.

This design was chosen to improve upon the previous experiments through two avenues. Firstly, in previous designs, the cavity mounting structure was found to exhibit mechanical resonances in the low acoustic range (≈ 500 Hz). These resonances prohibited the use of feedback at higher frequencies, and as a result the quality of the cavity length stabilisation was severely impaired. In order to measure the properties of the cavity when on resonance with the atomic transition, a smart 'post-selection' technique[8] was employed to filter measurement cycles where the cavity detuning was above a certain threshold. This technique reduced the rate of successful measurements, and should ideally be avoided in future experiments.

To combat acoustic mechanical resonances in the mounting structure design, we used finite element analysis software to determine the approximate resonance frequencies and adapted the design to increase the frequency of the lowest resonances. The lowest mechanical resonance of the structure was at approximately 16 kHz, achieved through the use of a stiff titanium structure.

Secondly, after the bake-out procedure of the second 935 nm cavity described in [88], the cavity resonance signal was no longer visible. It was found to be possible to recover the coupling by heating the cavity with a focused laser beam, applying approximately 100 mW of localised heating. Despite the success of this approach, the heating laser caused a number of undesirable effects such as increased background pressure and unstable stray electric fields. In order to explain the temperature dependence of the coupling, there must have been an amount of plastic

[8]The 'post-selection' technique is described in [88].

deformation in the cavity mounting structure. It was concluded that this was most likely caused by the glue, and in order to minimise the impact on future cavities, the size of the gaps where the cavity is supported by glue should be minimised.

Reduction of glue usage was achieved by producing the structure in such a way that the two tube carriers (see figure 4.4) were at the same height above the mounting structure after assembly. The stacks of alumina plates and piezos were glued whilst held in a precision drill press, guaranteeing that the upper surfaces of the tube carriers were parallel and at the same height above the substrate. This procedure was successful and during the final cavity assembly a gap of approximately 20 µm underneath one of the cavity tubes was bridged with glue, which compares favourably to the $\approx 200\,\mu m$ required in earlier designs.

In order to determine whether the cavity alignment would remain after ultra-high vacuum bake-out, we performed a thermal cycling of the cavity mounting structure in air to simulate the conditions during bake-out. The cavity structure was heated over one hour to a maximum temperature of 100 °C, held at this temperature for a further hour, then cooled back to room temperature over one hour. During this procedure, the cavity mode-matching was monitored via the reflected power of the cavity on resonance. We observed that the mode-matching of cavity gradually reduced as the temperature increased, becoming too low to measure after approximately 60 °C. When the cavity mount had returned to room temperature no further cavity signal was observed.

4.2.2 Adjustable cavity mount

To overcome the issue of bake-out induced misalignment of the cavity structure, a new structure was designed which could be realigned *in situ*. One way to achieve this is to use a piezo-actuated mechanical translation stage[9]. However, based on our experience building the cavity for the bake-out test, we ruled out using one of these for this cavity because the stage has medium-Q mechanical resonances in the low acoustic range. The second option we considered for this was the use of multilayered piezo actuators. These actuators provide less stroke than mechanical translation stages since they contain no lever arms, however the higher stiffness and lower mass of multilayered piezo structures are more suited to cavity construction.

The structure, shown in figure 4.5, is broadly based on the previous design, with the addition of two stacked piezo actuators oriented in such a way that they each act to change the relative position of the fibre mirrors transverse to the cavity axis. The piezo actuators used in this design

[9] Such as 'Tritor38' from Piezosystem Jena

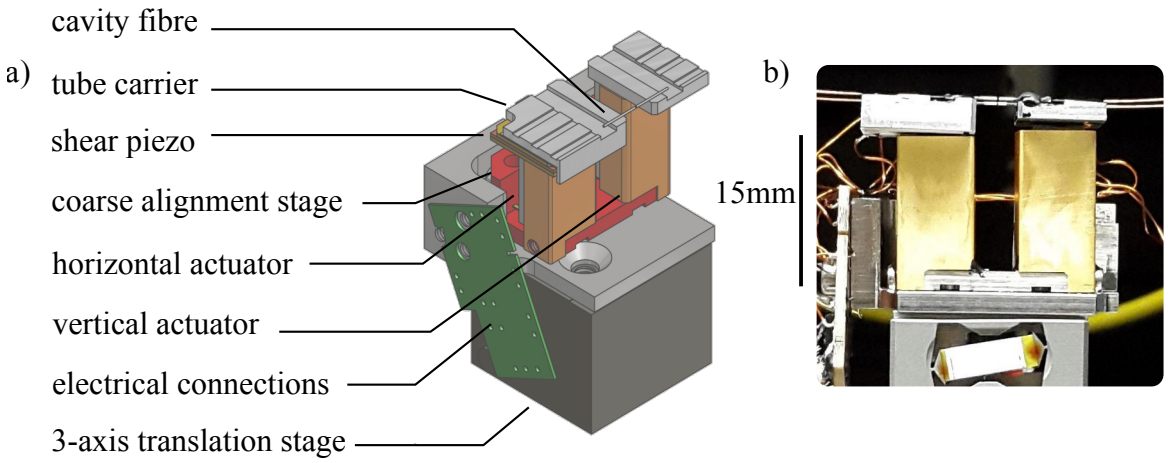

Figure 4.5: a) CAD drawing of the adjustable cavity mounting structure. b) Photograph of the assembled structure.

were custom manufactured[10] in order to achieve a stroke in each case which would allow for compensation of the expected degree of misalignment. The two piezo actuators have dimensions 5 mm × 5 mm × 14 mm, and produce a specified stroke of 31.5 µm (from −320 V to 320 V) for the stack employing the shear mode (along the horizontal direction in figure 4.5), and 21 µm (from 0 V to 150 V) for the longitudinal mode (along the vertical direction).

In a similar way to before, the cavity fibres are glued in stainless steel tubes which themselves sit on top of aluminium 'tube carriers'. In figure 4.5 a), the tube carriers can be seen positioned on top of the vertical and horizontal piezo actuators. A shear piezo is incorporated between the top of the horizontal actuator and left tube carrier in order to adjust the cavity length. Several additional alumina sheets were needed to provide insulating layers between the various electric elements.

For assembly, the entire structure, approximately 20 mm in height, was held in position with a jig in a drill press during gluing. This ensured that the upper surfaces of the tube carriers were parallel and at the same height. After construction of the mount, the cavity fibres were introduced and glued onto the tube carriers. During the fibre gluing process, the vertical and horizontal actuators were biased to their mid-range voltage, as the direction of any posible misalignment was not known.

[10]The stacked piezo actuators were manufactured by Noliac, with part numbers 'NAC2402-H13.4-A01' for the horizontal direction (shear), and 'NCA2013-H14-C01' for the vertical direction (longitudinal).

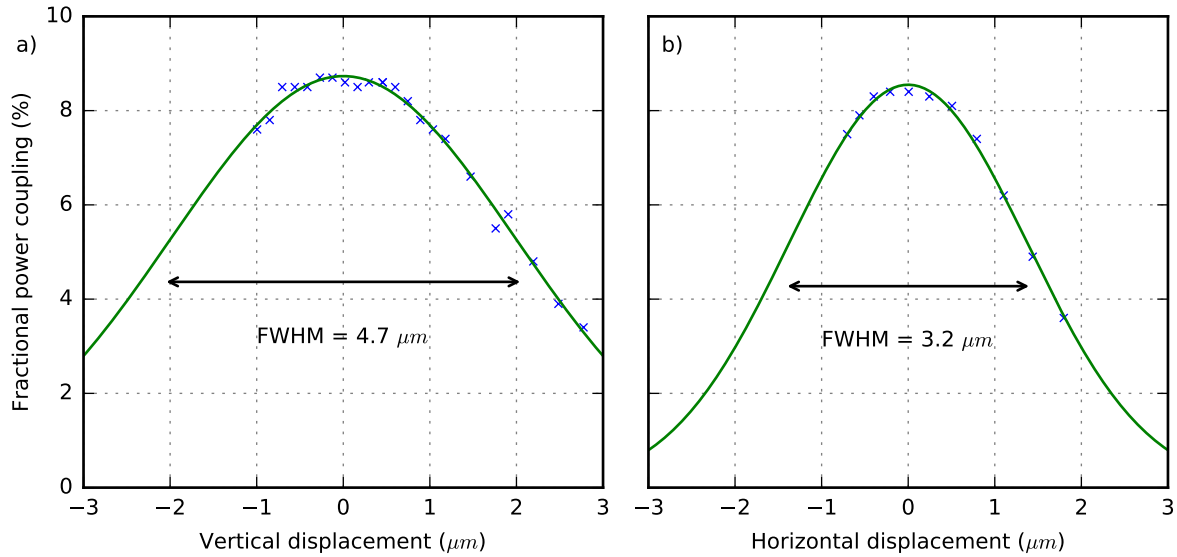

Figure 4.6: Measurement of the fibre-cavity mode matching under transverse displacement of the cavity fibres using a) the vertical piezo actuator, and b) the horizontal. The vertical axis in both graphs represents the fractional in-coupled laser power into the cavity when it is resonant with the probe laser near 370 nm. The line represents a Gaussian fit to the data. The lower than expected in-coupled fraction under optimally alignment is due to optical losses in the coating explained in section 4.4. The vertical displacement was calibrated under a microscope, and the horizontal displacement was estimated using the formula for shear displacement given in Ref. [90].

After the cavity mounting structure was installed into the experiment, the vacuum chamber was evacuated. At this point, the positions of optimal cavity in-coupling were determined and was found to be the same as during construction. The vacuum system was baked out at a peak temperature of 60 °C for two weeks. After this process, the actuator position required for maximum cavity in-coupling was found to be shifted by approximately 11 µm in the vertical direction, and no measurable shift in the horizontal direction. This result is qualitatively the same as found with the bake-out test cavity: that the misalignment occurs only in the direction of gravity.

Although the source of the misalignment is still unknown, with the built-in actuators it is possible to fully recover the full cavity mode matching. Figure 4.6 shows a measurement of the cavity in-coupling after the vacuum bake-out procedure. This measurement confirms that

cavity is able to reach its optimally aligned position, and the fitted tolerances are in qualitative agreement with their expected values. The smaller tolerance value in the horizontal alignment is likely due to the approximate scaling of the graph x axis through the use of the formula presented in Ref. [90].

4.3 Mechanical resonances

As we have discussed earlier, the mechanical stability the cavity mounting structure is of great experimental importance. In order to design a cavity mounting structure which meets these requirements, it is necessary to understand the appearance and Q factors of these resonances. In this section, the two techniques used to probe the mechanical resonances of cavity mounting structures are described, along with the measurement data for the adjustable cavity mount described in section 4.2.2.

4.3.1 Dynamic impedance sensing

The first method we have used to detect and analyse the mechanical resonances of the mounting structures is based on the dynamic impedance of the built-in piezo transducers. The piezo transducer produces charge in response to a force,

$$Q = dF, \tag{4.29}$$

where d is the piezoelectric coefficient for the material along the direction of the force.

In order to probe the system, we apply a sinusoidal current to the piezo $I(t) = I_0 e^{i\omega t}$, which results in a corresponding force of

$$F(t) = \frac{Q(t)}{d} = \frac{\omega I_0}{d} e^{i\omega t - i\pi/2}. \tag{4.30}$$

We assume that the driving force is coupled to the mechanical resonance with a factor η representing the projection of the force vector from the piezo along the principal axis of the motional mode. The system can be described with the equations of motion for a driven damped harmonic oscillator, i.e.

$$\ddot{x} + \frac{\omega_0}{Q}\dot{x} + \omega_0^2 x = \frac{\omega I_0 \eta}{dm} e^{i\omega t - i\pi/2}, \tag{4.31}$$

where Q and ω_0 are the quality factor and undamped frequency of the mechanical resonance.

The steady state solution of this system is given by

$$x(t) = \frac{I_0 \eta}{dmZ_{\mathrm{m}}} e^{i\omega t + i\phi - i\pi/2}, \tag{4.32}$$

where Z_{m} is the mechanical impedance of the resonance, given by

$$Z_{\mathrm{m}} = \sqrt{\frac{\omega_0^2}{Q^2} + \frac{(\omega_0^2 - \omega^2)^2}{\omega^2}}, \tag{4.33}$$

and

$$\phi = \arctan\left(\frac{\omega\omega_0}{Q(\omega^2 - \omega_0^2)}\right). \tag{4.34}$$

The voltage formed across the piezo is the sum the voltage due to the device capacitance and the voltage induced by the piezoelectric effect

$$V(t) = V_{\mathrm{c}} + V_{\mathrm{p}} = \frac{1}{C}\int I(t)dt + \frac{1}{d}x(t), \tag{4.35}$$

and therefore the dynamic impedance has the form

$$Z = \frac{V}{I} = \frac{1}{i\omega C} + \frac{\eta}{d^2 m Z_{\mathrm{m}}} e^{i\phi - i\pi/2}. \tag{4.36}$$

By measuring the impedance of a piezo actuator in the mount, we therefore have access (through Z_{m}) to the frequency and quality factor of all of the mechanical resonances which have a measurable coupling to the actuator motion.

One simple way of measuring the impedance of the piezo actuator is shown in figure 4.7 a). In this method, we form an RC filter using the capacitance of the piezo. The resistance is chosen in order to maximise the sensitivity of the measurement near the frequencies of interest. The voltage transfer function of the filter can then be measured using a lock-in amplifier. The amplitude response of one such measurement is shown in figure 4.7 b).

After fitting the curve with an RC filter response, the mechanical resonances can be seen clearly in the fit residuals. Figure 4.8 shows a measurement of the mechanical resonances of the adjustable cavity mount which couple to a) the horizontal displacement actuator, and b) the vertical displacement actuator. From these measurements we observe that the lowest visible motional mode occurs at approximately 900 Hz, and the next lowest at 1.25 kHz. Measurements were also made using the cavity length actuator, where the impact of resonances is thought to be the strongest. The first and only visible resonance below 15 kHz was observed at approximately 8 kHz.

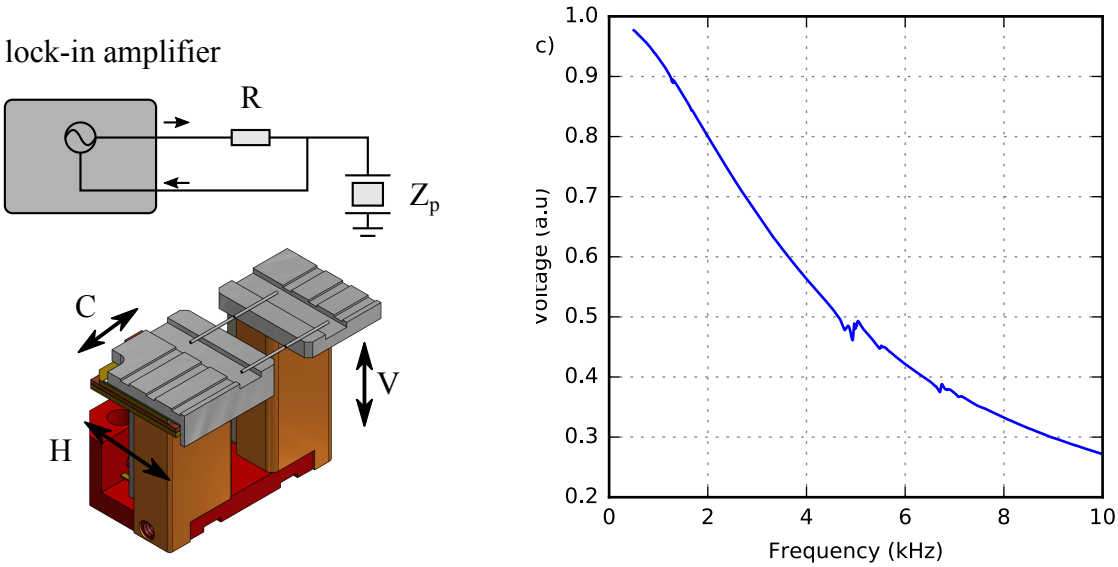

Figure 4.7: a) Low-pass filter based dynamic impedance measurement scheme. b) Available actuator directions (C: cavity length, H: horizontal cavity displacement, V: vertical cavity displacement). c) An example of a measured voltage amplitude response curve of the system. The general profile of the curve follows the response of an RC filter, with the addition of small deviations due to the mechanical resonances.

Our conclusion drawn from this analysis was that the cavity mounting structure should perform better than those used in the earlier experiments with the 935 nm cavities in our group. The first mechanical resonance which couples to the cavity scan actuator (8 kHz) is much higher than the $\approx$ 500 Hz achieved previously. The numerous lower frequency mechanical resonances which couple to the vertical and horizontal displacement actuators were assumed to be unimportant as the active feedback used to lock the cavity length does not drive these actuators.

After the cavity was installed into the vacuum chamber and the system was baked out, the cavity stability was assessed and an attempt was made to actively stabilise the cavity length using a side-of-fringe derived error signal combined with a PID controller. During this time, it became apparent that the assumptions made about the mechanical resonances observed which coupled to the vertical and horizontal displacement actuators were not correct. In order to understand the physical situation more clearly, we employed a second technique to measure the impact of the mechanical resonances on the locking performance.

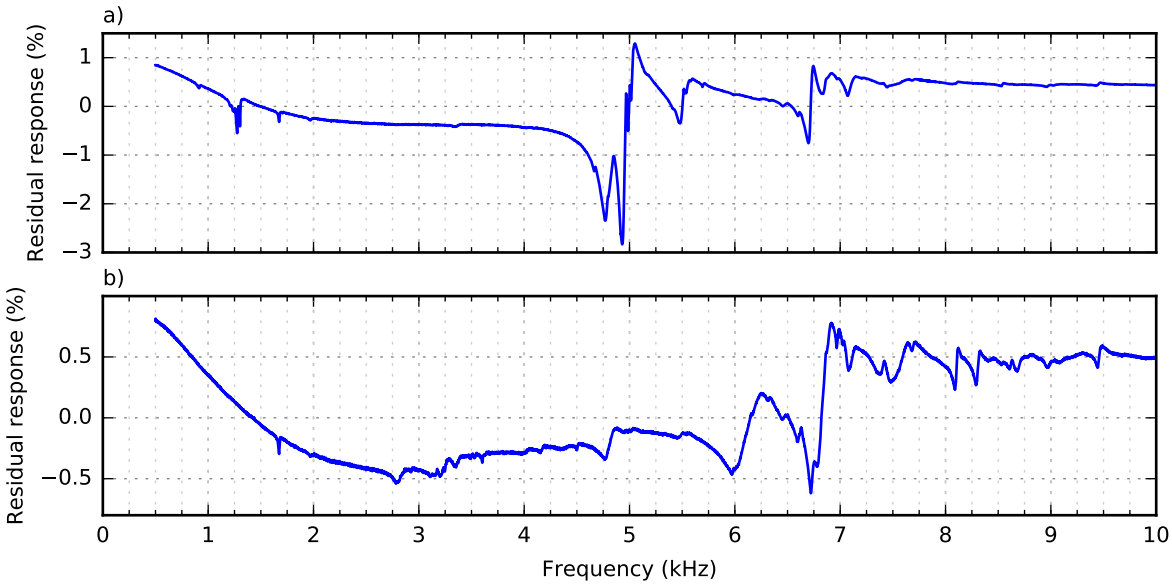

Figure 4.8: Measurement of the mechanical resonances in the adjustable cavity mount, probed using the dynamic impedance method using a) the horizontal cavity displacement piezo, and b) the vertical cavity displacement piezo. From this data, the frequency and quality factor of the mechanical resonances of the structure can be extracted.

4.3.2 Optical interferometry

The second technique we have used to measure the mechanical properties of the adjustable cavity mounting structure is based on optical interferometry. With the measurement setup is shown in figure 4.9, it is possible to directly measure the transfer function between the cavity length displacement and the applied voltage amplitude. In the language of control theory, this transfer function is the open-loop response function of the system. Understanding this transfer function allows one to determine how feedback can be applied to the system in order to optimally stabilise the length. The infrared fibre-cavity, which was intended to be used in a transfer looking scheme (see section 4.2.2), has a finesse of approximately 1 when probed with 640 nm light, which provides a convenient tool for measuring the length of the cavity on the nm scale.

Measurement data for the adjustable cavity mounting structure is presented in figure 4.10. This data indicates that the system response is approximately flat until 900 Hz. In addition to the broad resonance/antiresonance pair centred near 1.3 kHz, there are several sharp changes in phase above 1.5 kHz.

The cavity can be locked after filtering the feedback signal with a two-pole digital low-pass

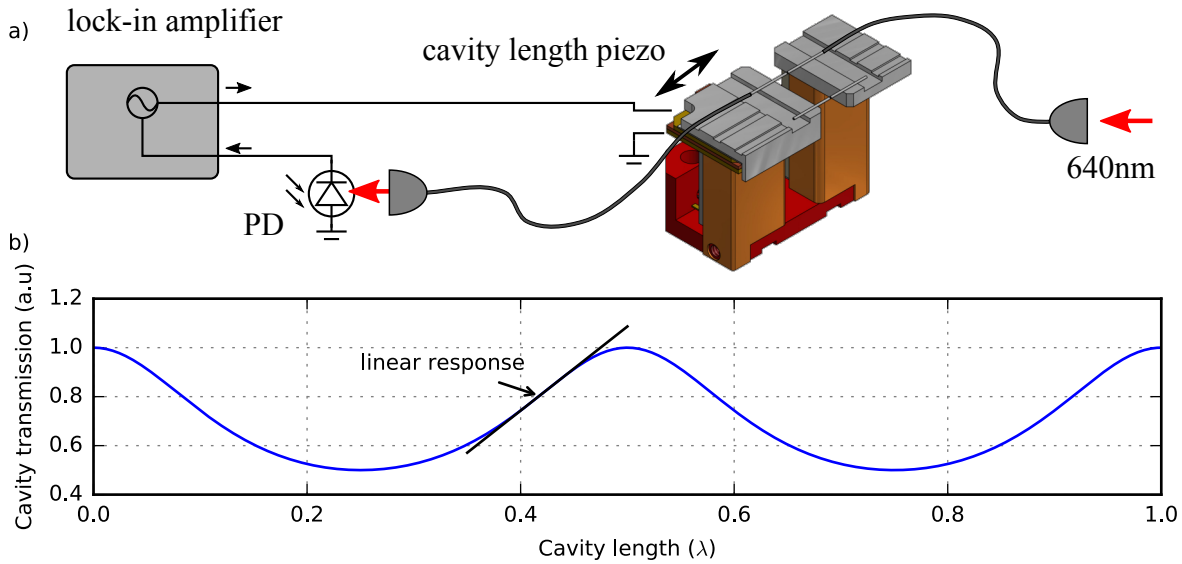

Figure 4.9: Optical interferometric technique used to measure the open-loop response of the cavity length actuator. a) Schematic diagram of the setup used. b) Cavity transmission signal for a low finesse cavity ($\mathcal{F} = 1$). The linear response of this signal to changes in the cavity length allows measurement of the open-loop response function.

filter with $f_{3\text{dB}} = 100\,\text{Hz}$. However, the RMS error signal corresponded to deviations of the cavity length from resonance by some nm, the majority of which were at approximately 1.7 kHz. The frequency of this noise matches the abrupt change in the open-loop phase response, and also matches a high-Q resonance observed in the earlier impedance-based analysis. Furthermore, the 1.7 kHz noise on the error signal is present independent of whether feedback is applied. We are therefore lead to the conclusion that this high-Q resonance ($Q \approx 60$) is being excited by mechanical noise which is coupled through to the cavity through the metal support structure connected to the vacuum chamber.

This analysis has lead to a greater understanding of the requirements for building future cavity mounts. It is not sufficient to have no mechanical resonances coupling to the cavity length actuator, but rather all the mechanical resonances need to be considered. One approach to engineering a better mounting structure could be to measure the resonance during construction and selectively add dissipative materials to reduce the Q of the resonances.

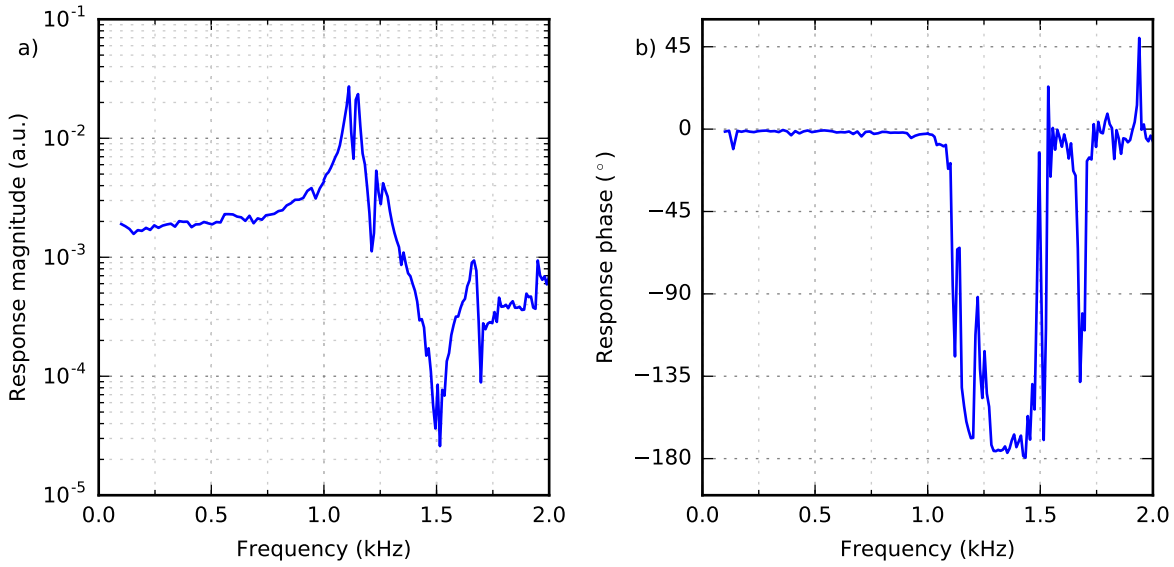

Figure 4.10: Measurement of the open-loop response of the cavity length actuator on the adjustable cavity mount using the optical interferometry technique.

4.4 Coating losses

One of the key parameters in cavity-QED systems is the electric field decay rate, κ, which is approximately proportional to total cavity optical losses via equation 4.10. Although it is possible to design and manufacture dielectric optical coatings with extremely low optical losses in the near infrared region [91], operation in the near ultraviolet spectral range remains challenging. It is therefore important to characterise the optical losses in our cavity system, so that there is a clear understanding of what the limitations are with our cavity.

In past experiments which have included optical cavities working in the ultraviolet spectral region, the observation has been made that optical losses in the dielectric coating have increased after prolonged exposure to an ultra-high vacuum environment (see Refs. [63, 92, 43]). It was hypothesised that the mechanism of these vacuum-induced losses was the diffusion of oxygen out of the top layer of the dielectric coating (in all cases tantalum (V) oxide), and this was later supported by a detailed study [93].

The ultraviolet optical fibres which have been used in the thesis were coated with a 38 layer dielectric coating composed of SiO_2 and Ta_2O_5. The upper-most layer is a half-wave SiO_2 (122 nm) protective layer expected to reduce effects of the oxygen diffusion [93]. The coating

is designed to have a transmission of 1000 ppm at 370 nm, with absorption losses expected to be below 100 ppm based on the performance of similar coatings from the manufacturer at 355 nm. The surface roughness of the curved mirror substrates is expected to be similar to those presented in Ref. [37] with a RMS deviation of $\sigma_{\mathrm{rms}} = 0.2$ nm. The losses due to scattering can be approximated by $L_s \approx (4\pi\sigma_{\mathrm{rms}}/\lambda)^2$ =72 ppm [94].

4.4.1 Measurements in air

When a cavity is formed from two of these fibre substrates, we measure cavity finesse of 1500 ± 100 which is independent of the length of the cavity. This is consistent with a total loss per mirror of (2100 ± 140) ppm. Working on the assumption that the transmission losses of the dielectric coating meet the specification, we estimate the combined scattering and absorption losses per mirror to be (1100 ± 140) ppm.

In order to protect the fibres from fracturing during bending, the outside surfaces of the fibre were coated with a thin layer of copper using the procedure described in appendix A. Care was taken to protect the mirror surface from the acidic electrolyte solution during this process. Immediately after the copper deposition process, the fibre mirrors were tested by checking that they could still form a cavity with the same finesse.

After a period of about two weeks, the same fibre mirrors were measured again, and the finesse of the resulting cavity had dropped to 1140 ± 40. It was confirmed that this effect was due to the copper deposition process by measuring the finesse of cavities formed with fibres which were stored in the same location but had not undergone copper deposition. It is reasonable to assume that the transmission properties of dielectric coating were not affected by the copper deposition process, so we therefore attribute the drop in finesse to an increased scattering and absorption loss per mirror of (1760 ± 100) ppm. The mechanism for the increase in losses is not understood.

The final cavity assembled onto the adjustable cavity mount was formed from two of the 'degraded' fibre mirrors. The linewidth of the cavity was measured to be (875 ± 6) MHz, and the power reflectivity of the cavity on resonance was measured to be (70 ± 2) %. For a Fabry-Pérot cavity formed from mirrors with known transmission, absorption and scattering losses, we can estimate the impedance matching coefficient Z using equation 4.7. However, since this measurement was performed with a Fabry-Pérot cavity formed from single-mode fibre mirrors the analysis is not quite so simple. The reflectivity of the cavity mirror on resonance is measured here using only the fraction of power reflected from the mirror which is coupled back into the

fibre, which acts as a mode filter. A detailed analysis of this effect is given in Ref. [95].

The power reflectivity measured out of the fibre on resonance, σ_{ref}, is given by [95]

$$\sigma_{\text{ref}} = |1 - \varepsilon + \bar{\rho}\varepsilon|^2 \tag{4.37}$$

where ε is the intensity mode-matching coefficient, and $\bar{\rho}$ is the field reflectivity of the cavity on resonance. For a cavity with two identical lossy mirrors, the field reflectivity is given by

$$\bar{\rho} = \frac{L}{L+T}, \tag{4.38}$$

where T is the per mirror transmission loss, and L is the combined scattering and absorption loss per mirror. In this case, since $\bar{\rho} > 0$, the intensity mode-matching coefficient can be written as

$$\varepsilon = \frac{1 - \sqrt{\sigma_{\text{ref}}}}{1 - \bar{\rho}}. \tag{4.39}$$

Using the specified per mirror transmission of (1000 ± 100) ppm and the scattering and absorption loss per mirror of (1760 ± 100) ppm determined through the linewidth measurement, we find $\bar{\rho} = 0.64 \pm 0.04$. The resulting value of the mode-matching coefficient is then $\varepsilon = 0.45 \pm 0.06$, which is in agreement with the value expected from theory in section 4.1.4.

4.4.2 Measurements *in vacuo*

The fibre-cavity assembled on the adjustable cavity mount was installed into the main experiment vacuum chamber. A measurement of the cavity in-coupled power was taken directly after installation, confirming that no measurable change in the cavity losses had occurred during the installation process. The system was baked out under vacuum at approximately 60 °C for two weeks. After realignment of the cavity using the vertical and horizontal actuators, the cavity in-coupling had dropped.

Over the course of the following weeks, the ion trap was successfully loaded with the cavity in place around the ion trap, and the cavity in-coupling decreased further. As the process of loading involves producing an atomic beam which intersects with the trap, one possible explanation for the increase in intracavity losses could be contamination of the mirror surfaces with ytterbium.

In order to fix some problems related to the ion trap, it was necessary to open the vacuum chamber to air. During this process, we observed that in-coupled power into the cavity increased over the coarse of a few hours, returning to near its original value. This recovery indicates that the additional losses observed are not due to ytterbium deposition.

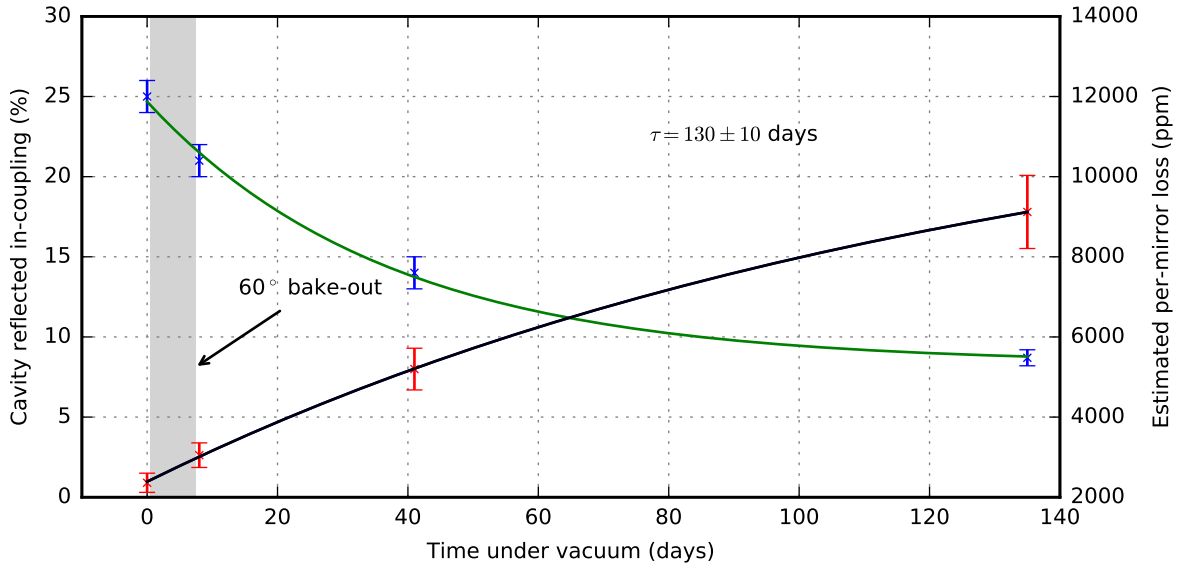

Figure 4.11: Observed increase in intracavity losses whilst under vacuum conditions. The blue data points are the measured cavity in-coupling and are with an exponential decay. The red data points represent the total per-mirror scattering and absorption losses which are estimated from the in-coupled power assuming a constant mode-matching coefficient of (45 ± 6) %. The black line is a fit to the exponential loss model described in the text, with time constant 130 ± 10 days.

The data shown in figure 4.11 show the behaviour of the cavity during a later bake-out procedure of the vacuum system lasting this time only eight days. The in-coupled power was measured before and immediately after the procedure, in both cases after checking for optimal alignment of the cavity fibres.

Under the assumption that both the transmission losses of the coating and the mode-matching coefficient are constant, we model the reduction in cavity in-coupled power as an increase in the absorption losses of the mirrors. Equations 4.38 and 4.39 can be rewritten to find L as a function of the cavity reflectivity, giving

$$L(\sigma_{\text{ref}}) = T\left(\frac{\varepsilon}{1-\sqrt{\sigma_{\text{ref}}}} - 1\right). \tag{4.40}$$

These losses are shown as the red data points in figure 4.11, and the data points are fitted with the exponential model

$$L(t) = L(0) + \Delta L\left[1 - e^{-t/\tau}\right] \tag{4.41}$$

which is presented in Ref. [93]. The data fit to a time constant τ of 130 ± 10 days.

The observed time-scale of the increase in intracavity losses is similar to the results presented in [93], where the conclusion is drawn that these effects can be mitigated with a sufficiently large SiO_2 passivating layer top of the dielectric coating. Our data appears to contradict this conclusion, and indicates that further study is necessary in this area. One possible candidate for these losses is contamination from carbon due to the dissociation of hydrocarbons in the residual gas of the vacuum chamber, which is frequency a problem in extreme ultraviolet optics [96].

4.5 Summary

In this chapter we have reviewed the important parameters for constructing fibre-cavities to be integrated into ion traps. We have demonstrated the operation of the first fibre-cavity technology in the ultraviolet range, and made the observation that at these small wavelength and long cavity length, misalignment of the cavity during bake-out may be a problem in future designs. We have shown that bake-out induced misalignment can be overcome by integrating piezoelectric degrees of freedom into the cavity structure, but this process may lead to compromised mechanical stability.

As the complexity of the fibre-cavity mounting structure increases, it will become more important to test their mechanical properties during construction. We have introduced two techniques which can be used to quantitatively measure the frequency and Q of mechanical resonances in the structure. With these methods, resonances in future cavity structures can be damped during construction which is necessary in order to attain the high mechanical stability required for optical cavities.

Finally, we have observed the occurrence of vacuum-induced losses in our ultraviolet cavity. This effect has been observed and analysed before, however, our data appears to contradict previous conclusions. Going forward, the source of these losses needs to be fully identified in order to produce high quality optical cavities.

Chapter 5

Apparatus

The measurements presented in the following two chapters in this thesis were performed with an ion trap which was built for this task. In this chapter the experimental apparatus is described in detail including the geometric setup, the main optical beam paths, and details of the laser system used for trapping and pulsed excitation. The imaging system for detection and state readout is described, along with the novel technique used to align the beams through the microscopic trap whilst compensating for astigmatism at the focus. The setup used for polarisation analysis of the photons coupled out of the cavity is presented. Finally, a brief description is given of the hardware and software control systems which have been developed in a modular way, allowing for the experiment to be expanded to include several ion trap 'nodes'.

5.1 Experiment chamber

The core of the experiment is a Paul trap housed inside an ultra-high vacuum chamber. In order to integrate a fibre-cavity into the trap, special considerations have to be made because of the potential for charging of the cavity mirror surfaces and the need for the cavity to be on a translation stage. Details of these considerations and the chosen trap design are given in chapter 3.

The main vacuum chamber is a DN100CF spherical octagon[1]. This is a great choice as a vacuum chamber for ion traps as it has two large DN100CF flanges on the front and back, and 8 smaller DN40CF arranged around the circumference, providing a good degree of optical access to the centre of the chamber. A photograph of the experimental setup inside the vacuum

[1] MCF600-SphOct-F2C8 from Kimball Physics

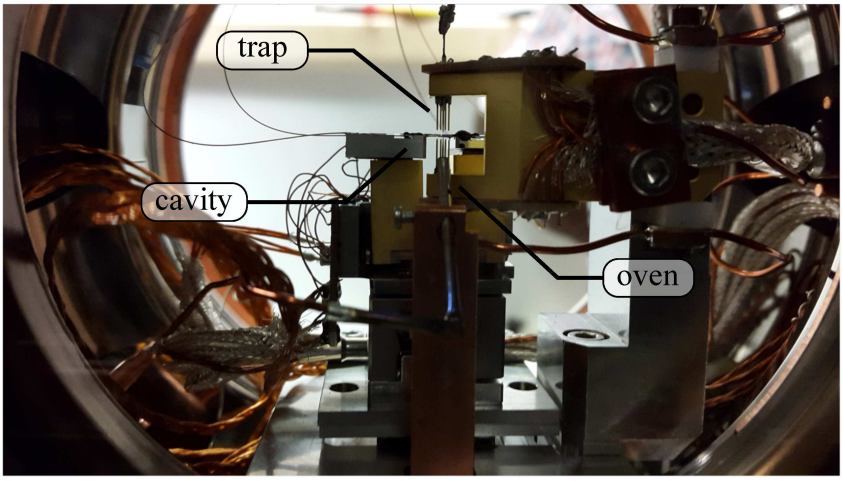

Figure 5.1: Photograph of the ion trap viewed front on to the vacuum chamber. The experiment is shown with the adjustable cavity mounting structure described in chapter 4.

chamber is presented in figure 5.1.

The ion trap is driven using a helical resonator based on the designs presented in [97]. The resonator has a Q of approximately 100 and a resonance frequency of 30 MHz. The trap is normally operated at a voltage of ≈ 75 V which lead to secular frequencies of 6, 5 and 2 MHz.

Figure 5.2 shows the arrangement of the experimental apparatus on an optical table. The imaging system and beam optics are positioned to the side of the chamber. Three pairs of magnetic fields coils surround the vacuum chamber which are used to produce a magnetic field to define the quantisation axis in an arbitrary direction. The coils are made from approximate 30 turns of 6x1 mm rectangular section copper wire and are distanced approximately 100 mm away from the position of the ion. The orientation of the coils was chosen such that each pair produces a field component primarily along the x, y and z axes of the global coordinate system shown figure 5.2 and defined in figure 3.4. Each pair of coils can produce a field of approximately 5 G.

The trap is positioned close to the front window of the chamber. This allows all the beams necessary for manipulation of the trapped ion to enter through this single window on the front side, leaving the back side open for installing and replacing the cavity. With the trap close to the front window, it is possible to use a higher collection solid angle for the imaging system than would otherwise be achievable if the trap were in the geometric centre.

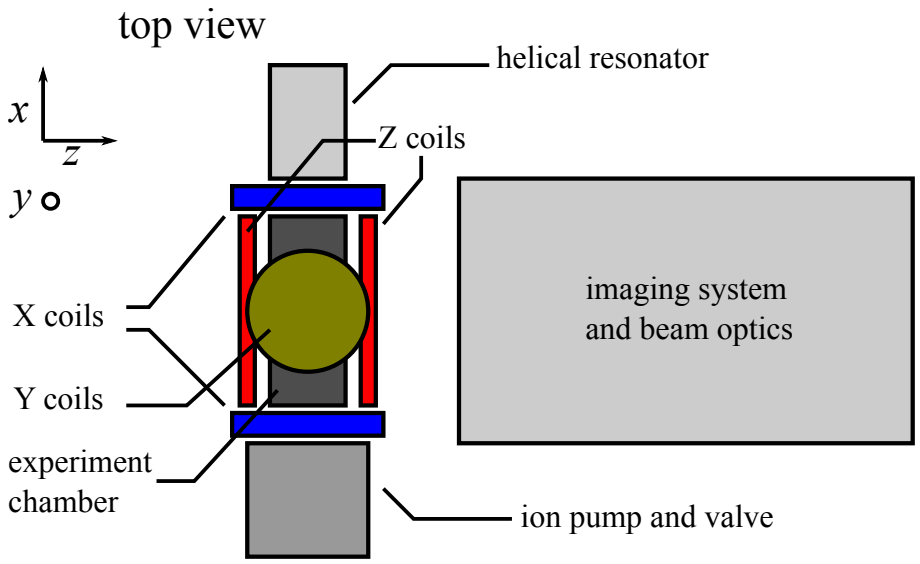

Figure 5.2: Schematic layout of the experiment on the optical table. The main vacuum chamber is surrounded by three pairs of coils used to produce a magnetic field in an arbitrary direction.

Figure 5.3 shows the orientation of the several possible beam paths planned for the chamber. In order to align beams through the chamber in this trap, it is necessary to have the beam exit the chamber. Because the trap centre is offset from the chamber centre, beams which enter the chamber at steep angles will not pass through the rear side of the chamber. To overcome this, a set of UV enhanced aluminium mirrors were placed inside the chamber to reflect out the beams after passing through the trap. It was therefore necessary to plan the beam paths before assembling the chamber so that the mirrors were guaranteed to be in the correct positions.

Ions are loaded into the trap from an atomic beam using a two-photon ionisation procedure described in section 3.5.1. The atomic beam is produced from a resistively heated stainless steel tube which contains a piece of natural abundance ytterbium metal. For optimal isotope selectivity during loading, the photoionisation beam needs to be perpendicular to the atomic oven axis. The oven axis is shown in figure 5.3 c). The angle of beam path B was chosen such that this condition is met.

In order to have efficient Doppler cooling from a single beam, it is necessary for the beam to have a strong component along each trap axis. For this reason, path D is chosen for cooling and state readout, although path E would also be suitable. Ultra-fast Rabi oscillations performed with the pulsed laser use beam path C because this axis has no component in the cavity direction

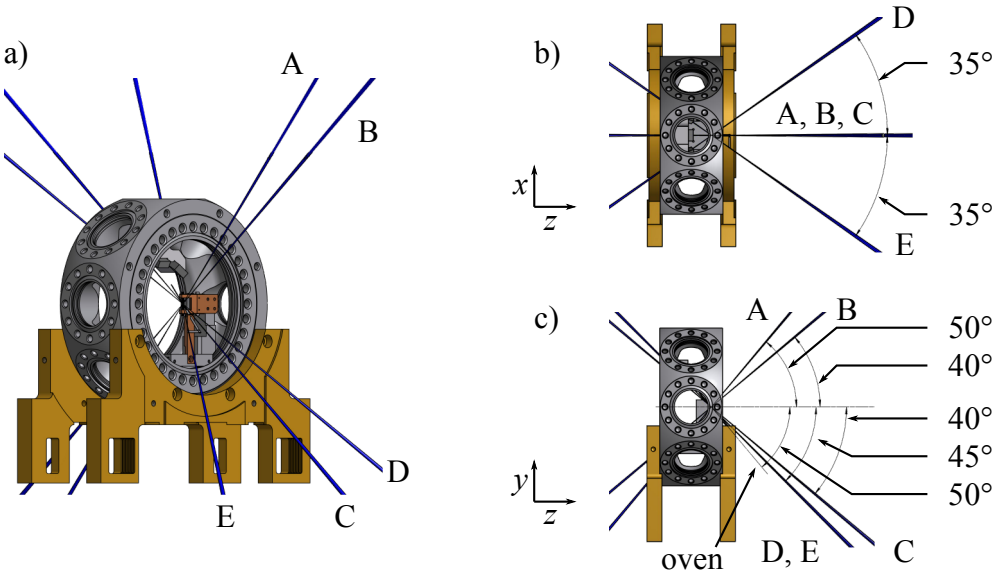

Figure 5.3: The planned beam paths for the chamber. The five beam paths (A-E) are described in the text.

(x). The excitation needs to drive only π transitions, and since the magnetic field axis lies along the cavity axis, this condition is achievable if the beam is linearly (horizontally) polarised. The beam paths are summarised in table 5.1.

Beam	x-z angle	y-z angle	Use
A	0	$+50°$	repumper
B	0	$+40°$	photoionisation
C	0	$-40°$	pulsed excitation
D	$+35°$	$-45°$	cooler
E	$-35°$	$-45°$	unused

Table 5.1: Summary of angles of the planned beam paths.

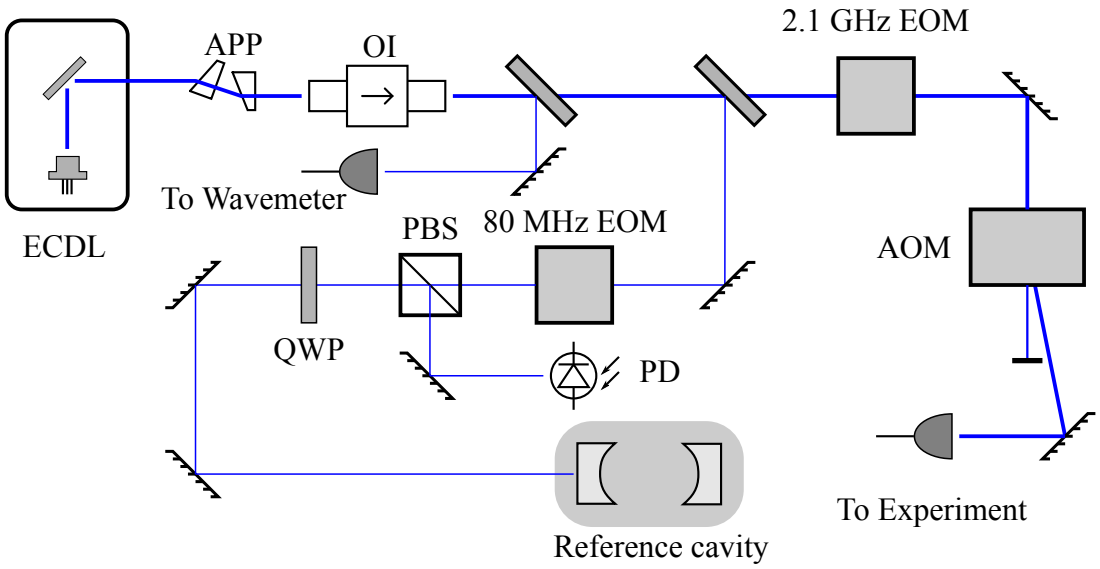

Figure 5.4: Optical setup for main Doppler cooling laser. ECDL: external cavity diode laser, APP: anamorphic prism pair, OI: optical isolator, EOM: electro-optical modulator, AOM: acousto-optical modulator, PBS: polarising beam-splitter, QWP: quarter-wave plate, PD: photodiode. The reference cavity centre frequency is tuned by measuring resonance fluorescence with a trapped ion.

5.2 Laser system

5.2.1 Trapping lasers

In order to load and trap ytterbium ions, three laser sources are required: one for Doppler cooling, one for repumping out of the $D_{3/2}$ state and a third for the resonant step in the photoionisation process.

Figure 5.4 shows the schematic layout of the main 370 nm laser used for Doppler cooling of the ion. The laser source is a 'NDU1113E' diode from Nichia which has been selected for free-running operation within 370 nm to 371 nm. The diode is placed in a home-built external cavity diode laser (ECDL) head in Littrow configuration based on the design presented in [98]. The diode needs to be cooled to about 15 °C in order to lase at 369.5 nm and produces about 5 mW of light.

The laser is locked using a Pound-Drever-Hall lock [99] to a home-built reference cavity based on the design presented in [100]. The cavity is designed to have a low coefficient of

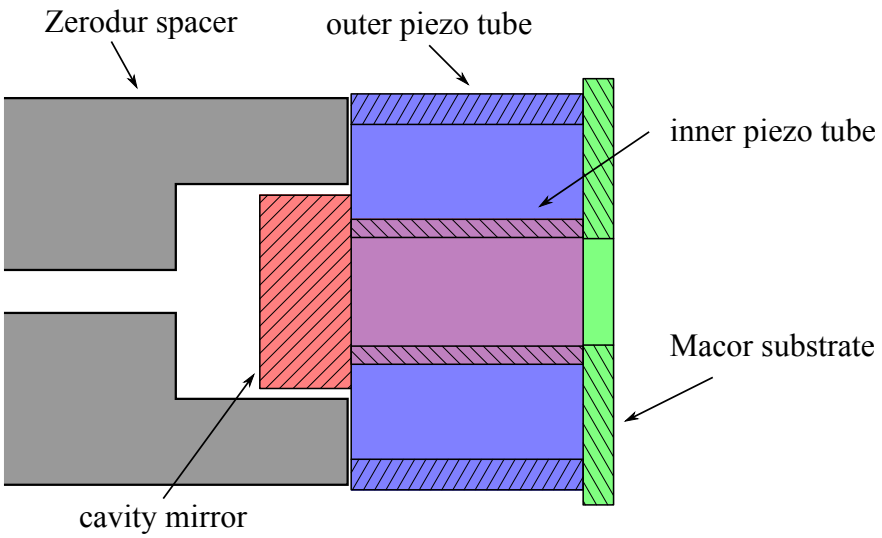

Figure 5.5: Temperature compensated piezoelectric actuator stack which allows tunability of the optical reference cavity. The parts were glued together in a jig using a small amount vacuum compatible glue, making sure that the surfaces are parallel and that the glue layer is thin. The thermal expansion of the two piezo tubes acts in opposite direction, cancelling the contribution to the cavity length.

thermal expansion for passive stability while at the same time allow for tunability of a few GHz. The passive stability is achieved by building the cavity spacer out of a low expansion glass substrate[2] and placing the cavity inside a temperature-stabilised vacuum chamber at $\approx 10^{-7}$ mbar.

Tunability of the cavity is gained through use of a temperature compensated piezoelectric actuator stack which is shown in figure 5.5. As both piezo tubes are made from the same material[3], their thermal expansion coefficients are approximately matched. Expansion of both tubes by an equal amount leads to no net change of the cavity length.

The expected worst case thermal expansion coefficient of the cavity is $\approx 0.18\,\mathrm{ppm/K}$ and the measured coefficient is $\approx 0.31\,\mathrm{ppm/K}$, which leads to a temperature dependence of the cavity features of $\approx 250\,\mathrm{MHz/K}$. Although this coefficient is larger than expected, the temperature stability of the system is good enough that the optical reference the cavity provides is sufficient

[2] We used standard grade TSG from Corning

[3] The piezo tubes are made from 'PZT-5H'

for operation of the trap.

The majority of the light from the Doppler laser passes through an electro-optical modulator (EOM) which provides side-bands at 2.1 GHz which are used for optical pumping during state preparation for $^{171}Yb^{+}$ described in chapter 7. Finally, the light is focused through an acousto-optical modulator (AOM) and the first diffraction order is coupled into an optical fibre which leads to the experiment chamber. The AOM provides electronic intensity control and allows the beam to be turned on and off with rise time $< 1\,\mu s$ which are the control time-scales necessary for state readout. Approximately 50 µW of light is available out of the fibre at the chamber which is sufficient for trapping and loading. The majority of optical loss is incurred via absorption losses from the optical elements and matching losses between the modes of the diode and the fibre.

Repumping of the atomic population out of the $^2D_{3/2}$ state is performed with a second laser near 935 nm. The laser setup is very similar to that shown in figure 5.4 and uses an anti-reflection coated diode[4]. This laser is also locked to a tunable home-built reference cavity with similar parameters. An AOM is also used to provide fast switching of the beam.

The third laser, near 399 nm, is used for the resonant step in the two-photon ionisation process for loading ytterbium ions into the trap. Also an ECDL[5], the required frequency accuracy of this laser is only ≈ 50 MHz so the laser frequency is stabilised using a wavemeter[6].

5.2.2 Pulsed laser

In order to produce single photons within the cavity, we will use pulse of light near 370 nm shorter than the lifetime of the $^2P_{1/2}$ state. This allows the ion to be excited into this state with unit probability.

The pulses are generated by a mode-locked Titanium-Sapphire laser running near 740 nm. The laser is a Mira Optima 900 with the 'Long pulse' Gires-Tournois interferometer (GTI) which produces 6 ps pulses when correctly mode-locked. Additionally, we use 'cavity dumper' option, which replaces the normal out-coupling mirror and extends the cavity to include a Bragg cell. The removal of the out-coupling mirror allows for a larger intracavity power, and the Bragg cell provides 'on-demand' out-coupling of a single pulse, resulting in an increase of the available pulse energy by a factor of 5 to 10.

[4] EYP-RWE-0980-08020-1500 from Eagleyard
[5] ML320G2-11 from Mitsubishi
[6] HighFinesse WS7

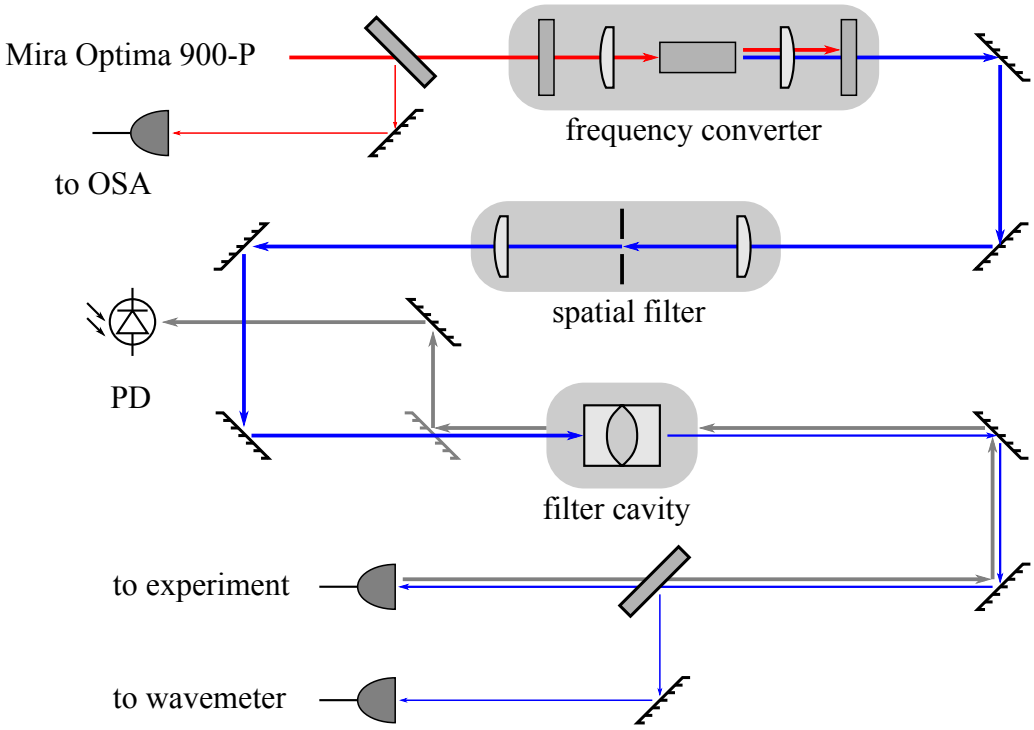

Figure 5.6: Optical setup for frequency doubling and spectral filtering of the pulsed laser. The Mira produces 6 ps long pulses at 740 nm which are converted via a non-linear frequency doubling process to 370 nm. The output mode of the doubling stage is spatially filtered and then coupled into spectral filter cavity. The output of the cavity is coupled into a single mode fibre to bring the light to the experiment chamber. The grey arrows represent light path used for optimisation of filter cavity mode matching (described in the text).

Figure 5.6 shows the setup used for frequency conversion and spectral filtering of the 740 nm pulses. A fraction of the light from the laser is diverted to an optical spectrum analyser[7] which is used to monitor the centre frequency and spectral width of the pulses.

In order for the light pulses to interact resonantly with the ion, their frequency needs to be doubled. This is performed with a home-built single pass non-linear crystal doubling stage using angle phase matching [101]. An optimal doubling efficiency of $\approx 50\,\%$ was achieved with a 15 mm long plane-cut Bismuth Triborate (BiBO) crystal[8].

After the frequency doubling stage there is a spectral filter cavity. The filter cavity is used to reduce the spectral width of the frequency doubled pulses from ≈ 100 GHz to 1 GHz, which

[7] LSA from HighFinesse

[8] The BiBO crystal was cut with $\theta = 145.6°$, $\phi = 90°$ from GWU-Lasertechnik

is beneficial for several reasons. In earlier experiments with photon production on the 935 nm transition it was found that light from the excitation pulse can be observed at the output fibre of the cavity, even though the laser was incident perpendicular to the cavity mode [102]. If the excitation pulse is shorter than the cavity photon lifetime, then the decay rate of the stray light will be given by the cavity photon decay rate. In our case, because the excited state lifetime is less than the cavity photon lifetime, any stray light scattered into the mode would be indistinguishable from photons generated by the ion. With the excitation scheme we plan to use which is described in chapter 7, the excitation transition is 12.6 GHz blue detuned from the photon production transition, so by narrowing the excitation pulse to less than this separation, the fraction of stray light scattered into the cavity can be minimised.

Spectral narrowing of the pulse provides the additional benefit that the energy required to perform a π pulse decreases with decreasing spectral width. This comes about as a result of the narrowing because the pulse becomes longer in time, which means a lower peak Rabi frequency is required in order to achieve the same π rotation. Estimation of the energy required to drive a π rotation between $^2S_{1/2}$ and $^2P_{1/2}$ in our system using calculations presented in [103] leads to $E_\pi \approx 40$ pJ for a 6 ps long pulse focused to a waist of 20 µm. For a bandwidth limited pulse of FWHM length 318 ps, $E_\pi \approx 0.7$ pJ.

In order to provide a narrow focus onto the ion, it is desirable to use optical fibre to transport the light from the laser system to the chamber, thus separating the alignment of the laser system and focusing onto the ion. Since the instantaneous power is rather large ($I_{max} \approx 6.7$ W for a 40 pJ, 6 ps pulse), it is necessary to consider non-linear effects inside the fibre. Measurement of the spectral width of the frequency doubled 6 ps pulses on an optical spectrum analyser after traversing a 1 m long optical fibre[9] indicate that the onset of non-linear effects occurs between 16 pJ and 58 pJ (see figure 5.7). After spectral filtering, the pulse length is extended by approximately a factor of 50, so the instantaneous power for the same energy pulse is reduced by the same factor. This allows for the use of optical fibres with the pulse at the energy necessary for a π rotation without significant non-linear effects.

The filter cavity is constructed from two curved mirror substrates with 98.5 % reflectivity and radius of curvature of 100 mm which are held together face on. This resulting cavity has a free spectral range of ≈ 200 GHz and a linewidth of ≈ 1 GHz.

In order to drive resonance rotations, the centre frequency of the cavity needs to be tuned to the transition frequency with an accuracy which is determined by the Rabi frequency of the driven rotations. In our case, the Rabi frequency is $\Omega = \pi/\Delta_t \approx 2\pi \times 1.6$ GHz, so we would like

[9] PM-S350-HP

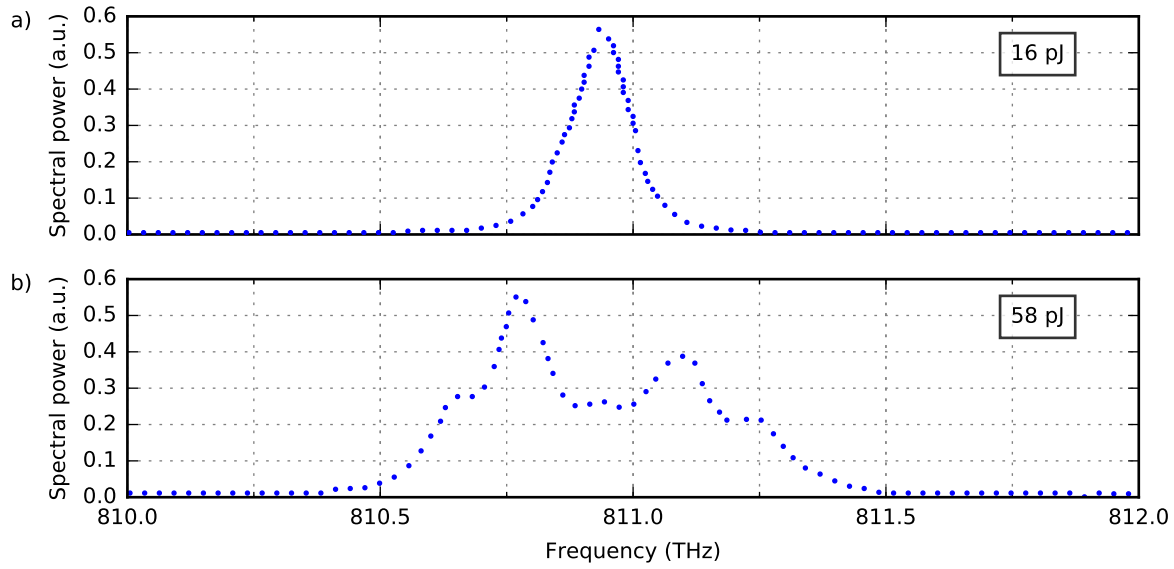

Figure 5.7: Measurement of non-linear effects with 6 ps pulses of light at 370 nm within one metre of PM-S350-HP fibre, measured with an optical spectrum analyser. a) No broadening is observed with pulse energy 16 pJ. b) Non-linear effects start to broaden the spectrum.

the cavity frequency to be stable to within 10 % of this. It is possible to achieve this stability with a temperature stabilised cavity in air.

Figure 5.8 shows two important measurements for characterising the cavity. The linewidth of the cavity is measured in figure 5.8 a). This was performed with the cavity temperature held constant with a PID controller while an ECDL, referenced to a wavemeter, was scanned. The optical transmission of the laser through the cavity was measured on a photodiode, and a Lorentzian curve fitted to the data allows the cavity linewidth to be determined. The second measurement, shown in figure 5.8 b), determines the temperature dependence of the frequency of the cavity modes. This measurement is taken by keeping the laser at a fixed frequency using the wavemeter and adjusting the temperature set-point of the PID controller. After the temperature of the cavity has stabilised, the optical transmission of the cavity was recorded. The resulting transmission peaks are fitted with Lorentzian curves, and, since the cavity linewidth is known, the temperature dependence of the cavity mode frequency (temperature coefficient) is given by the ratio of the widths. For the final cavity used in this experiment, the temperature coefficient at 370 nm was measured to be $(3.45 \pm 0.04)\,\mathrm{GHz/K}$. Initially, a cavity was built by mechanically forcing the two mirrors together inside a lens tube, however this resulted in a

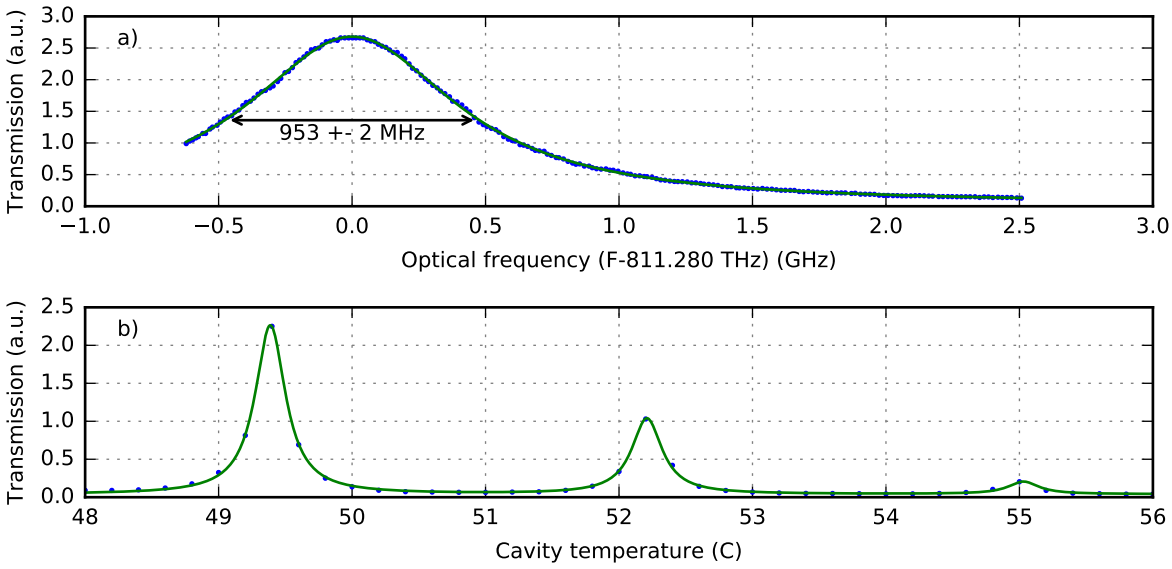

Figure 5.8: a) Measurement of filter cavity linewidth from cavity transmission while scanning an ECDL over GHz. Frequency measured with WS7 wavemeter. b) Measurement of the effects of temperature on the cavity. The cavity temperature is tuned for a fixed laser frequency. These two measurements together provide accurate determination of the the temperature coefficient of the cavity. The large peak corresponds to a TEM00 mode, and the two smaller peaks correspond to higher order transverse modes.

temperature coefficient much larger than that expected from the materials ($\approx 200\,\mathrm{GHz/K}$) due to the temperature dependence of the compressive force. The final cavity was built by gluing the two mirrors together under minimal mechanical stress.

The bandwidth of the pulse before the spectral filter cavity is much larger than the transverse mode splitting. This means the pulse contains light resonant with a large number of the modes that the cavity supports. The frequency spectrum of the light coupled out of the cavity will be given by the convolution of the input beam-cavity mode overlap and frequency spectrum of the pulse.

Before the light is coupled into the spectral filter cavity, the output mode of the doubling crystal is spatially filtered by focusing the beam through a 30 µm aperture. This filtering helps to reduce the coupling to transverse modes within the cavity, although it does not remove it completely.

The transmitted mode of the filter cavity is coupled into a polarisation maintaining fibre. It

is important that the overlap between the fibre mode and the Gaussian mode of the cavity is good, as imperfect mode matching causes parasitic coupling to higher order modes in the cavity (due to orthogonality of the modes) which can lead to an undesirable amount of additional spectral components in the output pulse. In practice, it was found that optimising the total power through the fibre was insufficient to couple well to only the Gaussian mode, observed by the presence of several spectral peaks when the fibre is connected to the wavemeter. Instead, the most successful strategy found was to optimise the fibre mode-cavity mode overlap by sending CW laser light backwards through the fibre and measuring the power transmission through the cavity on a photodiode. The optics and beam path for this is shown in grey in figure 5.6.

5.3 Imaging system

A microscope is used to collect fluorescence light from the an ion when it is cooled inside the trap. For the quantum state readout process described later in chapter 7, there are two important parameters for this microscope: the collection efficiency and the stray light performance. The collection efficiency is the fraction of photons produced by the ion which are collected by the microscope, and a high collection efficiency is achieved by having a large numerical aperture. The stray light performance determines how many photons pass through the microscope which are not due to fluorescence from the ion.

Figure 5.9 shows the optical components of the microscope used in this experiment. It is built from commercially available parts and sits completely outside of the vacuum chamber. The objective lens is a 50 mm diameter fused silica aspheric lens[10] which has a specified working distance of 48 mm and an effective focal length of 60 mm. The tube lens is a 750 mm focal length fused silica plano-convex lens. In front of the objective lens is a 6.35 mm thick fused silica vacuum window. Both lenses are anti-reflection coated for UV light, and the numerical aperture of the imaging system to limited to 0.39 by an aperture stop in front of the objective lens.

The microscope forms a primary image at a position approximately 750 mm from the tube lens. Due to the small geometric size of the trap, and the fact that the Doppler cooling laser passes through the centre of the trap, there is a reasonable fraction of light near 370 nm scattered from the tips of the needles. In order to filter out this light from the fluorescence, a 200 µm aperture is held in place at the primary image focus on a three axis translation stage. The

[10]The lens is 'A50-60FPX' from Asphericon.

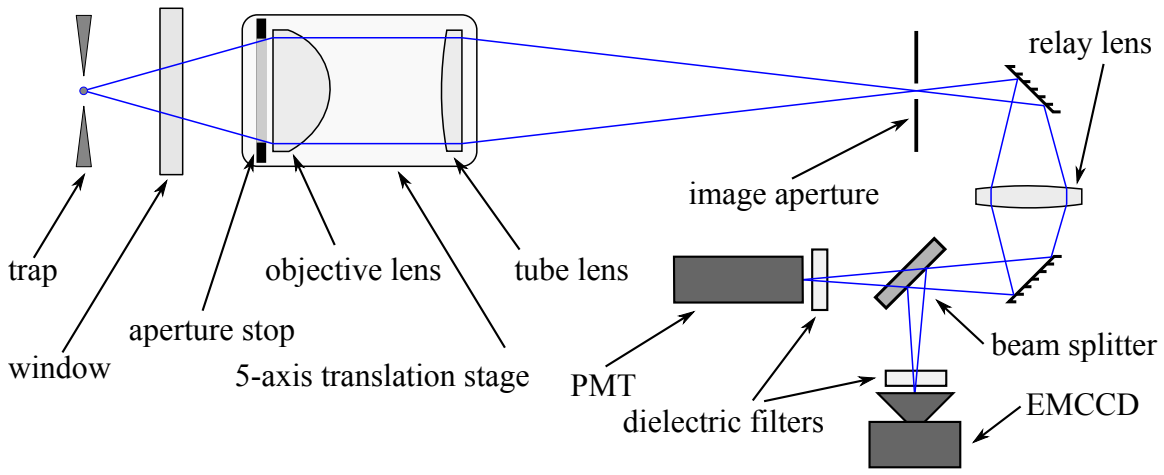

Figure 5.9: Schematic diagram of the microscope used for detection and imaging of the ion.

aperture acts as a spatial filter, removing light scattered from the trap in the image plane.

After the image aperture the light passes through a one-to-one imaging system formed by 100 mm focal length plano-convex lens, which produces a secondary focus approximately 400 mm away from the primary image. Before the secondary focus, the light passes through a 50:50 beam-splitter on a flip-mount which allows for a portion of the light to be focused on a camera[11]. The remaining portion of the light strikes a photo-multiplier tube[12] (PMT).

Including the one-to-one imaging system allows one to accurately position the aperture in the image plane prior to initial trapping by observing the resulting image on the camera. Due to the large amount of stray light from the trap structure, the aperture needs to be in place in order not saturate the PMT. When attempting to load an ion into the trap, it is very helpful to have the guarantee that the aperture is placed correctly for diagnosing potential problems. The numerical aperture of the system in the primary image plane is approximately 0.033, which means that imperfect alignment of the one-to-one imaging system has a much lower impact on the optical aberrations of microscope than the objective lens.

Directly in front of the PMT and the camera there are dielectric bandpass filters[13] which have a very low transmission outside of the range 365 nm to 375 nm. This filter removes almost all of the light outside of band of interest for the ion fluorescence (370 nm), meaning that we need not worry about blocking scatter from ambient room light, nor the contribution of light

[11]The camera is an electron multiplying CCD camera (Luca EMCCD from Andor), with a pixel size of $4\,\mu m \times 4\,\mu m$.

[12]The photon counter is 'H7360-01' from Hamamatsu.

[13]FF01-370/10-25 from Semrock

scattered from the trap from the 399 nm and 935 nm beams.

For state detection it is desirable to maximise the collection efficiency of the imaging system. Although for our purposes we do not require high spatial resolution for locating the ion, the resolution of the microscope will have an impact on the performance of the image aperture. Ideally the microscope would be diffraction-limited: the imaging system would focus all the light that enters the microscope faithfully at the image plane. In this case the fraction of light collected is given by

$$\varepsilon_{CE} = \frac{\Omega}{4\pi} = \frac{1}{2}\left[1 - \cos(\alpha)\right], \tag{5.1}$$

where α is the maximum half-angle subtended by the aperture stop, which is related to the numerical aperture via $NA = \sin(\alpha)$ in air. The radius of a point source determined by the Rayleigh criterion limit is given by

$$r = \frac{1.22\lambda}{NA}. \tag{5.2}$$

From the numerical aperture of our microscope operating at 370 nm, we expect the image of the ion to be focused to a radius of ≈ 600 nm in the object plane, or ≈ 7 µm in the image plane. The ideal diameter of the image aperture would be a few multiples of this distance in order to let the majority of ion fluorescence through while restricting background scatter as much as possible.

At the maximum numerical aperture of the microscope, the presence of the window has quite an impact the performance of the system. In order to understand the effects of the vacuum chamber window on the imaging system, ray tracing simulations were performed in OSLO [14]. In the face of aberrations of a real imaging system, it is helpful to define criteria to evaluate performance of the system relative to the ideal case. In the following analysis, we have quantified the aberrations in terms of the Strehl ratio which is defined as the ratio of the maximum value of the real point spread function to the system to that of an ideal system with the same numerical aperture. A microscope is said to be 'diffraction-limited' when its Strehl ratio is above 0.8 [104, p. 18].

When the simulated numerical aperture is below 0.2, the system performs well at the specified working distance with a Strehl ratio ≈ 1. As the numerical aperture is increased, the aberration introduced by the window increases and leads to a rapid decrease in the Strehl ratio when the objective is maintained at the specified working distance.

If the window is aligned perfectly normal to the optical axis, and has no wedge, then the window can only cause radially symmetric aberrations. The lowest order radially symmetric aberration is known as defocus, and can be compensated for by adjusting the front focal length.

[14] http://www.lambdares.com/oslo

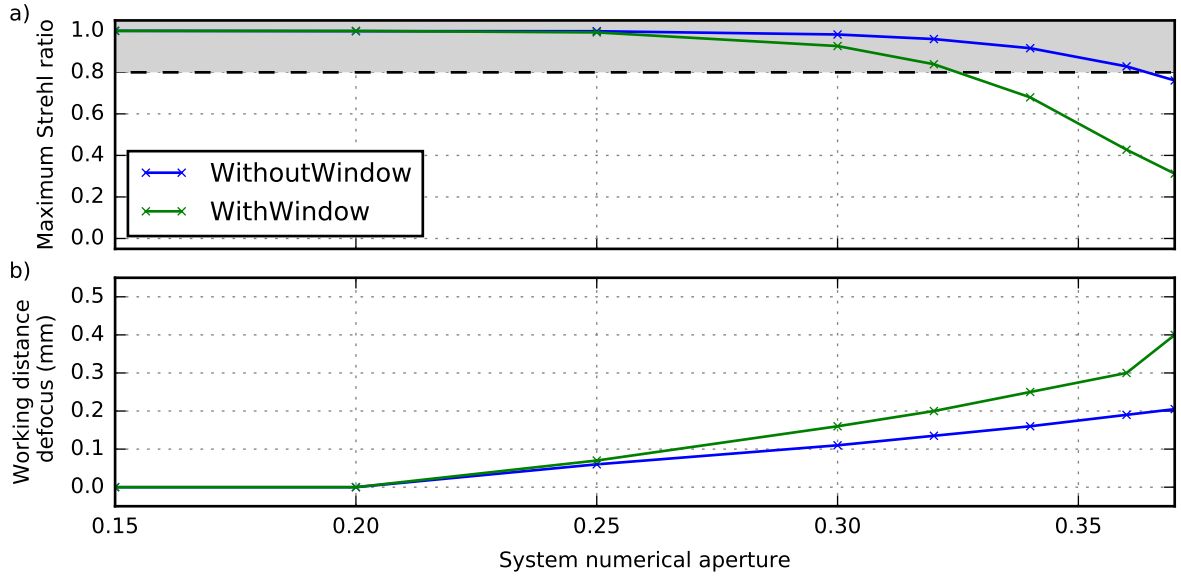

Figure 5.10: a) Strehl ratio taking the defocus into account, and b) corresponding working distance defocus of the imaging system for different numerical apertures. Without the window, the system is diffraction limited up to $NA = 0.37$, whereas with the window the diffraction limit is reached at just above $NA = 0.32$.

The next lowest order radially symmetric aberration is known as third order spherical aberration. It is possible to reduce the impact of the third order spherical aberration by applying a small defocus aberration, known as defocus compensation.

Figure 5.10 shows the result of simulations of the imaging system used to gauge the effectiveness of defocus compensation is this case. The maximum Strehl ratio is found by setting the front focal distance of the objective lens (working distance defocus) then finding the back focal plane of the system and comparing the peak height of the point spread function (PSF) to the height expected for an ideal system with the same numerical aperture. The simulations show that focus compensation will allow the system to be diffraction limited up to $NA = 0.32$ with the 6.35 mm window in place.

The total detection efficiency of the microscope can be measured directly using the fluorescence from the ion. If the photon emission rate of the ion R_e can be measured at the same time as the mean photon detection rate R_d, then the total detection efficiency can be found with $DE = R_d/R_e$. In $^{174}Yb^+$, one method for measuring the photon emission rate of the ion is to observe the pumping into the $^2D_{3/2}$ state which occurs when the 935 nm repump is turned off.

The branching ratio from $^2\mathrm{P}_{1/2}$ into this state has been precisely measured in literature to be $BR[^2P_{1/2} \rightarrow {}^2D_{3/2}] = 0.0050(2)$ [77], and hence from the optical pumping time constant we can infer the rate of photon emission via

$$R_e = \frac{1}{\tau \cdot BR[^2P_{1/2} \rightarrow {}^2D_{3/2}]}. \tag{5.3}$$

A measurement of the total detection efficiency taken in this way after defocus compensation is shown in figure 5.11. The ion is continuously Doppler cooled with a fixed laser power during one measurement, and the repump laser is turned off after 48 µs. The detected photon arrival times on the imaging system PMT are recorded and the process is repeated 10^4 times for statistics. A fit to the exponential decay reveals the dark state pumping rate ($1/\tau$) and the mean detected photon rate when the repump laser is turned on R_d. Although strictly only one measurement is required to fully determine the detection efficiency in this way, the measurement is repeated for several different laser powers in order to rule out systematic errors. The mean detection efficiency from this measurement is (0.49 ± 0.04) %.

Similar measurements taken before application of the defocus compensation lead to detection efficiencies of ≈ 0.2 % even though the same numerical aperture was used. From the maximum numerical aperture, taking into account the light lost due to reflections at both surfaces of the window ($T_{window} = 0.92$) and the quantum efficiency of the PMT ($QE = 0.14$), we expect a net detection efficiency of 0.51 %. Even though as shown in the simulation, the imaging system is not diffraction-limited at its full numerical aperture, after defocus compensation we are still able to focus the majority of light through the image aperture. The success of this method has shown the possibility of using relatively inexpensive standard aspheric lenses for ion trap microscopes which include windows. This is an attractive alternative to building or purchasing a custom objective which is compensated for the spherical aberration incurred by the window.

5.4 Beam alignment

Since both the trap and the cavity are small targets, alignment of the laser beams to the centre of these features is challenging. In particular, it is desirable that both the 370 nm and 399 nm beams pass through the trap without striking any of surfaces near the ion which could lead to charge build-up [105] producing static electric fields. Additionally, the 370 nm beam should not scatter light into the imaging system as this stray light will directly cause a reduction in

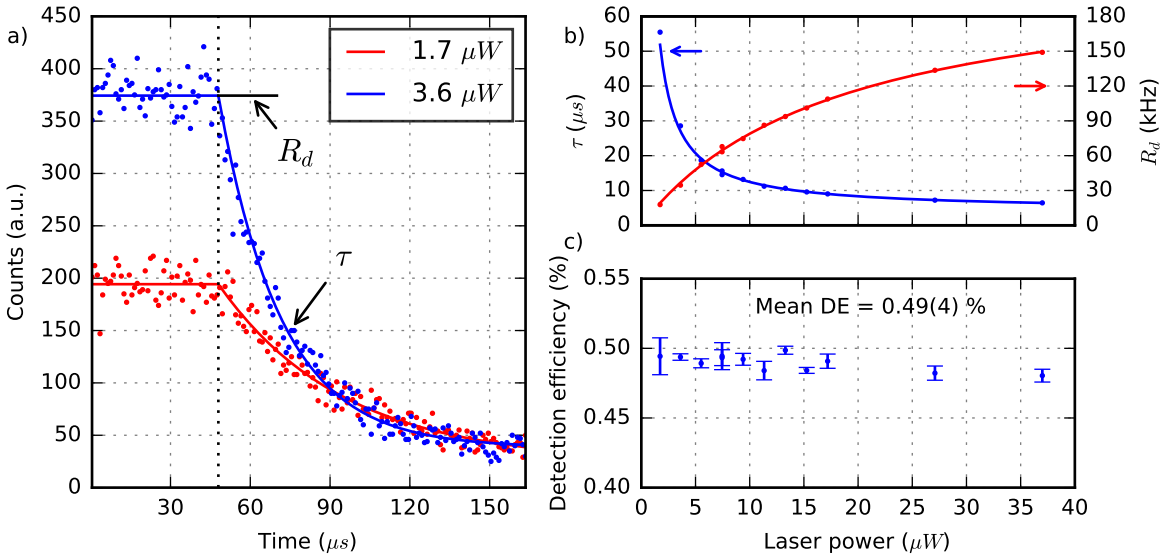

Figure 5.11: Measurement of the net detection efficiency of the imaging system with an ion. a) Decay of the excited state population into the $^2D_{3/2}$ state during continuous Doppler cooling is observed when the repump laser is disabled. This provides a measurement of the mean detector count rate R_d and the decay constant τ. b) A sequence of data are recorded for different powers of the Doppler cooling laser. c) Detection efficiency is inferred from the mean detector count rate and the excited state population required to produce pumping into the $^2D_{3/2}$ state with the measured decay constant. The mean detection efficiency in this measurement is (0.49 ± 0.04) %.

the signal to noise ratio of photon counting measurements, and is particularly important in the quantum state readout process. In this section the particular challenge of focusing these lasers to waists on the order of 15 µm through the window at steep angles is discussed.

In the absence of a window on the vacuum chamber, a waist of 15 µm at the position of the ion could be achieved with a 200 mm focal length lens and a collimated beam of ≈ 2.4 mm. However, because the beam must be focused through the vacuum window at an angle of $\approx 50°$ to the surface normal, the focus is astigmatic.

If the lens position is chosen such that one of the directions is in focus at the position of the ion, the width in the second direction is larger. Alternatively, if the lens position is chosen at the midpoint between the two foci, the beam will look symmetric but the width will be larger in both directions.

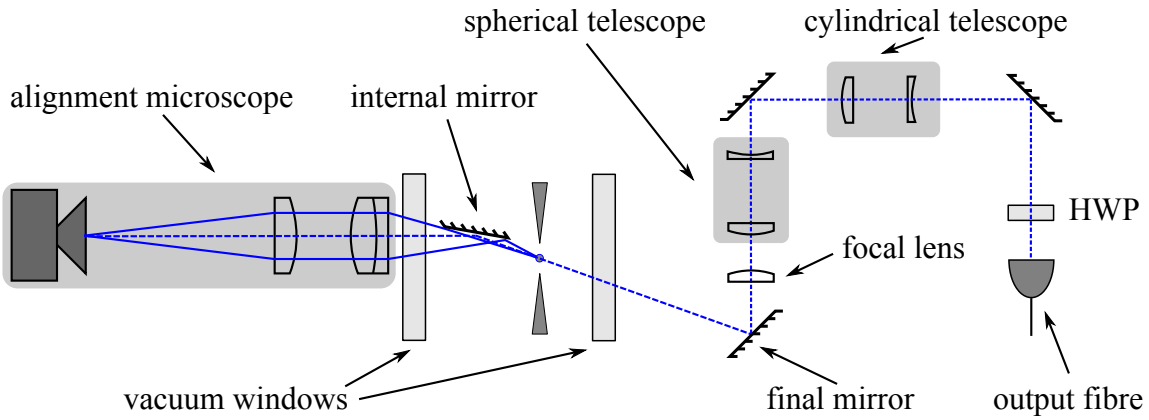

Figure 5.12: Optical setup for focusing UV beams into the chamber. Linearly polarised light arrives from the laser table via a polarisation maintaining fibre. The polarisation angle is controlled with a half-wave plate (HWP). The light passes through a cylindrical telescope and a spherical telescope before being focused into the chamber. After passing through the trap centre, the beam is reflected out of the chamber with an internal mirror and an image of the focus is formed with the alignment microscope.

Initially, when the trap was operated without the cavity, the beam was focused to minimise the width of the beam in the trap rf electrode direction. Although it was only possible to achieve a Gaussian equivalent waist of $\approx 30\,\mu m$[15], the increased width of the beam in the axis near perpendicular to the rf electrode direction did not contribute significantly to the scattered light. After introduction of the cavity into the trap however, the large width along the second axis caused light to scatter off the cavity electrodes into the imaging system. The large amount of scattered light made it very difficult to observe any fluorescence from the ion at all, and adjusting the position of the lens to produce a symmetric focus did not ameliorate this. Instead, we needed to reduce the degree of astigmatism in the beam.

Figure 5.12 shows the setup used for focusing the beam onto the ion with the cavity in place. The astigmatism introduced by the window is compensated for by applying a weak astigmatism to the beam before focusing into the chamber. This was performed with a Galilean cylindrical telescope, slightly short of its correct separation, with near unity magnification (formed with 100 mm and -75 mm focal length lenses) on rotatable mounts. The beam then passes through a spherically symmetric telescope to increase the width before being focused into the chamber.

[15]The Gaussian equivalent waist is the waist that corresponds to the measured intensity of light at the ion

It was not possible to correctly pre-position the cylindrical lenses because of uncertainty in the beam parameters and path lengths. Instead, a specially designed microscope was aligned to the beam as it exits the chamber which was used to provide an image of the beam at the position of the trap. The microscope is formed from a 100 mm focal length achromatic doublet as the objective lens, and a 200 mm plano-convex lens for the tube lens. Once the lenses are aligned to the beam behind the chamber, an image is formed on a camera. In order to correctly align the focal plane of the microscope to the trap, the focal lens before the chamber is removed resulting in a collimated beam passing through the trap. With the uniform illumination now provided by the beam, the image of the trap rf electrodes on the microscope can be brought into focus. When the focal lens is replaced, the microscope shows a faithful representation of the beam at the position of the ion.

With the image of the beam at the ion on the camera, it was possible to adjust the angle and separation of the cylindrical telescope to visually correct for the aberration caused by the window and produce a symmetric focus with a waist of 15 µm. A subtlety of this approach lies in the use of the internal mirror. If the optical axis of the microscope entered the chamber at the same angle through the second window as the laser beam through the first, then this would cause aberration in the microscope image which would be indistinguishable from the aberration we are trying to correct. However, because the optical axis has a near normal angle of incidence with the window thanks to the internal mirror, this is not a problem and the microscope image can be trusted.

Application of this method has allowed us to achieve near symmetric foci at the position of the ion with waists on the order of 15 µm for beams which enter through the window at steep angles. For the main Doppler cooling beam this was a particularly important step after introduction of the cavity, and has allowed us to work with the system without having to reduce the window incidence angle which, for space reasons, would require a smaller numerical aperture of the microscope objective lens.

5.5 Cavity photon analysis setup

In order to measure the properties of the ion-cavity system, it is important to have a good degree of control of the polarisation of light entering and exciting the cavity. One of the potential advantages of working with optical fibre cavities is the intrinsic coupling to optical fibre. This means that the transfer of the light in and out of the chamber can be greatly simplified, as the cavity light analysis optics do not have to be aligned to the cavity in the chamber. However,

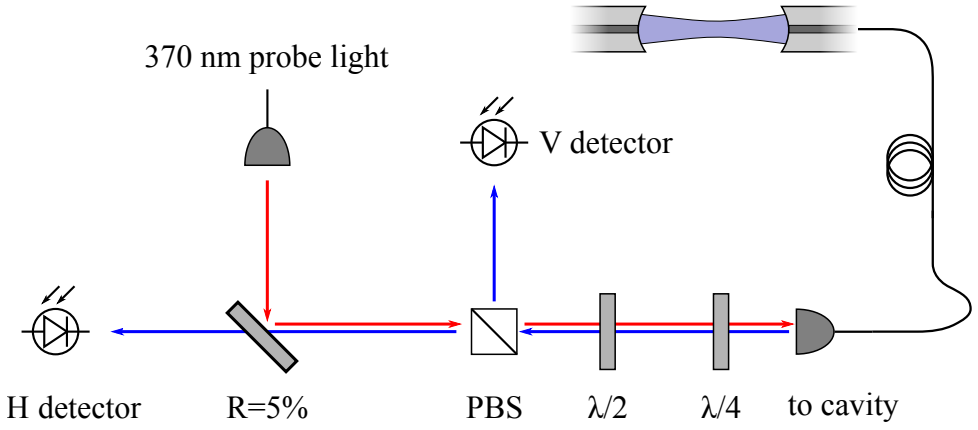

Figure 5.13: Optical setup used for cavity photon analysis. When the probe light is off, single photons leaving the cavity can be measured in any desired polarisation basis on the H and V single photon detectors. When the probe light is turned on, the light reflected from the cavity mirror can be used to measure the cavity resonance and detect birefringence in the optical fibre leading to the cavity. Fibre birefringence can be fully analysed and corrected for with the half- and quarter-wave plates in front of the fibre.

the polarisation state of light guided by the single mode fibre may be modified by birefringence and losses due to bending of the fibre. To use a ion-fibre cavity system to produce photons with defined polarisation states, is important to understand these properties.

Figure 5.13 shows the optical setup used to couple light in and out of the fibre cavity. Light which leaves the cavity passes through a quarter-wave plate, a half-wave plate and is then incident on a polarising beam splitter. The pair of wave-plates allows for the polarisation state of light leaving the fibre to be transformed into any desired basis. On each arm of the beam splitter there is photon counter[16] which makes it possible to detect the single photons generated by the ion.

In the H- arm of setup, there is a 5 % reflectivity beam sampler which allows for horizontally polarised light to be coupled into the cavity from an external diode source which can be tuned into resonance with the atomic transition. This light allows the cavity resonance to be probed in the same setup as used for photon polarisation analysis. Furthermore, it allows for characterisation of the system and correction of the fibre birefringence independently of the ion.

[16]Count Blue APD from Laser Components and H7360-01 PMT from Hamamatsu.

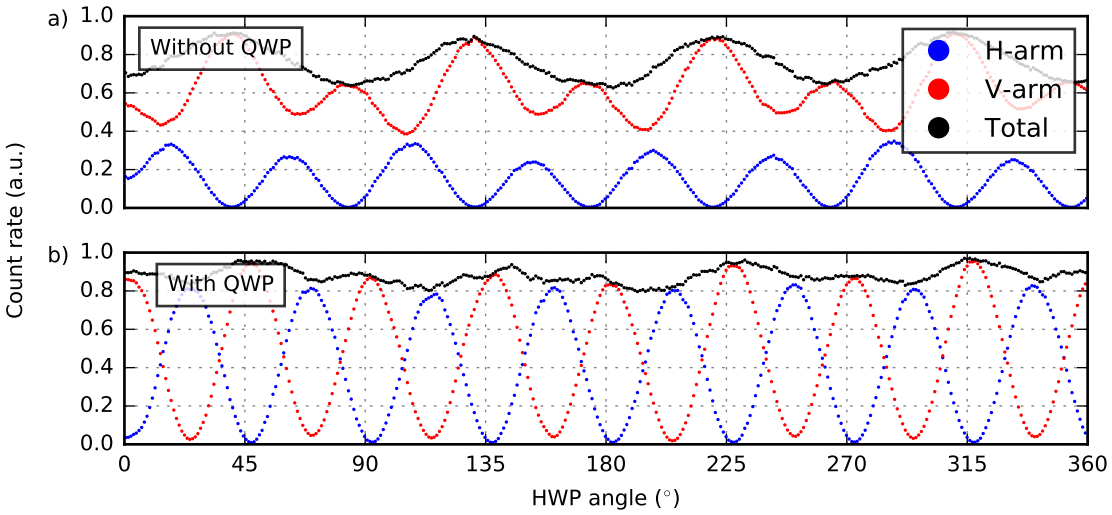

Figure 5.14: Polarisation analysis of probe light reflected from cavity fibre. The polarisation of the probe light is fixed and angle of the half-wave plate is adjusted by one full revolution, while monitoring the photon count rate on the two arms of the detector. A measurement is performed a) without the quarter-wave plate present and b) with the quarter-wave plate adjusted to compensate the fibre birefringence.

Figure 5.14 shows a measurement taken to evaluate the performance of the analysis setup. The cavity was probed with light which is not resonant with the cavity so that all the light is reflected. The probe light passes once through the half-wave plate and once through the quarter-wave plate before entering the fibre. The measurement in 5.14 a) was taken with the quarter-wave plate removed to measure the effects of the fibre birefringence alone. If there were no birefringence in the fibre, the light detected on each arm the of analyser would follow Malus' law and oscillate sinusoidally with 100 % visibility and an an angular frequency of 8 cycles per revolution. This measurement reveals that the fibre has significant birefringence which needs to be compensated for in order to transform the polarisation state of photons leaving the cavity into a more clearly defined basis, such as H and V. In addition, there appears to be some polarisation dependent loss observed as modulation in the total count rate.

Compensation of the birefringence can be achieved by minimising the signal on the V-arm through successive rotations of the half- and quarter-wave plates. In the absence of polarisation dependent losses, this optimisation strategy will lead to the H-V states at the polarising beam

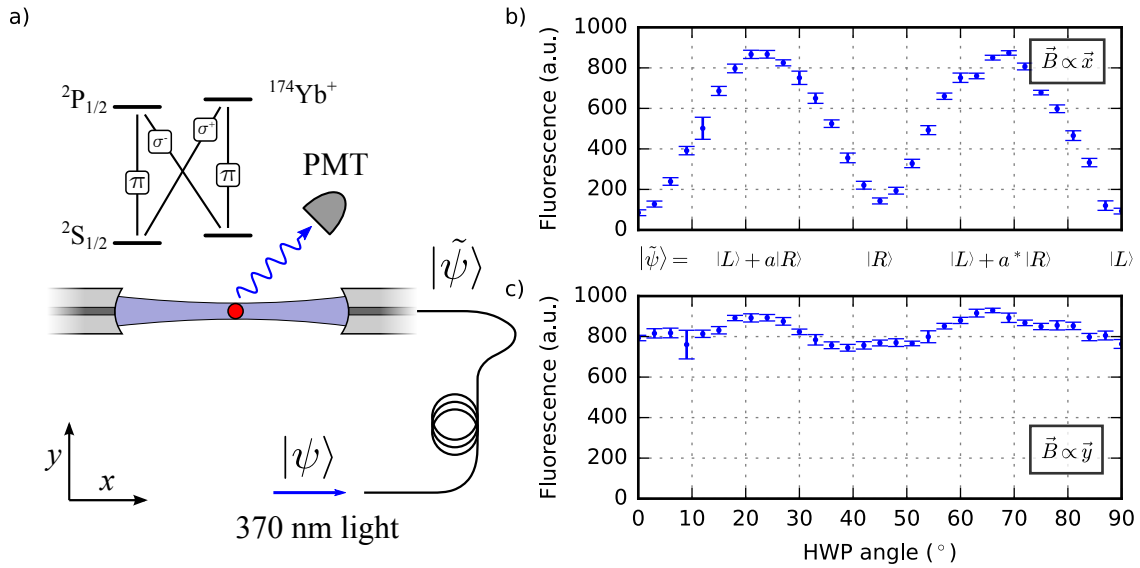

Figure 5.15: Measurement of polarisation dark state of an ion which confirms the polarisation of the light at the ion. a) Fluorescence is observed through the imaging system from a trapped ion inside the cavity excited via light coupled into the cavity from the polarisation analysis setup. b) The magnetic field is oriented along the cavity axis (x) while the half-wave plate is rotated, and polarisation dark states are observed. c) The measurement is repeated with the magnetic field along an axis transverse to the cavity (y), and no polarisation dark state is observed.

splitter being mapped to the L-R circularly polarised states of the cavity, and a mathematical proof of this strategy using Jones calculus is presented in appendix B.

Figure 5.14 b) shows a similar measurement taken after the birefringence compensation procedure. Here the presence of minima in the V arm signal which extend almost to zero show that the birefringence has been successfully compensated for with the quarter-wave plate.

In order to confirm that the polarisation is correctly configured, we have performed a measurement with a trapped $^{174}Yb^+$ ion inside the cavity shown in figure 5.15. The polarisation analysis setup is adjusted such that the fibre birefringence is compensated using the method described previously. The laser providing the cavity probe light is tuned to be on resonance with the atomic transition, and the power is adjusted so that the ion is below saturation. When the half-wave plate in the analysis setup is rotated, the polarisation of the light incident on the cavity is transformed between the $|L\rangle$ and $|R\rangle$ circular basis. The fluorescence of the ion due to the cavity probe laser is recorded though the imaging system. In figure 5.15 b) the magnetic

field is oriented along the cavity axis. The pure $|L\rangle$ and $|R\rangle$ polarisation states will drive only one σ transition and therefore optically pump the ion population into one of the m_j states. The optical pumping results in a complete reduction in fluorescence from the ion. The measurement is repeated with the magnetic field oriented perpendicular to the cavity axis in figure 5.15 c) so that the circular states drive $\sigma^{\pm}$ transitions equally. Only a very small modulation in the fluorescence is observed, which confirms that the drop in fluorescence in b) is due to optical pumping and not any other effects like polarisation dependent loss in the fibre.

5.6 Experimental control

The majority of the experiment is controlled by the equipment shown in figure 5.16. Control can be split into two broad categories: slow diagnostic control such as optimisation of ion fluorescence with typical time-scales of 100s of milliseconds, and fast pulse sequence control such as state preparation and readout with time-scales of 1-100 microseconds. In both cases, the data input is almost exclusively the rate and arrival time of single photons generated by the ion. In this section, the hardware and software which has been developed in order to control this experiment in a modular fashion is described. By controlling the experiment in this way, the same control scheme will be used for several interconnected ion-cavity experiments which is necessary in order to build a quantum network of trapped ions.

The fast control is performed with home-built hardware known as the Fast Experimental Control System (FECS). The system is based on a FPGA board[17] which is connected to a home-made breakout board containing 16 5 V capable TTL output lines, 8 3.3 V and 5 V compatible logic input lines, and an external phase lock circuit. The FPGA unit is connected to a computer via a USB2 port, allowing for loading of the FPGA configuration and transfer of data.

We have developed firmware for the FPGA which implements a small home-made instruction parsing unit (IPU). This firmware allows arbitrary control sequences to be executed in real time, removing the need to compile control sequences in a hardware description language such as Verilog. The IPU executes a sequence of 32 bit instructions held in internal RAM, which has been loaded with a sequence of instructions via the USB connection. Because the control sequences are created off-line before being executed, the experiment can be made to programmatically change the control sequence after a number of measurements have been made. This is useful, for instance, for measurements where the length of a pulse is to be varied.

[17] XEM6001 from Opal Kelly

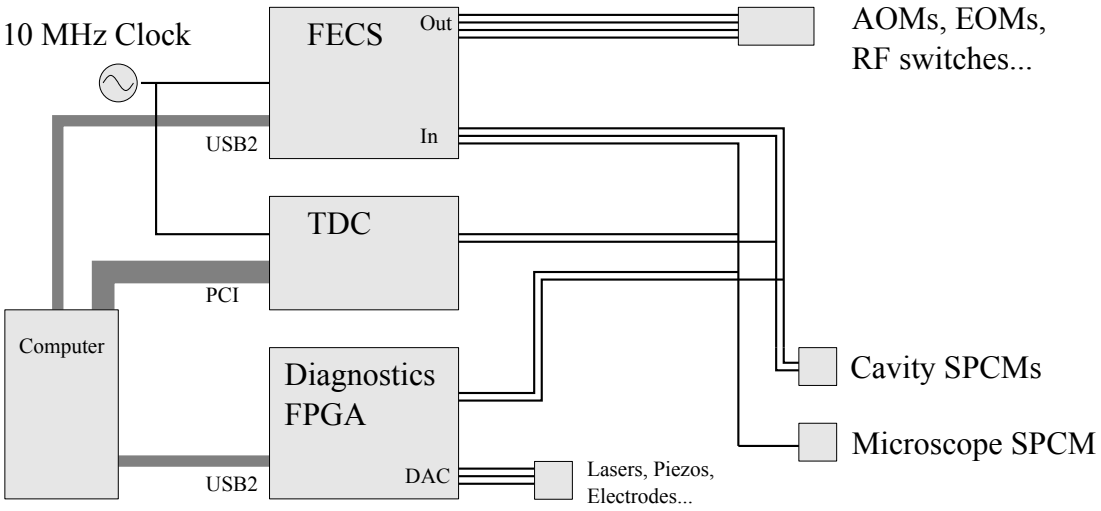

Figure 5.16: Diagram of the experimental control scheme used for this experiment. FECS: Fast Experimental Control System, TDC: Time-to-Digital Converter, SPCM: Single Photon Counting Module.

The IPU has a small set of instructions which can be used to build a control sequence. These instructions are: *set*, *wait*, *end of sequence*, *gate counter*, and *conditional jump*.

The first three instructions allow for deterministic pulse sequence generation by configuring the logic state of the output bus with *set* commands, and delaying between successive *sets* with the *wait* command. The IPU is clocked with a 100 MHz signal derived from our atomic clock, providing a pulse timing resolution of 10 ns.

The latter three commands add the possibility of conditional logic within sequences based on the number of photons counted within certain time windows. This feature will be very useful when operating the ion-cavity system as a photonic entanglement generation node. Here the experiment operation can be optimised by only running the state readout when a photon incidence has been registered. Often in trapped ion experimental sequences, the state readout process takes the largest fraction of time. By only performing it when it is needed, the average sequence repetition rate can be significantly increased. For the work presented in this thesis this feature was not necessary, but will become increasingly important in the future.

Another key tool is the time-to-digital converter (TDC)[18] card which allows for high-resolution

[18]TDC8HP from RoentDek

tagging of the arrival time of electrical pulses on up to 8 channels. The card has a 25 ps resolution and is clocked from our atomic clock so that it is phase coherent with the FECS. The TDC assigns a 48-bit timestamp to each electrical pulse (for example, when a photon is detected on the microscope SPCM), which allows for precise identification of its occurrence within a pulse sequence.

Both the FECS and TDC are linked to a desktop computer which controls their operation. Using home-built software, a schematic representation of a pulse sequence designed by the experimenter is compiled into a set of instructions for the IPU. The instruction sequence is loaded into FECS over the USB link and the sequence is executed. After completion of the sequence, the data buffers are read out from the TDC and the photon arrival times are decoded and correlated with the sequence, ready for more in-depth analysis.

A second FPGA is used to provide slow general diagnostic control required for daily operation. This hardware implements digital-to-analog converters (DACs) and several different pulse counters which can be gated with between 4 µs and 260 ms. The DACs are used for general purpose operations such as controlling feedback for ECDL lasers, controlling piezo-based positioning stages, and driving trap compensation electrodes. The counters are used to record count rates for measurements which do not require precise timing, for example measuring the fluorescence of the ion as a function of laser detuning.

5.7 Summary

In this chapter the experimental apparatus which is used to trap and control single Yb^+ ions inside a fibre-cavity is described. The design has been based on the previous experimental apparatus combining an ion trap and fibre-cavity, however significant improvements have been made. The entire system has been built in such a way that the experimental footprint is small. This will enable the use of several such apparatuses in a laboratory setting where they can be used to produce distributed entanglement.

The system of lasers used for manipulation of trapped ions has been built in a compact and extensible way. With the exception of the pulsed laser for ultra-fast excitation, the lasers are built from diodes which are either stabilised to low-drift optical reference cavities or a wavemeter. This reduced complexity of this system as compared with transfer locking schemes to atomic references allows the lasers needed for operating the trap to be contained in a small space, enabling future ion traps to be run from independent laser systems which is helpful during the development stage. On the other hand, the pulsed laser which has been built will be used for

excitation in two traps at the same time. The optical power that is produced by this laser is sufficient to drive several experiments concurrently.

A microscope, used for imaging the single ion and collecting the resonance fluorescence, has been developed with off-the-shelf parts. We have shown that by applying a defocus to the imaging system, the impact of spherical aberration caused by the vacuum window can be reduced, which allows the microscope to operate near the diffraction limit at its full geometric numerical aperture. This provides a simple yet effective system for working with trapped ion experiments which benefit from the collection efficiency of high-numerical aperture imaging systems.

In reducing the overall size of the experimental setup, the system has been designed such that all beams incident on the ion enter the vacuum chamber from a single window. To achieve this, we have employed laser beams which are focused through this vacuum window at a steep angle. This approach has been made possible by the use of an aberration compensation scheme which allows for the astigmatism introduced as the beam passes through the window to be measured and reduced.

We have developed an optical setup to analyse the polarisation of single photons produced by the ion out of the cavity. Our setup is designed in such a way that its operation can tested *in situ* independently from interaction with the ion. Specifically, this allows us to analyse and compensate birefringence which occurs as a result of propagation of the photons through the single-mode fibre. Since the measurement is 'off-line' with respect to the atomic interaction, this simplifies these calibration measurements which will be important when several systems are operated in unison.

The experimental control scheme which has been developed during this thesis is built with the operation of several ion traps in mind. The modular approach which has been taken will allow for a simple transition to synchronous control of two or mode ion-cavity systems. Furthermore, the implementation of fast conditional logic within the control hardware allows for state readout operations to be performed only after successful detection of heralded entanglement, a feature which will significantly boost the effective rate of entanglement generation.

Chapter 6

Ion-cavity experiments

In this chapter the successful coupling of the dipole transition of $^{174}Yb^{+}$ to a fibre-cavity is demonstrated and characterised. In section 6.1, the geometry of the cavity mode is measured via its interaction with the ion. From this measurement we verify the mode volume of the cavity, and hence determine the maximum atom-cavity coupling rate allowed by our cavity geometry. After our initial measurement of the atom-cavity coupling, we investigate single photon generation from an ion inside the cavity in section 6.2. With a Hanbury Brown and Twiss measurement setup, we determine that the light which is coupled out of the cavity fibres is highly non-classical and exhibits photon anti-bunching. Due to the Purcell effect, the lifetime of the atomic excited state is shortened in the presence of the resonant cavity. In section 6.3 this effect is measured and the cavity-QED parameters of the system are extracted. In section 6.4 we investigate the properties of the system when driven by an external field as it diverges from the Purcell picture which excludes excitation. To this end, we measure correlations between the light emitted into free-space versus the cavity mode in the driven Jaynes-Cummings model. We observe enhancement and suppression of the total photoemission rate of the system which occur as a result of interference between the driving field and the field which builds up inside the cavity as a result of light scattered from the ion. This interference can be tuned by adjusting the length of the cavity, which determines the relative phase of the two fields. Measurement of the enhancement and suppression caused by the interference will prove useful as a technique to accurately determine the cooperativity of cavity-QED systems in the fast-cavity regime. I acknowledge support from Hendrik-Marten Meyer with the theoretical analysis of the driven Jaynes-Cummings model in this chapter.

6.1 Measurement of the cavity field

The strong advantage that fibre-cavities present over macroscopic cavities is the much smaller geometric size of their modes, which allows smaller mode-volumes and hence large atom-cavity coupling rates. However, as the size of the mode decreases, so increases the technical difficulty in alignment of the mode with the ion. In this section, we use the interaction between light in the cavity mode and the ion to determine the transverse extent of the fundamental mode. Since the cavity length is well characterised, this measurement allows us to confirm the cavity mode volume, and hence the expected atom-cavity coupling rate for our transition. Using the same technique, we also measure the standing-wave profile of the mode along the cavity axis and determine the localisation of the ion.

The ion trap is mounted at a fixed position within the chamber, and the relative position between the ion and the cavity mode is adjusted by moving the cavity. The cavity is mounted on two translation stages for this purpose. The first stage[1] employs a slip-stick piezo motor and provides approximately 12 mm of travel along the z direction of the global coordinate system which is shown relative to the trap in figure 3.4. This translation stage includes a position sensor with a resolution of ~ 1 nm, and allows for closed-loop control with a repeatability of ~ 25 nm. The second stage[2] is held on top of the first, and allows translation aligned along the three axes (x, y, and z) each with approximately 38 µm travel. Since this stage is open-loop and relies on piezos, the translation is not well calibrated.

The fundamental mode of the cavity electric field follows a Gaussian distribution in the directions perpendicular to the cavity axis, and a standing wave along the cavity axis. At the waist of the cavity, the field is given by

$$\vec{E}(\vec{r}_\perp, x) = \vec{E}_0 \cos(kx) e^{-r_\perp^2/w_0^2}, \tag{6.1}$$

where $\vec{E}_0$ is electric field vector on axis, $\vec{r}_\perp$ is the perpendicular displacement from the cavity axis, and w_0 is the cavity mode waist. Since the atom-cavity coupling rate g is proportional to the electric field distribution of the cavity mode, it follows that

$$g(\vec{r}_\perp, x) = \cos(kx) g_0 e^{-r^2/w_0^2}. \tag{6.2}$$

In the Jaynes-Cummings model with a weakly driven cavity, the population of the atomic

[1] SLC-1720-S-UHV from SmarAct GmbH

[2] Tritor-38 from PiezoSystemJena

excited state is given by [106]

$$\langle \rho_{ee} \rangle = \tilde{n} \frac{g^2}{\Delta_L^2 + (\Gamma/2)^2}, \tag{6.3}$$

where $\tilde{n}$ is the expectation value of the intracavity photon number. For a constant power and detuning of the driving field, the excited state population is proportional to the square of the atom-cavity coupling rate. Since the rate of photons scattered into free space by the ion is given by $\Gamma\rho_{ee}$, we find

$$R_{4\pi} \propto g^2(\vec{r}_\perp, x) = g_0^2 \cos^2(kx)\, e^{-2r^2/w_0^2}. \tag{6.4}$$

This allows us to perform measurements of the spatial mode profile of the cavity by observing changes in the resonance fluorescence of the ion, which was first experimentally demonstrated with ions in [58].

In our experiment we have performed measurements of the cavity mode profile along each of the three directions. These measurements were taken by moving the cavity relative to the ion trap while a laser resonant with the atomic transition is coupled into the cavity. The cavity is scanned across the atomic resonance to avoid systematic effects caused by thermal drift of the cavity, and the power of the driving laser is chosen such that the excited state population of the ion is below 0.1 with the cavity on resonance. In order to maintain stable trapping during the measurement cycle, the ion is periodically Doppler cooled.

Figure 6.1 shows a measurement of the transverse mode profile of the cavity using this method. The data fit well to the Gaussian function expected for a TEM_{00} cavity mode, and with this information is it possible to adjust set the position in the two transverse directions such that the ion sits in the centre of the mode. From the measurement along the z direction in figure 6.1 c), we recover a FWHM from the Gaussian fit of $(3.91 \pm 0.15)\,\mu\mathrm{m}$ using the length scale provided by the SmarAct translation stage which is specified to have a closed loop with repeatability of 25 nm.

Taking into account the effect of motion of the cavity electrodes on the trap potential, we find from the analysis in chapter 3.3.3 that the relative motion of the ion and the cavity mode is increased by a factor of 1.08 along the z direction. As a result, the real FWHM of the cavity mode is $(3.62 \pm 0.14)\,\mu\mathrm{m}$, which corresponds to a Gaussian $1/e^2$ radius of $w = (3.07 \pm 0.12)\,\mu\mathrm{m}$. Since the ion is approximately centred between the two mirrors, this is a measurement of the cavity mode waist. This measurement differs slightly from the mode waist of $3.38\,\mu\mathrm{m}$ which expected from the radius of curvature of the mirrors, and is likely caused by error in the measurement of the radius of curvature.

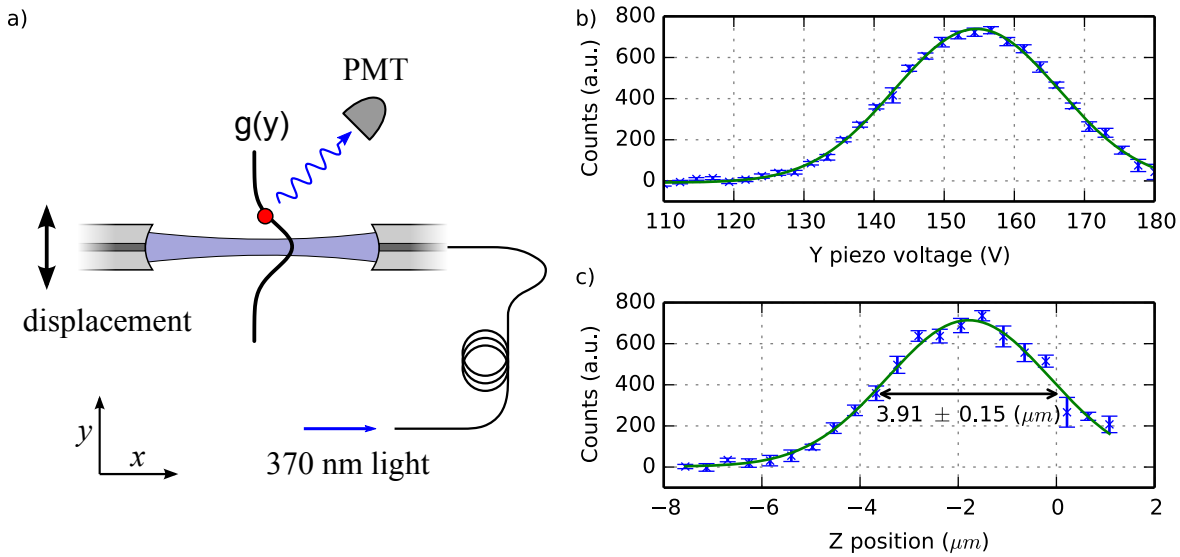

Figure 6.1: Measurement of the transverse cavity mode with the ion. a) Light resonant with the atomic transition is coupled into the cavity, and the strength of the ion excitation is measured via the detected fluorescence rate into free space. b),c) The position of the cavity relative to the ion trap is scanned in the two directions transverse to the cavity axis. Translation along the z axis is performed with the slip-stick stage which has a repeatability of 25 nm. The data are fitted with a Gaussian function, and the error bars are statistical.

The cavity mode propagates as a Gaussian beam, so a single measurement of the waist fully determines the form of the mode. Under the assumption that the mode is radially symmetric, and given the measured cavity length, we can calculate the mode volume of the cavity. The corresponding value of g_0 is $2\pi\times(117\pm9)$ MHz, which becomes $2\pi\times(96\pm7)$ MHz when the Clebsch-Gordan coefficient of $\sqrt{2/3}$ for the σ-transition is taken into account, which is the case for $^{174}Yb^{+}$ when the magnetic field axis is aligned along the cavity axis.

A measurement of the longitudinal structure of the cavity is shown in figure 6.2. The data reveals the expected pattern of the standing wave field, with a visibility of (39 ± 4) %. Under thermal equilibrium the visibility of the standing wave pattern is linked to the spread of the ion's wavefunction b via the relation $V\approx\exp\left[-(2\pi b/\lambda)^2\right]$ [58], which reveals a spread for this measurement of (57 ± 6) nm.

The trap frequency along the cavity direction is approximately 5 MHz, so the ground state spread of the ion is approximately 2.4 nm. The measured spread is significantly larger than

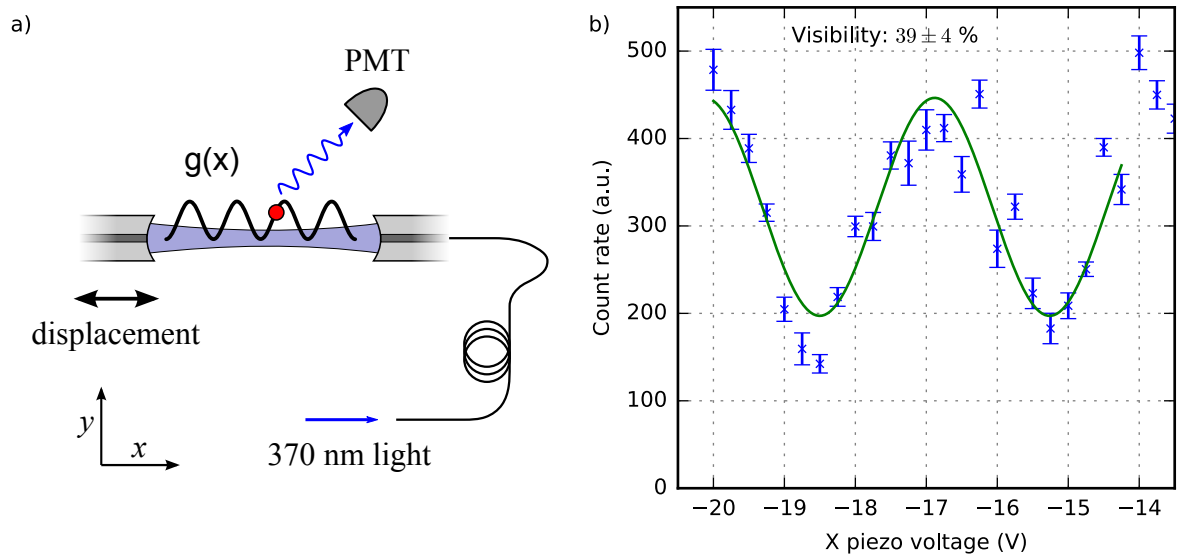

Figure 6.2: Measurement of the longitudinal structure of the cavity mode. The cavity is translated along its axis relative to the ion and the excitation is measured similarly to figure 6.1. The standing wave of the cavity mode is evident, and a sinusoidal fit reveals a visibility of (39 ± 4) %.

expected from Doppler cooling, and is likely caused by excess micromotion along the cavity axis. Repeated measurements of the standing wave pattern have shown that this data is not entirely reproducible, most of the time resulting in almost no visibility. This is most likely caused by our incomplete compensation of stray electric fields along the cavity which comes as a result of only using two beams for measuring the fluorescence modulation described in chapter 3.6.1.

6.2 Photon production

In order to establish the ion-cavity system as a source of single photons, a measurement of the $g^{(2)}(\tau)$ correlation of photons coupled out of the cavity was performed.

The second-order quantum coherence function is defined as [49, p. 114]

$$g^{(2)}(\tau) = \frac{\langle a^\dagger(t)a^\dagger(t+\tau)a(t+\tau)a(t)\rangle}{\langle a^\dagger a\rangle} \tag{6.5}$$

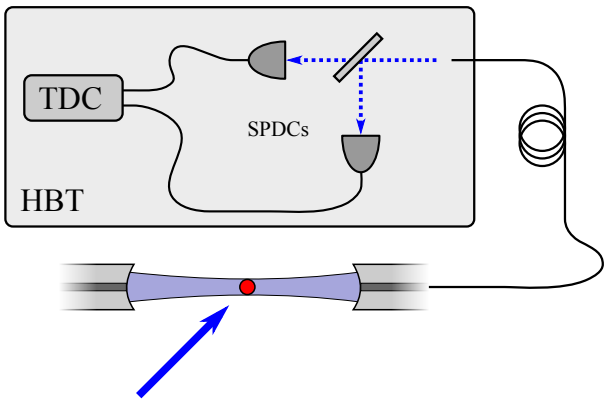

Figure 6.3: Hanbury Brown and Twiss setup used to measure the second order coherence of photons coupled from the ion with the cavity. The ion is excited with a laser near resonant with the ion, and a fraction of the resonance fluorescence from the ion is coupled into the cavity as predicted by the Purcell effect. The arrival of these photons is detected with single photon counting modules (SPCM), and their arrival times are measured using a time to digital converter (TDC).

and represents the joint probability of detecting a photon at time t and $t+\tau$, which was first measured by Hanbury Brown and Twiss [107].

The value of $g^{(2)}(\tau = 0)$ is of great importance as it determines the quantum nature of the light it describes. It is classically forbidden for light to have a value of $g^{(2)}(\tau = 0) < 1$.

The optical setup used to measure the second-order coherence employs the Hanbury Brown and Twiss method, and is shown in figure 6.3. A single $^{174}Yb^{+}$ ion is driven with a laser perpendicular to the cavity axis, which is near resonant with the $^2S_{1/2} \rightarrow {}^2P_{1/2}$ transition. The intensity of the laser field is set such that the saturation parameter of the system without the cavity is $s \approx 14$ and the detuning is set to $\Delta_L = -\Gamma$. The cavity is tuned near resonance with the atomic transition, thereby maximising the resonance fluorescence which is emitted from the ion into the cavity mode. Because the decay rate of the cavity mode is much larger than the coherent coupling ($\kappa > g$), photons inside the cavity are most likely to leave the cavity without further interaction with the ion.

When an atom is driven continuously with a field which resonant with the atomic transition and has Rabi frequency Ω, the second-order coherence of the scattered light is given by [109,

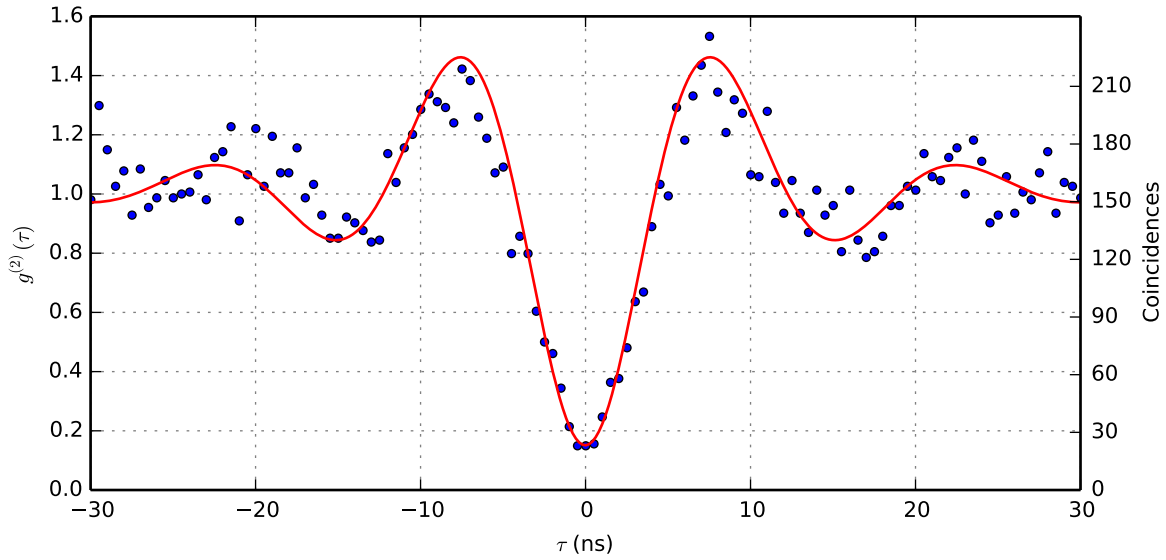

Figure 6.4: Measurement of the second-order quantum coherence of photons produced by the ion inside the cavity. A timing offset of ≈ 20 ns due to mismatched electrical signal pathways was removed. The dataset is fitted with $\Gamma = 2\pi \times 23.6$ MHz, $\Omega = 2\pi \times 62.4$ MHz and $\Delta_L = -\Gamma$ with the formula for $g^{(2)}(\tau)$ for laser with non-zero detuning given in Ref. [108]. During the least-squares fitting procedure, the analytic $g^{(2)}(\tau)$ function is convolved with a Gaussian kernel of FWHM 3.2 ns to take into account photon arrival time jitter due to the detectors. The measured value of $g^{(2)}(\tau = 0)$ is 0.15, limited by arrival time jitter.

p. 358]

$$g^{(2)}(\tau) = 1 - \exp(-3\Gamma\tau/2)\left[\cos(\Omega\tau) + \frac{3\Gamma}{2\Omega}\sin(\Omega\tau)\right]. \tag{6.6}$$

When the atom is driven with a detuned field, the form of the expression becomes more complex, and is given in full in [108].

Figure 6.4 shows the result of a measurement with our setup. A photo-multiplier tube[3] is used as the single photon detector on one arm, and a silicon APD[4] is used on the second arm. The arrival times of the electrical pulses from the single photon detectors are measured with a time-to-digital converter with 25 ps resolution[5]. The measurement shown in figure 6.4 includes a total integration time of 1020 s. After recording the arrival time of all photons during the

[3] H7360-01 from Hamamatsu
[4] Count-Blue from Laser Components
[5] TDC8HP from Roentdek

measurement period, coincidence events were generated in post-processing, allowing for the measurement of positive and negative values of τ.

Firstly, from this dataset we can extract the peak count rates on each arm of the detector. The rates measured with this setup when the cavity was on resonance with the ion were $R_{\text{det}}^{\text{PMT}} = (14.6 \pm 0.1) \times 10^3\ \text{s}^{-1}$ and $R_{\text{det}}^{\text{APD}} = (22.0 \pm 0.1) \times 10^3\ \text{s}^{-1}$. The rates are derived from the mean value of ten 100 ms counting windows, and the quoted errors are the sample standard errors. These numbers are presented in table 6.1. Additionally, the count rates on the detectors when no ion was present in the trap were measured to be $R_{\text{bg}}^{\text{PMT}} \approx 170\,\text{s}^{-1}$ and $R_{\text{bg}}^{\text{APD}} \approx 210\,\text{s}^{-1}$.

The data in 6.4 are presented without any subtraction of background counts. When the data are fitted with the full expression for $g^{(2)}(\tau)$ given in [108], there is an offset of approximately 0.15 at $\tau = 0$. The influence of dark counts on the detectors can be estimated from the fluorescence and background count rates R_{det} and R_{bg} respectively. Given that $R_{\text{bg}} \ll R_{\text{det}}$ probability of measuring a coincidence due to the background is dominated by events which contain one photon from the ion and one from the background. The relative probability of detecting a background-influenced coincidence is given by

$$P = \frac{\mathcal{P}(R_{\text{det}} + R_{\text{bg}}, 2) - \mathcal{P}(R_{\text{det}}, 2)}{\mathcal{P}(R_{\text{det}}, 2)} \approx 2\frac{R_{\text{bg}}}{R_{\text{det}}}, \tag{6.7}$$

where $\mathcal{P}(R,2)$ the Poisson distribution probability of detecting two events from a source with rate R, and we have assumed that the sampling interval is chosen such that $\mathcal{P}(R,1) \ll 1$. From this expression, we expect the value to $g^{(2)}(0)$ to be on the order of 2 %, which is much lower than the measured value.

In order to fully explain the data we need to take into account the finite timing resolution of the detectors which comes as a result of electronic jitter introduced by the pulse discrimination circuitry inside the modules. This jitter was measured independently by detecting the electronic arrival time of photons from 6 ps pulses generated by the laser described in chapter 5.2.2 relative to a reference electronic signal triggered on the laser pulses with approximately 50 ps FWHM jitter. Since the laser pulse is short relative to the time-scales we are interested in, this measurement extracts the impulse response function of the detectors. From these measurements, we find a FWHM jitter of approximately 1.4 ns and 2.9 ns for the PMT and ADP respectively. The curve fitted in figure 6.4 is the convolution of the full $g^{(2)}(\tau)$ formula with a Gaussian kernel of 3.2 ns FHWM which comes from the quadrature sum measured jitter FWHMs. The data fit well to this curve, indicating that the light emitted from the cavity exhibits strong anti-bunching behaviour.

The quantum efficiencies from the specifications of the detectors at 370 nm are $\eta_{\mathrm{PMT}} = 14.1\,\%$[6] and $\eta_{\mathrm{APD}} = 42.0\,\%$. These values were not independently verified and a systematic error could be introduced here. The rates of photons incident on the two detectors can be estimated from these values, and are given in table 6.1. The non-polarising beam splitter used in the HBT setup[7] is specified to have a reflectivity of $(50 \pm 10)\,\%$. The rate of incident photons on each detector, shown in table 6.1, differ by approximately a factor or two, which is greater than the maximum expected from the uncertainty of the beam splitter reflectivity. The diameter of the active area of the APD is 100 µm, whereas the PMT active area is 22 mm. We therefore assume that this discrepancy is caused by sub-optimal focusing of the fibre mode onto the APD. The light which strikes the PMT is collimated with a $1/e^2$ diameter of 2 mm, so all of the light in the PMT arm is accepted by the PMT. The total rate of photons leaving the fibre is estimated from the rate of photons incident on the PMT, and we find a value of $(210 \pm 40) \times 10^3\ \mathrm{s}^{-1}$.

$R_{\mathrm{det}}^{\mathrm{PMT}}$	$(14.6 \pm 0.1) \times 10^3\ \mathrm{s}^{-1}$	Measured rate of detected photons
$R_{\mathrm{det}}^{\mathrm{APD}}$	$(22.0 \pm 0.1) \times 10^3\ \mathrm{s}^{-1}$	
$R_{\mathrm{inc}}^{\mathrm{PMT}}$	$(103.7 \pm 0.9) \times 10^3\ \mathrm{s}^{-1}$	Estimated rate of incident photons
$R_{\mathrm{inc}}^{\mathrm{APD}}$	$(52.5 \pm 0.3) \times 10^3\ \mathrm{s}^{-1}$	
$R_{\mathrm{out}}^{\mathrm{fibre}}$	$(210 \pm 40) \times 10^3\ \mathrm{s}^{-1}$	Estimated rate of photons exiting fibre

Table 6.1: Summary of photon generation rates in the second-order coherence measurement

6.3 Enhancement of excited state decay rate

We first investigate the reduction in the excited state lifetime of the atom which is predicted by the Purcell effect, and described in chapter 2.2.1. We study our system experimentally by exciting the ion with a laser field applied transversely to the cavity. The rate of photons emitted into free space by the ion is measured with our imaging system, which has a net detection efficiency calibrated with measurements similar to those presented in chapter 5.3.

The excited state decay rate given by equation 2.40 is plotted in figure 6.5. When the cavity resonance frequency is tuned far from the atomic frequency, i.e. $\Delta_{\mathrm{C}} \gg \kappa, \Gamma$, the decay rate is

[6] This number is derived from the count sensitivity read from the curve given in the datasheet for the H7360-01 PMT

[7] #48-190 from Edmund Optics

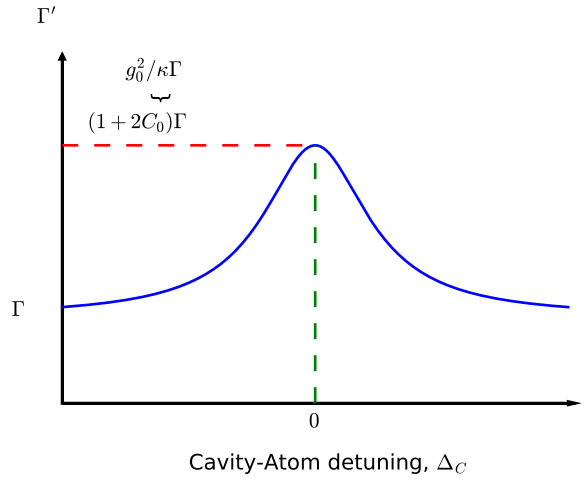

Figure 6.5: Behaviour of the excited state decay rate as a function of cavity-atom detuning.

given by the Γ. Near resonance, the decay rate is enhanced by a Lorentzian factor with a peak value of $(1+2C_0)$ and a FWHM of 2κ.

An intuitive way of measuring the excited state decay rate is to excite the ion with a laser field of constant intensity and observe the change in excited state population which occurs as a result of a varying decay rate. From the steady state solution of a driven two level system in equation 2.22 with $\Delta_L = 0$, we can rewrite the equation to have the total decay rate as the subject

$$\Gamma'(\langle\rho_{ee}\rangle) = \Omega\sqrt{\frac{1-2\langle\rho_{ee}\rangle}{\langle\rho_{ee}\rangle}} \tag{6.8}$$

where Γ' is the total excited state decay rate, written here explicitly as a function of the average excited state population $\langle\rho_{ee}\rangle$, and Ω is the Rabi frequency of the radiation field which does not depend on the cavity detuning since it is proportional to $d_{12}E$. It is possible to experimentally measure $\Gamma\langle\rho_{ee}\rangle$ by measuring the rate of photons incident on the imaging system PMT, since the net detection efficiency is known from calibration.

A measurement of the excited state decay rate using this method is shown in figure 6.6. This measurement was performed by recording the resonance fluorescence rate of the ion exposed to only the external drive laser resonant with the $^2S_{1/2} \rightarrow {}^2P_{1/2}$ transition. In order to maintain stable trapping, it was necessary to regularly cool the ion with a red-detuned laser. The cooling

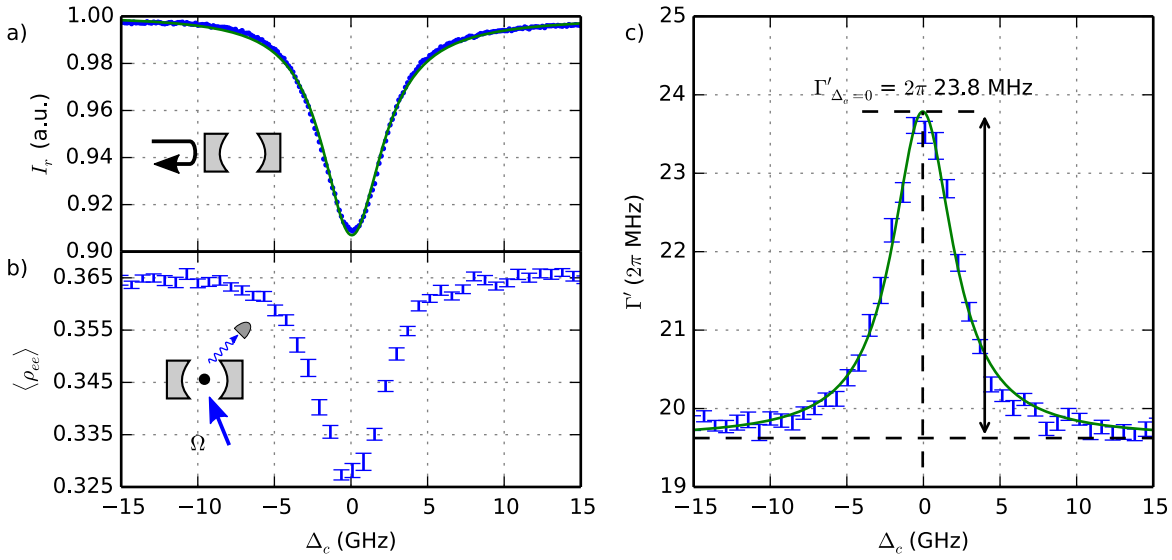

Figure 6.6: Measurement of the excited state decay rate Γ' as a function of cavity-atom detuning Δ_C. a) Reflection signal from the empty cavity used to provide a reference for the cavity detuning. b) Excited state population determined from free space fluorescence rate. c) Excited state decay rate inferred from population using equation 6.8. This measurement was taken with laser saturation parameter $s = 2.75$ with the laser tuned onto resonance with the atomic transition. The error bars in b) and c) represent the statistical errors in the measurement.

and drive lasers were alternated with a 50% duty cycle and period of 40 µs to avoid heating dynamics.

Due to experimental issues with vibration of the cavity, the data for this measurement and those that follow were taken using an averaging technique described in detail appendix C, termed the *scanning cavity lock*. This technique, which also provides a means to stabilise the cavity length over long time-scales, causes the fluorescence rate of the ion to be time correlated with cavity detuning, and thus enables the cavity detuning to be determined accurately during post-processing despite the presence of mechanical vibration which would otherwise disturb such a measurement. The application of this technique here allows the signal-to-noise of measurements to be significantly improved above what could be achieved otherwise, and does not affect the physical interpretation of the following results.

Figure 6.6 a) shows the cavity reflection signal during the measurement which is used for the scanning cavity lock correlation which fits well to the dispersive Lorentzian curve expected

for our fibre-cavity [85]. After the measured fluorescence is time-binned and associated with the cavity reflection signal, the time axis is scaled with the cavity FWHM of (4.78 ± 0.10) GHz which is known from the measurement shown later in figure D.1. The excited state population was then determined by dividing the average resonance fluorescence rate by the absolute detection efficiency of the imaging system, and is shown in figure 6.6 b). The data in c) are calculated via equation 6.8 from the measured excited state population, and are fitted with a Lorentzian curve. The FWHM derived from the fit is (4.8 ± 0.2) GHz which agrees with the value expected from the cavity linewidth.

Although this approach is intuitive, it is not quantitatively correct as it does not take into account the complete action of the drive laser on the system. Specifically, it ignores the effect of the cavity field which builds up as a result of photon emission into the cavity mode. A proper analysis of the problem requires the addition of the transverse field terms into the Jaynes-Cummings Hamiltonian which is introduced in chapter 2.2.2.

In order to provide a fairer measure for the excited state decay rate, we consider the properties of the system as the laser frequency is changed. To do this, we monitor the drop of the fluorescence rate of the ion collected through the imaging system as we change the laser-atom detuning Δ_L while keeping the cavity resonant with the atomic transition ($\Delta_C = 0$). In the absence of the cavity, fluorescence is emitted uniformly into free-space by $^{174}Yb^+$ under excitation with linearly polarised light. The fluorescence rate detected over the solid angle subtended by the imaging system is therefore proportional to the total rate emitted by the ion into free-space. We then normalise this rate to the case without the cavity $R_{4\pi}^{(0)}$.

The data for this measurement is shown in figure 6.7. Due to the presence of mechanical vibrations in the cavity mounting structure, it was not possible to hold the cavity at a fixed detuning relative to the atom transition during the measurement. Instead, each data point is generated from a measurement similar to that shown in figure 6.6, where the cavity-atom detuning is scanned with the laser at a fixed detuning. In order to find the value of $R_{4\pi\text{-c}}$, the measured data is interpolated by taking a weighted average of the two bins with cavity-atom detuning nearest to zero. This value is normalised by the rate of fluorescence when the cavity is far off-resonance which is equal to $R_{4\pi}^{(0)}$ to a good approximation because the solid angle of the cavity is small.

Repeated measurement of the interpolated value of $R_{4\pi\text{-c}}$ produced values consistent with the statistical errors within the range $-38 \geq \Delta_L/2\pi \geq 0$ MHz. However, outside of this range, the interpolated values varied by significantly above their expected statistical errors, indicative of systematic error, and are therefore excluded from the Lorentzian fit to the data in figure 6.7.

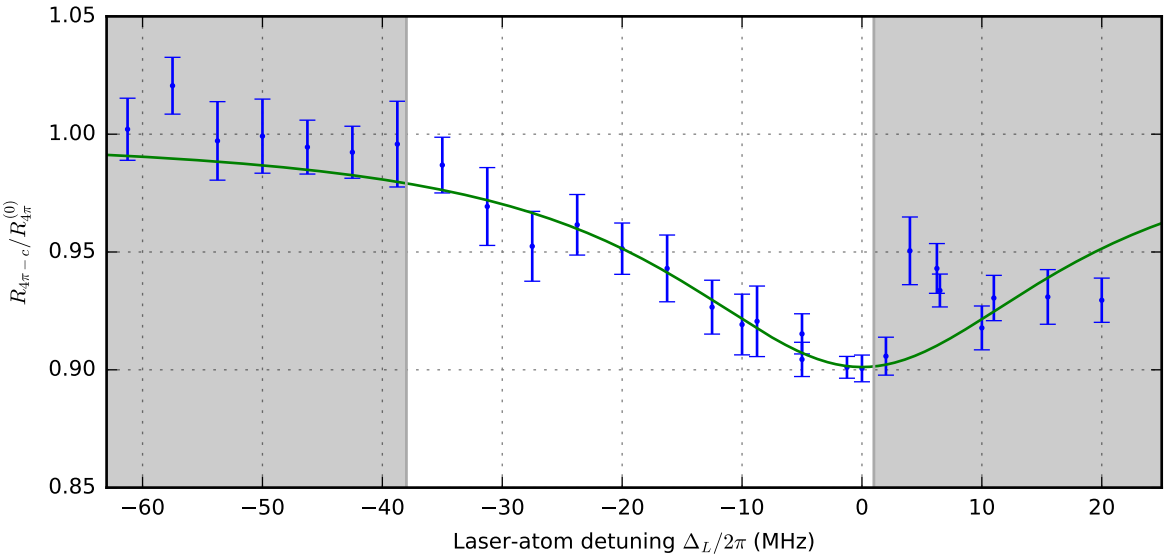

Figure 6.7: Measurement of the free-space scattering rate ($R_{4\pi\text{-c}}$) against the laser-atom detuning. Each data point is interpolated from a measurement of the excited state population as a function of cavity detuning, similar to the measurement shown in figure 6.6. The interpolation is explained in more detail in the text. The data points are fitted with a Lorentzian curve within the range $-38 \geq \Delta_L/2\pi \geq 0$ MHz, resulting in a FWHM of (39 ± 4) MHz. The data points within the two grey regions are excluded from the fit for reasons explained in the text.

Under the approximation that the laser-atom detuning is small relative to Γ, the analytical solution of the master equation for this system predicts that this curve is Lorentzian in form and has a FWHM determined by

$$W^2 = \Gamma^2 \left[(1+2C_0)^2 + s\right] = \Gamma'^2 + s\Gamma^2, \tag{6.9}$$

where s is the saturation parameter of the ion for the given laser power without the presence of the cavity. From the fit to the experimental data, we calculate the value of $\Gamma'/2\pi$ to be (22 ± 8) MHz from which we find $C_0 = 0.06 \pm 0.02$. This value differs from the expected value of 0.20 ± 0.03 which is inferred from the measured value of κ and the value of g_0 estimated from the mode waist in section 6.1. The difference is suspected to be caused by imperfect localisation of the ion wave-packet due to excess micromotion, which can lead to a reduction in the effective atom-cavity coupling by up to a factor two, leading to a factor of four reduction in the value of C_0.

6.4 Interference between driving and cavity back-action fields

In this section we investigate the question of how to measure the cavity-QED parameters of a continuously driven system.

During the measurements taken in the previous section to determine the excited state decay rate, we have observed changes in the fluorescence rate of the ion into free-space under continuous drive due to the effect of the cavity on the atomic system. When the laser-atom detuning is non-zero, we observe changes in the total fluorescence rate of the system. In this section we investigate this effect and determine that it is due to interference between the cavity field and the driving laser.

When the ion-cavity system is driven from the side with a near-resonant laser, a fraction of the light field generated by the atom is stored in the cavity which acts back on the emitter. The ion responds to the drive laser according to its electric polarisability $\alpha(\omega_{\mathrm{L}})$ and scatters an electric field both into the cavity mode and into vacuum which is $\propto \alpha(\omega_{\mathrm{L}})E_{\mathrm{d}}$ where E_{d} is the amplitude of the driving field. The component of the electric field scattered into the cavity mode is reflected from the mirrors with a certain amplitude and leads to an additional field at the ion. The intracavity field E_{c} and the driving field E_{d} interfere with each other at the location of the ion leading to a modification of the excitation rate of the ion. In an extreme case, it has been theoretically pointed out that the resonance fluorescence of an emitter inside a lossless cavity is completely suppressed by this effect [110], due to fully destructive interference between the cavity and driving fields. In general, the argument used by Purcell regarding the ratio between emission rates into the cavity mode and free-space remains quantitatively valid, however, depending on the degree of the back-action of the cavity field on the ion, the total emission rate of the system $R_{\mathrm{c}}+R_{4\pi\text{-c}}$ can be enhanced or suppressed relative to the case without the cavity $R_{4\pi}^{(0)}$, an effect which has not yet been experimentally observed.

In the weakly driven case, the effect of the cavity back-action can be calculated analytically [111]. The intracavity field which is generated has the same frequency as the driving field, but with a phase offset which is determined by $\Delta_{\mathrm{A}}^{(\mathrm{L})}$ and $\Delta_{\mathrm{C}}^{(\mathrm{L})}$ which are the detunings of the atom and cavity relative to the drive laser. The detuning $\Delta_{\mathrm{A}}^{(\mathrm{L})}$ controls the relative phase between the driving field and the field radiated by the atomic dipole, while $\Delta_{\mathrm{C}}^{(\mathrm{L})}$ controls the phase accumulated in the round trip through the cavity. When both detunings are small, i.e. $\Delta_{\mathrm{A}}^{(\mathrm{L})} \ll \Gamma, \Delta_{\mathrm{C}}^{(\mathrm{L})} \ll \kappa$, and for weak cooperativity $C_0 < 1$, the intracavity field can be approximated by

$$\frac{E_{\mathrm{c}}}{E_{\mathrm{d}}} \approx -C_0 \frac{\Gamma^2}{\Gamma^2 + \Delta_{\mathrm{A}}^{(\mathrm{L})2}} \exp\left(i \left[\frac{\Delta_{\mathrm{C}}^{(\mathrm{L})}}{\kappa} - \frac{\Delta_{\mathrm{A}}^{(\mathrm{L})}}{\Gamma} \right] \right). \tag{6.10}$$

Here, the exponential factor determines the nature of the interference caused by the back-action from the cavity, with the phase determined by the phase shift of a photon in a detuned resonator of width κ and the photon emitted from a driven dipole. When these two phase shifts cancel, the intracavity electric field is π out of phase with the drive laser field leading to a reduction in the excitation of the ion due to the destructive interference. However, the destructive interference is only partial since the amplitude of the intracavity field is diminished by the Lorentzian prefactor with detuning $\Delta_{\mathrm{A}}^{(\mathrm{L})}$. With this in mind, our setup allows for the independent tuning of the phase and amplitude of the back-action of the cavity environment onto the ion. The argument given here is valid for all detunings, and constructive (+) and destructive (-) interference occur for

$$\frac{\Delta_{C,\pm}^{(\mathrm{L})}}{\kappa} = \frac{\Gamma(C_0+1) \pm \sqrt{4{\Delta_{\mathrm{A}}^{(\mathrm{L})}}^2 + \Gamma^2(C_0+1)^2}}{2\Delta_{\mathrm{A}}^{(\mathrm{L})}}. \tag{6.11}$$

It is interesting to note that the physics described by our classical description based on atomic polarisability is closely related to recent work with neutral atoms in a highly dissipative cavity [112]. There, a formal mapping of the system onto electromagnetically-induced transparency is presented, however our classical model is sufficient to quantitatively explain the effects for low atomic excitation. Only when considering large excitation intensities is a fully quantum mechanical description required, which can be obtained through the solution of the master equation for the driven Jaynes-Cummings model introduced in chapter 2.2.2.

We begin analysis of the experimental data by looking at the effects of the back-action on the excited state population at non-zero laser-atom detuning. For excitation which results in a low average occupancy of the cavity ($\bar{n} \ll 1$), the analytical solution of the excited state population in the steady state is given by

$$\langle \rho_{ee} \rangle = \frac{1}{2}\left[1 - \frac{1}{1+\Omega^2\left(\frac{\kappa^2+{\Delta_{\mathrm{C}}^{(\mathrm{L})}}^2}{(-\Delta_{\mathrm{C}}^{(\mathrm{L})}\Gamma/2+\Delta_{\mathrm{A}}^{(\mathrm{L})}\kappa)^2+(g^2+\Delta_{\mathrm{A}}^{(\mathrm{L})}\Delta_{\mathrm{C}}^{(\mathrm{L})}+\kappa\Gamma)^2}\right)}\right] \tag{6.12}$$

where the two detunings defined relative to the laser, and Ω is the Rabi frequency of the driving laser field in the absence of the cavity. The approximation used for low cavity occupancy is valid in all of the following analysis, and hence the analytical solution has been used. Figure 6.8 shows the measured excited state population of the ion while the cavity is scanned, with the drive laser tuned to a) $\Delta_{\mathrm{A}}^{(\mathrm{L})} = -\Gamma/2$ and b) $\Delta_{\mathrm{A}}^{(\mathrm{L})} = +\Gamma/2$. Both graphs are fit well to the theoretical model, with the maximum and minimum of the excited state population visible at cavity detunings of $\Delta_{\mathrm{C},+}^{(\mathrm{L})}$ and $\Delta_{\mathrm{C},-}^{(\mathrm{L})}$ respectively.

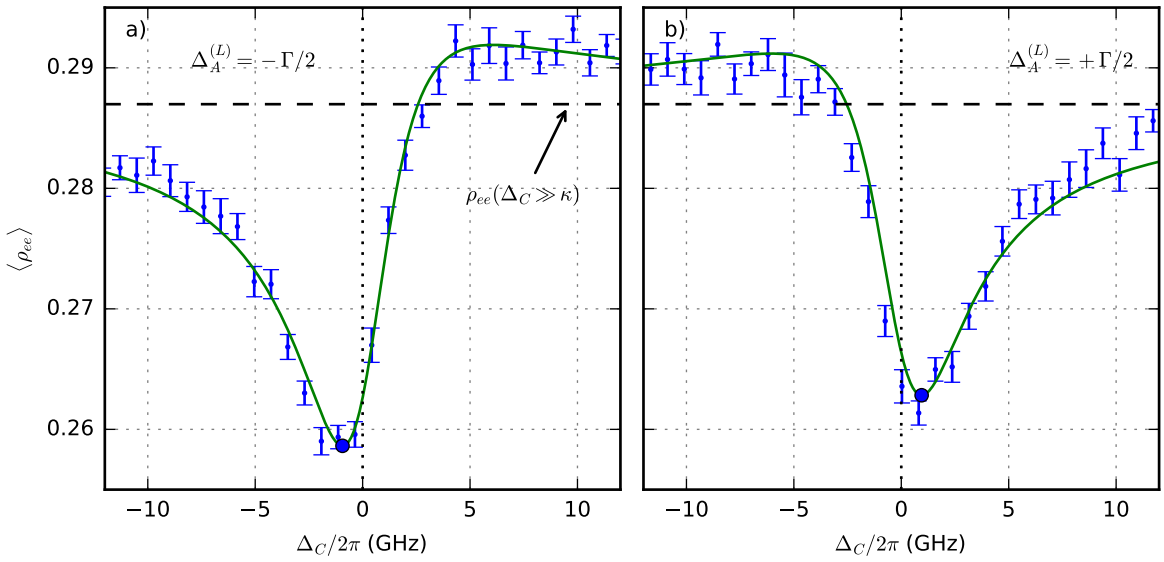

Figure 6.8: Measurement of the excited state population vs cavity detuning for non-zero laser detuning. Both measurements were taken with saturation parameter 2.75. a) $\Delta_L = -\Gamma/2$. b) $\Delta_L = \Gamma/2$. The green curves are fits to the experimental data using the analytical formula given in equation 6.12, with the cavity-atom coupling g as the only free parameter. The remaining parameters are fixed to values determined through independent measurements, including an absolute photon detection efficiency of the imaging system. The horizontal dashed line shows the value of $\langle \rho_{ee} \rangle$ derived from the mean of the data where the cavity is far detuned (not plotted).

Since all the parameters in equation 6.12 are known except for g, we can use fits to our experimental data to determine the atom-cavity coupling rate. A large dataset was taken at several values of the laser-atom detuning and fitted with the theoretical curve. The fitted values of g are given in figure 6.9. From this dataset, we extract an average value of $g/2\pi$ of (67 ± 2) MHz, determined by taking the mean of the fitted parameters within the range where the experimental data fit well to equation 6.12. The data taken with positive Δ_L qualitatively fit our model, but the g parameter exhibits a variance which is likely due to Doppler heating from the drive laser.

So far we have shown that the excited state population under continuous excitation is modified by the presence of the cavity. In order to demonstrate enhancement and suppression of the total emission rate of the ion, it is necessary to measure the rate of photon emission out of the cavity R_c in addition to the rate of emission into free-space $R_{4\pi\text{-}c}$ which we have used to

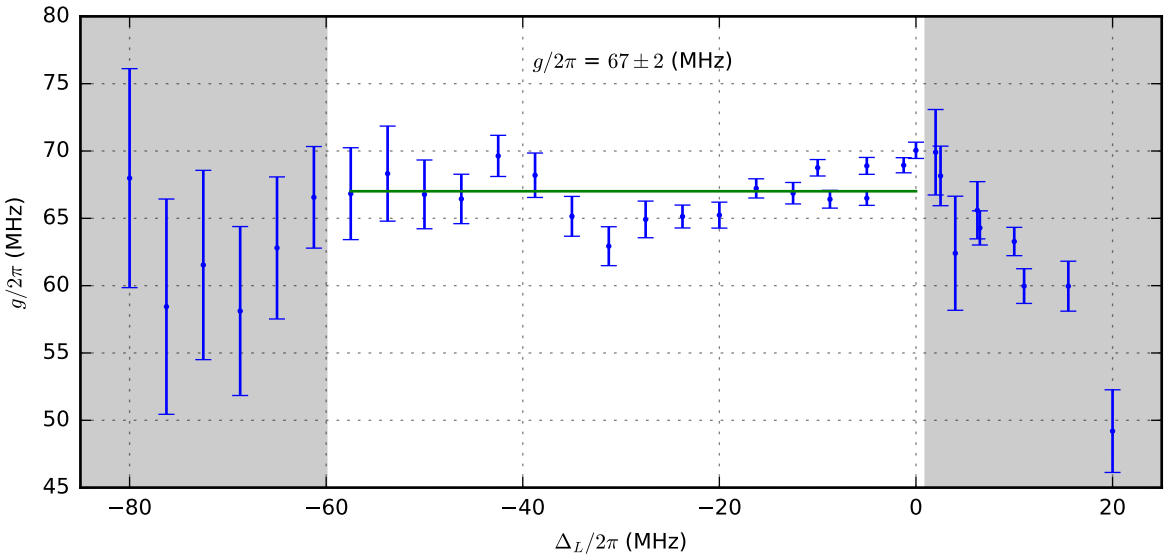

Figure 6.9: Fitted values for atom-cavity coupling parameter, g, for a range of laser-atom detunings, Δ_L. The error bars indicate the standard error of the fit. We expect g to be independent of Δ_L. This data shows some non-statistical variation of the value of g which is indicative of systematic error. The line shows the mean value of g within the range $-60 \leq \Delta_L/2\pi \leq 0$ MHz. The lower frequency limit to this range is chosen since the non-linear fits of equation 6.12 do not fit the data well at large negative detunings because of the reduced photon scattering rate. The upper frequency limit was chosen to be the point where the laser is resonant with the ion, since when the $\Delta_L > 0$ the laser heats the ion causing a modified response which is not included in the model. Since the values of g vary by more than the statistical error bars, even within the range where the measurement performs well, the RMS value of standard error (0.4 MHz) is likely to be an underestimate of the true uncertainty. Instead, the uncertainty quoted is the standard deviation of the fitted values of g, resulting in $g/2\pi = (67 \pm 2)$ MHz.

infer the excited state population. To do this, we measure the average rate of photons leaking out of the cavity on the same PMT which is used to derive the scanning cavity locking signal. The light used to generate the locking signal is gated off when the ion is probed with the drive laser. The rate of photon emission from the cavity can be estimated from the measured rate via the relation $R_c^{meas} = \eta_{net} R_c$, where η_{net} is the net losses in the detection system. The losses which contribute are the out-coupling efficiency of the cavity mirror ($\eta_c = 3.33 \pm 0.4\%$)[8], the

[8]This was determined by the linewidth measurement in appendix D and the specified coating transmission

mode-matching losses between the mirror and the fibre ($\eta_{\mathrm{mm}} = 0.45 \pm 0.06$), the polarising beam splitter in the analysis setup ($\eta_{\mathrm{bs}} = 0.50$)[9], and the specified quantum efficiency of the detector ($\eta_{\mathrm{qe}} = 0.14\%$). From the known losses, we estimate $\eta_{\mathrm{net}} = (1.1 \pm 0.2) \times 10^{-3}$.

The emission rates, measured for $s = 2.75$ and $\Delta_{\mathrm{A}}^{(\mathrm{L})} = -\Gamma/2$, for free-space and into the cavity are shown in figure 6.10 b) and c) respectively, where they have been normalised to $R_{4\pi}^{(0)}$. The cavity emission rate is approximately given by a Lorentzian curve with its centre given by $C_0\kappa \approx 200\,\mathrm{MHz}$. The height of the normalised curve, is given by $2C_0/\left(1+2C_0+2C_0^2\right)$. Figure 6.10 d) is the sum of the two rates, which shows both the enhancement and suppression of the total emission rate due to the back-action of the cavity field, depending on the cavity detuning $\Delta_{\mathrm{C}}^{(\mathrm{L})}$. The solid lines in b), c) and d) are the steady-state solution of the master equation in Lindblad form for the driven Jaynes-Cummings Hamiltonian (equation 2.49) given the measured parameters of the system[10]. An additional loss term in the cavity emission detection efficiency (η_{net}) of 90 % was included as a free parameter, which is in agreement with the expected transmission of the fibre.

In order to highlight the sensitivity of the cavity-induced back-action to the relative phases between the drive laser, the atomic dipole and the cavity field, we have extracted the positions of the local minima $\Delta_{\mathrm{C},-}^{(\mathrm{L})}$ of the emission rate into free-space which was measured in the dataset for figure 6.9. The result of this analysis is given in figure 6.11, and the data agree with the detunings for destructive interference predicted by equation 6.11. This supports our interpretation that the observed effects occur as a result of interference due to cavity back-action. Due to the shallower curvature near the maxima, we have not been able to infer $\Delta_{\mathrm{C},+}^{(\mathrm{L})}$ from our data. For small values of $\Delta_{\mathrm{C}}^{(\mathrm{L})}$, the curve has a linear dependence $\Delta_{\mathrm{C},-}^{(\mathrm{L})} \approx -\Delta_{\mathrm{A}}^{(\mathrm{L})}\kappa/[\Gamma(1+2C_0)]$, denoted by the dashed line in figure 6.11. This relation may prove useful in future experiments in the fast-cavity regime, as it allows for accurate measurement of the cooperativity since its experimental signature is enhanced by a factor of $\approx \kappa/\Gamma$ which is necessarily large. It is interesting to note that even though the average occupation of the cavity mode is only $\bar{n} \approx 2C_0\Gamma/\kappa \approx 10^{-3}$, this still leads to a measurable back-action since the effect is based on the interference of the electric field amplitudes, and so is proportional to $\sqrt{\bar{n}} \approx 5\%$.

[9] Since on average photon emission from $^{174}\mathrm{Yb}^{+}$ into the cavity occurs at equal rates for $\sigma+$ and $\sigma-$, the polarising beam splitter reduces the rate by a factor of two regardless of its orientation

[10] The parameters used are $(g,\kappa,\Gamma)/2\pi = (67, 2400, 19.6)$MHz, with saturation parameter $s = 2.75$, and including fibre transmission loss of 10 %.

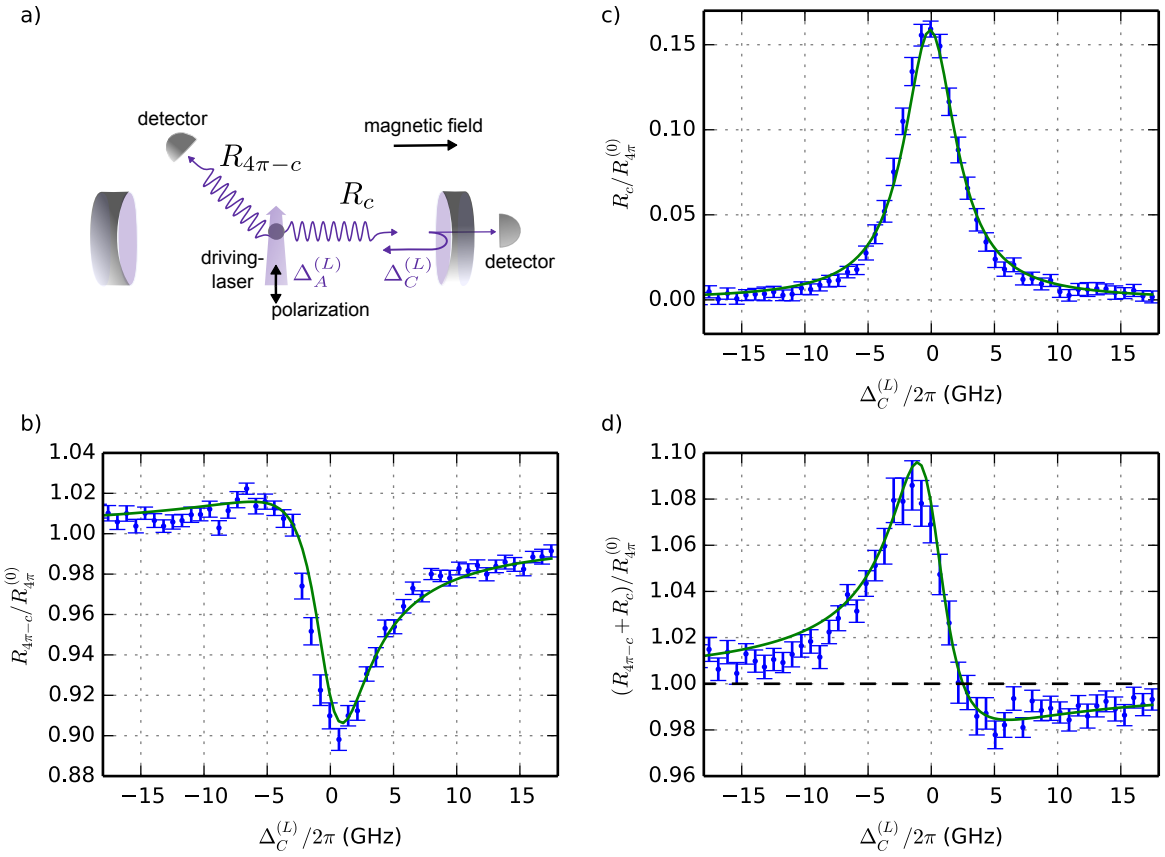

Figure 6.10: Measurement of the total photon emission rate from the ion-cavity system under continuous drive. a) Photon emission from the system is monitored via two detectors, providing measurement of R_{c} and $R_{4\pi\text{-c}}$. b) Emission rate into free-space normalised to the emission rate of the system without the cavity ($R_{4\pi}^{(0)}$). c) Normalised emission rate out of the cavity. c) Total emission rate of the ion-cavity system. The cavity-induced back-action causes the total emission rate to both increase and decrease as compared with the system without cavity.

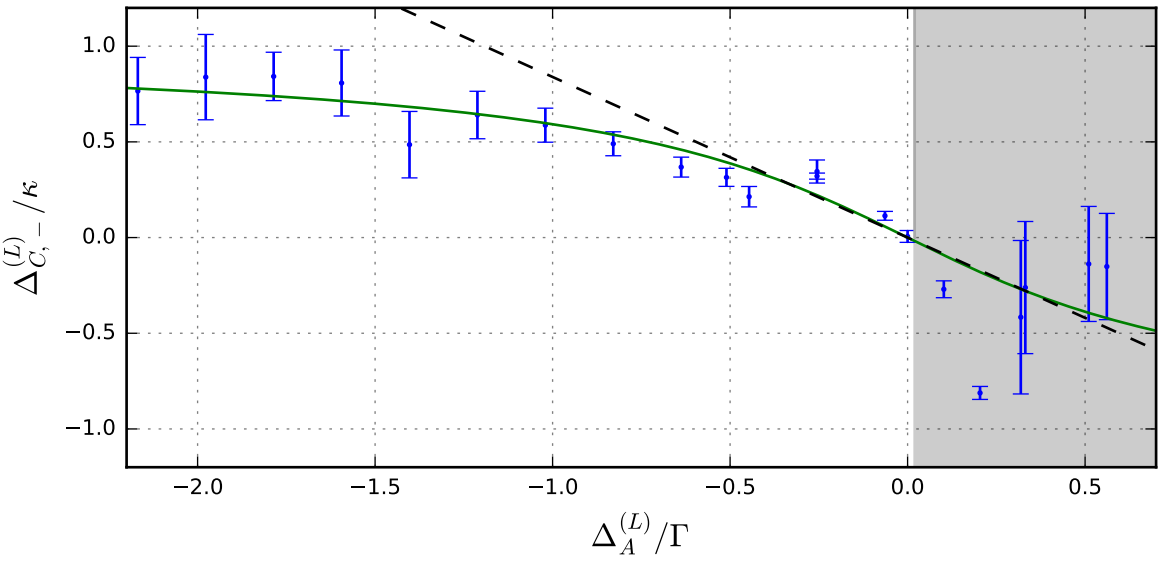

Figure 6.11: Measured values of the cavity detuning for maximal destructive interference $\Delta_{\mathrm{C},-}^{(\mathrm{L})}$ for several values of the laser-atom detuning $\Delta_{\mathrm{A}}^{(\mathrm{L})}$. The solid curve represents the values expected from the interference model, and the dashed line shows the linear dependence near $\Delta_{\mathrm{A}}^{(\mathrm{L})} = 0$. Data points within the grey region represent measurements where the laser was blue-detuned from the atomic transition, and are therefore subject to Doppler heating during the experiment. Although the data points in this region qualitatively agree with the interference model, the value of the points exhibits a non-statistical spread which is thought to occur due to presence of Doppler heating.

6.5 Summary of results

This section provides a summary of the results of the measured cavity parameters along with the design parameters. In order to clarify the effect that the increase in the coating losses after exposure to UHV has caused, we use the experimentally measured g to infer the parameters that the system would have had with a) the coating design without losses and b) the coating with the losses before being placed in UHV.

For the three cases considered, the absorption and scattering losses of the mirrors are calculated from the measured finesse, given the specified mirror coating transmission (1000 ppm). Using the calculated losses, the single mirror out-coupling efficiency is estimated using equation 4.13, which gives the fraction of photons in the cavity mode which are transmitted through one of the mirrors. The cooperativity of the resulting ion-cavity system is then calculated using the formula $C_0 = g^2/\kappa\Gamma$ using the value of g measured in section 6.4. The probability of photon emission into the cavity mode is given by $P_\mathrm{e} = 2C_0/(2C_0+1)$, and the net probability of a single decay of the atom leaving the system after being coupled into the fibre is given by $P_\mathrm{out} = \eta_\mathrm{mm}\eta_\mathrm{c}P_\mathrm{e}$ where η_mm is the fibre-cavity mode-matching measured in chapter 4.4 to be (45 ± 6) %. The values are summarised in table 6.2.

Parameters	a) Design	b) Real, air	c) Real, UHV	
$\mathcal{F}$	3100	1140(40)	209(8)	Cavity finesse
$T+L$, ppm	1000	2750(90)	15000(600)	Total single mirror losses
$\kappa/2\pi$, MHz	160	438(3)	2390(50)	Field decay rate
η_c	50%	18(2) %	3.3(4)%	Cavity out-coupling efficiency
C_0	≈ 1.44	≈ 0.52	$9.6(2)\times 10^{-2}$	Cooperativity
P_e	$\approx 74\%$	$\approx 51\%$	16.1(3)%	P of emission into cavity
P_{out}	$\approx 17\%$	$\approx 4.2\%$	0.7(3)%	P of emission out of fibre

Table 6.2: Summary of the parameters of the atom-cavity system which are relevant for photon generation. The three systems considered are a) the cavity with the designed coating parameters, b) with the measured coating parameters in air, and c) the measured parameters after six months under UHV. The errors given are statistical and come from the combined measurement uncertainties, including the atom-cavity coupling ($g = 67(2)$ MHz) and the cavity-fibre mode-matching coefficient ($\varepsilon_{mm} = 45(6)\%$).

Chapter 7

Qubit coherent control

In order to establish the ion-cavity system as capable of producing atom-photon entangled states, it is necessary to have quantum control of the state of the ion. Firstly, the ground state hyperfine qubit in $^{171}Yb^{+}$ which will be used for this purpose is introduced, and the quantum state initialisation and readout procedures are described. Control of the local magnetic field is essential when working with atomic qubits, so detection and compensation of the static magnetic field is demonstrated using a Ramsey interference measurement scheme. In order to generate photons at a high rate and with well-defined temporal shape, we demonstrate ultrafast Rabi oscillations using picosecond light pulses and show that we can excite the atomic population with near-unit probability. Finally, the planned scheme for generation and measurement of atom-photon entangled states is described, and estimates of the entanglement rate are given based on the known cavity parameters.

7.1 Hyperfine qubit

Ytterbium-171 has nuclear spin 1/2 which makes it an ideal candidate for quantum communication protocols making use of polarisation qubits. This is due both to the strong and symmetric Clebsch-Gordan coefficients from the excited state, and to the low number of extra states which can be populated. The hyperfine structure in $^{171}Yb^{+}$ is shown in figure 7.1.

Doppler cooling of this isotope is performed on the $^{2}S_{1/2}|F=1\rangle \rightarrow {}^{2}P_{1/2}|F=0\rangle$ transition. The decay of population from the $^{2}P_{1/2}|F=0\rangle$ into the $^{2}S_{1/2}|F=0\rangle$ ground state is forbidden by the dipole selection rules, however, during Doppler cooling population is transferred into this state via off-resonant coupling of the cooling laser to the $^{2}P_{1/2}|F=1\rangle$ state.

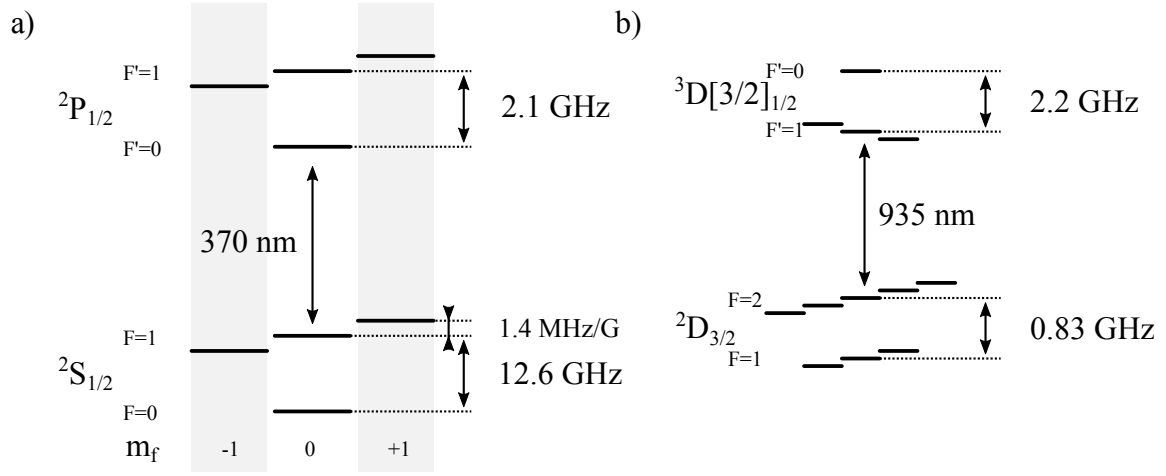

Figure 7.1: Hyperfine structure in $^{171}Yb^+$. Approximate splitting frequencies are from Ref. [21].

In order maintain a closed cooling cycle, microwaves near 12.6 GHz are applied to the trap to transfer population between the $|F=0\rangle$ and $|F=1\rangle$ states.

From the excited $^2P_{1/2}|F=0\rangle$ state, there are dipole allowed decays into the $^2D_{3/2}|F=1\rangle$ manifold with some 0.05 % branching ratio. Population trapped in this state is cleared out by a laser operating on the $^2D_{3/2}|F=1\rangle \rightarrow {}^3D[3/2]_{1/2}|F=0\rangle$ transition near 935 nm. This upper state is chosen rather than the $^3D[3/2]_{1/2}|F=1\rangle$ state, because decay from $^3D[3/2]_{1/2}|F=0\rangle$ into the $^2S_{1/2}|F=0\rangle$ state is forbidden. Very occasionally (on the order of once every 10 ms with standard operating parameters), population becomes trapped in the $^2D_{3/2}|F=2\rangle$ state due to off-resonant scattering of the Doppler cooling laser from the $^2P_{1/2}|F=1\rangle$ state. In order to clear out this population, weak side-bands are modulated onto the 935 nm laser with an EOM at 3.07 GHz so that the -1st order will drive the $^2D_{3/2}|F=2\rangle \rightarrow {}^3D[3/2]_{1/2}|F=1\rangle$ transition.

During Doppler cooling a sizeable fraction of the population becomes trapped in a coherent dark state within the $^2S_{1/2}|F=1\rangle$ manifold. This is a natural result of the fact that the transition has a higher degeneracy in the lower states than the higher state. This effect is well understood and a practical overview of it is presented in [113]. The formation of the coherent dark state occurs for all polarisations of the Doppler cooling beam, however it can be minimised by using linearly polarised light at an angle of 57.5° relative to the quantisation axis [114]. The occupation of the dark state is also dependent on the Zeeman splitting of the lower states, and is reduced by applying stronger magnetic fields. In our case, we apply a field of approximately

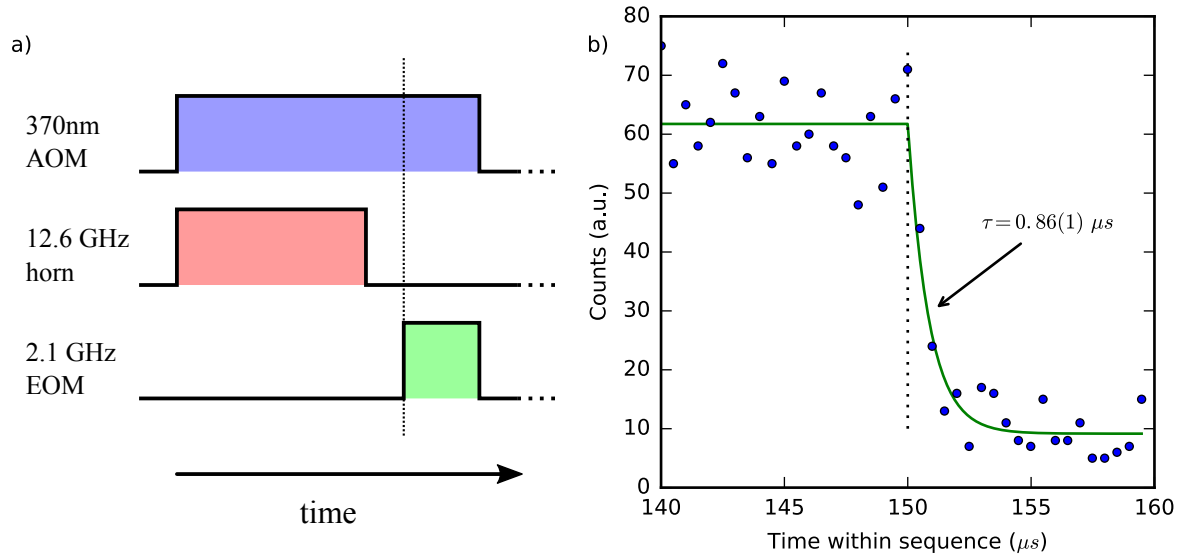

Figure 7.2: a) Pulse sequence used for initialisation into $^2S_{1/2}|F=0,0\rangle$. b) Measurement of optical pumping rate.

5 G which produces a splitting of ≈ 7 MHz.

7.2 State initialisation, manipulation and readout

In this section the techniques used for initialisation, coherent manipulation and readout of the quantum state of the ion are described. State initialisation is performed by optically pumping population into the $^2S_{1/2}|F=0,0\rangle$ state with light resonant with the $^2S_{1/2}|F=1\rangle \rightarrow {}^2P_{1/2}|F=1\rangle$ transition. This light is generated by modulating optical side-bands onto the Doppler cooling laser using a 2.1 GHz resonant EOM.

Figure 7.2 shows a measurement determining the optical pumping rate in the $^2S_{1/2}|F=0,0\rangle$ state which is used for initialisation. During the optical pumping procedure, there is very little leakage of population out of the target $^2S_{1/2}|F=0,0\rangle$ state because the pumping laser is far detuned ($\approx$12.6 GHz) from the only allowed dipole transition out of this state (to $^2P_{1/2}|F=1\rangle$). This means that high fidelity state initialisation can be performed in a short time. In figure 7.2 b), we measure the decay time into the ground state to be (0.86 ± 0.01) µs for our standard laser parameters ($s=1$ with the EOM operating with a modulation depth of approximately 1). In order to achieve an error of less than 0.1 %, we therefore require only 4 µs of pumping. After

applying the pumping laser for 10 µs, we expect the initialisation error to be $< 1 \times 10^{-4}$.

Coherent manipulation of population within the ground state can be performed either through directly driving magnetic dipole transitions between the levels in the ground state using microwaves near 12.6 GHz, or by driving stimulated Raman transitions using optical frequencies. For the measurements performed in this chapter we have performed these operations with microwaves, however after integrating the fibre cavity into the trap we found that the microwave transition could not be driven without strong ohmic heating of the cavity. As the cavity structure may permanently misalign from being heated, it was decided that a laser system should be developed to drive stimulated Raman transitions. This is discussed further in section 7.5.

In order to directly drive the magnetic dipole transitions, we have used a microwave horn[1] which provides 10 dB of directional gain. The horn driven by up to 10 W of microwave power, and is directed through the front window of the vacuum chamber in such a way that couples to both σ and π transitions. The microwave signal is generated by mixing an rf signal near 200 MHz generated by a DDS with a signal near 12.4 GHz generated by a microwave synthesiser. Both synthesisers are locked to our 10 MHz reference clock. In this way, control of the precise frequency, phase and amplitude of the microwave tone is achieved through control of the rf DDS.

Readout of the quantum state has been implemented based on the scheme described in [115]. During the readout process, a laser pulse is applied to the ion which is near resonant with the $^2\mathrm{S}_{1/2}|F=1\rangle \rightarrow {}^2\mathrm{P}_{1/2}|F=0\rangle$ transition, which is the same as used for Doppler cooling. In this way, population in the $^2\mathrm{S}_{1/2}|F=1\rangle$ states will be driven by the laser and produce resonance fluorescence, whereas any population in the $^2\mathrm{S}_{1/2}|F=0\rangle$ state will remain dark. The fluorescence photons are detected with a photomultiplier tube and when the number of photons detected during the readout period is greater than a predetermined threshold the ion is said to be in the bright state, otherwise is it in the dark state.

The fidelity of a readout process is a measure of how accurately the result of the measurement reflects the true state of the ion. It is normally defined as $1-\varepsilon$ where $\varepsilon = 1/2(\varepsilon_\mathrm{B} + \varepsilon_\mathrm{D})$ is the average readout error [116]. ε_B is the fraction of experiments where the ion prepared in the bright state was detected to be in the dark state, and ε_D is similarly defined. Preparation in the dark state is achieved through the optical pumping procedure described earlier, and preparation in the bright state is performed by applying a resonant microwave π pulse to the dark state. The error of these processes are both expected to be $< 1 \times 10^{-4}$.

A detailed analysis of the error sources in the $^{171}\mathrm{Yb}^+$ readout process is described in [117].

[1] 'HD18572' from HDCom

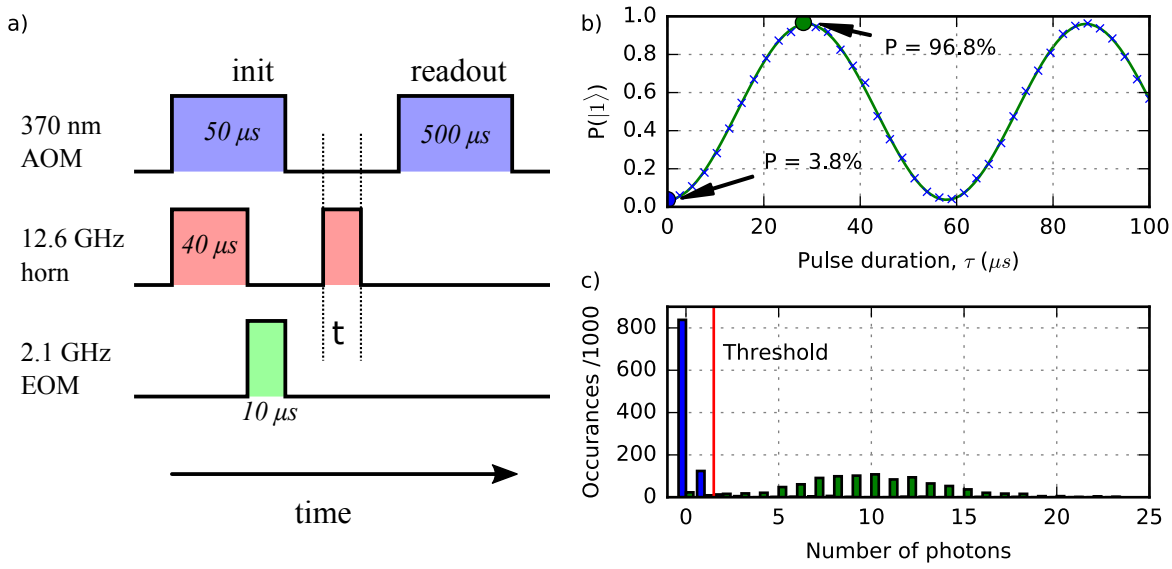

Figure 7.3: Rabi oscillations driven by microwave pulses near 12.6 GHz used to characterise and optimise the quantum state detection. a) Experimental pulse sequence used to observe Rabi oscillations. b) Measured average population in the 'bright' $|1\rangle$ state as the microwave pulse length is varied. Each data point represents an average of 1000 measurement of the ion state. c) Histogram of number of photons detected per measurement for no microwave pulse (blue) and a 29 μs microwave pulse (green), indicating the points of lowest and highest 'bright' detection probability on b) respectively. The red line shows the photon counting threshold used to distinguish between bright and dark measurements ($n > 1 \rightarrow$'bright').

When well optimised, the dominant source of bright state error is off-resonant scattering of the readout laser from the $^2P_{1/2}|F=1\rangle$ levels (Δ =2.1 GHz) into the dark state. The dark state error process is off-resonant scattering from $^2S_{1/2}|F=0\rangle$ to $^2P_{1/2}|F=1\rangle$ which is 14.7 GHz detuned from the readout laser. The achievable readout fidelity is strongly dependent on the system photon detection efficiency and the associated dark count rate.

Figure 7.3 shows a measurement used to determine the errors in the readout process. An experimental sequence is set up to drive Rabi oscillations on the $^2S_{1/2}|F=0,0\rangle$ to $^2S_{1/2}|F=1,0\rangle$ transition after initialisation into the $^2S_{1/2}|F=0,0\rangle$ state. From the data figure 7.3 b) we measure errors of $\varepsilon_D \approx 3.8\%$ and $\varepsilon_B \approx 3.2\%$, leading to a readout fidelity of $\approx 96.5\,\%$. This data was taken with a readout time of 500 μs, a photon detection efficiency of approximately 0.4 %, and the readout laser parameters were $s \approx 1$ with $\Delta_L \approx 2\pi \times 8$ MHz to the red. Figure 7.3 c)

shows photon number histograms of the two highlighted data-points in b), which correspond to the purely dark and bright states of the ion.

The major source of dark state error in our system is not due to off-resonant scattering, but rather the high count rate which results from light scattered from trap electrodes into the imaging system. For a shorter readout time of 200 µs with similar parameters but with a lower photon counting threshold, this error reduces the fidelity to $\approx 94\,\%$. Future improvements in the speed and fidelity of the readout process can be made by reducing the scattered light either by using a tighter focus on the readout beam or by improving the spatial filtering in the imaging system.

7.3 Magnetic field characterisation using Ramsey interference

Knowledge of the orientation and magnitude of the magnetic field at the position of the ion is very important when working with quantum states. In the earlier experiment working with the 935 nm fibre cavity, it was found that the stainless steel tubes which surrounded the fibre mirrors had been unintentionally magnetised, and produced a static magnetic field of approximately 2 G at the position of the ion near-parallel to the cavity axis. As stainless steel tubes are integral to the cavity design used in this thesis, and detection of the microscopic field produced by the tubes is challenging with standard instrumentation, it is important that the magnetic field at the position of the ion can be measured and controlled.

An arbitrary magnetic field can be applied at the position using the set of three pairs of coils arranged along the x, y and z axes of the global coordinate system which align with the cavity axis, the trap rf electrode axis and imaging axis respectively. These coils are described in chapter 5 and a shown in figure 5.2.

The technique described in this section is based on Ramsey interference working with the ground state clock transition ($|0,0\rangle \rightarrow |1,0\rangle$) which is magnetically insensitive to first order. Ramsey interrogation, which is a form of atom interferometry, was chosen since the interference pattern can be observed for long interrogation periods, allowing almost arbitrary precision in the measurement of the transition frequency. The clock transition was chosen because the transition frequency depends only on the absolute value of the field at the ion, and therefore provides a measure which is independent of the orientation of the field.

The ion, initially in the $|0\rangle$ state, is excited by two square microwave pulses each with

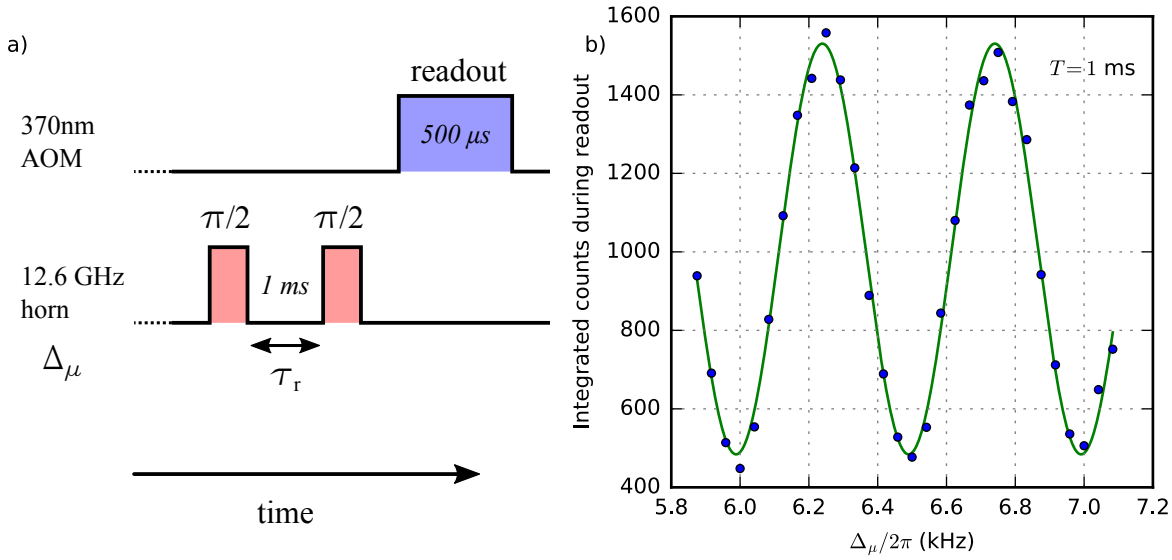

Figure 7.4: Ramsey interference measurement used to characterise the magnetic field at the ion. a) The ion is initialised in the hyperfine ground state, then pulses are applied in the sequence shown. b) Measurement of the total fluorescence during the readout period for various microwave detunings Δ_μ, which exhibit Ramsey interference.

duration τ_p but separated in time by T, with a frequency detuned from the transition frequency by Δ_μ. In this case, each microwave pulse will lead to the same rotation of the state on the Bloch sphere. However, during the time between the two pulses population in the excited state gains phase at an increased rate ($+\omega_0$) relative to the ground state. The direction of the rotation caused by the second pulse on the Bloch sphere is dependent on the relative phase between the probability amplitudes in the ground and excited states. This feature means that after the second pulse, if the relative phase is 0, the amplitude in the excited state is maximum, whereas for π is it minimum.

Mathematical analysis of the probability amplitudes leads to the probability of the measuring the ion in the excited state given by [45]

$$|\langle 1|\psi\rangle|^2 = P = \left|\frac{\Omega\tau_p}{2}\right|^2 \left[\frac{\sin\left(\Delta_\mu\tau_p/2\right)}{\Delta_\mu\tau_p/2}\right]^2 \cos^2\left(\frac{\Delta_\mu T}{2}\right), \tag{7.1}$$

where Ω is the Rabi frequency of the microwave pulses. In the case where $\tau_p = (2/\Omega)$, and

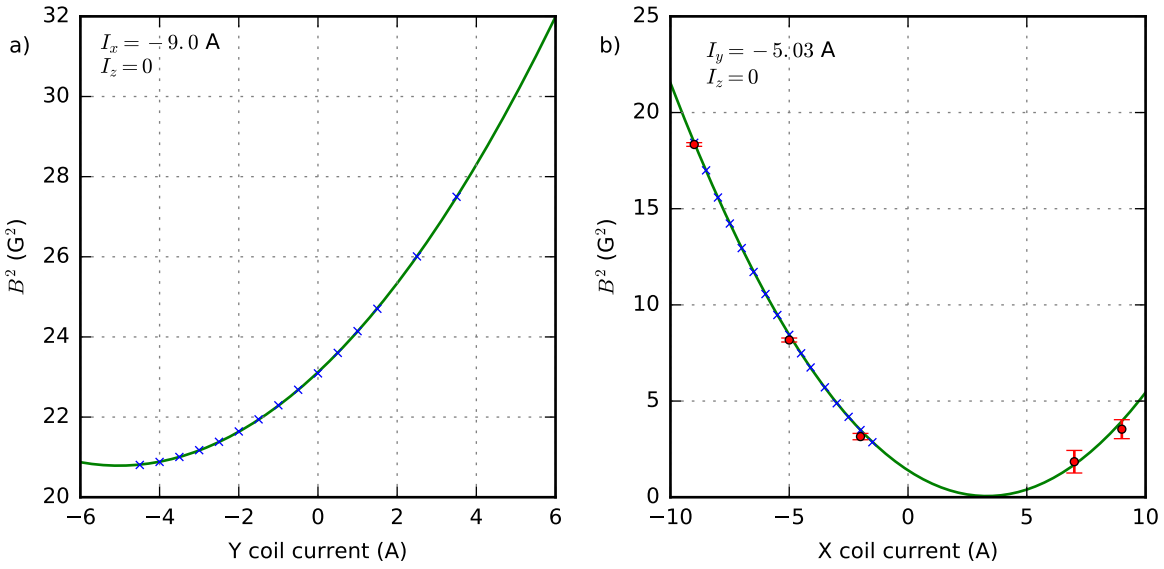

Figure 7.5: Measurements used to calibrate magnetic field coils and determine the static offset field. a) Current in the Y coil is scanned while a strong static field along x is produced by the X coil. The turning point of this graph corresponds to the case where the static magnetic field in along the y axis is cancelled by the field due to the Y coil. b) With the static magnetic field nullified in the y direction by applying approximately -5 A to the Y coil, the magnetic field magnitude is probed along the x direction. Both graphs are fitted with a quadratic function. Red data points correspond to measurements with a Ramsey time of 100 µs with error bars derived from the fit standard error, and blue data points correspond to a Ramsey time of 2 ms with error bars too small to resolve on this scale.

$\Delta_\mu \tau_p \ll 1$, then the excited state population becomes

$$P \approx \cos^2\left(\frac{\Delta_\mu T}{2}\right). \tag{7.2}$$

The transition frequency of the clock qubit has been measured precisely in Ref. [118], and is given by $\omega_0 = (12\,624\,812\,118.466 \pm 0.002)$ Hz. Since the transition is insensitive to magnetic fields to first order, the frequency is shifted only by a second order Zeeman shift of $\delta_z = 310.8 \times B^2$ Hz, where B is expressed in Gauss. In this case, under the same conditions as before, the population becomes

$$P = \cos^2\left(\left[\omega_\mu - \omega_0(B^2)\right] T/2\right) = \cos^2\left(\left[\Delta_\mu - \delta_z(B^2)\right] T/2\right). \tag{7.3}$$

Figure 7.4 b) shows a measurement taken whilst scanning the microwave detuning over a few fringes for a fixed magnetic field. Due to the periodic nature of the signal, a single measurement taken is not sufficient to fully determine the value of δ_z, as the phase recovered from the fitted data is only determined modulo π. However, when the Ramsey time T is varied for a fixed magnetic field, the true value of $\delta_z(B^2)$ will be constant whereas those that are off by factors of π will vary.

Using this Ramsey interference measurement technique, the absolute magnitude of the magnetic field at the position of the ion can be measured. By varying the current driving the magnetic field coils, it is possible to determine both the strength of the field generated by each coil for a given current, and the absolute value and direction of a static offset field if one exists.

The measurements shown in figure 7.5 fit excellently to the expected quadratic curve, and have allowed us to characterise the magnetic fields present. We have measured that the coils produce fields of approximately $0.4\,\mathrm{G/A}$ at the position of the ion. Further, the measurements indicate the presence of a static field of $(1.2\hat{x}, -1.5\hat{y}, 0\hat{z})$ G for the trap without the cavity present. The origin of the offset field is likely a combination of the earth's magnetic field ($\approx 0.5\,\mathrm{G}$) and the fringe field from the rare-earth magnets used in the ion getter pump which is located nearby to the chamber. The success of this method has shown that we will be able to identify and compensate for any magnetic field introduced by the cavity.

7.4 Ultrafast Rabi flops

Producing single photons with a well defined temporal profile from an ion is a basic requirement for producing useful ion-photon entangled states. One approach for this which is applicable to the $^{171}\mathrm{Yb}^{+}$ hyperfine qubit has been demonstrated in [119] and employs a weak 50 ns long laser pulse which excites a small fraction of the ground state population into the excited P state. The duration of the pulse is longer than the excited state lifetime, so during excitation the ion can spontaneously decay several times, however the strength of the pulse is chosen to be low enough that the probability of two photons being produced during one pulse ($P_{\mathrm{exc}}^{(2)}$) is low. Although producing weak pulses with durations on the order of 50 ns is readily achievable with CW lasers and bulk optics, the disadvantage of this approach is that the probability of producing a single photon per pulse ($P_{\mathrm{exc}}^{(1)}$) must necessarily be low in order that $P_{\mathrm{exc}}^{(2)}$ is low. This strongly reduces the rate of entanglement generation.

An alternative approach is to use a strong pulse which has a duration less than the excited state lifetime, first shown in [21]. In this way, the dynamics of the pulse occur on a time-scale

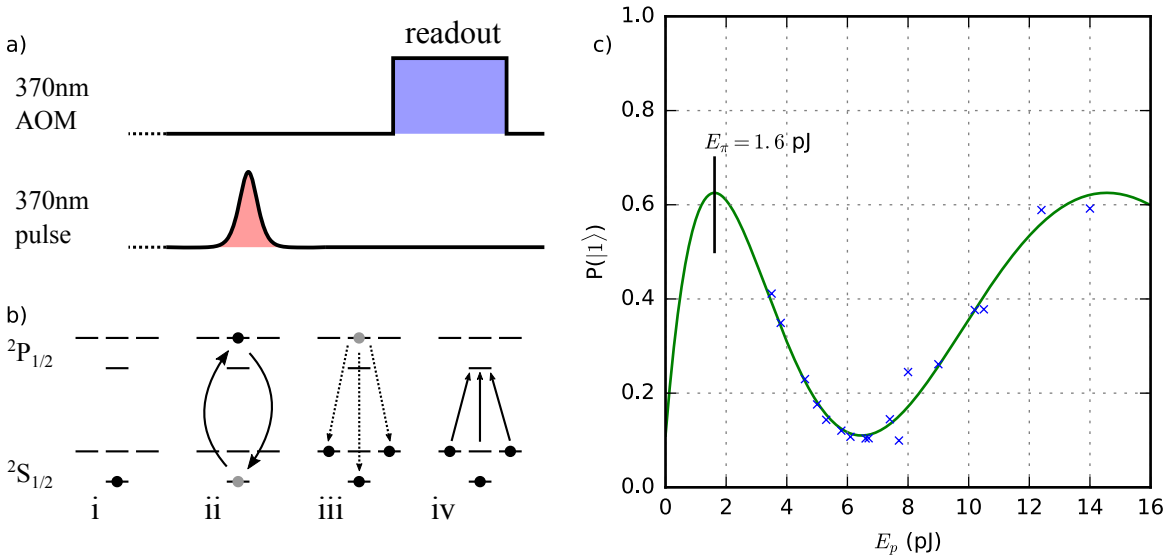

Figure 7.6: Demonstration of ultrafast excitation on the $^2S_{1/2} \rightarrow {}^2P_{1/2}$ transition. a) Experimental pulse sequence. b) Stages of pulse sequence: i) initialisation into $|0,0\rangle$ state. ii) Ultrafast Rabi flopping during pulse. iii) Decay of excited state population. iv) Readout of $^2S_{1/2}$ population within F=1 manifold. c) Measured probability of ion being found in the F=1 manifold as a function of pulse energy.

where the dissipative effects of the atomic decay can be neglected. When a short pulse is present at the ion, the population will undergo Rabi oscillations between the ground and excited states. If the energy and duration of the pulse are chosen correctly, it is possible to drive the excited state population to unity during the pulse. In this case, the temporal shape of the photon will be determined by the excited state lifetime, and the probability that the ion produces a single photon per excitation pulse is unity, whilst $P^{(2)}$ is zero. We plan to use this approach to generate single photons within the cavity with a high rate. In this section, we demonstrate control of Rabi flops on the $^2S_{1/2} \rightarrow {}^2P_{1/2}$ transition of $^{171}Yb^+$. The pulsed laser source which produces approximately 300 ps long pulses is described in section 5.2.2.

The simplest method to observe Rabi oscillations on this transition is to measure the probability of the ion emitting a photon after application of the pulse. The probability of the ion emitting a photon is proportional to the excited state population at the end of the excitation. If the Rabi frequency or the duration of the pulse is changed, then the resulting population in the excited state will change accordingly, which leads to the periodic signature of Rabi oscillations.

The population in the excited state as a function of pulse energy is given by

$$P = \sin^2\left(\Omega_{\text{eff}}\Delta_t/2\right) = \sin^2\left(\frac{\pi}{2}\sqrt{\frac{E}{E_\pi}}\right), \tag{7.4}$$

where Ω_{eff} is the effective average Rabi frequency of the pulse, and the width of the pulse in time is Δ_t. In order to calculate Ω_{eff}, the shape of the pulse is important, however, for a given pulse time the details of this can be absorbed into the constant E_π which represents the pulse energy required the population to be fully in the excited state.

Initially we made attempts to directly observe these photons created by the ultrafast excitation on our imaging system PMT. This was ultimately unsuccessful however, because the probability of detecting a stray light photon from the pulse was much larger than the expected signal, and the jitter in arrival time of the detector meant that the stray light could not be simply removed by time binning.

Instead of directly measuring the photons produced, an alternative scheme employing the state detection was used which could reach the same result. Figure 7.6 a) shows the measurement scheme for this technique. After initialisation into the hyperfine ground state, a single pulse from the laser was sent to the ion. The laser was tuned to be on resonance with the $^2\mathrm{S}_{1/2}\,|F=0\rangle \rightarrow {}^2\mathrm{P}_{1/2}\,|F=1\rangle$ manifold, and the polarisation of the pulse was adjusted such that the pulse only coupled to the π transition. While the pulse is present at the position of the ion, the population undergoes Rabi oscillations between the $|0,0\rangle$ state in the $^2\mathrm{S}_{1/2}$ manifold and the $|1,0\rangle$ state in the $^2\mathrm{P}_{1/2}$ manifold. After the pulse leaves the ion, the fraction of the population which is left in the excited state undergoes spontaneous decay on the time-scale of 8 ns. From the $^2\mathrm{P}_{1/2}$ $|1,0\rangle$ state, there are three allowed dipole transitions, which each have Clebsch-Gordan coefficients $1/\sqrt{3}$. Two of these decay paths leave the ion in the $^2\mathrm{S}_{1/2}\,|F=1\rangle$ manifold. After the decay, the population in the $F=1$ manifold is read out with the quantum state readout procedure described earlier.

Figure 7.6 b) shows the result of a measurement of the $F=1$ population while the pulse energy is varied. The data are fitted with equation 7.4, which gives a value of E_π of 1.6 pJ. During this measurement, the infidelity of the readout process was independently measured to be approximately $\varepsilon_{\mathrm{D}} = 0.06$ and $\varepsilon_{\mathrm{B}} = 0.12$. The maximum value of the fit is 0.63(2) which is approximately equal to the expected value of 0.61 from the 2/3 branching ratio and the measured readout infidelities. The minimum value is slightly larger than the value expected from the readout process alone, and is likely due to imperfect π polarisation of the excitation pulse which leads to additional pulsed excitation on the $\sigma\pm$ transitions with a lower Rabi frequency.

This measurement shows that with our pulsed laser we can drive Rabi flops across the $^2S_{1/2} \rightarrow {}^2P_{1/2}$ transition and control the resulting population in the excited state. The maximum value of the fit is in agreement with the expected unity excited state population when driven by a resonant pulse with energy E_π.

7.5 Towards spin-photon entanglement

All the necessary elements for demonstrating the entanglement between photons emitted from the cavity and the resulting state of the ion have been individually set up and tested. However, due to the excessive heating of the cavity which occurs when the microwaves are applied coupled with the temperature sensitivity of the cavity, the sensible approach is to build a laser source which can drive stimulated Raman transitions between $^2S_{1/2}|F=0\rangle$ and $^2S_{1/2}|F=1\rangle$ to replace the microwaves. In this section, the planned scheme for generation of the entangled state is described accompanied with realistic estimates of achievable rates with the measured cavity parameters.

The proposed scheme for entanglement is shown in figure 7.7. The ion is initially prepared in the $^2S_{1/2}|F=0,0\rangle$ state, and is excited with a π polarised pulse of light resonant with the $^2S_{1/2}|F=0,0\rangle \rightarrow {}^2P_{1/2}|F=1,0\rangle$ transition. The energy of the pulse is tuned such that it will leave the ion with near-unit population in the excited state as shown in section 7.4. The population decays out of the excited state following an exponential decay with time constant equal to the excited state lifetime 8 ns. For this decay, there are three allowed transitions: $\sigma^\pm$ into $^2S_{1/2}|F=1,\pm1\rangle$, and π into $^2S_{1/2}|F=0,0\rangle$. With the magnetic field axis oriented along the cavity axis, the cavity mode only couples to the σ transitions because of the zero emission probability of π photons along the quantisation axis.

When the cavity is tuned to be resonant with the $^2S_{1/2}|F=1\rangle \rightarrow {}^2P_{1/2}|F=1\rangle$ transition, the probability of photon emission into the cavity mode is determined by $P_e = 2C_0/(2C_0+1)$, and the probability of the photon leaving the cavity is determined by the cavity out-coupling efficiency and mode-matching into the fibre.

The output from the fibre cavity is measured in the polarisation analysis stage described in section 5.5, which has two single photon detectors arranged to measure orthogonal polarisation states of the incident light. The polarisation detection basis can adjusted by means of quarter- and half-wave plates. Given that the ion has decayed into the $^2S_{1/2}|F=1\rangle$ state, the system has

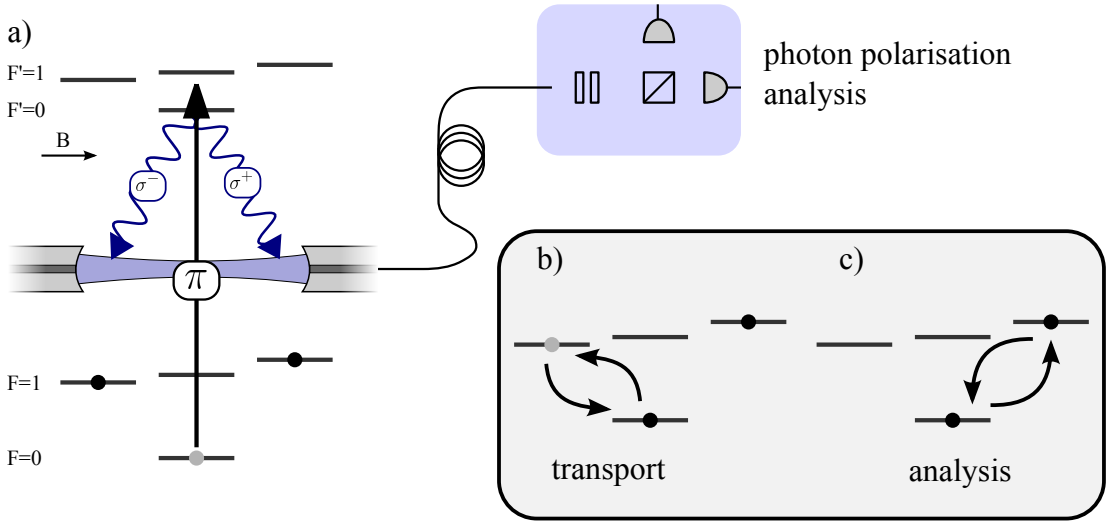

Figure 7.7: Proposed entanglement generation and measurement scheme for polarisation entangled photons. a) The ion is excited with a π polarised laser pulse which results in $\sigma^{\pm}$ photons being coupled into the cavity. Photons which leave the cavity into the fibre are measured on a pair of single photon detectors which detect in orthogonal polarisation bases. b) After photon emission has occurred, population amplitude is transferred from the $^2S_{1/2}|F=1,-1\rangle$ state into the $^2S_{1/2}|F=0,0\rangle$ state with a resonant π pulse. c) An additional resonant $\pi/2$ rotation can be performed between the $^2S_{1/2}|F=0,0\rangle$ and $^2S_{1/2}|F=1,1\rangle$ before eventual measurement of the ion state.

the following state

$$|\psi\rangle = \frac{1}{\sqrt{2}}|F=1,-1\rangle \otimes |\sigma^-\rangle + \frac{1}{\sqrt{2}}|F=1,1\rangle \otimes |\sigma^+\rangle . \tag{7.5}$$

The detection of the photon on one of the detectors in the analyser is a projective measurement on the photon state. If the wave plates in the analyser are oriented in such a way that the σ^+ photons are detected on one arm, and σ^- on the other, then a click on the σ^+ detector will be correlated with the ion being in the $|F=1,1\rangle$ state, and σ^- similarly with $|F=1,-1\rangle$.

In order to distinguish between the two resulting ion states, the population in one of the states needs to be transferred to the $|F=0,0\rangle$ state. This can be achieved with high accuracy by applying either the microwave field or a Raman field which is tuned to the $|0,0\rangle \rightarrow |1,-1\rangle$ transition, with the duration set to that $\Omega\Delta_t = \pi$. After the population in $|1,-1\rangle$ is fully trans-

ferred to $|0,0\rangle$, the state readout can be applied, and the correlation between $|F=1\rangle$ and σ^+ should be observed.

A measurement of the correlation is important, but on its own it is not able to distinguish between the ion-photon system being in an entangled state or just being in a classically statistically correlated state. To demonstrate that the state of the system is indeed an entangled state, it is necessary to show the presence of quantum correlations which can be done by repeating the measurement of the state after rotating both measurement bases by 45° on the Bloch sphere [119]. In our case we can achieve this via aligning the polarisation measurement basis to distinguish horizontal and vertical polarisation photons, and applying a second radiation pulse to the ion which is resonant with the $|0,0\rangle \rightarrow |1,1\rangle$ with $\Omega\Delta_t = \pi/2$.

The cavity emission probability for the σ transitions can be calculated from the value of g measured in chapter 6. After accounting for the difference in Clebsch-Gordan coefficients ($\sqrt{2/3}$ in the measurement with $^{174}Yb^+$ vs $\sqrt{1/3}$ here), we find $C_\sigma = 0.048$ giving $P_e^\sigma = 9\,\%$. Due to losses in the cavity mirror coatings, only a small fraction of photons which are emitted into the cavity mode leave the cavity though the out-coupling mirror. The probability of detecting a single photon after successful emission into the cavity mode is give by $\eta_{net} = \eta_c \varepsilon_{mm} \eta_{QE} = (3.3\%)(45\%)(14\%) \approx 2.1 \times 10^{-3}$, where η_c is the cavity out-coupling efficiency, ε_{mm} is the mode-matching coefficient, and η_{QE} is the quantum efficiency of the detectors (assumed to be PMTs). The probabilities involved in detection of the photons with our pulsed excitation scheme are summarised in table 7.1.

$P(F=1)$	2/3	Probability of decay into $^2S_{1/2}\,\|F=1\rangle$
P_e^σ	0.09	Cavity emission probability for σ transitions
η_{net}	2.1×10^{-3}	Probability of detection of a photon after emission
P_{tot}	1.2×10^{-4}	Total probability of photon detection after one excitation

Table 7.1: Summary of photon detection probabilities in the proposed scheme with $^{171}Yb^+$.

Based on the measurements described earlier in this chapter with $^{171}Yb^+$, we predict that we will be able to operate this measurement with a repetition rate of ≈ 3.3 kHz, coming from 200 µs for state detection, 50 µs for rotations and 50 µs for Doppler cooling and initialisation. This indicates that we will be able to generate our spin-photon entangled state with an average rate of ≈ 0.4 /s. This rate can be increased by only performing rotation and state readout when a photon is detected using the conditional sequence logic built into the hardware which is described in

chapter 5.6. In this case, the average repetition rate can be increased to approximately 50 kHz[2], which will lead to a success rate of ≈ 6 /s. This rate is not yet competitive with the current state-of-the-art using high numerical aperture lenses to collect photons. For instance, in Ref. [120], the combined probability of detection of a single photon is $P_{\mathrm{tot}} = 4.7 \times 10^{-3}$, and during the described experiment, this process is repeated at a rate of 470 kHz, giving an average success rate of 2200 /s.

The major limitation in the generation rate with our system is the intracavity loss described in chapter 4.4. If the coating loss increase mechanism is understood and inhibited, then with all other parameters remaining the same, we expect the cooperativity of the cavity to increase to $C_\sigma \approx 0.72$, leading to a cavity emission probability of $P_{\mathrm{e}} \approx 59\%$. In the absence of intracavity losses, the out-coupling efficiency of the cavity (η_{c}) would also be improved from 3.3 % to 50 %. Taking into account the mode-matching of $\varepsilon_{\mathrm{mm}} = 45(6)\%$, the total probability of photon being coupled into the fibre after one excitation would then be ≈ 8.9 %, and the total detection probability using the current photon detectors would be ≈ 1.2 %. This would represent a 100-fold improvement over the current total photon detection probability, and an improvement over the result given in Ref. [120] of more than two.

[2]For this rate, we assume a cycle of 20 µs composed mainly of Doppler cooling and initialisation. This could conceivably be reduced further by performing the state initialisation with higher optical power. The average success rate is given by $R = 1/[(P_{\mathrm{tot}} 300\,\mu\mathrm{s}) + (1 - P_{\mathrm{tot}}) 20\,\mu\mathrm{s}]$.

Chapter 8

Conclusion

In this thesis we have demonstrated the first coupling of a single ion to a fibre-cavity operating in the ultraviolet spectral range. By combining the benefits of the miniaturised mode volume provided by fibre-cavities with the strong primary dipole transitions of trapped ions, we have built a platform which will provide access to strong coherent ion-photon interaction.

To achieve this, we have developed the first optical fibre-based Fabry-Pérot cavities which work at ultraviolet wavelengths. We have found that at these shorter wavelengths the fibre-cavity is very sensitive to the alignment of the fibres. In combination with the requirement that the vacuum system must be heated to achieve ultra-high vacuum, we have found that ultraviolet fibre-cavities are significantly more technically challenging to build than at longer wavelengths. This challenge has been overcome by building electronic actuators into the mounting structure which allow the fibre-cavity to be mechanically aligned *in situ*.

In order to integrate our fibre-cavity very close to the ion, we have constructed a new Paul trap apparatus. In this experimental setup, we have been able to trap an ion at a distance of 75 µm from our two cavity mirrors, which is to our knowledge the shortest optical cavity used to date with trapped ions[1]. Additionally, the new apparatus, along with the supporting laser systems and electronics, has a small enough experimental footprint that several such devices can be operated in one laboratory.

With our experimental apparatus, we have shown that use of a fibre-cavity in the ultraviolet allows for the production of pure single photons at a high rate into a single spatial mode. Ad-

[1] In a recently published paper [121], an ion has been trapped at a distance of 50 µm from a planar HR mirror. Although a very promising result, it is however not directly comparable to our result as there is no optical cavity formed.

ditionally, we have demonstrated the highest coherent atom-cavity coupling rate with a single trapped ion achieved to date. This coupling has been verified by means of two independent measurements: a measurement of the geometric mode volume, and a measurement of the system cooperativity. The mode volume was determined by measuring the spatial dependence of the atom-cavity coupling, which determines the mode waist, combined with a measurement of the cavity length. The coupling strength could then be calculated from the properties of the atomic transition, which are well known. Measurement of the cooperativity was achieved by observing an increase in the linewidth of the atomic transition in the presence of the resonant cavity. Along with a measurement of the cavity linewidth, this provides a direct measure of the atom-cavity coupling strength. The two measurements of the coherent coupling rate differ by a factor which is explained by imperfect localisation of the ion wave-packet along the cavity direction.

The high atom-cavity coupling strength of this system, together with the high degree of control available with trapped ions, has allowed us to probe the driven Jaynes-Cummings model in a previously uncharted regime. We have observed phase-sensitive correlations between emission into free-space and into the cavity mode, which can be explained by a cavity induced back-action effect on a driven dipole. With this we have demonstrated that the cavity can be used as a tailored environment, which can act to suppress or enhance the total emission rate of an atom by tuning the phase of the back-action field. These phase-sensitive correlations will provide a convenient way to accurately measure the cooperativity in future experiments which operate in the fast-cavity regime.

Finally, we have made progress towards showing the entanglement between the photons emitted by the cavity and the resulting state of the ion. We have implemented coherent control and quantum state readout for the hyperfine qubit in $^{171}Yb^{+}$ using microwaves. However, after integration of the fibre-cavity into the experiment, we have found that the high microwave power required for fast manipulation is incompatible with our fibre-cavity technology. This will be overcome through use of a laser which drives optical Raman transitions. Accurate determination and compensation of the static magnetic field at the position of the ion has been achieved by using Ramsey interference measurements. A laser system has been assembled which produces short pulses of light at 370 nm, which will allow for the production of entanglement at a high repetition rate. We have demonstrated that our pulsed laser allows us to excite the ion on time-scales shorter than the excited-state lifetime, and provides a method to excite the ion with near-unit probability. In chapter 7.5, a scheme for producing and detecting ion-photon entanglement in our system is presented. For this scheme we have estimated the entanglement generation rate

for the system using the measured cavity parameters.

Lab-scale entanglement

In the short term, the path towards measuring the entanglement between state of the ion and the emitted photon is clear. We will construct a laser source which can be used to drive optical Raman transitions for coherent control of the hyperfine qubit. This is necessary to replace the microwave drive which has thus far been used, but has proven itself to be incompatible with our fibre-cavity technology. When the Raman laser is operational, we will be able to analyse the properties of the entangled state. Building on the work of this thesis, when the mechanism which causes the intracavity losses is understood, a new fibre-cavity can be assembled which will meet the designed cavity finesse. The immediate effect of this upgrade on the spin-photon entanglement analysis is outlined in chapter 7.5, where the probability of a photon being coupled out of system in the fibre mode is calculated to be $\approx 8.9\,\%$. This number can be further increased by nearly a factor of two if a highly reflective coating is used on one of the mirrors to improve the cavity out-coupling efficiency, η_c.

With the high collection efficiency of our system, it will be possible to produce entanglement between two remote ion traps with a high success rate. This requires that a second ultraviolet cavity is built using the techniques developed in this thesis. The second cavity can be placed in the existing ion trap apparatus which was used in earlier experiments with the infrared cavity. In order to entangle two ions, we will perform measurements of two-photon interference with photons emitted after pulsed excitation, which will project the ions into an entangled state. This was first demonstrated in [21] where they achieved a heralded entanglement event approximately every 8.5 minutes. Using our photon emission probability, and an optimised repetition rate of 100 kHz, we estimate a heralded entanglement rate of $\sim 140\,/\mathrm{s}$ [2]. This would represent an increase of $\sim 10^5$ over the initial entanglement experiment, and an increase of ≈ 30 over the $4.5\,/\mathrm{s}$ rate recently achieved in Ref. [120].

In order to further optimise the photon emission probability, we can increase the finesse of the cavity. The optimal parameters for photon emission are reached when $g = \kappa$. In our

[2] This number includes the use of a highly reflective coating on one of the mirrors of each cavity, assumes perfect spatial and temporal mode matching of the two photons at the beam splitter, accounts for the factor of 1/4 for detecting the correct Bell state, and assumes the use of APDs with $\approx 45\,\%$ quantum efficiency.

case, with the designed $g/2\pi$ of $\sim 70\,\mathrm{MHz}$[3] and corresponding cavity length 150 µm, this is achieved with a finesse of ~ 7000. The emission probability from the cavity for a two-level system with these parameters would be $P_\mathrm{e} \sim 0.82$[4]. When taking into account the excitation scheme for $^{171}\mathrm{Yb}^+$ described in chapter 7.5, the probability of a photon being emitted from the cavity mode after pulsed excitation becomes $P_\mathrm{e}^\sigma = 0.75$[5].

Coupling this with the improvement of cavity-fibre mode-matching reaching 70 % which could come from using photonic crystal fibre, the total collection efficiency of the system could be $\sim 53\,\%$. An alternative approach to improving the mode-matching is available through the use of gradient-index (GRIN) lenses. Instead of machining the dielectric mirrors which form the cavity on the tips of optical fibres, mirrors could be machined out of GRIN lenses which are optimised for the matching the cavity mode into a fibre. These lenses could then be spliced onto the end of single-mode fibre and optical cavities similar to fibre-cavities could be formed. In this way, with the right material and profile of the GRIN lenses, near-perfect mode-matching could be achievable, leading to a net collection efficiency of 75 %.

Long-range entanglement

These record high rates will bring several new avenues of research into the realm of possibility. One of these is the investigation of quantum networks spanning large distances, which are not only interesting for cryptography applications, but also fields like quantum metrology [122]. Since the technology from which ion traps are made is very robust, and the ions have long storage times, it is feasible that such an experiment can be built up in a far-away location and operated remotely. With spin-entangled photons coupled out of these systems in single-mode fibres, remote experiments can be entangled using the proven techniques by placing a Bell state analyser in the centre of a length of fibre laid between two such ion traps. However, the distance over which this can be achieved would be strongly limited by the fibre technology at ultraviolet wavelengths. Typical optical loss for single-mode fibre operating near 370 nm are on the order of $30\,\mathrm{dB/km}$. The rate of successful heralded entanglement events with finite transmission in the fibre path is simply proportional to the total loss in the fibre, so the rate scales with

[3]This value of $g/2\pi$ comes from the value expected from the cavity mode volume and the Clebsch Gordan coefficient of the appropriate atomic transition, $1/\sqrt{3}$.

[4]The emission probability here is calculated from a numerical solution to the Jaynes-Cummings Hamiltonian since κ is of the same order as Γ.

[5]This includes that the branching ratio for the π transition is suppressed from $1/3$ to $\sim 1/12$ by the cavity.

30 dB/km. A 10 dB drop in rate occurs after $\sim$ 300 m, which makes this direct approach to spanning large distances challenging.

Recent advances in non-linear frequency conversion [123, 124] promise to significantly improve the range of these entanglement experiments. By fabricating waveguides in materials which exhibit strong second-order optical non-linearity such as periodically poled potassium-titanyl-phosphate (PPKTP) or lithium-niobate (PPLN), it is possible to use difference-frequency generation to efficiently convert the wavelength of light between ultraviolet and the telecom bands, where silica optical fibres have the lowest losses. The use of this waveguide technology to convert single photons to the telecom band for quantum information purposes has already shown great success with quantum dots [125]. The optical loss in telecom C-band near 1550 nm can be made as low as 0.15 dB/km [126]. If this technology is applied to our entanglement scheme, then we would see a 10 dB drop in entanglement generation rate only after $\sim$ 70 km.

Trapped-ion quantum network

In the long term, driven by quantum cryptography, there is a strong desire to progress from proof-of-principle experiments to the construction of vast networks which will allow the faithful transfer of a quantum state over distances on the global scale. In order to achieve this goal in the face of fibre attenuation and operational errors, a promising approach is presented by quantum repeaters [127] which can be feasibly implemented with trapped ion systems [128]. Quantum repeaters essentially solve the physical problem of loss by breaking up the total distance of communication into shorter sections which can be operated with high fidelity. The repeaters can also employ active mechanisms such as entanglement distillation [129, 130] to correct for operational errors which inevitably occur.

In proposed practical implementations of these distillation protocols [131], there are strong advantages to using more that one species of ion in linear trap geometries, which allow for shuttling and separation of the ions. In order to provide a reliable and scalable platform for these systems, the considerable advances in microelectromechanical systems (MEMS) fabrication can be applied to build complex yet precise structures which can form deep ion traps [132]. However, the information rate transferred across such a network will always be fundamentally limited by the rate of entanglement generation. For this reason, it is likely that the future nodes of a trapped ion quantum network will incorporate miniaturised optical cavities, similar to those which has been demonstrated in this thesis.

Microfabricated three-dimensional traps such as those demonstrated in [133] could include

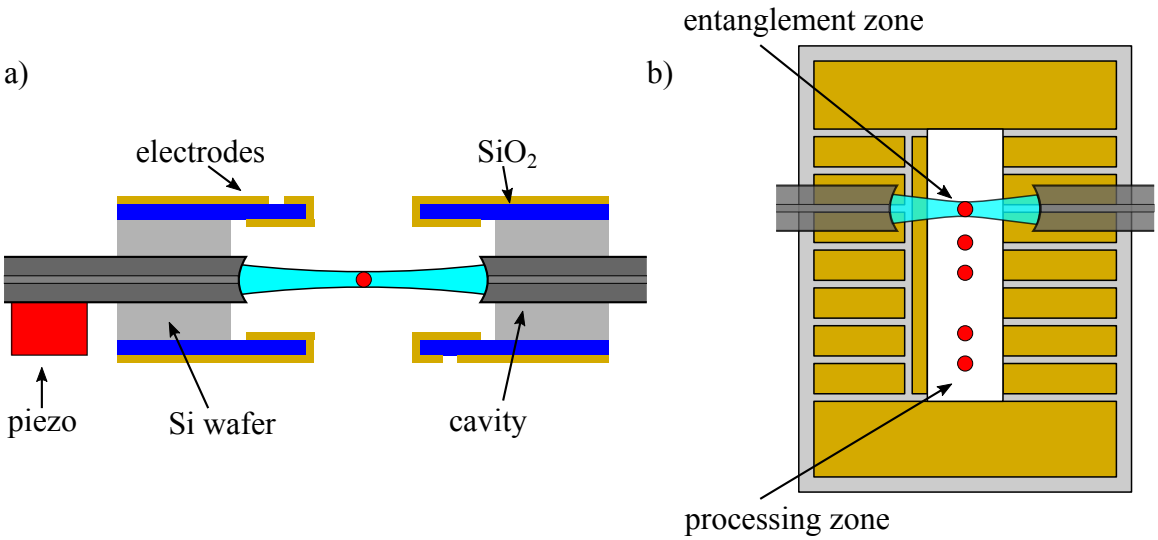

Figure 8.1: Possible microfabricated ion trap with integrated fibre-cavity. a) Side view and b) top view of a 3d Paul trap similar to the one demonstrated in [133] using silicon microfabrication techniques.

optical fibre technology, which would allow for near-unit photon-collection efficiency. One possible implementation of this is shown in figure 8.1. If holes or channels for optical fibres can be manufactured in the substrate with lithographic precision, then this could provide a scalable and compact solution for achieving high photon collection efficiency in a linear trap. Since the optical fibres are well shielded from all lasers in this design by the gold electrodes, charging of the dielectric surfaces will be minimised. Furthermore, if the presence of the cavity mirrors leads to excess motional heating, the surface area of the dielectric material exposed to the ion can be reduced by depositing a gold mask onto the mirror surface. Since the width of the cavity mode at the mirror is typically less than 10 µm, a significant reduction in the dielectric surface area can be achieved without imposing noticeable clipping losses to the cavity. Linear ion traps with fibre-cavities integrated in this way would allow for scalable and efficient quantum repeaters.

Appendix A

Copper deposition

This appendix describes the process used to deposit a metallic copper layer onto the outside of optical fibre for use in our ultraviolet fibre-cavities.

As the *S405-XP*[1] fibre used for the 370 nm fibre-cavities has an Acrylate coating which is not suitable for ultra-high vacuum us, it is necessary to remove the coating before placing the fibres in the vacuum chamber. Although bare fibre has a low out-gassing rate, its mechanical properties are far from ideal, as the fibre tends to break at much larger bend radii than is achievable with a protective coating. For some applications this is not a problem, however in order to position the cavity near our trap the fibres need to undergo several bends.

In early attempts we coated our fibres with a Kapton polymer[2] which had proven a viable technique in past experiments [89]. The monomer is supplied in volatile solution and can be painted onto surfaces, then the polymer is formed by heating the monomer residue to 200 °C. We found that on application to the surface of 125 µm diameter stripped optical fibre, the solution would form droplets whose surface tension would cause the fibre to bend before evaporating. The uneven coating that resulted would not protect the fibre from breaking under bending because of small gaps which would act to concentrate the stress at these points.

In order to provide a more solid and reproducible solution, we have developed a technique for applying a copper cladding layer to small quantities of bare optical fibre, with a high degree of control over the position and thickness of the coating. With this process, it is also possible to apply the coating up to 10 mm from the cavity mirror. This process uses electro-deposition to form a metallic copper layer on top of an initial graphite coating.

[1] Manufactured by Nufern

[2] Epo-Tek 390

Graphite coating

The coating process begins with depositing a thin layer of graphite onto the bare fibre. To do this, we use a colloidal graphite solution[3]. The fibre is coated by pulling it through a droplet of the graphite solution using a mechanical jig. The solution adheres to the fibre through surface tension, and if the motion is constant then the droplet deposits a uniform and symmetric layer at the wetting boundary. After the solution has dried, the graphite coating is annealed at $\sim 65\,^{\circ}\mathrm{C}$ to improve the electrical conductivity.

Electroplating

A layer of metallic copper is formed on top of the graphite-coated fibre by electro-deposition. We use a commercial copper electroplating electrolyte solution[4] which contains approximately 2 molar $CuSO_{4(aq)}$ and 2.5 % H_2SO_4. The fibre is suspended in the centre of a 25 mm copper tube, sealed at one end, containing the electrolyte which forms the anode. A constant voltage of 0.2 V is applied between the graphite coating at one end of the fibre (the cathode) and the copper tube. This is shown in figure A.1 a).

When the voltage is applied, the local copper deposition rate at any point along the fibre is proportional to the current density, which in turn is proportional to the local electric field density. Since the graphite coating has a finite resistance, and the fibre is only electrically connected on one end, the voltage is not constant along the length of the fibre during the deposition process. As copper is deposited over the graphite surface, the local resistivity drops strongly. This leads to an electric field gradient which propagates along the length of the fibre until the surface is fully coated.

As the gradient propagates along the fibre, the total plating current increases due to the increasing current density. We exploit this phenomenon to determine the time at which the fibre is fully coated, and therefore control the thickness and uniformity of the coating. Figure A.1 b) shows the form of the current throughout the coating process. From the experimental data, we observe three distinct phases: I) The current is unstable for the first few minutes, then the current rises approximately quadratically. II) The rate of change of current abruptly changes to be constant, and remains so for approximately 80 minutes. III) The rate of increase of current

[3]The graphite solution is made from '16051' from Ted Pella which is diluted with distilled water to an even volumetric ratio

[4]531227-62 from Conrad Electronic SE

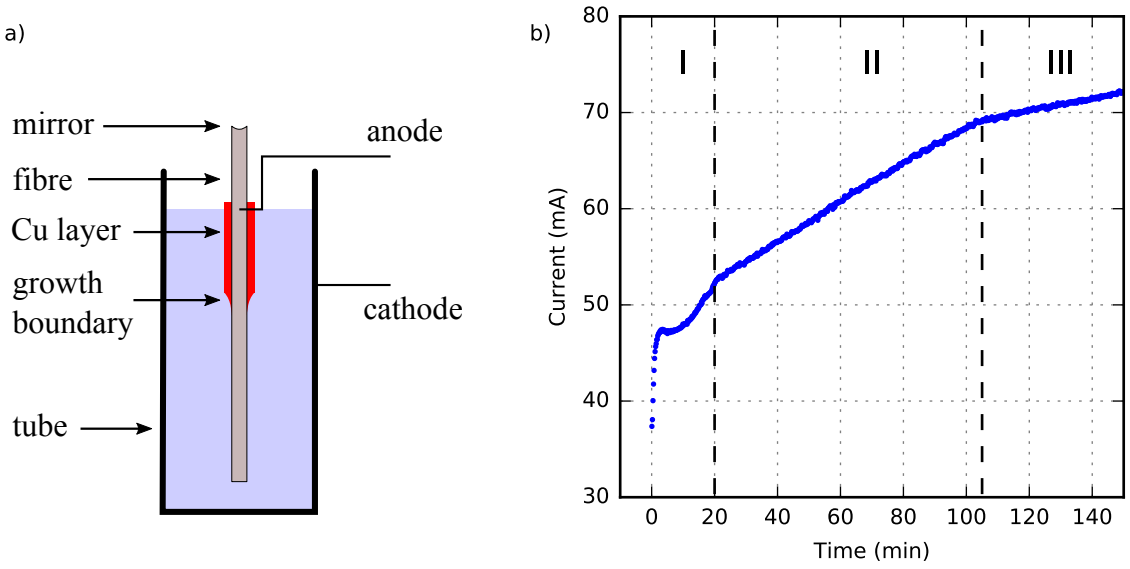

Figure A.1: Fibre electro-deposition process. a) The graphite-coated fibre is held in the electrolyte solution with the cavity-mirror above the liquid surface. A voltage is applied between the outer anode and the fibre cathode, which leads to the electro-deposition of copper onto the fibre. b) The electroplating current between the anode and cathode during the process. The three distinct phases of the process are described in the text.

makes a second abrupt change, to another constant but distinct value. These phases can be qualitatively understood by analysing the deposition process.

Electrochemical deposition is governed by Faraday's law

$$T(t) = \frac{JM}{\rho F n} t = \beta t, \tag{A.1}$$

where T is the thickness of the deposit as a function of time, J is the current density, M is the molar weight of the cation, ρ is the mass density of the metallic deposit, F is Faraday's constant, and n is the valence of the cations in solution. β is the combination of the various constants, and determines the uniform plating rate. During deposition, the finite resistance of the graphite leads to a voltage gradient along the length of the fibre. However, because the conductivity of copper is very high, as soon as thin layer is deposited, the resistance drops and the voltage becomes almost uniform.

We first consider the case where a copper layer exists across the whole length of the fibre, and therefore the voltage is constant across the surface of the fibre. The fibre is held in the centre

of the anode cylinder, which has a much larger diameter than the fibre. The electric field at the surface of the fibre is one of the factors that determines the rate of deposition. Since the radius of the coated fibre does not change significantly on the length scale of the anode diameter, the fixed voltage leads to an approximately constant uniform electric field across the surface of the fibre. The total plating current I is given by

$$I = \int J d\sigma, \tag{A.2}$$

where σ is the surface area of the fibre, and J is the current density. At a position z along the length of the fibre, the radius of the coated fibre increases linearly with time. This is a result of the increasing surface area from the uniform radial deposition and the constant local current density. Consequently, the plating current increases linearly with time

$$\frac{dI}{dt} = 2\pi L J \beta. \tag{A.3}$$

This uniform radial growth occurs in phase III of figure A.1 b).

During phase II of figure A.1 b), the copper coating is propagating along the length of the fibre. To analyse this growth, we need to take into account the finite resistance of the graphite coating. In a simple model, we assume that the growth boundary is abrupt: radial growth occurs as before up to the boundary, and no growth occurs afterwards. Additionally in this model, the boundary propagates along the fibre surface at a constant rate γ. In this case, the total surface area of the fibre as a function of time while the boundary is propagating is given by

$$\sigma(t) = 2\pi r_0 \gamma + 2\pi\beta\gamma t^2, \tag{A.4}$$

where r_0 is the radius of the fibre before coating. The first derivative of the plating current is then given by

$$\frac{dI}{dt} = 2\pi r_0 \gamma J + 4\pi\beta\gamma J t. \tag{A.5}$$

If the radial thickness of the deposited layer is small compared to the fibre radius before coating, then $2\beta t \ll r_0$, which indicates that the constant term in the above equation dominates. This is the behaviour which causes the distinct linear growth in phase II.

Using this technique along with the simple model described here, we are able to monitor the growth of the copper coating in real time by measuring the plating current. This allows us to stop after the process after the coating has grown to a certain thickness despite changes in the electrochemical process, such as temperature and concentration, which is important in order to produce reliable and deterministic results.

Appendix B

Fibre birefringence compensation

We seek to prove that by minimising the power of the back reflection on the H-arm of the polarisation analyser described in chapter 5.5, we adjust the combination of wave plates such that linear states at the PBS map to circular states in the cavity.

In Jones calculus [134], the polarisation state of light is described with a complex-valued two-component vector. Much like a two-level quantum system, any state can be represented as a superposition of two orthogonal basis states. By convention, we define the horizontal-vertical basis to be

$$|H\rangle = \begin{pmatrix} 1 \\ 0 \end{pmatrix}, |V\rangle = \begin{pmatrix} 0 \\ 1 \end{pmatrix}. \tag{B.1}$$

Objects which transform the polarisation state of a Jones vector, such as wave plates, are represented by 2x2 complex valued matrices known as Jones matrices.

Between the PBS and the cavity we have three transformation objects: the half-wave plate, the quarter-wave plate, and the fibre. The state of light at the cavity mirror is given by

$$|\tilde{\psi}\rangle = M_F M_{QWP} M_{HWP} |\psi\rangle, \tag{B.2}$$

where $|\psi\rangle$ is the polarisation state after the PBS.

Under the assumption that the fibre and wave plates have no optical loss, we can represent the above transformation with three matrices A, B and C

$$|\tilde{\psi}\rangle = CBA |\psi\rangle, \tag{B.3}$$

where A and C are real and unitary, and

$$B = \begin{pmatrix} e^{i\theta} & 0 \\ 0 & e^{i(\theta+\phi)} \end{pmatrix}, \tag{B.4}$$

with ϕ and $\theta \in \mathbb{R}$. This is allowed because real unitary matrices represent rotations of the coordinate system and B represents a phase retarder whose slow axis is aligned along H.

The polarisation state of light which is reflected from the cavity is given by

$$\left|\psi'\right\rangle = M^r_{HWP} \cdot M^r_{QWP} \cdot M^r_F \cdot M_F \cdot M_{QWP} \cdot M_{HWP} \left|\psi\right\rangle \tag{B.5}$$

$$\left|\psi'\right\rangle = A^r B^r C^r C B A \left|\psi\right\rangle ., \tag{B.6}$$

where M^r is the reciprocal transformation of M defined by

$$M^r = \begin{pmatrix} 1 & 0 \\ 0 & -1 \end{pmatrix} M^T \begin{pmatrix} 1 & 0 \\ 0 & -1 \end{pmatrix}, \tag{B.7}$$

which represents reversal of propagation direction through the transformation object [135].

If M is real and unitary, then $M^r M = 1$. If M is diagonal, then $M^r = M$. By applying this to equation B.6 we find

$$\left|\psi'\right\rangle = A^r B^2 A \left|\psi\right\rangle. \tag{B.8}$$

The optimisation procedure seeks to reduce the back reflection from the cavity through the PBS, which is aligned to transmit horizontally polarised light ($\left|\psi\right\rangle = \left|H\right\rangle$). Mathematically, optimisation results in

$$\left\langle H\right| A^r B^2 A \left|H\right\rangle = 0, \tag{B.9}$$

from which it follows that

$$\left\langle V\right| A^r B^2 A \left|H\right\rangle = 1, \tag{B.10}$$

and therefore

$$B^2 A \left|H\right\rangle = A \left|V\right\rangle. \tag{B.11}$$

Since A is unitary, and $\left|H\right\rangle$ and $\left|V\right\rangle$ are orthogonal, it follows that $A\left|H\right\rangle$ and $A\left|V\right\rangle$ are also orthogonal. We define complex coefficients α and β such that

$$A\left|H\right\rangle = \alpha\left|H\right\rangle + \beta\left|V\right\rangle, \tag{B.12}$$

then due to orthogonality, we must have

$$A\left|V\right\rangle = \pm(\beta^*\left|H\right\rangle - \alpha^*\left|V\right\rangle) \tag{B.13}$$

where the freedom to choose the sign represents an arbitrary global phase. In the following we chose the positive sign.

Applying equation B.11 to the explicit forms of $A|H\rangle$ and $A|V\rangle$, we find

$$e^{2i\sigma}\alpha = \beta^* \tag{B.14}$$

$$e^{2i\sigma}e^{2i\phi}\beta = -\alpha^*, \tag{B.15}$$

from which we find

$$e^{-2i\phi} = -1 \tag{B.16}$$

and therefore

$$\phi = \pm\frac{\pi}{2} \tag{B.17}$$

so

$$\beta = \alpha^* e^{-2i\sigma}. \tag{B.18}$$

As A is unitary, and $|H\rangle$ has unit norm, $A|H\rangle$ must also have unit norm. We can now write

$$A|H\rangle = \frac{1}{\sqrt{2}}(|H\rangle + e^{-2i\sigma}|V\rangle), \tag{B.19}$$

which, however, must have only real coefficients due to the fact that A is real, so can be further simplified to

$$A|H\rangle = \frac{1}{\sqrt{2}}(|H\rangle \pm |V\rangle). \tag{B.20}$$

Going further we find

$$BA|H\rangle = \frac{e^{i\theta}}{\sqrt{2}}(|H\rangle \pm i|V\rangle) \tag{B.21}$$

$$BA|V\rangle = \frac{e^{i\theta}}{\sqrt{2}}(|H\rangle \mp i|V\rangle), \tag{B.22}$$

which are pure circular polarisation states.

Since C has real coefficients, the phase difference between the $|H\rangle$ and $|V\rangle$ components of $BA|H\rangle$ and $BA|V\rangle$ cannot be changed by its operation, the the states only pick up a global phase change. The polarisation states in the cavity are therefore

$$CBA|H\rangle = \frac{e^{i\zeta}}{\sqrt{2}}(|H\rangle \pm i|V\rangle) \tag{B.23}$$

$$CBA|V\rangle = \frac{e^{i\zeta}}{\sqrt{2}}(|H\rangle \mp i|V\rangle), \tag{B.24}$$

where ζ is the combined global phase. We have therefore shown that the operation of adjusting the two wave plate angles to minimise the back reflection through the PBS leads to the $|H\rangle$ and $|V\rangle$ states of the PBS being mapped to the $|L\rangle$ and $|R\rangle$ states inside the cavity.

Appendix C

Scanning cavity lock technique

Since the adjustable cavity mounting structure exhibits a high-Q mechanical resonance near 1.7 kHz, active stabilisation of the cavity length is not possible near this frequency. Mechanical noise on the cavity length which is coupled into the mounting structure has an amplitude of approximately one cavity linewidth, which makes measurements with the system challenging as the cavity is continuously vibrating though the atomic resonance. In this appendix, the novel technique which was developed to overcome this experimental limitation is described.

Generating an error signal for our cavity is difficult for several reasons:

- Since the fibre is only single-mode in the ultraviolet to blue spectral region, and the cavity coating is only specified between 370 nm to 400 nm, we are limited to using this ultraviolet light where optics are lossy to generate an error signal.

- We have measured that the cavity produces noticeable charging effects on the ion after several seconds when we couple approximately 10 µW of light at 399 nm into the cavity. This sets an upper limit on the power we can use for an error signal.

- We only have access to one of the fibre mirrors, as the optical fibre connecting to the second mirror appears to be fractured inside the vacuum chamber.

- The power reflected from the cavity fluctuates on acoustic time-scales by approximately 2 % due to interference which appears to be caused by a reflection from the fibre surface. This is significant since the cavity coupling limits the reflected cavity signal to approximately 9 %.

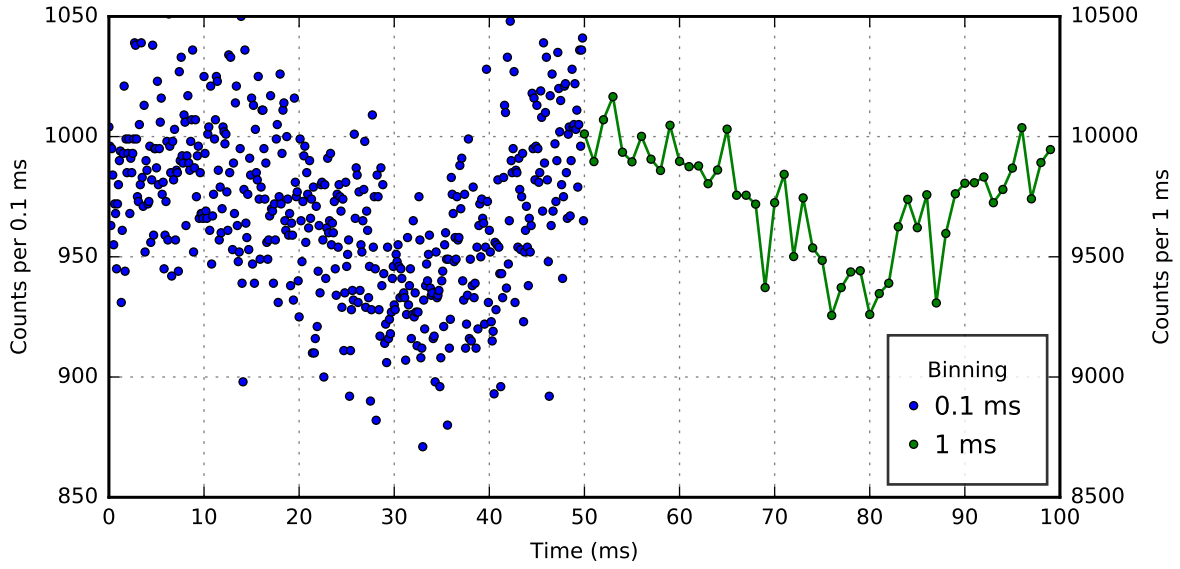

Figure C.1: Histogram of photons reflected from the cavity while the cavity length is scanned back and forth across resonance with the probe laser. The photon arrival times are binned with 0.1 ms and 1 ms binning on the left and right respectively.

- The cavity needs to be locked during measurements which generate single photons near 370 nm, so the error signal must not contribute to the count rate of the single photon counters when they are measuring, but it still needs to be coupled through the same fibre.

One solution to the above problems is to use light near 400 nm to generate the error signal, and employ a dichroic beam splitter or a diffraction grating to combine and separate the error signal light from the 370 nm photons. A diffraction grating would lead to unacceptable losses in the 370 nm path, whereas a dichroic beam splitter to split these two wavelengths would need to be custom manufactured. Furthermore, the optical power used to generate the error signal should be significantly below 10 µW in order to not charge the cavity. Coupled with the low sensitivity of silicon photodiodes and the small signal from the cavity, the opto-electronic system would have to be very well designed in order that the noise is low enough at the required bandwidth.

To avoid these problems, we have chosen to use the photon counters to create an error signal. In the cavity photon analysis setup described in chapter 5.5, probe laser light near 370 nm which is reflected from the fibre-cavity is incident on the single photon detectors. When the laser frequency is fixed and the cavity length is scanned so that the cavity passes across resonance

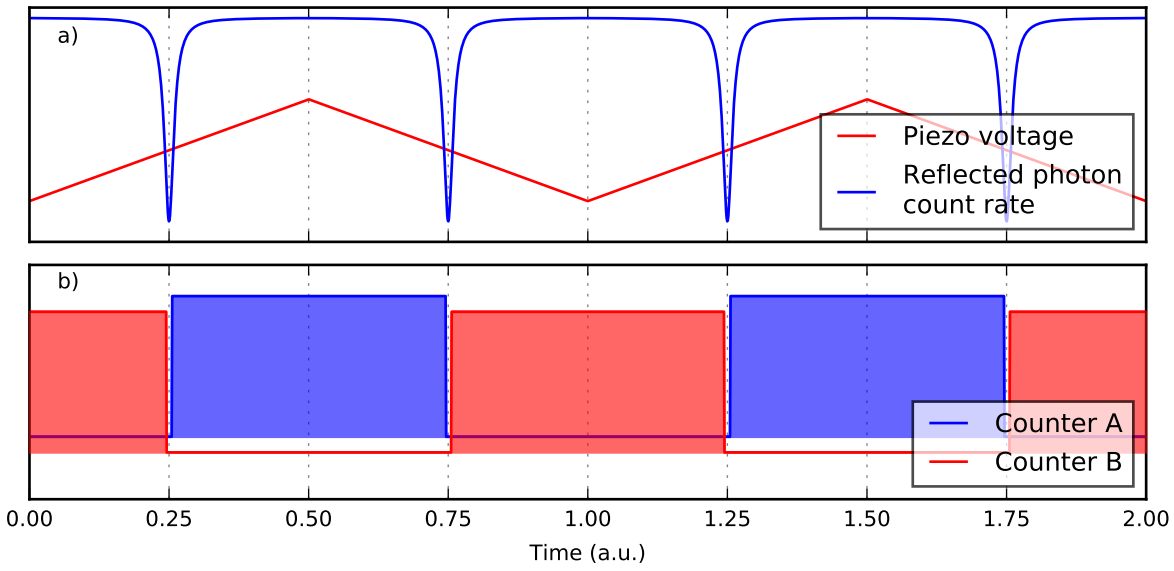

Figure C.2: a) Photon count rate from light reflected by the cavity from the probe laser as the cavity is scanned across resonance using the cavity length piezo. b) Periods during which counters A and B are active in order to generate the cavity error signal.

with the laser, the reflected light has the inverse Lorentzian profile associated with the cavity resonance. Figure C.1 shows a measurement of the photons reflected from the cavity, detected on the H-arm of photon analysis setup. The intensity of the light incident on the cavity is adjusted such that the off-resonant count rate is near the maximum of the detector, 10^7 /s.

From the rate of photons reflected from the cavity, it should be possible to construct an error signal using a side-of-fringe technique. The noise of the count rate signal when dominated by shot noise is given by $\sqrt{n}$ where n is the average number of counts per bin. With the 0.1 ms binning used in figure C.1 shot noise dominates. However, when 1 ms binning is used, acoustic noise in the cavity length becomes the dominant.

We have developed a technique which allows us to derive a digital error signal in real time from the reflected photon count rate, despite the presence of the acoustic vibrations. The cavity length is scanned with the piezo across resonance with the ion by approximately 10 linewidths at a rate of 10 Hz derived from our atomic clock. A probe laser is coupled into the cavity, and the light reflected from the cavity is shown in figure C.2 a). The photon detector, which measures the reflected light, outputs TTL pulses which are picked up by an FPGA which samples the pulses.

Two counters are implemented with the FPGA, counter A and counter B. Both counters are connected to the photon detector, and are read out and reset at a rate of 10 Hz, however the counters are gated alternately with the pulse sequence shown in figure C.2 b). By taking the sum and difference of the two counters, a digital error signal can be generated which is zero when the cavity resonance is centred within the scanning region. In the following, we derive the form of this error signal.

After each full scan, both counters have been gated and read out. We define the error signal to be

$$E = \frac{S^A - S^B}{S^A + S^B} \tag{C.1}$$

where S^A and S^B are the values of counter A and B respectively.

For the first half-period of the scan, where the cavity length is increasing, the number of photons counted by each counter are approximations of integrals

$$\begin{aligned} S^A &= \int_{x_0-\sigma}^{x_0} R(x,\delta)dx \\ S^B &= \int_{x_0}^{x_0+\sigma} R(x,\delta)dx \end{aligned} \tag{C.2}$$

where $R(x,\delta)$ is rate at which photons are reflected by the cavity from the probe laser. This rate is a function of cavity piezo extension, x, with the resonance condition satisfied when $x = \delta$. x_0 is piezo extension at the centre of the scan, and $x_0 \pm \sigma$ are the maximum and minimum extensions reached during the scan.

The numerator of the error signal therefore approximates

$$\int_{x_0-\sigma}^{x_0} R(x,\delta)dx + \int_{x_0}^{x_0+\sigma} R(x,\delta)dx \tag{C.3}$$

$$= 2\int_{x_0}^{x_0+\sigma} R_o(x,\delta)dx \tag{C.4}$$

where $R_o(x,\delta)$ is the odd part of the cavity reflection signal. Similarly, the denominator is given by

$$= 2\int_{x_0}^{x_0+\sigma} R_e(x,\delta)dx \tag{C.5}$$

The power reflected from the cavity is proportional to a Lorentzian centred on the resonance, so

$$R(x,\delta) = \frac{1}{1+(x-\delta)^2} \tag{C.6}$$

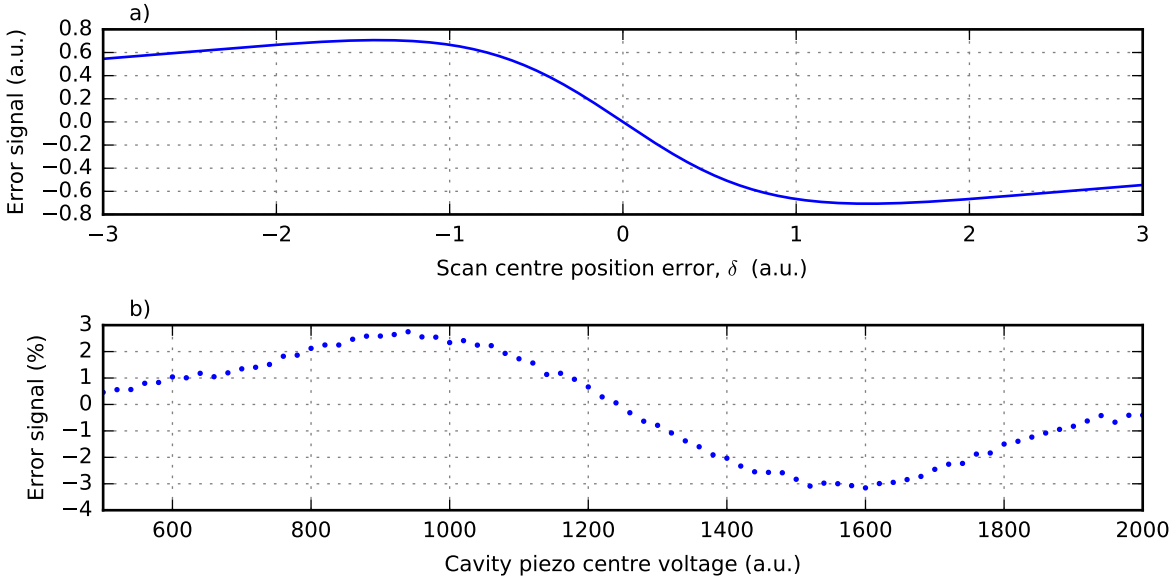

Figure C.3: a) Value of the equation C.7 as a function of the scan centre error, δ. The presence of the linear region about $\delta = 0$ can be used to lock the cavity. b) Experimental measurement of this error signal. Each point is averaged for 1 s, and the measurement is made over and range of different values of the cavity piezo centre voltage, which determines the average length of the cavity.

For this function, the error signal for the first half-period of the scan is given by

$$E(\delta) = \frac{-2\delta\sigma}{1+\delta^2+\sigma^2} \tag{C.7}$$

where δ is piezo extension when the cavity is on resonance with the probe laser. The value of the error signal for the second half-period, similarly, is the same as the first.

The important result of equation C.7 is that the error signal is an odd function and is approximately linear for small values of δ. This feature can now be used to create a feedback loop which keeps $\delta \approx x_0$ over time-scales longer than the scan period, thereby keeping the piezo extension scanning about the extension where the cavity is on resonance with the probe laser. This error signal is shown in figure C.3 a).

Figure C.3 b) shows this error signal for our cavity generated in this way for changes in the cavity piezo centre voltage. The cavity piezo is driven with a triangle wave at 10 Hz centred about this voltage, similar to that shown in figure C.2. This error signal clearly shows the linear behaviour near resonance expected from equation C.7.

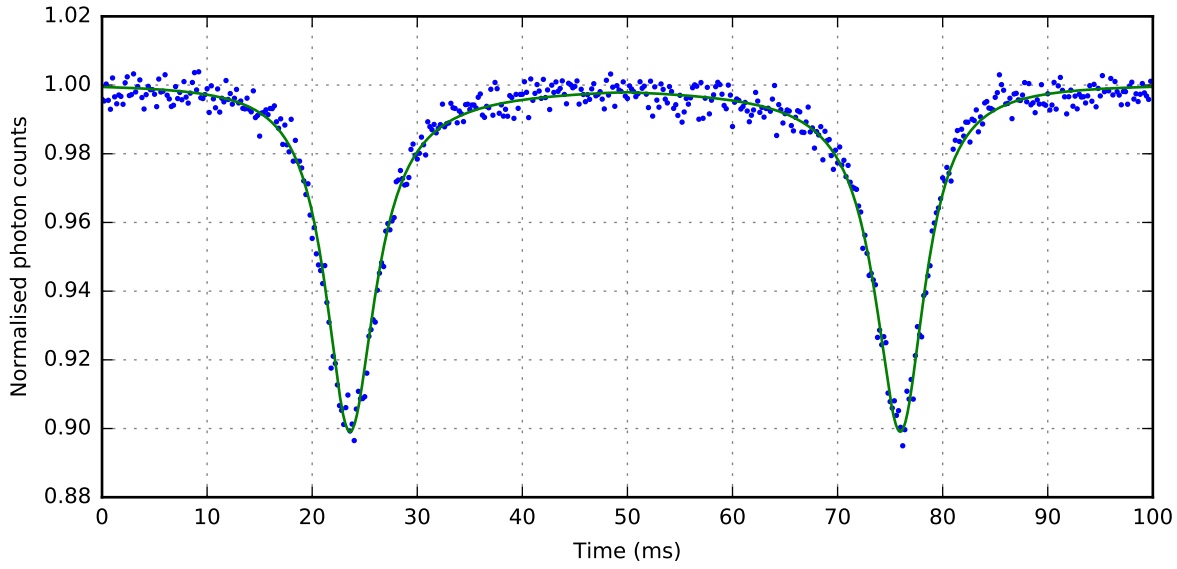

Figure C.4: Measurement of the cavity reflection signal averaged over 10 s with the cavity length stabilised using the method described here. The Lorentzian line-shape of the fibre-cavity reflection signal is clearly visible, and has been used to determine the impedance matching of the cavity mirrors after the occurrence of the intracavity losses associated with UHV (see chapter 4.4.

The error signal generated in this way is digitally read out from the FPGA and fed into a simple digital PID feedback loop which controls the cavity piezo centre voltage, and stabilises the average cavity length such that the cavity is on resonance with the probe laser at the centre of the scan. With this, it is possible to average the cavity reflection signal for long times. Fluctuations over short time-scale will still be present, but if they are not phase stable with the cavity scan, they will be averaged out. Figure C.4 shows a measurement of power reflected from the cavity measured over 10 seconds with the cavity locked using this technique. This can be compared to figure C.1 which shows the signal-to-noise of the data before averaging.

While the cavity is locked using this technique, although the cavity is continuously scanned across resonance with the laser, its average detuning at a given point in time is known due to the phase lock. When data is recorded which is sensitive to the cavity detuning, such at the measurements presented in chapter 6.3 and 6.4, the experimental data will exhibit a time-correlation with the cavity detuning. By binning the experimental data based on its phase relative to the cavity scan signal, the detuning of the cavity can be accurately determined. Additionally, the

lock laser can be strobed during an experimental sequence so that it does not interact with the ion when it is being measured.

C.1 Noise analysis

In order to validate the use of this averaging method on our experimental data, a numerical study has been performed on the effect of the averaging on the cavity reflection signal. The response of the cavity is simulated in the presence of noise acting on the cavity length by sampling from a Gaussian distribution of variance σ_n^2. Individual noisy measurements can then be added together to form an average in the same way as in the experiment.

Figure C.5 shows the resulting cavity reflection signal for varying degrees of noise, both a) before and b) after averaging. The effectiveness of this method in improving the signal to noise of the data is visible, however a systematic broadening of the Lorentzian cavity profile after averaging is visible when the standard deviation of the cavity length noise approaches the cavity linewidth in length terms. The simulated data does not take into account additional shot noise which is present in the experiment due to the Poissonian statistics of the photon counting. The shot noise will not lead to any broadening of the apparent Lorentzian.

The effect of the broadening due to cavity length noise is explored further in figure C.6. Here, a simulation using an average from 100 samples is performed and the resulting curve is fitted with a Lorentzian. Figure C.6 a) shows two of the fitted curves with cavity length noise of $\sigma_n/\Delta\nu_c = 0$ and 0.5. From this data, we see that the Lorentzian curve does not match the profile perfectly after averaging when significant noise is present. Figure C.6 b) shows the fitted value of the Lorentzian FWHM for a series of simulated data with length noise between the two datasets shown in a). We observe that the apparent width of the feature indeed increases significantly when the length noise is comparable to the cavity linewidth.

In order to determine whether our experimental data, which employs this averaging method, is systematically broadened, we need to determine the degree of cavity length noise that is present.

Figure C.7 a) shows a fit to simulated data with a Lorentzian and a Voigt profile[1]. The fit residuals for the Lorentzian curve (red in figure C.7 a)) appear to have a slightly non-statistical form, however, the fit residuals for the Voigt curve appear to be purely statistically distributed.

[1]In order for the simulation to match the experimental data as best as possible, the simulated data here is formed from using a slightly dispersive Lorentzian line-shape[85]. The function used to perform the fit is therefore a 'dispersive' Voigt profile formed by convolution of a Gaussian kernel with a dispersive Lorentzian.

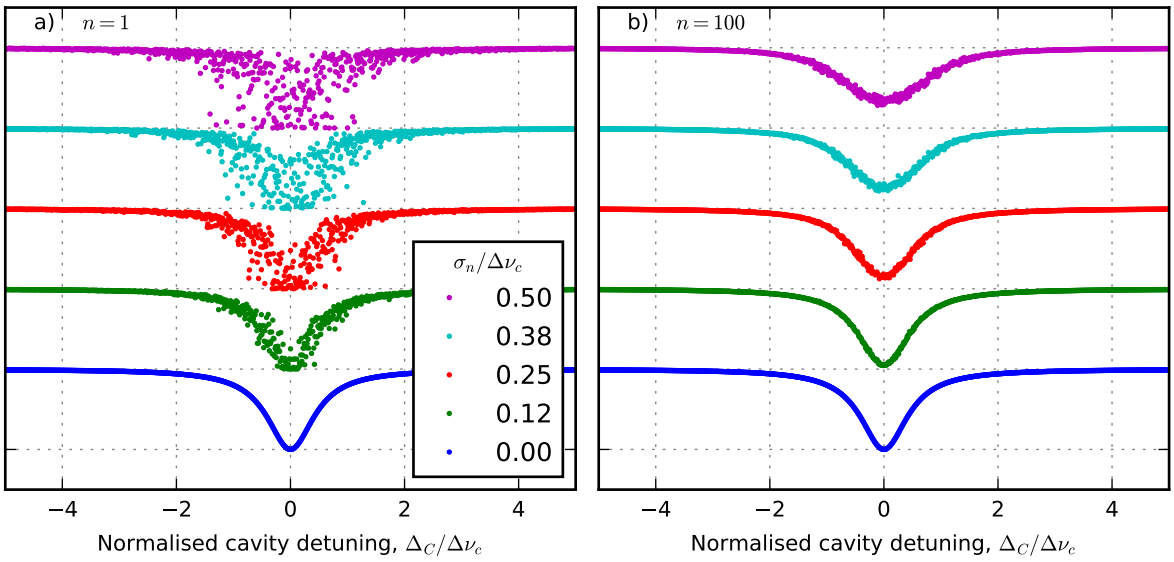

Figure C.5: Simulated cavity reflectance scans with varying degrees of noise on the cavity length. a) Single scans. b) Average of 100 scans. The cavity length is modulated by *noise* sampled from a Gaussian distribution with variance σ_{n}^2 in units of the simulated cavity linewidth $\Delta\nu_{\mathrm{c}}$. These results show in this case that when the variance of the cavity length noise is comparable to the cavity linewidth, the averaged scan will appear broader than the actual cavity linewidth.

The Voigt fit provides a value for the Gaussian kernel standard deviation of $\sigma_g/\Delta\nu_{\mathrm{c}} \approx 0.5$ which approximately matches standard deviation of the cavity length noise used to generate the simulated data ($\sigma_n/\Delta\nu_{\mathrm{c}} = 0.5$). The correspondence of the Voigt profile Gaussian width to the cavity length noise is not coincidental, and can actually be seen as a result of application of the central limit theorem to the successive sampling of the data.

The correspondence between the Voigt profile Gaussian width and the cavity length noise can be used to identify the level of noise present in the experimental data. The reflection signal of the scanning locked cavity from figure C.4 with Lorentz and Voigt profile fits is shown in figure C.7 b). Upon inspection of the fit residuals, the experimental data does not show any systematic error consistent with the systematic broadening investigated here. The precise level of the cavity length noise is not clear due to the presence of shot noise in the data, however an upper bound of $\sigma_{\mathrm{n}}/\Delta\nu_{\mathrm{c}} < 0.5$ can be given by comparison to the simulated data in figure C.7 a). This means that the apparent width of the cavity reflection signal cannot have a systematic

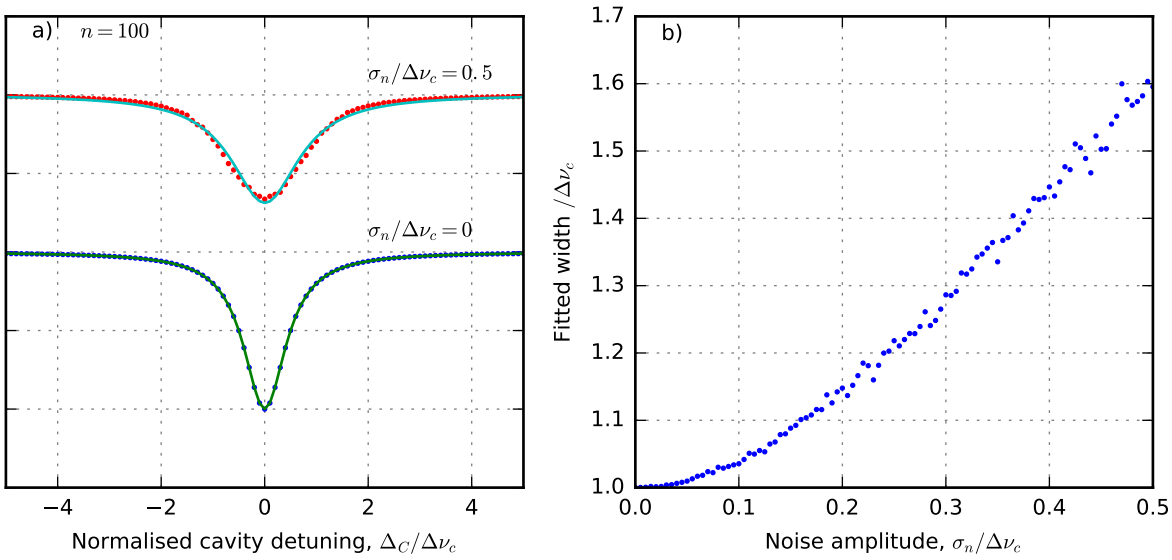

Figure C.6: The effects of fitting to averaged noisy data. a) Two sets of averaged simulated data with $\sigma_n/\Delta\nu_c = 0$ and 0.5, fitted with a Lorentzian profile. b) The fitted value of the Lorentzian FWHM for a series of different values of cavity length noise, σ_n.

broadening of more than 60 % based on comparison with the fitted widths in figure C.6 b).

The analysis here has been performed with the Lorentzian line-shape of the power reflected from the cavity as it is scanned. The experimental data showing the interaction between the atom and the cavity presented in chapter 6, however, consists of measurements of the fluorescence from the ion, averaged in the same way. Since the interaction of the cavity with the ion is dependent on the field strength of the cavity mode, rather and the intensity, the full width at half maximum of features probed in this way is larger by a factor of $\sqrt{3}$[2]. The increase in the feature size will reduce the impact of systematic broadening from the averaging for measurements of the fluorescence from the ion.

[2]This is because the electric field at the ion is the square root of the intensity at the ion which follows a Lorentzian, and the FWHM of the square root of a Lorentzian is $\sqrt{3}$ times the FWHM of the Lorentzian.

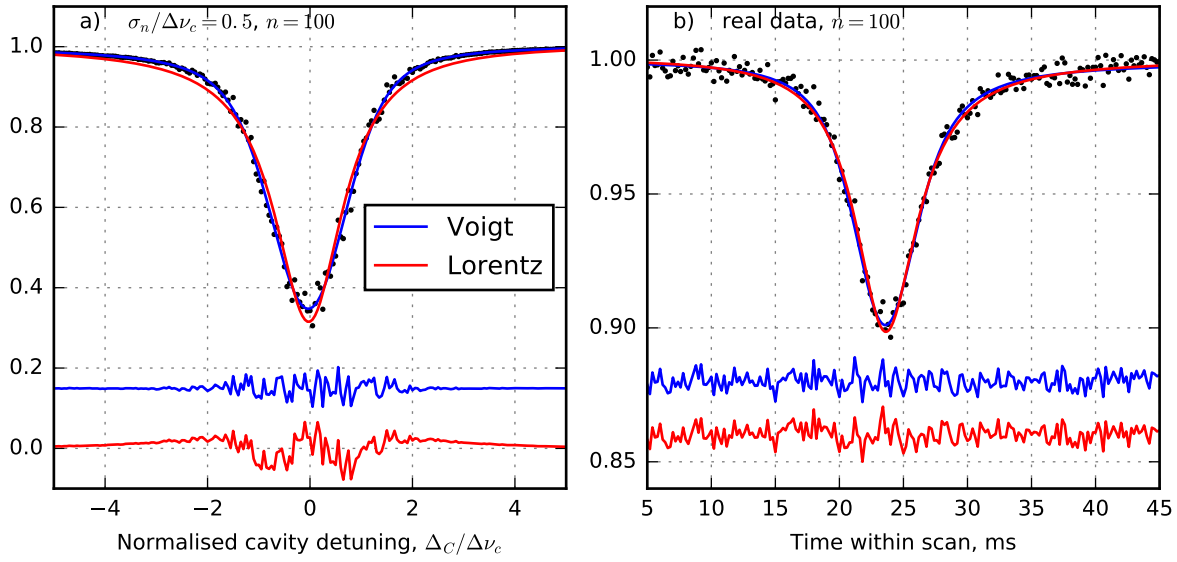

Figure C.7: The result of fitting a) simulated data and b) real data with Voigt profiles (blue) versus Lorentz profiles (red). The respective residuals of the fit are plotted in the bottom section of the graphs.

Appendix D

Cavity linewidth measurement

In this appendix the measurement used to determine the cavity linewidth after its degradation in vacuum is described. Earlier measurements of the linewidth of this cavity were performed by modulating side-bands at 2.1 GHz onto a laser which probes the cavity in reflection. However, after exposure of the cavity to ultra-high vacuum it was no longer possible to resolve the optical side-bands Since the intracavity losses increased significantly, the linewidth increased above the range which was measurable with the electro-optical modulators which were available. Instead, cavity linewidth was measured using the scanning cavity lock technique described in appendix C and the cavity induced back-action described in chapter 6.4.

With the scanning cavity lock technique, the length of the cavity is stabilised such that the cavity is resonant at the centre of the scan with the lock laser used to generate the error signal. When the frequency of the lock laser is changed, the length of the cavity is also changed. A measurement of the back-action of the cavity, like those described in chapter 6.4, is sensitive to the absolute frequency of cavity, and is independent of the lock laser. By measuring the centre position of the back-action Fano-like profile relative to the reflection resonance with the lock laser, it is possible to determine the absolute linewidth of the cavity.

Figure D.1 shows a dataset used to measure the cavity linewidth. The cavity-induced back-action was measured as before in chapter 6.4 with $\Delta_L = -\Gamma$, providing a clear signal to fit equation 6.12 to. The laser used to generate the error signal, which previously had been tuned to the atomic resonance, is now detuned red and blue by several hundred MHz using a wavemeter lock. As before, the cavity lock light is strobed such that it does not interact with the ion while the population is being measured.

Each curve is fitted and the difference between the cavity reflection signal resonance and

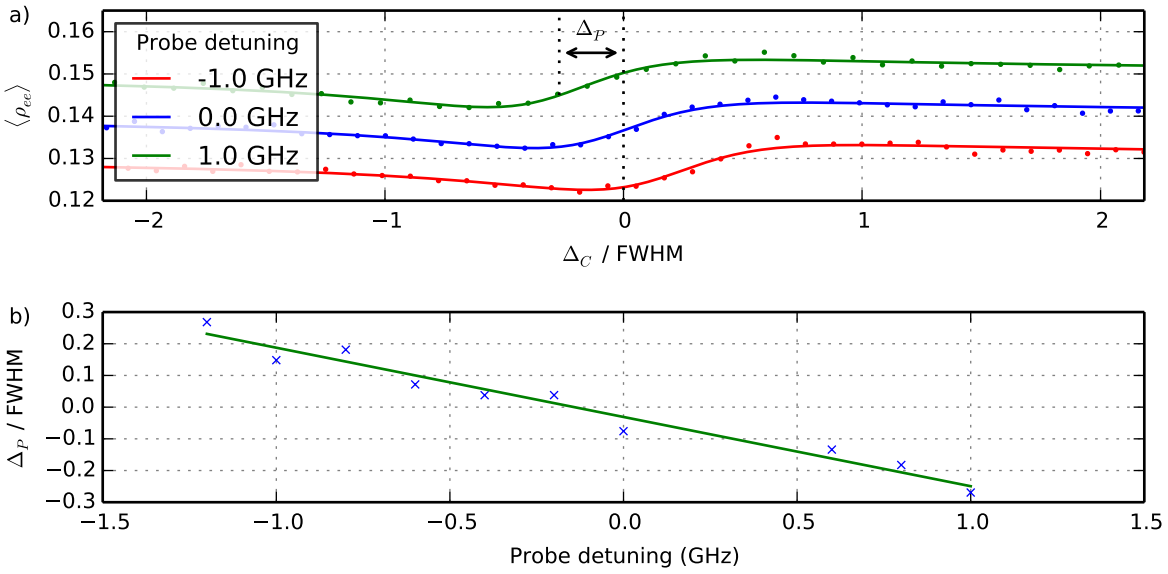

Figure D.1: a) Measurement of the cavity-induced excited state population modulation for a fixed side-laser power and detuning ($s = 2.75$ and $\Delta_L = -\Gamma$), for three different values of the cavity lock laser detuning. The experimental fits provide a measurement of the offset between the cavity resonance and the atomic resonance (Δ_P) in terms of the cavity FWHM. b) Δ_P is measured for several different laser detunings, and the gradient is fitted to determine the FWHM. This measurement indicates the cavity linewidth is (4.78 ± 0.10) GHz.

the atomic feature centre, Δ_P, is calculated in terms of the cavity FWHM. Figure D.1 b) shows a plot of each measured Δ_P versus the cavity lock laser frequency. The gradient of the resulting line provides a measurement of the cavity linewidth, which was found to be (4.78 ± 0.10) GHz.

Bibliography

[1] J. P. Dowling and G. J. Milburn. "Quantum technology: the second quantum revolution". In: *Philosophical Transactions of the Royal Society A: Mathematical, Physical and Engineering Sciences* 361.1809 (Aug. 2003), pp. 1655–1674. DOI: 10.1098/rsta.2003.1227.

[2] R. P. Feynman. "Simulating physics with computers". In: *International Journal of Theoretical Physics* 21.6-7 (June 1982), pp. 467–488. DOI: 10.1007/BF02650179.

[3] V. Giovannetti, S. Lloyd, and L. Maccone. "Quantum Metrology". In: *Physical Review Letters* 96.1 (Jan. 2006), p. 010401. DOI: 10.1103/PhysRevLett.96.010401. arXiv: arXiv:1102.2318v1.

[4] A. K. Ekert. "Quantum cryptography based on Bell's theorem". In: *Physical Review Letters* 67.6 (Aug. 1991), pp. 661–663. DOI: 10.1103/PhysRevLett.67.661. arXiv: 0911.4171v2.

[5] H. J. Kimble. "The quantum internet". In: *Nature* 453.7198 (June 2008), pp. 1023–30. DOI: 10.1038/nature07127.

[6] Y. Makhlin, G. Schön, and A. Shnirman. "Quantum-state engineering with Josephson-junction devices". In: *Reviews of Modern Physics* 73.2 (May 2001), pp. 357–400. DOI: 10.1103/RevModPhys.73.357. arXiv: 0011269 [cond-mat].

[7] D. Loss and D. P. DiVincenzo. "Quantum computation with quantum dots". In: *Physical Review A* 57.1 (Jan. 1998), pp. 120–126. DOI: 10.1103/PhysRevA.57.120. arXiv: 9701055 [cond-mat].

[8] L. Childress and R. Hanson. "Diamond NV centers for quantum computing and quantum networks". In: *MRS Bulletin* 38.02 (Feb. 2013), pp. 134–138. DOI: 10.1557/mrs.2013.20.

[9] H. J. Briegel, T. Calarco, D. Jaksch, J. I. Cirac, and P. Zoller. “Quantum computing with neutral atoms”. In: *Journal of Modern Optics* 47.2-3 (Feb. 2000), pp. 415–451. DOI: 10.1080/09500340008244052. arXiv: 9904010 [quant-ph].

[10] J. I. Cirac and P. Zoller. “Quantum Computations with Cold Trapped Ions”. In: *Physical Review Letters* 74.20 (May 1995), pp. 4091–4094. DOI: 10.1103/PhysRevLett.74.4091.

[11] C. H. Bennett, G. Brassard, C. Crépeau, R. Jozsa, A. Peres, and W. K. Wootters. “Teleporting an unknown quantum state via dual classical and Einstein-Podolsky-Rosen channels”. In: *Physical Review Letters* 70.13 (Mar. 1993), pp. 1895–1899. DOI: 10.1103/PhysRevLett.70.1895. arXiv: 9710013 [quant-ph].

[12] D. Bouwmeester, J.-W. Pan, K. Mattle, M. Eibl, H. Weinfurter, and A. Zeilinger. “Experimental quantum teleportation”. In: *Nature* 390.6660 (Dec. 1997), pp. 575–579. DOI: 10.1038/37539.

[13] M. A. Nielsen, E. Knill, and R. Laflamme. “Complete quantum teleportation using nuclear magnetic resonance”. In: *Nature* 396.6706 (Nov. 1998), pp. 52–55. DOI: 10.1038/23891.

[14] M. D. Barrett, J. Chiaverini, T. Schaetz, J. Britton, W. M. Itano, J. D. Jost, E. Knill, C. Langer, D. Leibfried, R. Ozeri, and D. J. Wineland. “Deterministic quantum teleportation of atomic qubits”. In: *Nature* 429.6993 (June 2004), pp. 737–739. DOI: 10.1038/nature02608.

[15] M. Riebe, H. Häffner, C. F. Roos, W. Hänsel, J. Benhelm, G. P. T. Lancaster, T. W. Körber, C. Becher, F. Schmidt-Kaler, D. F. V. James, and R. Blatt. “Deterministic quantum teleportation with atoms”. In: *Nature* 429.6993 (June 2004), pp. 734–737. DOI: 10.1038/nature02570.

[16] A. Aspect, P. Grangier, and G. Roger. “Experimental Tests of Realistic Local Theories via Bell’s Theorem”. In: *Physical Review Letters* 47.7 (Aug. 1981), pp. 460–463. DOI: 10.1103/PhysRevLett.47.460.

[17] P. G. Kwiat, K. Mattle, H. Weinfurter, A. Zeilinger, A. V. Sergienko, and Y. Shih. “New High-Intensity Source of Polarization-Entangled Photon Pairs”. In: *Physical Review Letters* 75.24 (Dec. 1995), pp. 4337–4341. DOI: 10.1103/PhysRevLett.75.4337.

[18] R. Valivarthi, M. G. Puigibert, Q. Zhou, G. H. Aguilar, V. B. Verma, F. Marsili, M. D. Shaw, S. W. Nam, D. Oblak, and W. Tittel. "Quantum teleportation across a metropolitan fibre network". In: *Nature Photonics* September (2016), pp. 1–6. DOI: 10.1038/nphoton.2016.180. arXiv: 1605.08814.

[19] Q. C. Sun, Y. L. Mao, S. J. Chen, W. Zhang, Y. F. Jiang, Y. B. Zhang, W. J. Zhang, S. Miki, T. Yamashita, H. Terai, X. Jiang, T. Y. Chen, L. X. You, X. F. Chen, Z. Wang, J. Y. Fan, Q. Zhang, and J. W. Pan. "Quantum teleportation with independent sources over an optical fibre network". In: *Nature Photonics* September (2016), pp. 1–11. DOI: 10.1038/nphoton.2016.179. arXiv: 1602.07081.

[20] H. Krovi, S. Guha, Z. Dutton, J. A. Slater, C. Simon, and W. Tittel. "Practical quantum repeaters with parametric down-conversion sources". In: *Applied Physics B* 122.3 (Mar. 2016), p. 52. DOI: 10.1007/s00340-015-6297-4. arXiv: 1505.03470.

[21] D. L. Moehring, P. Maunz, S. Olmschenk, K. C. Younge, D. N. Matsukevich, L.-M. Duan, and C. Monroe. "Entanglement of single-atom quantum bits at a distance". In: *Nature* 449.7158 (Sept. 2007), pp. 68–71. DOI: 10.1038/nature06118.

[22] S. Ritter, C. Nölleke, C. Hahn, A. Reiserer, A. Neuzner, M. Uphoff, M. Mücke, E. Figueroa, J. Bochmann, and G. Rempe. "An elementary quantum network of single atoms in optical cavities". In: *Nature* 484.7393 (Apr. 2012), pp. 195–200. DOI: 10.1038/nature11023.

[23] H. Bernien, B. Hensen, W. Pfaff, G. Koolstra, M. S. Blok, L. Robledo, T. H. Taminiau, M. Markham, D. J. Twitchen, L. Childress, and R. Hanson. "Heralded entanglement between solid-state qubits separated by three metres". In: *Nature* 497.7447 (2013), pp. 86–90. DOI: 10.1038/nature12016. arXiv: 1212.6136.

[24] A. Delteil, Z. Sun, W. B. Gao, E. Togan, S. Faelt, and A. Imamo lu. "Generation of heralded entanglement between distant hole spins". In: *Nature Physics* 12.3 (Dec. 2015), pp. 218–223. DOI: 10.1038/nphys3605. arXiv: arXiv:1507.00465v1.

[25] D. P. DiVincenzo. "The Physical Implementation of Quantum Computation". In: *Fortschritte der Physik* 48.9-11 (2000), pp. 771–783. DOI: 10.1002/1521-3978(200009)48:9/11<771::AID-PROP771>3.0.CO;2-E. arXiv: 0002077 [quant-ph].

[26] C. J. Ballance, T. P. Harty, N. M. Linke, M. A. Sepiol, and D. M. Lucas. "High-Fidelity Quantum Logic Gates Using Trapped-Ion Hyperfine Qubits". In: *Physical Review Letters* 117.6 (2016), p. 060504. DOI: 10.1103/PhysRevLett.117.060504.

[27] E. Knill. “Quantum computing with realistically noisy devices.” In: *Nature* 434.7029 (2005), pp. 39–44. DOI: 10.1038/nature03350. arXiv: 0410199 [quant-ph].

[28] R. Maiwald, D. Leibfried, J. Britton, J. C. Bergquist, G. Leuchs, and D. J. Wineland. “Stylus ion trap for enhanced access and sensing”. In: *Nature Physics* 5.8 (Aug. 2009), pp. 551–554. DOI: 10.1038/nphys1311.

[29] E. W. Streed, B. G. Norton, J. J. Chapman, and D. Kielpinski. “Scalable, efficient ion-photon coupling with phase Fresnel lenses for large-scale quantum computing”. In: *Quantum Information and Computation* 9.3-4 (2009), pp. 0203–0214. arXiv: arXiv:0805.2437v1.

[30] C. K. Law and H. J. Kimble. “Deterministic generation of a bit-stream of single-photon pulses”. In: *Journal of Modern Optics* 44.11-12 (Nov. 1997), pp. 2067–2074. DOI: 10.1080/09500349708231869.

[31] M. Pelton, C. Santori, J. Vucković, B. Zhang, G. S. Solomon, J. Plant, and Y. Yamamoto. “Efficient Source of Single Photons: A Single Quantum Dot in a Micropost Microcavity”. In: *Physical Review Letters* 89.23 (Nov. 2002), p. 233602. DOI: 10.1103/PhysRevLett.89.233602. arXiv: 0208054 [quant-ph].

[32] J. McKeever, A. Boca, A. D. Boozer, R. Miller, J. R. Buck, A. Kuzmich, and H. J. Kimble. “Deterministic Generation of Single Photons from One Atom Trapped in a Cavity”. In: *Science* 303.5666 (Mar. 2004), pp. 1992–1994. DOI: 10.1126/science.1095232.

[33] C. H. Su, A. D. Greentree, and L. C. L. Hollenberg. “Towards a picosecond transform-limited nitrogen-vacancy based single photon source”. In: *Optics Express* 16.9 (Apr. 2008), p. 6240. DOI: 10.1364/OE.16.006240. arXiv: 0711.3505.

[34] M. Keller, B. Lange, K. Hayasaka, W. Lange, and H. Walther. “A calcium ion in a cavity as a controlled single-photon source”. In: *New Journal of Physics* 6 (2004), pp. 1–22. DOI: 10.1088/1367-2630/6/1/095.

[35] A. Stute, B. Casabone, B. Brandstätter, D. Habicher, H. G. Barros, P. O. Schmidt, T. E. Northup, and R. Blatt. “Toward an ion-photon quantum interface in an optical cavity”. In: *Applied Physics B* 107.4 (June 2012), pp. 1145–1157. DOI: 10.1007/s00340-011-4861-0.

[36] T. Steinmetz, Y. Colombe, D. Hunger, T.W. Hänsch, A. Balocchi, R. J. Warburton, and J. Reichel. "Stable fiber-based Fabry-Pérot cavity". In: *Applied Physics Letters* 89.11 (2006), pp. 3–6. DOI: 10.1063/1.2347892. arXiv: 0606231v1 [arXiv:physics].

[37] D. Hunger, T. Steinmetz, Y. Colombe, C. Deutsch, T.W. Hänsch, and J. Reichel. "A fiber Fabry-Perot cavity with high finesse". In: *New Journal of Physics* 12.6 (June 2010), p. 065038. DOI: 10.1088/1367-2630/12/6/065038.

[38] Y. Colombe, T. Steinmetz, G. Dubois, F. Linke, D. Hunger, and J. Reichel. "Strong atom–field coupling for Bose–Einstein condensates in an optical cavity on a chip". In: *Nature* 450.November (2007), p. 272. DOI: 10.1038/nature06331. arXiv: 0706.1390.

[39] J. Miguel-Sánchez, A. Reinhard, E. Togan, T. Volz, A. Imamoglu, B. Besga, J. Reichel, and J. Estève. "Cavity quantum electrodynamics with charge-controlled quantum dots coupled to a fiber Fabry-Perot cavity". In: *New Journal of Physics* 15.4 (Apr. 2013), p. 045002. DOI: 10.1088/1367-2630/15/4/045002. arXiv: 1211.4515.

[40] R. Albrecht, A. Bommer, C. Deutsch, J. Reichel, and C. Becher. "Coupling of a Single Nitrogen-Vacancy Center in Diamond to a Fiber-Based Microcavity". In: *Physical Review Letters* 110.24 (June 2013), p. 243602. DOI: 10.1103/PhysRevLett.110.243602.

[41] M. Steiner, H. M. Meyer, C. Deutsch, J. Reichel, and M. Köhl. "Single Ion Coupled to an Optical Fiber Cavity". In: *Physical Review Letters* 110.4 (Jan. 2013), p. 043003. DOI: 10.1103/PhysRevLett.110.043003.

[42] H. Takahashi, A. Wilson, A. Riley-Watson, F. Oručević, N. Seymour-Smith, M. Keller, and W. Lange. "An integrated fiber trap for single-ion photonics". In: *New Journal of Physics* 15.5 (May 2013), p. 053011. DOI: 10.1088/1367-2630/15/5/053011.

[43] B. Brandstätter, A. McClung, K. Schüppert, B. Casabone, K. Friebe, A. Stute, P. O. Schmidt, C. Deutsch, J. Reichel, R. Blatt, and T. E. Northup. "Integrated fiber-mirror ion trap for strong ion-cavity coupling". In: *Review of Scientific Instruments* 84.12 (2013), pp. 1–17. DOI: 10.1063/1.4838696. arXiv: arXiv:1311.6961v1.

[44] T. G. Ballance, H. M. Meyer, P. Kobel, K. Ott, J. Reichel, and M. Köhl. "Cavity-induced backaction in Purcell-enhanced photon emission of a single ion in an ultraviolet fiber cavity". In: *Phys. Rev. A* 95 (3 Mar. 2017), p. 033812. DOI: 10.1103/PhysRevA.95.033812.

[45] C. J. Foot. *Atomic physics*. Oxford University Press, 2005.

[46] C. Cohen-Tannoudji, B. Diu, and F. Laloe. *Quantum Mechanics - Volume one*. Wiley VCH, 1977.

[47] P. Meystre and M. Sargent. *Elements of quantum optics*. 4th. Springer, 2007. DOI: 10.1007/978-3-540-74211-1. arXiv: arXiv:1011.1669v3.

[48] M. Fox. *Quantum optics*. Oxford University Press, 2006.

[49] M. O. Scully and M. S. Zubairy. *Quantum Optics*. Cambridge University Press, 1997.

[50] C. J. Hood, M. S. Chapman, T. W. Lynn, and H. J. Kimble. "Real-Time Cavity QED with Single Atoms". In: *Physical Review Letters* 80.19 (May 1998), pp. 4157–4160. DOI: 10.1103/PhysRevLett.80.4157.

[51] K. M. Birnbaum, A. Boca, R. Miller, A. D. Boozer, T. E. Northup, and H. J. Kimble. "Photon blockade in an optical cavity with one trapped atom". In: *Nature* 436.7047 (July 2005), pp. 87–90. DOI: 10.1038/nature03804. arXiv: 0507065 [quant-ph].

[52] S. Rosenblum, S. Parkins, and B. Dayan. "Photon routing in cavity QED: Beyond the fundamental limit of photon blockade". In: *Physical Review A* 84.3 (Sept. 2011), p. 033854. DOI: 10.1103/PhysRevA.84.033854. arXiv: 1109.1197.

[53] W. Paul and M. Raether. "Das elektrische massenfilter". In: *Zeitschrift für Physik* 273.1955 (1955).

[54] J. E. Sträng. "On the characteristic exponents of Floquet solutions to the Mathieu equation". In: *arXiv preprint* (Oct. 2005), pp. 7–12. arXiv: 0510076 [math-ph].

[55] D. Leibfried, R. Blatt, C. Monroe, and D. J. Wineland. "Quantum dynamics of single trapped ions". In: *Reviews of Modern Physics* 75.1 (2003), pp. 281–324.

[56] H. G. Dehmelt. "Radiofrequency Spectroscopy of Stored Ions I: Storage". In: *Advances in Atomic, Molecular and Optical Physics* 3.C (1967), pp. 53–72. DOI: 10.1016/S0065-2199(08)60170-0.

[57] D. J. Berkeland, J. D. Miller, J. C. Bergquist, W. M. Itano, and D. J. Wineland. "Minimization of ion micromotion in a Paul trap". In: *Journal of Applied Physics* 83.10 (1998), p. 5025. DOI: 10.1063/1.367318. arXiv: 1211.0101.

[58] G. R. Guthöhrlein, M. Keller, K. Hayasaka, W. Lange, and H. Walther. "A single ion as a nanoscopic probe of an optical field." In: *Nature* 414.6859 (Nov. 2001), pp. 49–51. DOI: 10.1038/35102129.

[59] A. B. Mundt, A. Kreuter, C. Becher, D. Leibfried, J. Eschner, F. Schmidt-Kaler, and R. Blatt. "Coupling a single atomic quantum bit to a high finesse optical cavity." In: *Physical review letters* 89.10 (2002), p. 103001. DOI: 10.1103/PhysRevLett.89.103001. arXiv: 0202112 [quant-ph].

[60] M. Keller, B. Lange, K. Hayasaka, W. Lange, and H. Walther. "Deterministic coupling of single ions to an optical cavity". In: *Applied Physics B: Lasers and Optics* 76.2 (2003), pp. 125–128. DOI: 10.1007/s00340-003-1114-x.

[61] C. Russo, H. G. Barros, A. Stute, F. Dubin, E. S. Phillips, T. Monz, T. E. Northup, C. Becher, T. Salzburger, H. Ritsch, P. O. Schmidt, and R. Blatt. "Raman spectroscopy of a single ion coupled to a high-finesse cavity". In: *Applied Physics B* 95.2 (May 2009), pp. 205–212. DOI: 10.1007/s00340-009-3430-2. arXiv: 0810.2792.

[62] P. Herskind, A. Dantan, M. B. Langkilde-Lauesen, A. Mortensen, J. L. Sørensen, and M. Drewsen. "Loading of large ion Coulomb crystals into a linear Paul trap incorporating an optical cavity". In: *Applied Physics B: Lasers and Optics* 93.2-3 (2008), pp. 373–379. DOI: 10.1007/s00340-008-3199-8. arXiv: 0804.4589.

[63] J. D. Sterk, L. Luo, T. A. Manning, P. Maunz, and C. Monroe. "Photon collection from a trapped ion-cavity system". In: *Physical Review A - Atomic, Molecular, and Optical Physics* 85.6 (2012), pp. 1–8. DOI: 10.1103/PhysRevA.85.062308. arXiv: 1112.4489.

[64] J. D. Sterk. "Enhanced light collection from single trapped ions". PhD thesis. University of Michigan, 2011.

[65] A. D. Pfister, M. Salz, M. Hettrich, U. G. Poschinger, and F. Schmidt-Kaler. "A quantum repeater node with trapped ions: a realistic case example". In: *Applied Physics B* 122.4 (2016), p. 89. DOI: 10.1007/s00340-016-6362-7. arXiv: 1508.05272.

[66] A. Márquez Seco, H. Takahashi, and M. Keller. "Novel Ion Trap Design for Strong Ion-Cavity Coupling". In: *Atoms* 4.2 (2016), p. 15. DOI: 10.3390/atoms4020015.

[67] A. G. Riley-Watson. "A fibre-based single-photon source". PhD thesis. University of Sussex, 2012.

[68] C. A. Schrama, E. Peik, W. W. Smith, and H. Walther. "Novel miniature ion traps". In: *Optics communications* 101.1 (1993), pp. 32–36.

[69] K. Singer, U. G. Poschinger, M. Murphy, P. Ivanov, F. Ziesel, T. Calarco, and F. Schmidt-Kaler. "Colloquium: Trapped ions as quantum bits: Essential numerical tools". In: *Reviews of Modern Physics* 82.3 (2010), pp. 2609–2632. DOI: 10.1103/RevModPhys.82.2609. arXiv: 0912.0196.

[70] D. J. Wineland, R. E. Drullinger, and F. L. Walls. "Radiation-Pressure Cooling of Bound Resonant Absorbers". In: *Physical Review Letters* 40.25 (June 1978), pp. 1639–1642. DOI: 10.1103/PhysRevLett.40.1639. arXiv: arXiv:1011.1669v3.

[71] W. Neuhauser, M. Hohenstatt, P. Toschek, and H. Dehmelt. "Optical-Sideband Cooling of Visible Atom Cloud Confined in Parabolic Well". In: *Physical Review Letters* 41.4 (July 1978), pp. 233–236. DOI: 10.1103/PhysRevLett.41.233.

[72] J. I. Cirac, L. J. Garay, R. Blatt, A. S. Parkins, and P. Zoller. "Laser cooling of trapped ions: The influence of micromotion". In: *Physical Review A* 49.1 (Jan. 1994), pp. 421–432. DOI: 10.1103/PhysRevA.49.421.

[73] W. M. Itano and D. J. Wineland. "Laser cooling of ions stored in harmonic and Penning traps". In: *Physical Review A* 25.1 (1982), pp. 35–54. DOI: 10.1103/PhysRevA.25.35.

[74] N. Kjaergaard, L. Hornekaer, A. M. Thommesen, Z. Videsen, and M. Drewsen. "Isotope selective loading of an ion trap using resonance-enhanced two-photon ionization". In: *Applied Physics B* 71.2 (2000), pp. 207–210. DOI: 10.1007/s003400000296.

[75] Y. Onoda, K. Sugiyama, M. Ikeda, and M. Kitano. "Loading rate of Yb+ loaded through photoionization in radiofrequency ion trap". In: *Applied Physics B* 105.4 (May 2011), pp. 729–740. DOI: 10.1007/s00340-011-4576-2.

[76] A. Banerjee, U. D. Rapol, D. Das, A. Krishna, and V. Natarajan. "Precise measurements of UV atomic lines: Hyperfine structure and isotope shifts in the 398.8 nm line of Yb". In: *Europhysics Letters (EPL)* 63.3 (Aug. 2003), pp. 340–346. DOI: 10.1209/epl/i2003-00543-x. arXiv: 0307091 [physics].

[77] S. Olmschenk. "Quantum teleportation between distant matter qubits". PhD thesis. University of Michigan, 2009.

[78] N. Yu and L. Maleki. "Lifetime measurements of the 4f15 5d metastable states in single ytterbium ions". In: *Physical Review A* 61.2 (Jan. 2000), p. 022507. DOI: 10.1103/PhysRevA.61.022507.

[79] R. W. Berends, E. H. Pinnington, and B. Guo. “Beam-laser lifetime measurements for four resonance levels of Yb II”. In: *Journal of Physics B:* 701 (1993). DOI: 10.1088/0953-4075/26/20/003.

[80] Y. Ibaraki, U. Tanaka, and S. Urabe. “Detection of parametric resonance of trapped ions for micromotion compensation”. In: *Applied Physics B: Lasers and Optics* 105.2 (2011), pp. 219–223. DOI: 10.1007/s00340-011-4463-x.

[81] B. E. A. Saleh and M. C. Teich. *Fundamentals of photonics*. 2nd. Wiley, 2007.

[82] A. E. Siegman. *Lasers*. University Science Books, 1986.

[83] H. Kogelnik and T. Li. “Laser beams and resonators”. In: *Proceedings of the IEEE* 5.10 (1966), pp. 1550–1567. DOI: 10.1109/PROC.1966.5119.

[84] H. Takahashi, J. Morphew, F. Oručević, A. Noguchi, E. Kassa, and M. Keller. “Novel laser machining of optical fibers for long cavities with low birefringence.” In: *Optics express* 22.25 (2014), pp. 31317–28. DOI: 10.1364/OE.22.031317. arXiv: 1501.0145.

[85] J. Gallego, S. Ghosh, S. K. Alavi, W. Alt, M. Martinez-Dorantes, D. Meschede, and L. Ratschbacher. “High-finesse fiber Fabry-Perot cavities: stabilization and mode matching analysis”. In: *Applied Physics B* 122.3 (2016), pp. 1–14. DOI: 10.1007/s00340-015-6281-z.

[86] K. Ott, S. Garcia, R. Kohlhaas, K. Schüppert, P. Rosenbusch, R. Long, and J. Reichel. “Millimeter-long fiber Fabry-Perot cavities”. In: *Optics Express* 24.9 (2016), p. 9839. DOI: 10.1364/OE.24.009839.

[87] W. B. Joyce and B. C. DeLoach. “Alignment of Gaussian beams”. In: *Applied Optics* 23.23 (1984), p. 4187. DOI: 10.1364/AO.23.004187.

[88] H. M. Meyer. “A fibre-cavity based photonic interface for a single ion”. PhD thesis. University of Cambridge, 2014.

[89] A. P. Vandevender, Y. Colombe, J. Amini, D. Leibfried, and D. J. Wineland. “Efficient fiber optic detection of trapped ion fluorescence”. In: *Physical Review Letters* 105.2 (2010), pp. 1–4. DOI: 10.1103/PhysRevLett.105.023001. arXiv: 1004.0668.

[90] Noliac. *Piezo basics*. URL: http://www.noliac.com/fileadmin/user_upload/documents/Tutorials/Tutorials_Piezo_basics.pdf (visited on 10/07/2016).

[91] G. Rempe, R. J. Thompson, H. J. Kimble, and R. Lalezari. "Measurement of ultralow losses in an optical interferometer." In: *Optics letters* 17.5 (1992), pp. 363–365. DOI: 10.1364/OL.17.000363.

[92] M. Cetina, A. Bylinskii, L. Karpa, D. Gangloff, K. M. Beck, Y. Ge, M. Scholz, A. T. Grier, I. Chuang, and V. Vuletić. "One-dimensional array of ion chains coupled to an optical cavity". In: *New Journal of Physics* 15.5 (May 2013), p. 053001. DOI: 10.1088/1367-2630/15/5/053001. arXiv: 1302.2904.

[93] D. Gangloff, M. Shi, T. Wu, A. Bylinskii, B. Braverman, M. Gutierrez, R. Nichols, J. Li, K. Aichholz, M. Cetina, L. Karpa, B. Jelenković, I. Chuang, and V. Vuletić. "Preventing and reversing vacuum-induced optical losses in high-finesse tantalum (V) oxide mirror coatings". In: *Optics Express* 23.14 (2015), p. 18014. DOI: 10.1364/OE.23.018014. arXiv: arXiv:1505.03381v1.

[94] J. M. Bennett. "Recent developments in surface roughness characterization". In: *Measurement Science and Technology* 3.12 (Dec. 1992), pp. 1119–1127. DOI: 10.1088/0957-0233/3/12/001.

[95] A. Bick, C. Staarmann, P. Christoph, O. Hellmig, J. Heinze, K. Sengstock, and C. Becker. "The role of mode match in fiber cavities". In: *Review of Scientific Instruments* 87.1 (2016), p. 013102. DOI: 10.1063/1.4939046. eprint: http://dx.doi.org/10.1063/1.4939046.

[96] J. Hollenshead and L. Klebanoff. "Modeling radiation-induced carbon contamination of extreme ultraviolet optics". In: *Journal of Vacuum Science and Technology B: Microelectronics and Nanometer Structures* 24.1 (2006), p. 64. DOI: 10.1116/1.2140005.

[97] W. W. Macalpine and R. O. Schildknecht. "Coaxial Resonators with Helical Inner Conductor". In: *Proceedings of the IRE* 47.12 (Dec. 1959), pp. 2099–2105. DOI: 10.1109/JRPROC.1959.287128.

[98] L. Ricci, M. Weidemueller, T. Esslinger, A. Hemmerich, C. Zimmermann, V. Vuletić, W. Koenig, and T. W. Haensch. "A compact grating-stabilized diode laser system for atomic physics". In: *Optics Communications* 117.5-6 (1995), pp. 541–549. DOI: 10.1016/0030-4018(95)00146-Y.

[99] E. Black. *Notes on pound-drever-hall technique*. Tech. rep. 617. LIGO, 1998.

[100] S. A. Webster, M. Oxborrow, and P. Gill. "Vibration insensitive optical cavity". In: *Physical Review A* 75.1 (Jan. 2007), p. 011801. DOI: 10.1103/PhysRevA.75.011801.

[101] A. Kell. “Frequenzverdopplung eines Lasers”. Bachelor’s thesis. University of Bonn, 2014.

[102] M. Steiner. “A Single Ion Inside a Miniature Cavity”. PhD thesis. University of Cambridge, 2014.

[103] M. J. Madsen. “Advanced Ion Trap Development and Ultrafast Laser-Ion Interactions”. PhD thesis. University of Michigan, 2006.

[104] T. Williams. *The Optical Transfer Function of Imaging Systems*. Series in Optics and Optoelectronics. CRC Press, 1998.

[105] S. X. Wang, G. Hao Low, N. S. Lachenmyer, Y. Ge, P. F. Herskind, and I. L. Chuang. “Laser-induced charging of microfabricated ion traps”. In: *Journal of Applied Physics* 110.10 (2011), pp. 1–8. DOI: 10.1063/1.3662118. arXiv: 1108.0092.

[106] S. Ritter. “Probing coherence during Bose-Einstein condensation”. PhD thesis. ETH Zurich, 2007.

[107] R. Hanbury Brown and R. Q. Twiss. “Correlation between Photons in two Coherent Beams of Light”. In: *Nature* 177.4497 (Jan. 1956), pp. 27–29. DOI: 10.1038/177027a0.

[108] M. Dagenais and L. Mandel. “Investigation of two-time correlations in photon emissions from a single atom”. In: *Physical Review A* 18.5 (1978). DOI: 10.1103/PhysRevA.18.2217.

[109] R. Loudon. *The Quantum Theory of Light*. Oxford University Press, 2000.

[110] P. M. Alsing, D. A. Cardimona, and H. J. Carmichael. “Suppression of fluorescence in a lossless cavity”. In: *Physical Review A* 45.3 (Feb. 1992), pp. 1793–1803. DOI: 10.1103/PhysRevA.45.1793.

[111] H. Tanji-Suzuki, I. D. Leroux, M. H. Schleier-Smith, M. Cetina, A. T. Grier, J. Simon, and V. Vuletić. “Interaction between Atomic Ensembles and Optical Resonators”. In: *Advances in Atomic, Molecular and Optical Physics*. Vol. 60. Elsevier, 2011, pp. 201–237. DOI: 10.1016/B978-0-12-385508-4.00004-8.

[112] Y. H. Lien, G. Barontini, M. Scheucher, M. Mergenthaler, J. Goldwin, and E. A. Hinds. “Uncovering Coherence Effects in an Overdamped Quantum System”. In: *arXiv preprint* (July 2016), pp. 1–8. arXiv: 1607.02362.

[113] D. J. Berkeland and M. G. Boshier. “Destabilization of dark states and optical spectroscopy in Zeeman-degenerate atomic systems”. In: *Physical Review A* 65.3 (Feb. 2002), p. 033413. DOI: 10.1103/PhysRevA.65.033413.

[114] S. Ejtemaee, R. Thomas, and P. C. Haljan. “Optimization of Yb+ fluorescence and hyperfine-qubit detection”. In: *Physical Review A* 82.6 (Dec. 2010), p. 063419. DOI: 10.1103/PhysRevA.82.063419.

[115] S. Olmschenk, K. C. Younge, D. L. Moehring, D. N. Matsukevich, P. Maunz, and C. Monroe. “Manipulation and detection of a trapped Yb+ hyperfine qubit”. In: *Physical Review A* 76.5 (Nov. 2007), pp. 1–9. DOI: 10.1103/PhysRevA.76.052314.

[116] A. H. Myerson, D. J. Szwer, S. C. Webster, D. T C Allcock, M. J. Curtis, G. Imreh, J. A. Sherman, D. N. Stacey, A. M. Steane, and D. M. Lucas. “High-Fidelity Readout of Trapped-Ion Qubits”. In: *Physical Review Letters* 100.20 (May 2008), p. 200502. DOI: 10.1103/PhysRevLett.100.200502. arXiv: 0802.1684.

[117] R. Noek, G. Vrijsen, D. Gaultney, E. Mount, T. Kim, P. Maunz, and J. Kim. “High speed, high fidelity detection of an atomic hyperfine qubit.” In: *Optics letters* 38.22 (Nov. 2013), pp. 4735–8. DOI: 10.1364/OL.38.004735.

[118] P. T. H. Fisk, M. J. Sellars, M. A. Lawn, and G. Coles. “Accurate measurement of the 12.6 GHz ”clock” transition in trapped 171Yb+ ions”. In: *IEEE Transactions on Ultrasonics, Ferroelectrics and Frequency Control* 44.2 (Mar. 1997), pp. 344–354. DOI: 10.1109/58.585119.

[119] B. B. Blinov, D. L. Moehring, L. M. Duan, and C. Monroe. “Observation of entanglement between a single trapped atom and a single photon”. In: *Nature* 428.March (2004), pp. 153–157. DOI: 10.1038/nature02377.

[120] D. Hucul, I. V. Inlek, G. Vittorini, C. Crocker, S. Debnath, S. M. Clark, and C. Monroe. “Modular entanglement of atomic qubits using photons and phonons”. In: *Nature Physics* 11.1 (Nov. 2014), pp. 37–42. DOI: 10.1038/nphys3150. arXiv: 1403.3696.

[121] A. Van Rynbach, P. Maunz, and J. Kim. “An Integrated Mirror and Surface Ion Trap with a Tunable Trap Location”. In: (Aug. 2016), pp. 1–5. arXiv: 1608.06923.

[122] P. Kómár, E. M. Kessler, M. Bishof, L. Jiang, A. S. Sørensen, J. Ye, and M. D. Lukin. “A quantum network of clocks”. In: *Nature Physics* 10.8 (2014), pp. 582–587. DOI: 10.1038/nphys3000. arXiv: arXiv:1310.6045v1.

[123] H. Rütz, K. H. Luo, H. Suche, and C. Silberhorn. "Towards a quantum interface between telecommunication and UV wavelengths: design and classical performance". In: *Applied Physics B* 122.1 (Jan. 2016), p. 13. DOI: 10.1007/s00340-016-6325-z. arXiv: 1507.08802.

[124] S. Kasture, F. Lenzini, B. Haylock, A. Boes, A. Mitchell, E. W. Streed, and M. Lobino. "Frequency conversion between UV and telecom wavelengths in a lithium niobate waveguide for quantum communication with Yb+ trapped ions". In: (June 2016). arXiv: 1606.08127.

[125] K. De Greve, L. Yu, P. L. McMahon, J. S. Pelc, C. M. Natarajan, N. Y. Kim, E. Abe, S. Maier, C. Schneider, Martin Kamp, Sven Höfling, Robert H. Hadfield, Alfred Forchel, M. M. Fejer, and Yoshihisa Yamamoto. "Quantum-dot spin-photon entanglement via frequency downconversion to telecom wavelength". In: *Nature* 491.7424 (Nov. 2012), pp. 421–425. DOI: 10.1038/nature11577.

[126] K. Nagayama, M. Kakui, M. Matsui, T. Saitoh, and Y. Chigusa. "Ultra-low-loss (0.1484 dB/km) pure silica core fibre and extension of transmission distance". In: *Electronics Letters* 38.20 (2002), p. 1168. DOI: 10.1049/el:20020824.

[127] H.-J. Briegel, W. Dür, J. I. Cirac, and P. Zoller. "Quantum Repeaters: The Role of Imperfect Local Operations in Quantum Communication". In: *Physical Review Letters* 81.26 (1998), pp. 5932–5935. DOI: 10.1103/PhysRevLett.81.5932. arXiv: 9803056v1 [quant-ph].

[128] S. Muralidharan, L. Li, J. Kim, N. Lütkenhaus, M. D. Lukin, and L. Jiang. "Optimal architectures for long distance quantum communication". In: *Scientific Reports* 6.November 2015 (Feb. 2016), p. 20463. DOI: 10.1038/srep20463. arXiv: 1509.08435.

[129] C. H. Bennett, G. Brassard, S. Popescu, B. Schumacher, J. A. Smolin, and W. K. Wootters. "Purification of Noisy Entanglement and Faithful Teleportation via Noisy Channels". In: *Physical Review Letters* 76.5 (Jan. 1996), pp. 722–725. DOI: 10.1103/PhysRevLett.76.722. arXiv: 9511027 [quant-ph].

[130] W. Dür and H.-J. Briegel. "Entanglement Purification for Quantum Computation". In: *Phys. Rev. Lett.* 90.6 (Feb. 2003), p. 67901. DOI: 10.1103/PhysRevLett.90.067901. arXiv: 0210069 [quant-ph].

[131] R. Nigmatullin, C. J. Ballance, N. de Beaudrap, and S. C. Benjamin. “Minimally complex ion traps as modules for quantum communication and computing”. In: (Apr. 2016), pp. 1–15. arXiv: 1605.00111.

[132] D. I. Cho, S. Hong, M. Lee, and T. Kim. “A review of silicon microfabricated ion traps for quantum information processing”. In: *Micro and Nano Systems Letters* 3.1 (Dec. 2015), p. 2. DOI: 10.1186/s40486-015-0013-3.

[133] G. Wilpers, P. See, P. Gill, and A. G. Sinclair. “A monolithic array of three-dimensional ion traps fabricated with conventional semiconductor technology”. In: *Nature Nanotechnology* 7.9 (July 2012), pp. 572–576. DOI: 10.1038/nnano.2012.126.

[134] E. Hecht. *Optics*. 4th. Addison-Wesley, 2002.

[135] R. Bhandari. “Transpose symmetry of the Jones matrix and topological phases”. In: *Optics Letters* 33.8 (2008), pp. 854–856. DOI: 10.1364/OL.33.000854.